THE UNIVERSITY OF MANITOBA

ON LIQUATION CRACKING OF CAST INCONEL 738LC SUPERALLOY WELDS

OLANREWAJU AKANBI OJO

A Dissertation Submitted to the Faculty of Graduate Studies in Partial Fulfillment of the requirements for the degree of

Doctor of Philosophy

Department of Mechanical and Manufacturing Engineering

Winnipeg, Manitoba.

DECEMBER 2004

Your file Votre référence
ISBN: 0-612-97299-2
Our file Notre référence
ISBN: 0-612-97299-2

THE UNIVERSITY OF MANITOBA

FACULTY OF GRADUATE STUDIES

*****

COPYRIGHT PERMISSION

On Liquation Cracking of Cast Inconel 738LC Superalloy Welds

BY

Olanrewaju Akanbi Ojo

A Thesis/Practicum submitted to the Faculty of Graduate Studies of The University of Manitoba in partial fulfillment of the requirement of the degree

Of

DOCTOR OF PHILOSOPHY

ACKNOWLEDGMENTS

I would like express my gratitude to my adviser, Dr. M. C. Chaturvedi, first of all, for giving me the opportunity to work on this interesting project and his valuable guidance, timely suggestions, encouragement and support. I acknowledge Dr. N. L. Richards for the several helpful inputs and encouragement at various stages of this research. I acknowledge the financial support provided by Standard Aero Ltd, Bristol Aerospace, Boeing Canada Technologies Ltd, Manitoba Aerospace Association etc in support of this research project and by the University of Manitoba and NSERC in the form of graduate fellowship and scholarship. Sincere appreciation is extended to John Van Dorp, Don Mardis, Mike Boskwick and Dan, for their technical assistance.

I express my greatest appreciation to God almighty, the source of my wisdom and strength. Finally, I would like to thank my wife Sumbo for her patience, love and understanding throughout my studentship at the University of Manitoba.

ABSTRACT

The present dissertation reports the findings of a study on liquation cracking of cast IN 738LC superalloy welds. Microstructures of the base alloy, heat affected zone (HAZ) and fusion zone of welded specimens and Gleeble simulated HAZs were examined and characterized by the use of standard metallographic techniques involving optical microscopy, electron microprobe analysis, analytical scanning electron microscopy and analytical transmission electron microscopy. The hot ductility of the alloy in solution heat treated and overaged heat treated conditions was evaluated by the use of Gleeble thermo-mechanical simulation system.

Contrary to the generally accepted view that solidification in IN 738LC is completed by γ-γ' eutectic formation, terminal solidification reaction products consisting of M_3B_2, Ni-Zr and Ni-Ti based intermetallic compounds were observed in front of γ-γ' eutectic within interdendritic regions of the as-cast alloy, which was observed to be responsible for the incipient melting during high temperature heat treatment of the alloy. Likewise, analytical transmission electron microscopy revealed the occurrence of M_3B_2 and Ni_7Zr_2 ahead of interdendritic γ-γ' eutectic in the fusion zone of welded specimens, consideration of which, are suggested to be pertinent to the development of optimum post weld heat treatment for the alloy. A pseudo-ternary solidification diagram based on Ni-Ti-C system is adapted for IN 738 alloy, which adequately explains the as-solidified microstructures observed in the as-cast alloy as well as in the weld-metal zone.

Careful analytical electron microscopy examination of welded materials revealed formation of resolidified constituents along microfissured grain boundaries in the HAZs thereby indicating that HAZ cracking in this alloy involves liquation cracking.

Constitutional liquation of secondary solidification constituents (MC carbides, M_2SC sulphocarbide and M_3B_2 borides, γ-γ' eutectic) and γ' precipitate particles, which were present in the pre-weld specimens in considerable volume fraction, were found to be the vital cause of grain boundary liquation and the resultant intergranular microfissuring in the HAZs. Constitutional liquation of γ' precipitate particles, which is the major strengthening phase of this alloy and in most other precipitation hardened nickel-based superalloys, was observed and reported for the first time in the present work. Liquation of these phases, as well as characteristics of the intergranular liquid film contributing to the alloy's low resistance to HAZ cracking were discussed. Contrary to the generally accepted view that primary γ' precipitates undergo complete solid state dissolution in the HAZ regions that experienced peak temperatures above γ' solvus temperature, it was found that the particles constitutionally liquated above this temperature in IN 738, increased the volume of intergranular liquid film, and restricted the occurrence of grain boundary liquid film migration. These factors consequently, resulted in either microfissuring and/or formation of re-solidified eutectic constituents along such liquated grain boundaries, which could be the potential sites for crack initiation and/or propagation during subsequent post weld heat treatment. Gleeble hot ductility test results confirmed the effect of grain boundary liquation in damaging the on-cooling ductility of the alloy, and thus increasing the alloy's propensity to microfissuring under induced welding stresses.

Appropriate consideration of the different types of liquation phenomena discussed in this dissertation in conjunction with the effects of rapid γ' precipitation kinetics is

indispensable towards development of appropriate pre-weld and post weld heat treatments to minimize HAZ microfissuring in IN 738 weldments.

TABLE OF CONTENTS

List of Figures

List of Tables

Chapter 1

Introduction

Superalloys were developed and have been improved over the past 50 years for applications involving stringent operating conditions such as those experienced by components of gas turbine engines. Inconel 738 is a nickel base multi-component superalloy strengthened mainly by precipitation of intermetallic $Ni_3(Al, Ti)$ γ' phase. Its development fulfills the need for a structurally stable cast alloy combining the strength of alloy IN 713C with sulphidation and oxidation resistance of Udimet 500 [1]. It is extensively used commercially in hot sections of aero engines and land based gas turbines due to its excellent elevated temperature strength and remarkable hot corrosion resistance. The severe and harsh operating environment, however, causes the alloy to suffer various forms of damage in service such as creep, fatigue thermo-mechanical fatigue and surface degradation. Damaged components contribute to a significant decrease in operating efficiency and general degradation of structural integrity. In most cases, it is more economically viable to carry out a repair to return the degraded parts to a serviceable condition rather than total replacement due to higher manufacturing cost and longer delivery time of new components.

Welding is a desirable economical and versatile technique for joining nickel base superalloys, both during fabrication as well as to repair the damaged sections. Unfortunately, application of fusion welding to fabrication and repair of parts made of precipitation hardened nickel base superalloys like IN 738 has been severely restricted. This is because these alloys, especially those containing substantial amount of Al & Ti (> 6wt %), are highly susceptible to weld cracking predominantly in the heat affected zone

(HAZ) during welding and post weld heat treatment [2]. HAZ cracking during welding of IN 738 has been attributed mostly to a large shrinkage stress due to rapid γ' precipitation in addition to thermo-mechanical stresses generated during cooling from welding temperature [3]. However, it is generally known that weld cracking results from competition between mechanical driving force for cracking (stress/strain generation) and the material's intrinsic resistance to cracking. It has been found that liquation which could occur by different mechanisms is the primary cause of low HAZ crack resistance in most austenitic alloys including precipitation hardened Ni base superalloys [4]. Concurrent presence of continuous or semi-continuous liquid film on HAZ grain boundaries and welding stresses during weld cooling could results in HAZ liquation cracking by grain boundary separation due to reduction in the cohesive strength of liquated grain boundaries.

In addition, post weld heat treatment cracking, which affects all precipitation hardened superalloys, has been reported to initiate mainly in the HAZ regions that had liquated during welding operation [5]. It has been suggested that fully austenitic alloys that contain Nb and/or Ti can be highly susceptible to HAZ liquation cracking due to the formation of Nb and/or Ti rich low melting intergranular liquids [6]. In addition to cracking, another problem often associated with superalloy weldment is deterioration in its mechanical properties, which could also be related to liquation and formation of re-solidified product along the grain boundaries.

As fundamental as liquation phenomenon is to weld HAZ cracking and weldment structural integrity, very little information is available about its occurrence in IN 738 alloy. Considering the alloy's composition, substantial volume of possible liquating

phases, coarse grain structure and marked level of interdendritic segregation in the cast alloy, liquation can be expected to be a significant contributing factor to the alloy's high propensity to HAZ cracking. In addition, no comprehensive study of the fusion zone microstructures of this alloy is available, which is fundamental to understand the response of the alloy to post weld heat treatments, which are designed to modify the as-weld microstructures and relax the residual welding stresses in order to impart optimum reliable properties. Consequently, this PhD research programme is aimed at investigating the occurrence and nature of liquation in the weld HAZ of IN 738 alloy and its contribution to cracking and also to characterize the microstructures developed in the fusion zone of tungsten inert gas (TIG) welded alloy. This information will be valuable in developing pre and post weld heat treatments to maximize the properties of the alloy.

Chapter 2

Literature Review

A review of some aspect of physical metallurgy of Inconel 738 superalloy, fundamental theory of welding metallurgy of nickel base superalloy, the associated welding defects and weldability testing techniques are presented in this chapter. The literature is followed by the objectives of the present research.

2.1 Physical Metallurgy of IN 738 alloy

2.1.1 Introduction

The alloy IN 738 is a vacuum melted and investment cast alloy, which was developed at the Paul D. Merica research laboratory [1]. Hot Isostatic Processing (HIP) is usually applied to the cast alloy to partially eliminate micro-porosity formed during ingot solidification. There are basically two types of cast IN 738, low carbon version (C ~ 0.09 - .13 wt %) designated as IN-738 LC and a high carbon version (~0.15 – 0.20 wt %) called IN-738C [7]. The low carbon IN-738 LC also has a lower Zr content, which improves the alloy's castability in large section sizes, while tensile and stress rupture properties are not appreciably affected [7]. In critical components, trace elements such as selenium, thallium, tellurium, lead and bismuth, need to be held to very small (ppm) levels. This is accomplished by a careful selection of raw materials coupled with optimum melting practise. Table 2.1 [7] shows nominal composition of cast IN-738LC, while Table 2.2 [7] lists its mechanical & physical properties. It is important to note, however that, exposure to high temperatures has a significant effect on the alloy properties. Figure 2.1a demonstrates the effect of long term exposure on hardness and

Table 2.1 [7]

Nominal Composition of IN-738 Superalloy

Element	High Carbon IN-738C (Wt%)	Low Carbon IN-738LC (Wt%)
Carbon	0.17	0.11
Cobalt	8.50	8.50
Chromium	16.00	16.00
Molybdenum	1.75	1.75
Tungsten	2.60	2.60
Tantalum	1.75	1.75
Niobium	0.90	0.90
Aluminium	3.40	3.40
Titanium	3.40	3.40
Boron	0.010	0.010
Zirconium	0.10	0.05
Iron	LAP*	LAP*
Manganese	LAP	LAP
Silicon	LAP	LAP
Sulphur	LAP	LAP
Nickel	Balance (61)	Balance (61)

*Low as possible

Table 2.2 [7]

Mechanical and Physical Properties of Alloy IN-738

Temperature (°C)	Yield Strength (MPa)	Ultimate Tensile Strength (MPa)	Elongation (%)
21	951	1096	5.5
649	910	1055	7
760	793	965	6.5
871	552	772	11
982	345	455	13
Melting Range		1232 – 1315°C	
Density		8.11gm/cm^3	
Coefficient of Thermal Expansion		15.36 x 10^{-6} / °C	
Young Modulus		200.2 GPa	
Shear Modulus		78 GPa	
Poisson's Ratio		0.29	

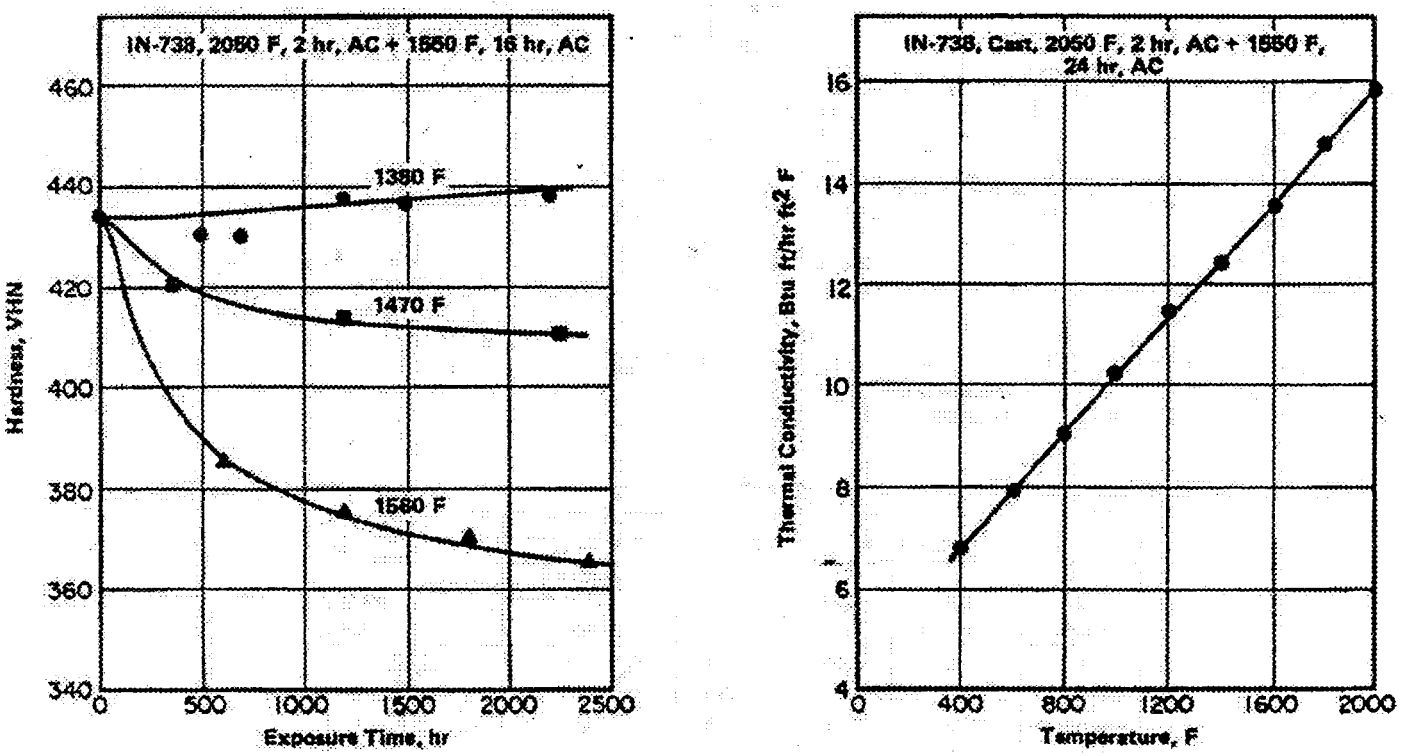

a

b

Figure 2.1 (a) Effects Of Long –Time Exposures To Temperature on Hardness at Room Temperature (b) Variation in thermal Conductivity with Temperature [8]

and Figure 2.1b shows the variation in thermal conductivity of the alloy with temperature [8]. Prior to use in service, Inconel 738 is normally given a heat treatment which consists solution heat treatment at 1120°C for 2 hrs air, cooled followed by a 24hr treatment at 845°C then air cooled.

2.1.2 Microstructure of Cast IN 738

Cast IN 738 alloy has a coarse grain structure (average size 1 - 3mm) that either directly or indirectly affects the nature of precipitates on its grain boundaries and, the mechanical properties of the alloy. The serrated grain boundary structure in the as-cast condition is preserved after the standard heat treatment and is known to provide a favourable balance between the intragranular and grain boundary strength [9]. The following major phases present in cast IN-738 contribute largely to its excellent high temperature strength.

1) Gamma Matrix (γ): This is the FCC nickel base austenitic matrix that contains high percentage of solid solution elements such as Co, Cr, Mo, W, Al & Ti. These elements, which differ from Ni in atomic diameter by 1 – 15 %, normally occupy substitutional atomic position in Ni crystal, producing a distorted lattice with spherical symmetrical stress field. This field can interact with the stress field around a dislocation, producing an elastic dislocation – solute atom interaction and provides solid solution strengthening.
2) Gamma Prime (γ'): The major contribution to the high strength of IN-738 is from the $\gamma' Ni_3$ (Al, Ti) precipitates. Ni_3 (Al, Ti) is an $L1_2$ - type phase, with ordered FCC crystal structure. It forms in alloys containing Ti & Al in amounts exceeding

their solubility in Ni. It has been suggested [10], that composition of γ' in IN-738 is: $(Ni_{.922}Co_{.058}Cr_{.017}Mo_{.002}W_{.002})(Al_{.518}Ti_{.352}Ta_{.046}Nb_{.41}W_{.014}Cr_{.020})$

The similarity between its crystal structure and that of the γ matrix and closeness in their lattice parameters causes a rapid aging response, with precipitates' growth occurring largely by the growth of large particles at the expense of small ones, known as Oswald ripening, rendering the γ' precipitates to be very stable at elevated temperature. Ardell [11] in his review on precipitation hardening, concluded that in Ni base superalloys, the γ' precipitation occurs by homogeneous nucleation followed by growth and coarsening, during which, the volume fraction of precipitates remains constant. Footner and Richards [12] discovered that the variation of γ' particle size with exposure time was complex, owing to the initial partial solution treatment and subsequent aging which resulted in the presence of a distinct 'bimodal distribution' of cuboidal & spheroidal γ' precipitates. The larger population (primary γ') are found to maintain a constant mean size on aging. In addition to the discrete γ' precipitate particles, γ-γ' eutectic product also form within the interdendritic regions of the alloy due to elemental microsegregation during ingot solidification.

3) Carbides: Carbon content is an important parameter in determining the amount of carbides in the alloy IN-738. Carbides form when the level of carbon concentrations is above 0.05% [13]. It combines with reactive and refractory elements such as Ti, Ta and Nb to form MC carbides, which usually form in cast products during cooling and occur as discrete particles distributed heterogeneously both in intergranular and transgranular positions. The primary

FCC carbides are generally strong and stable with size ranging from one micron to a hundred microns. It has been suggested [10] that MC carbides have the formula: $(Ti_{.5},Ta_{.2},Nb_{.2},W_{.04},Mo_{.03},Cr_{.02})C$. During heat treatment and service, it decomposes and generates into lower carbides such as M_6C and $M_{23}C_6$ ($MC + \gamma' \rightarrow M_{23}C_6 + \gamma$). $M_{23}C_6$ also forms from excess free carbon, when cast ingot cools through its solvus range (1000°C – 1050°C). When the super-saturation of carbon is high, there is a tendency for it to form cellular grain boundary particles, whose distribution can be continuous in nature. It however tends to form as globules along grain boundaries at aging temperature of 950°C - 1025°C [14]. Grain boundary $M_{23}C_6$ are known to have either a positive or negative effect on the creep properties of the alloy depending on its morphology, size and distribution. Heavy and/or continuous network of grain boundary $M_{23}C_6$ particles enhance grain boundary sliding and crack propagation by boundary – matrix decohesion. Discrete particles on the other hand are known to improve the creep life and ductility. Rong et al [15], by high-resolution transmission electron microscopy, also observed the grain boundary $M_{23}C_6$ in IN-738 to be discontinuous irregular shaped precipitates.

Hoffelner et al [16] identified by X-ray diffraction analysis the occurrence of a few other minor phases: M_3B_2 type boride and M_2SC sulphocarbide in the alloy after heat treatments and, sigma (σ) phase after long time exposure of 20,000 hours at 788°C. The sigma (σ) phase is composed of closed-packed layers of atoms aligned with the octahedral planes of the FCC matrix and are known as a topologically closed packed (TCP) phase. It is has a detrimental effect on rupture strength and ductility of the alloy.

McColvin [17] studied the effect of standard heat treatment on phase morphology and creep rupture properties of IN 738. He reported that only the fine γ' particles from the dendrite core region went into solution during heat treatment at 1120°C due to the smaller Al and Ti concentration levels in the core regions. Very fine γ' particles, resulting from air cooling, formed in the dendrite core and also between the large interdendritic particles and coarsened with aging at 843°C resulting in "bimodal" particle size distribution. Stevens et al [18] have determined the γ' solvus temperature for a complete solutioning of interdendritic γ' particles to be 1170 ± 3 °C. They verified that aging at 827°C produces a maximum γ' volume fraction of 45% and peak hardness of 430VHN.

2.1.3 Strengthening Mechanism by γ' Phase

The main strengthening of high strength nickel base superalloys like IN 738 is from precipitation of coherent ordered γ' $Ni_3(Al, Ti)$ phase. In stoichiometric composition of Ni_3Al it has a lattice parameter of 3.589Å. Mechanical properties of nickel based superalloys are strongly influenced by the morphology, distribution and size of γ' precipitates in the γ matrix. Strength is related to the interactions between γ' particles and moving dislocations. In general, when the particle size is small the moving dislocations tend to shear the particle while it is by-passed when the size is large. When particles are sheared, yielding of the alloy seems to be controlled mainly by two factors (i) Order hardening and (ii) Coherency or Misfit Hardening.

Order Hardening

Ordering or chemical hardening by γ' occurs when the ordered γ' particles are sheared by a glide dislocation during which an antiphase boundary (APB) is created within the

particle. The first dislocation is followed by another dislocation, which restores the order within the particle. Consequently, the shearing of the ordered particles occurs by coupled pair of dislocations [19]. For a single dislocation shearing, the strength increment is given by [20].

$$\Delta\tau = \gamma_o^{3/2} / b\,[4fr/\pi T]^{1/2} \qquad (2.1)$$

and for the dislocation pair

$$\Delta\tau = \gamma_o / 2b\,\{[4\,\gamma_o\, fr/\pi T]^{1/2} - f\} \qquad (2.2)$$

where γ_o is the specific APB energy, r the average dimension of the particle intersected by a slip band, b the burgers vector of the matrix, f the volume fraction precipitates and T the line tension of a dislocation; since faults other than APBs may occur, the formula is more correct when considering Γ, the fault energy for shearing, instead of γ_o.

Coherency or Misfit Hardening

The coherency or misfit hardening mechanism is attributed to the interaction of glide dislocations with the elastic coherency stress field around coherent γ' precipitates. Small differences between the lattice parameter of the matrix and precipitates give rise to coherent precipitates causing coherency strains in the matrix, which contribute to the alloy strengthening. The coherency strains can be effective both during cutting and by-pass mechanisms. The increment in the critical resolved shear stress (CRSS) can be given by [21]:

$$\Delta\tau_{CRSS} = 3\,GE^{3/2}\,[hf/2b]^{1/2} \qquad (2.3)$$

where G is the shear modulus, E the constrained lattice strain, h the mean particle diameter, f the volume fraction of γ' particles. The role of γ-γ' interface in hardening

mechanism seems to be significant at very low strain rates as found in creep tests. A fine and uniform γ' dispersion maximises creep properties, as shown by Jackson et al [22]; dislocation-particle interaction increases with uniform fine precipitate distribution, as interparticle spacing decreases, resulting in a decrease in the minimum creep rate ε.

Beardmore et al [23] showed that in a series of Ni-Cr-Al alloys the effect of γ' volume fraction on the alloys mechanical properties depended on testing temperature. At temperatures above 900°C the flow stress was directly proportional to the amount of γ' while at temperatures below 500°C, there was a peak in strength at 25% γ' volume fraction. The presence of hyperfine γ' resulting from cooling from the aging temperature, was reported to be responsible for a larger part of the strength of the alloy. Furthermore, the mismatch between the elastic modulus of γ and γ' phase could also contribute to hardening during dislocation cutting mechanism.

Dislocation By-passing of γ'

As the size of γ' particles increase, there is a tendency for them to be by-passed by a moving dislocation either by looping or by dislocation climb; the critical size for the change in mechanism from cutting into by-passing depends on the alloy, and can vary from about 300Å to 2500Å, the higher sizes for alloys with high γ' volume fraction. The increment in the critical resolved shear stress (CRSS) due to dislocation looping is given by [24]:

$$\Delta\tau_{CRSS} = 0.2\ Gb\ \Phi\ 2/\lambda\ \ln h/2b \qquad (2.4)$$

where h is the mean particle diameter, Φ is the angle between Burgers vector and tangent to the dislocation line, λ the mean interparticle spacing, G the shear modulus of the

matrix lattice. This relationship, however, applies to only to particle sizes bigger than those corresponding to the peak strength. Figure 2.2 shows how hardness changes in a Ni-Cr-Al-Ti alloy with the mean particle diameter [25].

2.1.4. Precipitation of γ' in Cast Nickel Base Superalloy.

High strength precipitation hardened nickel base superalloys are typically composed of high volume fractions of γ' precipitate ranging from 10% to as much as 70% in third generation single crystal superalloys. It has been recognised that the precipitation of γ' is a continuous process involving the three classical stages of nucleation, growth and ripening [26]. At temperatures close to the solidus, the γ phase is able to dissolve relatively large amounts of γ' forming elements, but the solubility range decreases sharply as the temperature falls. Due to the very small lattice misfit between γ and γ' phases, the precipitate nuclei are coherent with the matrix and the energy required for nucleation is low. Consequently, precipitation occurs easily without the need for a large degree of supercooling. For large super-saturation, it is often difficult to prevent precipitation, even at very high cooling rates. It has been suggested, however, that for certain compositions, under conditions of rapid cooling, the transformation could involve spinodal decomposition [27]. In this situation, the separation into two distinct phases is preceded by compositional modulation and local ordering. The γ-γ' microstructure of nickel base superalloys can undergo drastic changes during high temperature heat treatments. When cooled from the solution treatment temperature, a wide variety of precipitate morphologies can be observed in these alloys. γ' precipitate morphology is

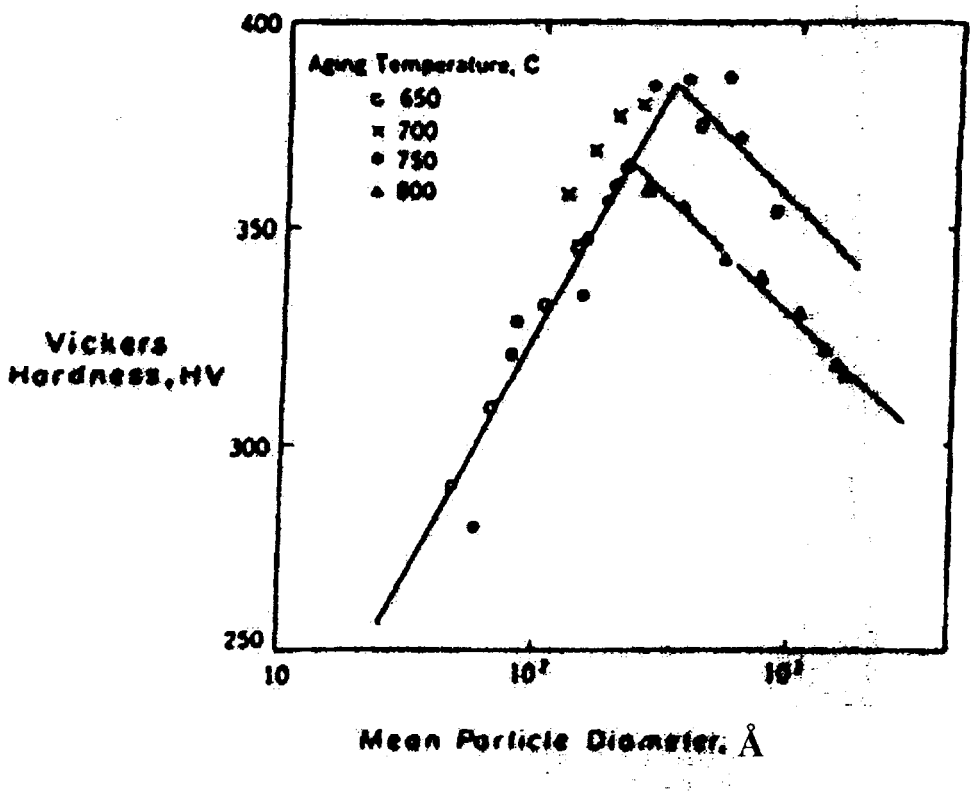

Figure 2.2: Effect of γ' particle size on hardness of Ni-Cr-Al-Ti alloys [25]

known to play an important role in influencing the properties of nickel base superalloys. During continuous cooling, the precipitates often change shape as they grow, spherical nuclei may develop into perfect cubes, which subsequently may evolve to "ogdoadically diced" cubes and more complex dendritic and star shapes, figures 2.3 and 2.4 [28]. The morphology of γ' precipitates evolves from different mechanisms [29]; (a) competitive coarsening in order to reduce the specific area of the γ-γ' interface (Oswald ripening) and (b) shape changes in order to minimize the sum of interfacial and elastic interaction energies. These mechanisms are important as long as the precipitates remain coherent. The associated microstructural changes are affected by the strong anisotropy of the two phases, γ and γ', the <001> directions being the softest. The equilibrium shapes result from the balance between interfacial and elastic energy contributions. The interfacial component is proportional to the γ/γ' interface area and tends to promote compact, isotropic shapes, while the elastic component is proportional to the particle volume and will favour faceting along the {001} softest planes. The magnitude of elastic energy depends not only on the precipitate volume but also on the degree of interaction between precipitates.

The γ' precipitate particles are believed to nucleate as spheres in order to minimize interfacial energy with low surface area/unit volume ratio. As the particles grow, the coherency strain increases and becomes significant, thus, the need to lower global internal energy leads to shape changes. The γ'size at which the initial shape transition occurs is influenced by the level of lattice mismatch (δ) between γ' phase and the γ matrix, which is given by:

$$\delta = 2\,(a_{\gamma'} - a_{\gamma}) / (a_{\gamma'} + a_{\gamma}) \qquad (2.5)$$

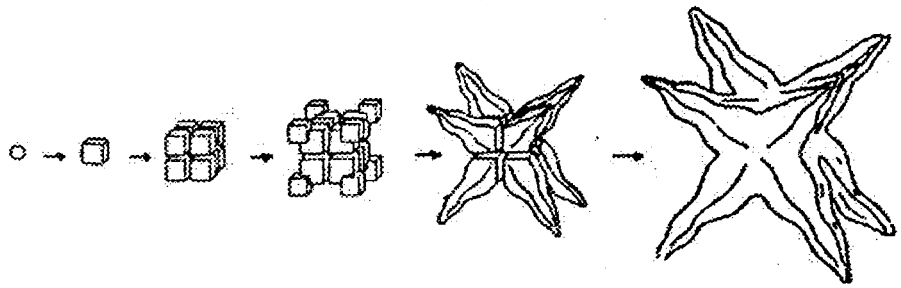

Interface controlled growth mechanism	Diffusion controlled growth mechanism
Coherent γ	Loss of coherency

Figure 2.3: Schematic diagram showing evolution of γ' during continuous cooling [28]

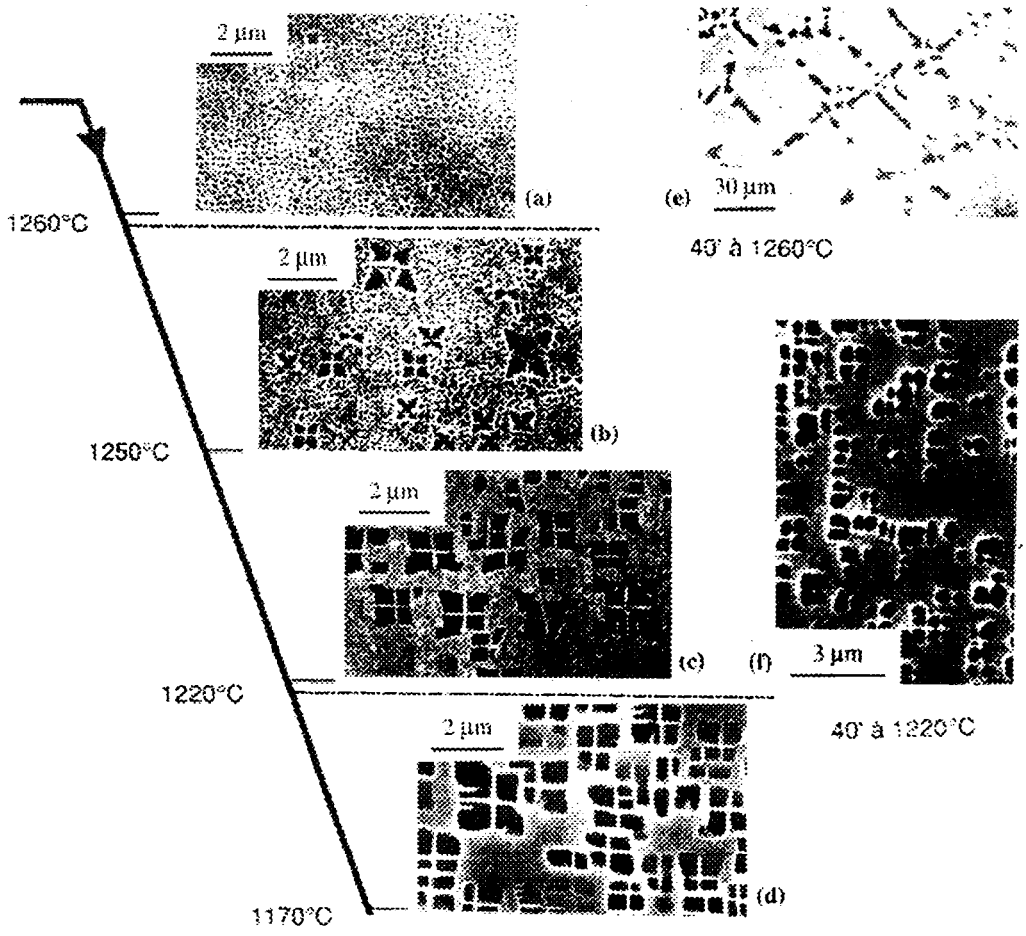

Figure 2.4 Micrograph showing evolution of γ' during continuous cooling [28]

where $a_{\gamma'}$ and a_{γ} are the lattice parameters for the γ' and γ phases respectively. The larger the lattice mismatch the smaller will be the size of γ' at which the transition take place. Ardell [29] reported that, in order for γ' to transform to cubes the lattice mismatch δ must be greater than 0.1%.

2.2 Welding

2.2.1 Welding of Superalloys

Welding can be defined as a process of joining two or more parts by means of heat and/or pressure, such that there is continuity in the nature of material between these parts. Fusion welding is defined as a type of welding process in which the weld is made between materials in a molten state without the application of pressure. A filler metal with melting temperature comparable to those of the parent materials may or may not be used. Fusion welding can be categorised into different types for example Gas Tungsten Arc Welding (GTAW), Submerged Arc Welding (SAW), Gas Metal Arc Welding (GMAW), Shielded Metal Arc Welding (SMAW), Resistance Welding (RW), Electron Beam Welding (EBW) and Laser Welding (LW). SMAW is a versatile process, though manual in nature and requires flux removal and has limited application to thin sections. GMAW uses a consumable electrode, can be inert-gas shielded, delivers high production rates and can be automated. RW can be automated but it requires lap-type joint and produces some deformation of the pieces being welded. The GTAW is one of the most versatile of the different welding processes and it can be performed manually or can be automated using filler metal or without filler (autogenous welding). EBW is performed in a vacuum chamber, which imposes size limitations on parts to be welded even though it

provides an ideal environment for producing contamination free welds. It is a high energy density welding process producing deep penetration (large depth to width ratio), low heat input and minimal distortion.

Since complicated components of the gas turbine engine cannot be manufactured completely as castings, forgings, wrought shaped or machined from solid pieces, it becomes necessary that a joining process be used during fabrication of various components. Fusion welding has been and will continue to be one of the main fabrication techniques for aero and land based turbine components made from nickel-based superalloys. Gas tungsten arc welding is one of the most commonly used method. It involves heating by producing an arc between a single tungsten electrode and the work piece by passage of electric current. Shielding from oxidation is obtained from a gas or gas mixture that flows around the tungsten electrode and over the work piece. Frequently used gases include argon and helium. Due to rapid heating and cooling, transient thermal strains and final residual stress, welding of nickel base superalloys can be plagued with various defects. Some of these defects such as oxide inclusions, lack of fusion, weld porosity and poor bead shape, are mainly a function of the practical application of welding process involved and are usually overcome without much difficulty. Much more harmful are the weld metal and heat affected zone cracks, which may occur during welding or subsequent heat treatment. Formation of crack in a weldment requires:

(1) That the microstructure of the material comprising the weldment contains a phase or combination of phases which possess a limited capacity to tolerate strains within some critical range of temperature.

(2) That the strain imposed unpon the weldment by combined action of restraints, thermal and shrinkage stresses within the critical range of temperature exceed the strain tolerance of the composite microstructure.

The first factor is primarily of metallurgical origin and is influenced by the constitution of the alloy and welding parameters. The second factor is strictly mechanical and could involve stresses produced by metallurgical phase transformations such as precipitation reaction. The complex metallurgical phenomenon accompanying welding can have dramatic effect on the mechanical properties and service behaviour of the weldment.

2.2.2 Microstructure of a Weld

A typical weld joint consists of weld metal zone also known as the fusion zone (FZ), a heat affected zone (HAZ) and the unaffected base metal surrounding the HAZ. This is illustrated in figure 2.5 [30], along with the stagnant layer of the FZ called the unmixed region, and the portion of the HAZ where some melting can occur called the partially melted zone. Heating and cooling rates of typical welding cycle are usually high often resulting in complex metallurgical reactions in both the fusion zone and the heat affected zone, which may in some situations impair the properties of the weldment. Cooling rates in welds may vary from 10 - 10^3 Ks^{-1} for conventional arc welding processes such as SMAW, SAW and GTAW. In the case of modern high-energy beam processes, such as electron beam and laser welding, cooling rates may vary from 10^3 – 10^6 Ks^{-1} depending on the welding parameters.

Interaction between a moving heat source and the metal part being joined in an autogenous welding process is shown schematically in figure 2.6 [31]. The shape of a

weld bead is primarily determined by the weld pool shape and size. Thermal conditions in and near the weld pool and the nature of fluid flow have been found to influence the size and shape of weld pool. In general, weld pool volume is influenced to a large extent by welding parameters. In the case of arc welding processes, the puddle shape changes from elliptical to tear drop shape as the welding speed increases. For high energy density processes the thermal gradients are steeper resulting in circular puddles at lower speeds and becoming more elongated and elliptical as welding speed increases. At high speeds it becomes tear drop shaped.

The geometry of weld bead is known to have large effect on the weld macro and microstructures [32]. In an elliptically and circularly shaped weld puddle, not only does the magnitude of the maximum thermal gradient change continuously from the fusion line to the weld centreline but also the direction of this gradient, as shown in figure 2.7 [33]. These invariably influence the grain structure development within the fusion zone during solidification. Changes in the puddle shape have been effectively used to refine fusion zone microstructure by controlling the welding parameters [32].

2.2.2.1 Fusion Zone

The solidification microstructures that develop in the fusion zone are often quite complex due to complete melting and re-solidification of the base metal. A weld zone may be considered as a small casting, often a continuous casting formed under special conditions; an intensely stirred liquid pool, high temperature gradients, rapid growth rates, intimate contact between the molten alloy and the mold including partial melting of

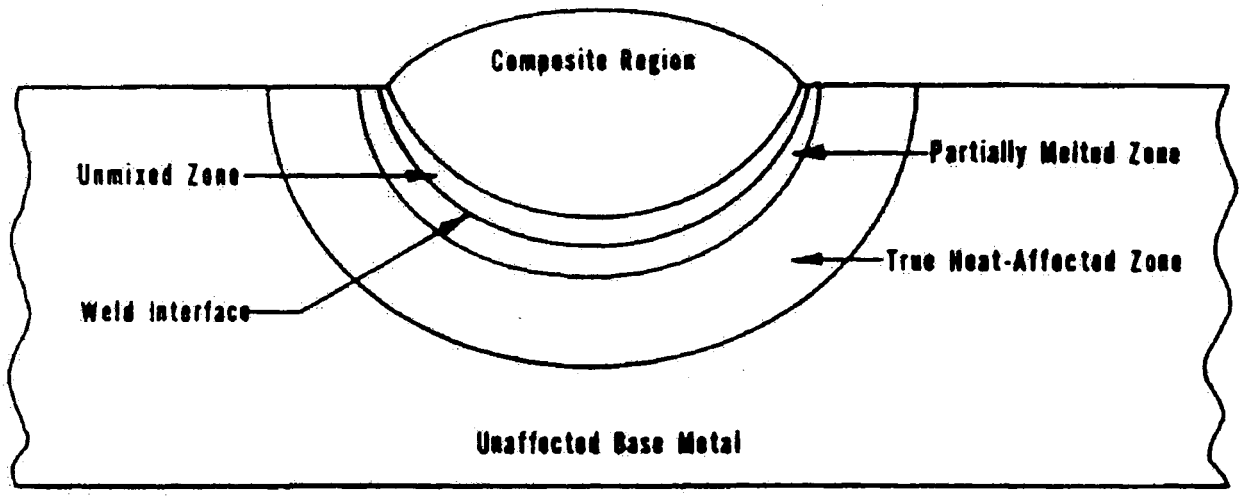

Figure 2.5: Schematic diagram showing different regions of a weld joint [30]

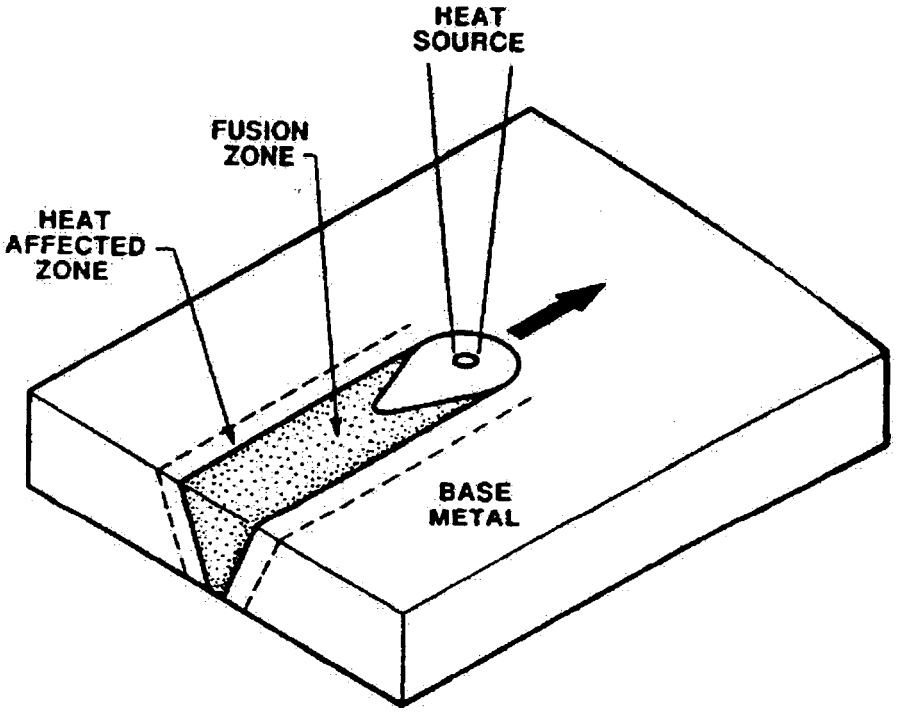

Figure 2.6 Schematic diagram of an autogenous welding process [31]

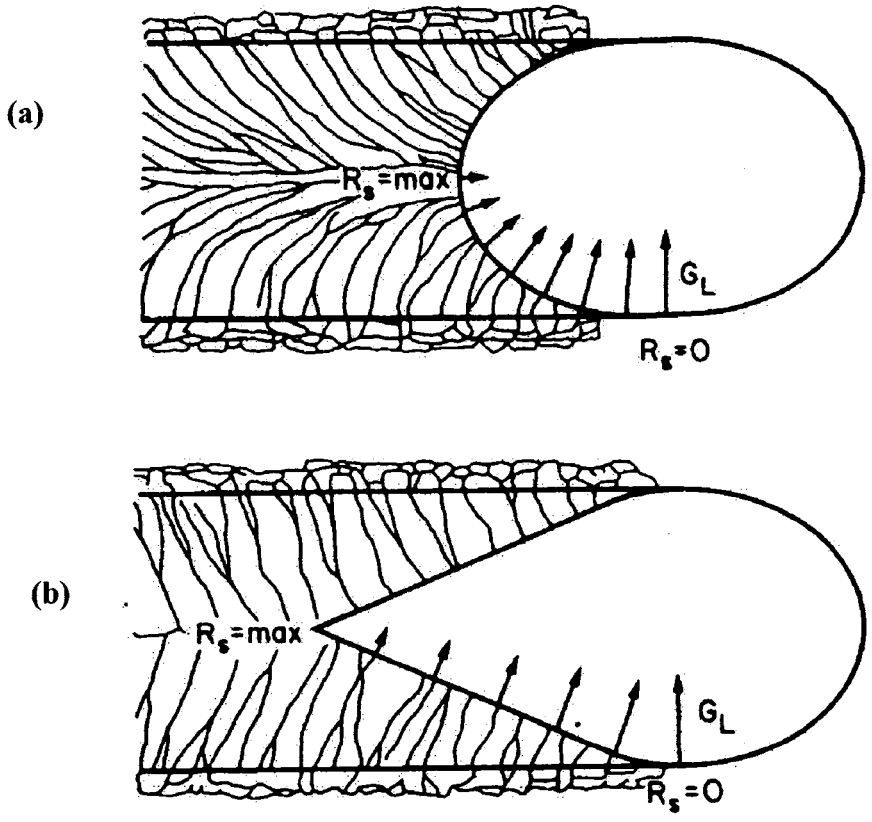

Figure 2.7: Variation of thermal gradient G_L and growth rate R_S along solidification front for (a) elliptical and (b) tear drop shaped weld pools [33].

the mold. The molten alloy freezes within a mold formed of the base metal by heterogeneous nucleation mechanism. Heterogeneous nucleation on a planar surface can be considered to illustrate the significant influence of preferred sites on solidification. As shown in figure 2.8 a balance between the energies of various types of surfaces involved is established such that;

$$\text{Cos } \beta = (\gamma_{ml} - \gamma_{sm}) / \gamma_{sl} \qquad (2.6)$$

where γ_{ml}, γ_{sm} and γ_{sl} are the surface energies for the metal/liquid, solid/metal and solid/liquid interfaces, respectively, and β is the contact angle between the solid particle and metal substrate. Welding involves a special case of heterogeneous nucleation. To a good approximation, $\gamma_{sm} = 0$ and $\gamma_{ml} = \gamma_{sl}$ since under autogenous welding conditions the molten metal composition is identical to the base material and initial growth occurs epitaxially as the heat of fusion is transferred to the base metal. Thus, Cos $\beta = 1$ as $\beta = 0$ and the nucleation barrier vanishes causing solidification to occur spontaneously below the liquidus temperature.

The base metal grain on the fusion boundary serves as a growth site for fusion zone grains, making the initial grain size of the fusion zone at the fusion line of the same order as the grain size of the base metal. In addition, the crystallographic orientation of each fusion grain will be the same as the orientation of the base metal on which it grows epitaxially. The grains at the fusion line grow in a direction roughly perpendicular to the fusion line by the addition of atoms from the liquid phase to the solid. The stability of the solidification front is critical in determining the microstructural characteristics within the fusion zone. During the growth of the solid, the microscopic shape of the solid/liquid interface is determined by the conditions in the immediate vicinity of the interface.

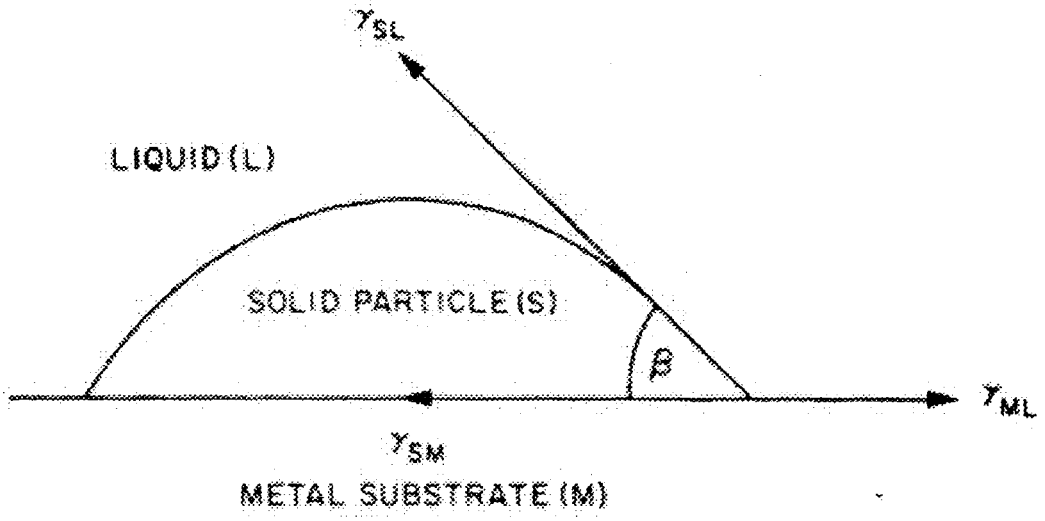

Figure 2.8: Surface forces present during heterogeneous nucleation of particle on solid substrate.

Theories have been developed for interface stability under equilibrium conditions at the interface. These theories and their modifications which consider non-equilibrium conditions at the interface can be extended to welds [31].

Several varieties of microstructural morphologies may develop because of the various growth forms that may exist during weld solidification. In general, these may be divided into planar, cellular and dendritic morphologies. A planar solid/liquid interface growth is controlled essentially by heat flow conditions and the direction of growth is perpendicular to the solidification front i.e. along the maximum thermal gradient. It is characterized by the lack of development of a substructure. Cellular growth is very similar to planar growth in that the direction of growth of the cells is controlled by heat flow conditions. This type of solidification is characterized by a growth front made up of many cells growing relatively uniformly parallel to one another. Dendritic growth is different from planar or cellular growth. It is controlled mainly by growth crystallography considerations. As the grains grow, there is a competition between the neighbouring grains. Some continue to grow while others do not and are terminated. The surviving grains are the ones that have preferred crystallographic axis closely aligned with the heat flow direction. In cubic alloys, the <100> directions are the preferred directions [34].

Dendritic growth is distinguished from cellular growth because cellular growth is antiparallel to heat flow direction but is not necessarily parallel to the easy growth directions. There are two major types of dendritic growth, columnar dendritic growth and equiaxed dendritic growth. Columnar dendritic growth is characterized by the growth of a packet of dendrites basically along the same direction. These essentially parallel dendrites combine to form one grain with well-developed substructure. Branching of these

dendrites may or may not be present. Without branching, columnar dendritic structure is very similar to cellular solidification structure and may, thus, be referred to as cellular solidification structure. Equiaxed dendritic growth, however, is characterized by the growth of dendrites of different orientations in a liquid cooled sufficiently below the liquidus temperature, so that spontaneous nucleation is possible. Neighbouring dendrites are not necessarily parallel to each other and therefore each dendrite comprises of a separate grain in the final solidified structure.

Any combination of columnar and equiaxed grains may form in a weld zone. Typically, weld zone grains are either totally columnar or columnar near the fusion the fusion line and change to equiaxed at the near centre. A transition from columnar to equiaxed grains is observed in large weld zones and in alloys with a wide freezing range. The formation of fine equiaxed grains is often desirable for optimum mechanical performance in metallurgical welds.

Dendrite Arm Spacing

The scale of solidification substructure, namely the cell, the primary and secondary arm spacings of dendrites is an important factor that affects the mechanical behaviour of weldments. It is an often-used measure of the effects of solidification conditions on the microstructure. Various studies have shown that the cell and dendrite arm spacings depend directly on the local solidification time [35,36]. Local solidification time is defined at any particular location in a casting or weld pool as the time from the start of solidification to the end of solidification. It is given by the relationship;

$$t_f = \Delta T' / GR \qquad (2.7)$$

where $\Delta T'$ is the non-equilibrium temperature range of solidification, G is the temperature gradient, R is the rate of solidification and the product GR is equivalent to the average cooling rate. An increase in t_f will produce an increase in the dendrite arm spacing resulting in a coarser solidification substructure. Thus, since cooling rate is much higher in welds than in castings, weld solidification substructures are often finer due to shorter local solidification time.

It has been shown [35,36] that the fundamental dependence of the primary arm spacing λ_p [37] and secondary arm spacing λ_s [38] on G and R may be different. These relations are given by;

$$\lambda_p = A_1 (G^2R)^{1/4} \tag{2.8}$$

and

$$\lambda_s = A_2 (GR)^{-n} \tag{2.9}$$

Where n = 1/3 to 1/2 and A_1 and A_2 are coefficients whose values are dependent on the alloy system. Hence, λ_p cannot be characterized by the cooling rate since its dependence on G and R has different exponents. The secondary arm spacing, however, depends on the product GR such that it can be correlated reasonably with cooling rate. Dendrite arm spacing in welds may also be correlated with heat input. Bouchard et al [39] have tested various theoretical dendrite and cell spacing formulas against experimental data obtained in unsteady and steady-state heat flow conditions. They found that the following exponential relationship between λ_s and GR adequately represents the control parameter dependence of experimental data in steady and unsteady state heat flow;

$$\lambda s = K (GR)^{1/3} \tag{2.10}$$

where K is a constant.

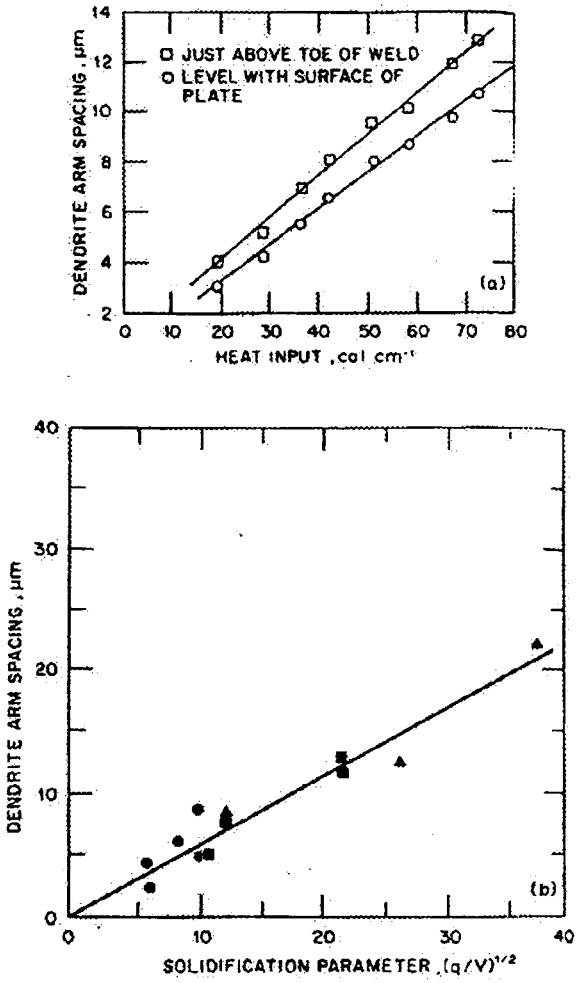

Figure 2.9: Relationship between dendrite arm spacing and heat input and solidification parameter (a) [40] (b) [41].

It should be noted, however, that the dendrite arm spacing could vary from the fusion line to the weld centreline in a particular weldment.

Solute Partitioning

Elemental solute partitioning or re-distribution is an important phenomenon during alloy solidification that can significantly influence the weld microstructure and weldability. On a fine scale of the order of dendrite arm spacing, it is refereed to as microsegregation whereas on larger scale is known as macrosegregation. Different models have been proposed to describe solute partitioning and the resultant segregation that exists in a solidified microstructure. In most of the models, it is generally assumed that equilibrium exists between the solid and liquid at the solid/liquid interface. Solute redistribution is more predominant during dendritic growth than in planar or cellular growth modes. During dendritic solidification, the temperature at the tip of the dendrites may be undercooled by ΔT_t degrees relative to the alloy liquidus as shown in figure 2.10 [41]. In weld solidification, dendrite tip undercooling can be approximated by the combination of constitutional undercooling and undercooling due to curvature effect i.e.

$$\Delta T_t = \Delta T_l + \Delta T_r \qquad (2.11)$$

Generally, the microstructures in castings are sufficiently coarse so that the contribution of curvature to the undercooling can be ignored. However, the contribution of curvature to undercooling could be significant in fine microstructure and in such situation ΔT_r may need to be considered in analysis of dendrite tip temperature. Burden et al [42] presented an analysis for the dendrite tip temperature given by;

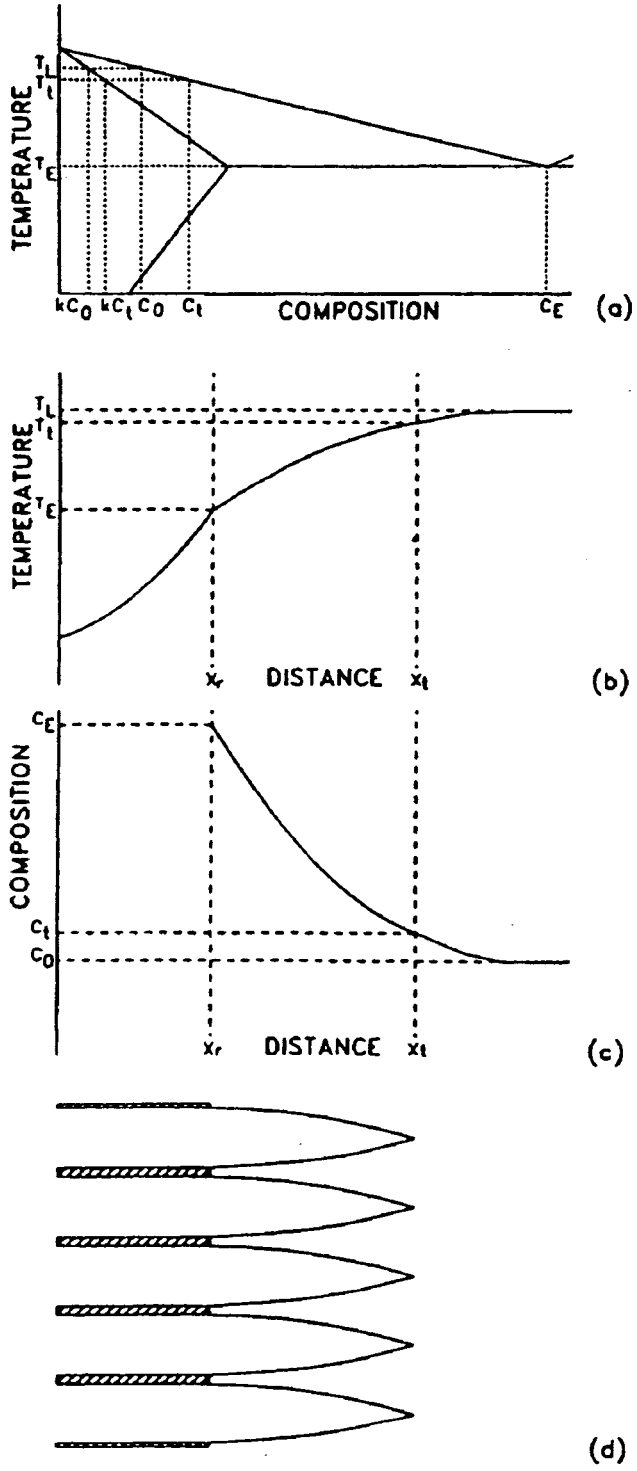

Figure 2.10: Variation of temperature and composition in vicinity of dendrite tip [41].

$$\Delta T_t = D_L G/R - M_L Rr(1-k)Co/D_L + 2\phi/R \qquad (2.12)$$

where D_L is the solute diffusion coefficient in liquid, G is the temperature gradient, R is the solidification growth rate, M_L slope of equilibrium liquidus line, k is equilibrium partition coefficient and r radius of curvature of solidification front and ϕ is the Gibbs-Thompson coefficient related to solid/liquid surface energy. The effect of increased undercooling at the dendrite tip would be to decrease segregation and the extent of formation of non-equilibrium phases. It can be seen from the equation 2.11, that dendrite tip undercooling and thus its influence on solute re-distribution can be significant with increase in growth rate.

The ratio of the solid to liquid composition at the solid/liquid interface during solidification is given by the partition coefficient. Under equilibrium conditions at the interface, the equilibrium partition coefficient k may be obtained from the tie lines in the phase diagram. At rapid solidification rates, the solid and liquid at the interface are not necessarily in equilibrium and because of the limited diffusion that may take place, the solid and liquid compositions tend to converge. Several models have been developed which allow for a non-equilibrium partition coefficient k' and its variation with solidification velocity [43]. These models allow the partition coefficient to vary between the equilibrium value associated with the phase diagram at low growth velocities and a value of 1 at extremely high growth rate. When k'=1, the solid that forms is of the same composition as the liquid and is referred to as partitionless solidification. Fig. 2.11 [43] shows an example of variation of k' as a function of the growth rate for several different models. An important consequence of non-equilibrium partitioning is that, at high solidification rates less solute redistribution occurs in solidified structure with a more

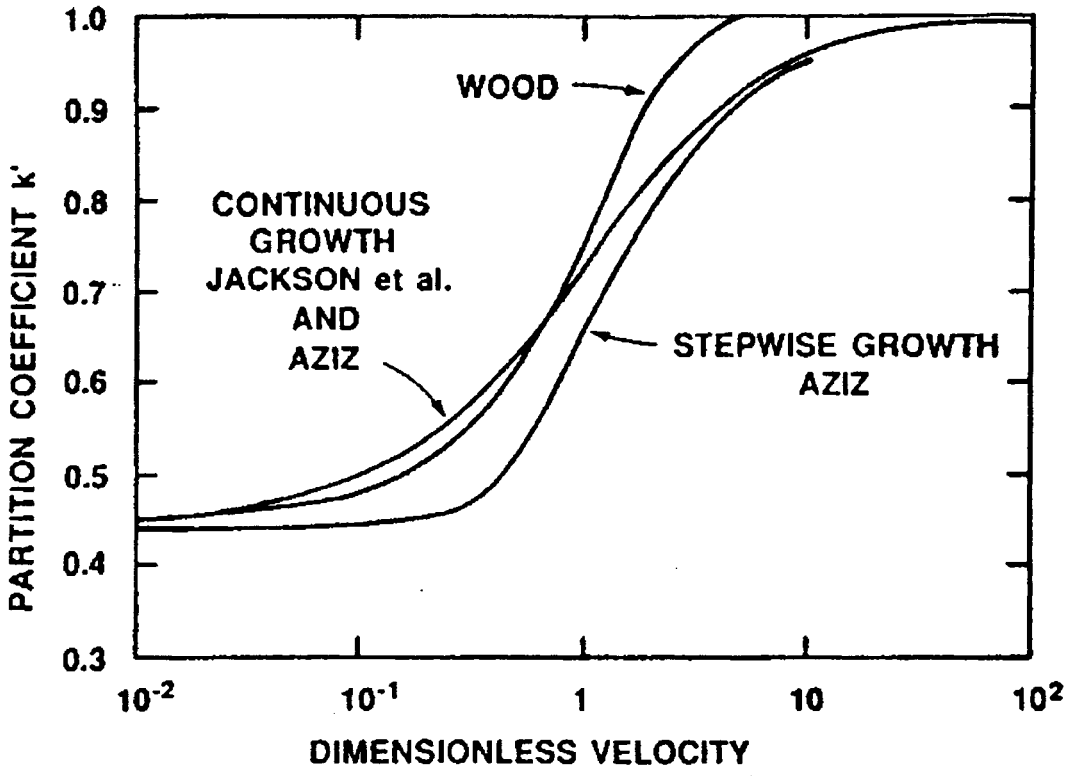

Figure 2.11 Calculated variation of partition coefficient with velocity using various models [43].

uniform composition. In extreme cases where less solute partitioning occurs, the appearance of normally occurring second phases may be avoided. These effects can be expected during rapid solidification of high energy density processes such as laser welding and electron beam welding.

Furthermore, a variety of non-equilibrium phases may be produced as a result of rapid rate of solidification. These phases may be present at other compositions as equilibrium phases, with their range of stability simply extended. They may also be new phases not normally found in the appropriate phase diagram of the alloy. It is to be noted that high cooling rates may have an indirect effect on the phases that form in the welded microstructure, even if solidification behaviour is not significantly affected. In some alloy systems, the as-solidified phases are not stable at low temperatures and as such undergo a solid-state transformation during cooling. If the solid-state cooling is sufficiently fast, this transformation may be altered or inhibited in the case of diffusion controlled reaction. Alternatively, the nature of the transformation may be altered if sufficient time for diffusion is not available. Segregation during weld pool solidification may lead to the occurrence of weld defects and/or variations in properties throughout the fusion zone.

Welding Residual Stress

Different regions in the vicinity of the fusion zone experience different extent of expansion and contraction compared with other areas around it during welding as shown in figure 2.12 [44]. As the temperature increases, the initial expansion of the section is restrained by the material further away from the heat source, which generates compressive stresses in the area (figure 2.13 [44]). The elastic region of the stress-strain

curve is non-linear due to the variation in Young modulus E with temperature distribution. At some critical temperature (point 2), the flow stress is exceeded and further heating results in a decline in stress as the metal becomes softer. The flow stress will continue to decline until it approaches zero near the melting temperature where considerable plastic strain may occur. At the temperature where the section reaches its peak value, the net strain is represented by the vector $1 \rightarrow 4$. On cooling, the reverse occurs i.e. a tensile stress will be generated in the area adjacent to the fusion zone. Point 6 in figure 2.13 represents the final residual stress and strain after the element has cooled to room temperature.

If the thermal stresses caused on heating a fully restrained bar are elastic, the bar will contract to its original size on cooling and no residual stresses will be generated. However, if the temperature is high enough to cause compressive yielding, then, during subsequent cooling, the bar will try to contract to a shorter length than the original distance between the restraining fixtures, resulting in a tensile residual stress. The residual stresses developed would depend upon the heat input, component geometry, and thermo-mechanical property of the material and the elastic modulus of the restraining material. Residual stresses in a severely restrained superalloy weldment could be of the order of yield strength of these materials [45] and illustrated in fig. 2.14 [45].

2.2.2.2 Heat Affected Zone

The HAZ of most weldments usually consists of different sub-regions with different microstructure and properties. The microstructure type and its sub-zone width are

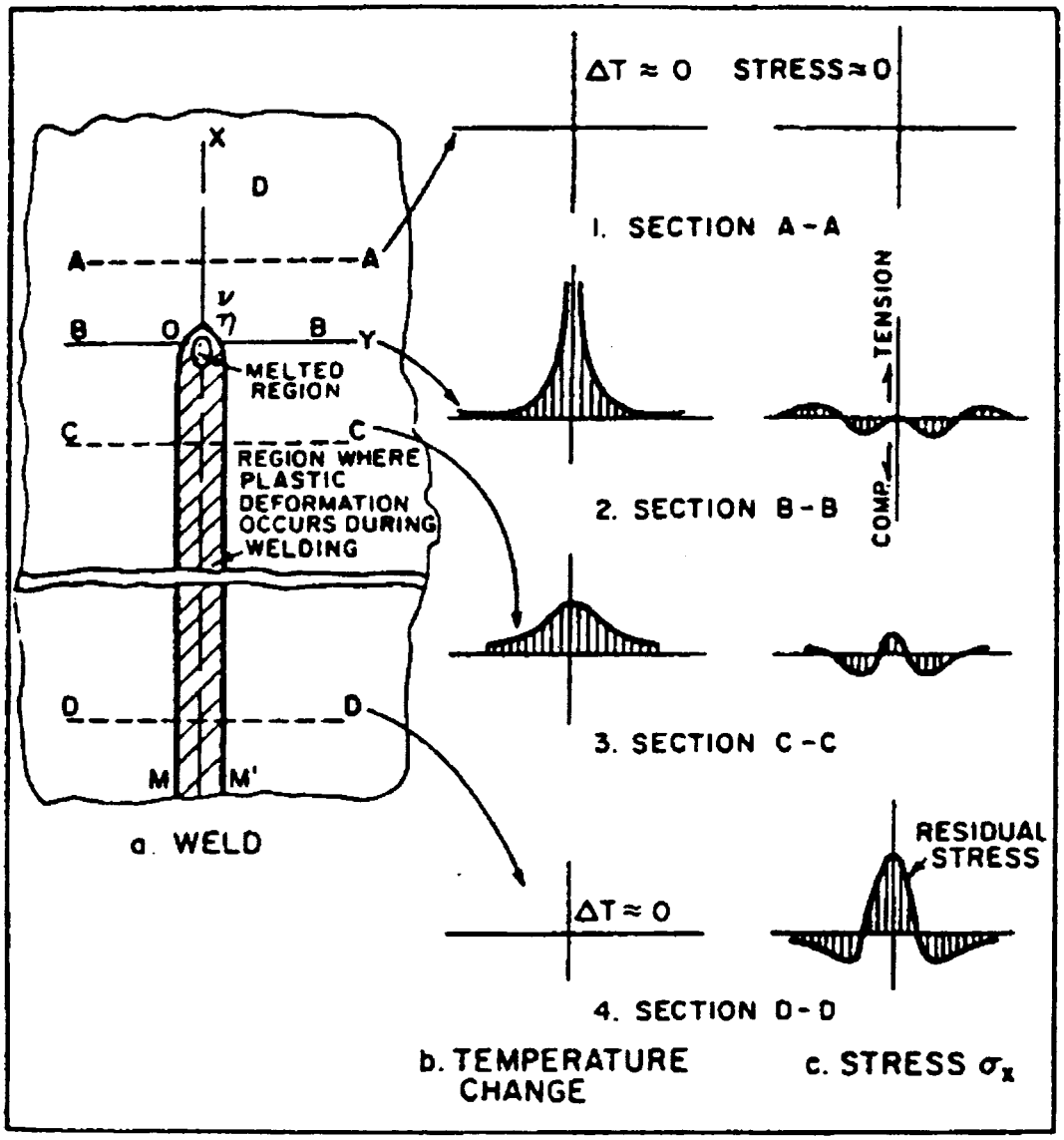

Figure 2.12: Schematic representation of variation of temperature and stresses during welding [44].

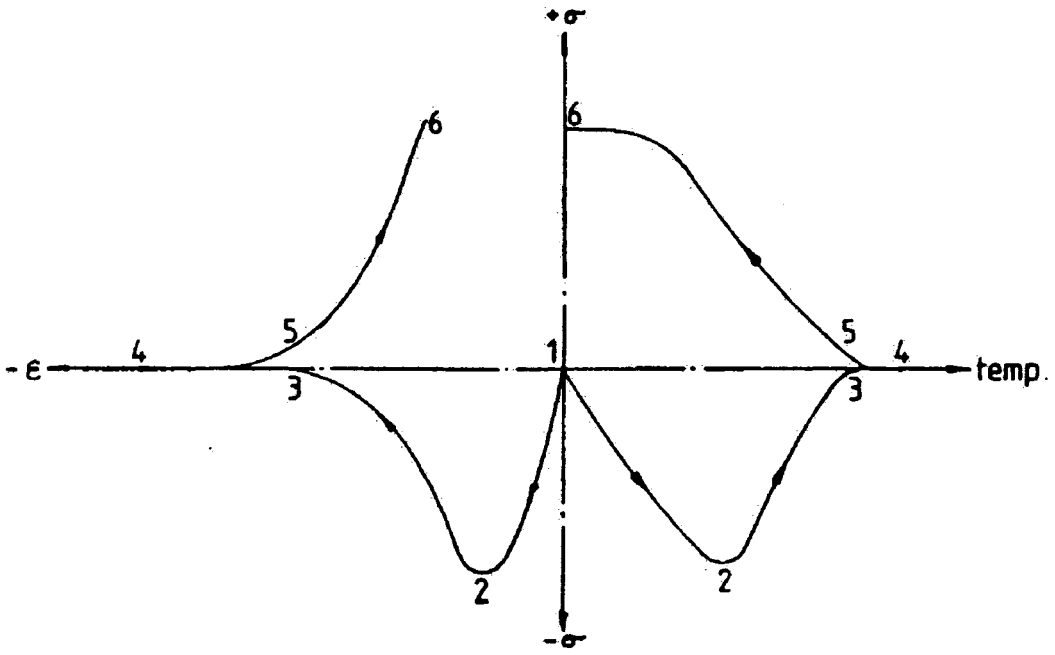

Figure 2.13: Schematic illustration of the variations in stress-temperature and stress-strain during a welding cycle [44].

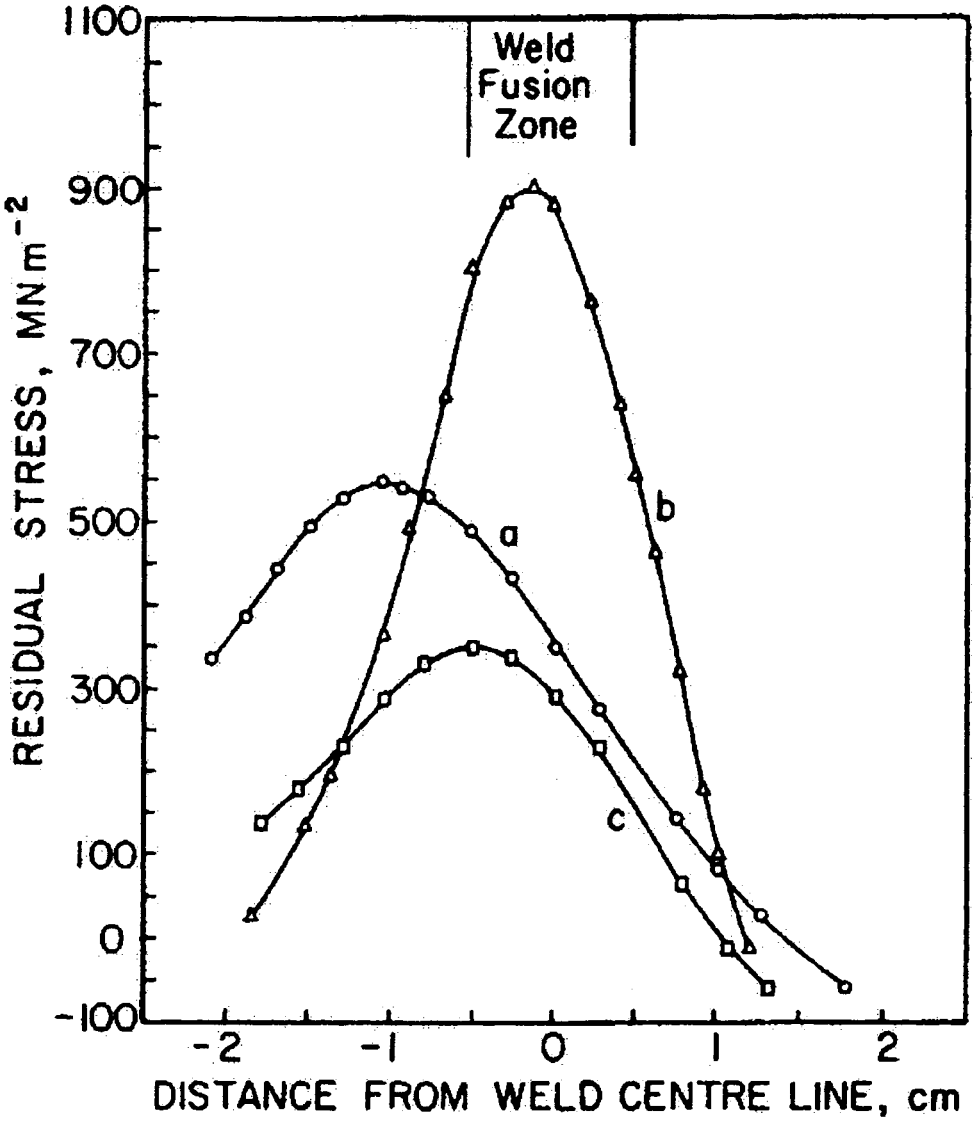

Figure 2.14: Residual stress distributions [45]. (a) GTA-welded Inconel 600; (b) GTA-welded Rene 41 and (c) EB-welded Inconel

partially determined by the thermal cycle and the thermal properties of the base material. Changes in the HAZ are sensitive to the prior thermal and mechanical history of the base alloy. For example, Rene 41 has a tendency to crack in the HAZ if welded in the fully heat-treated condition while solution treated material is less susceptible [46]. In Udimet 700, however, solution treated base metal has poor ductility compared with the fully heat-treated alloy at welding temperatures [4, 47]. Generally, it is considered that HAZ cracking is likely to be minimized in precipitation hardened superalloy weldment, if the base metal is overaged and hence relatively soft before welding. In cold-worked materials, re-crystallization often takes place in the HAZ during welding. This may cause the grain boundaries to migrate away from harmful elements being segregated there and thus reduce propensity to cracking. It has been found [48] that for 5-8 mm thick sheets of IN 718 and Waspaloy, cold work of about 30-40% significantly reduce occurrence of HAZ microfissuring. Alternatively, grain growth in the HAZ may lead to decrease in mechanical properties and or resistance to microfissuring. The onset and extent of grain growth are influenced by the presence of grain boundary precipitates and their solubility at high temperature.

In addition, there are a number of metallurgical changes involving phase transformations and elemental segregation that occur during weld thermal cycle, which may alter the properties of the HAZ. Prominent of these reactions is liquation reaction, which is known to be a fundamental cause of grain boundary embrittlement both during welding operation and the subsequent thermal exposure. Liquation reaction in the HAZ will be further discussed in the section devoted to mechanisms of HAZ cracking. The peak temperature experienced in the HAZ regions varies with distance from fusion line.

The maximum peak temperature is the liquidus temperature of the alloy at the fusion boundary.

2.3 Weld Defects

A wide range of weld defects may be encountered during welding of metallic alloy components. Typical types of defects that occur in arc welds are shown in figure 2.15 [14].

2.3.1 Porosity and Inclusions

Porosity is a general term normally used to describe gas pockets or voids in the weld metal. Typical causes for their formation include improper shielding, moisture, incorrect amperage and excessive arc length. When high amperage or a long arc length is used, deoxidiser that helps prevent porosity can be totally consumed when transferring across the arc. It has also been recognised that voids and grain boundary cavities often form when many superalloys are simply heated into the liquid + solid region and then solidified. In this case, where there are no long-range residual or internal stresses involved, the voids or cavities are believed to form as a result of local stresses or strains in the vicinity of the liquid pools. It has been suggested [49] that such voids form as a result of irreversible plastic expansion of the solid metal envelope around the liquid pools. On solidification, the liquid metal contracts and if it is unable to fill the whole void in the deformed solid, a permanent cavity is formed.

Inclusions are usually slag, oxides or other non-metallic solids entrapped in the weld metal between adjacent beads or between the weld and parent metal. Excessive

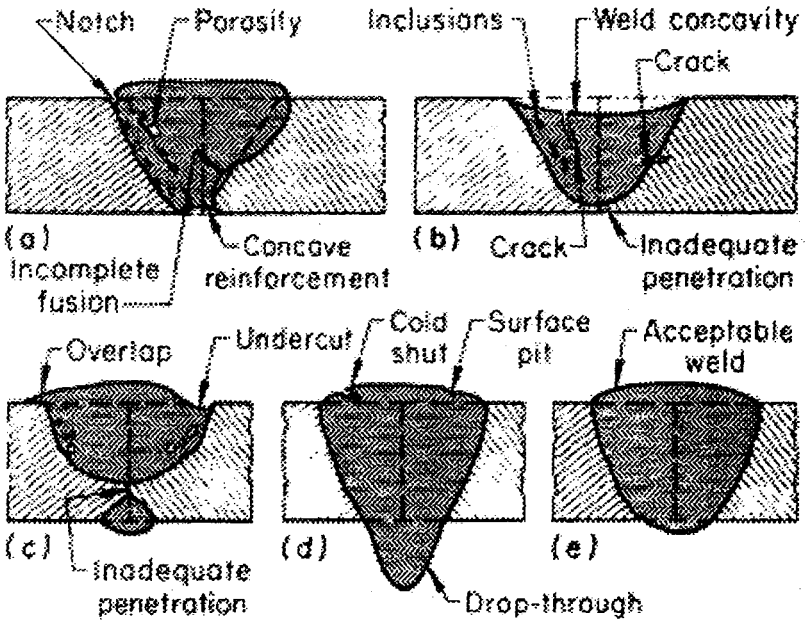

Figure 2.15: Schematic diagram of weld defects [14]

weld pool agitation, downhill welding and undercutting can lead to slag entrapment. Nevertheless, these conditions usually can be prevented by good welding practise and proper weld design.

2.3.2 Lack of Fusion and Penetration

Lack of fusion is a discontinuity caused by incomplete coalescence of some portion of the filler metal with the base metal. It can also form between weld beads in the case of multi-pass welds. These essentially two dimensional flaws occur when insufficient heat is absorbed by the underlying metal from the weld, causing incomplete melting at the interfaces of the weld and the base metal after successive passes. Lack of fusion is usually elongated in the direction of welding with either sharp or rounded edges, depending on the conditions of formation. Lack of penetration occurs when the weld metal has not penetrated to the bottom of the weld joint. It is often caused by incorrect welding technique or by improper root gap.

2.3.3 Cracks and Fissures

A crack is a discontinuity produced by a local rupture, which may arise from the effect of cooling or stresses. When a crack has microscopic dimensions, it is referred to as microfissure. Their detection is difficult by conventional non-destructive techniques and usually requires metallographic examination. The general types of cracks are (a) transverse cracks in the base metal perpendicular to the weld (b) longitudinal cracks in the base metal parallel to the weld (c) microcracks or macrocracks in the weld metal (d) centreline longitudinal weld metal cracks (e) crater cracks and (f) bridging cracks.

Transverse cracks usually are the result of external contamination or a base metal with poor weldability. Base metal cracking/HAZ cracking parallel to the weld is typically caused by the combination of a strong weld metal and a weak low-ductility HAZ/base metal. Weld metal microfissuring can be caused by contamination or impurities in the weld that reduces weldability. Centreline longitudinal cracking can result from concave beads or a very deep, narrow weld bead. Crater cracking occurs when the arc is extinguished over a relatively large weld pool. The resulting crater is often prone to shrinkage cracking. Bridging cracks occur in highly stressed joints where good penetration is not achieved at the arc initiation point. Applied tensile strain is required to cause cracking; the amount needed to initiate cracking depends on the toughness of the material. Metallic alloys are always subject to some type of strain either from external or internal sources during welding. Welding parameters have been found to profoundly influence the extent of welding strain generated in a particular material for a given welding process.

Hot Cracking: Hot cracking is a general term used for weld cracking that occur in the fusion zone and heat affected zone during solidification. It includes cracks that form while a weld is solidifying or when a weldment is re-heated. The cracks are typically intergranular in nature. Solidification cracking, liquation cracking, ductility dip cracking and strain age cracking are types of hot cracking.

Solidification Cracking: Solidification cracking occurs predominantly along centreline of fusion zone but could also occur between the weld columnar grains. It is believed to be caused by a combined effect of contraction welding stresses and the presence of intergranular low melting point constituents that form as a result of segregation during

liquid to solid phase transformation. It has been recognised that fusion zone cracking is generally not a difficult problem to solve and that it can be avoided by good welding practice involving proper weld design and appropriate choice of filler alloy [50].

Ductility-Dip Cracking: A number of alloys including austenitic chromium-nickel steels and nickel base alloys exhibit a temperature range over which their ductility and tensile strength drop sharply. Within this temperature range, fracture is intergranular and brittle. In austenitic stainless steels it is normally attributed to segregation of impurity atoms such as S and P to grain boundaries leading to solid-state embrittlement. In precipitation hardened nickel base alloys grain boundary embrittlement is sometimes attributed to the extensive intragranular precipitation of hardening γ' phase which hardens the grains compare to almost precipitate free grain boundaries. This could cause stresses to be concentrated on the weaker grain boundaries, leading to solid-state embrittlement. In some, cases, cracking may be initiated by other forms of hot cracking followed by ductility-dip cracking.

HAZ Liquation Cracking: HAZ liquation cracking is a major problem associated with welding of nickel base superalloys. Its occurrence has been reported in a variety of nickel base alloy weldments including Waspalloy [51], Udimet 700 [51], and Inconel 718 [52, 53]. It is normally associated with local or "partial" melting in the weld HAZ. It has been observed that such partial melting in nickel base superalloys is enhanced in the vicinity of carbide and boride. When the liquid in this region becomes coincident with grain boundaries under stresses and strains associated with welding, cracking may result. Liquation can occur both below and above equilibrium solidus of these alloys during welding. Initiation of liquation at sub-solidus temperature is known to be more

deleterious in relation to cracking in that it extends the effective melting temperature range and also influences the nature of melting at super-solidus temperatures by altering the kinetics of reaction during subsequent heating. Sub-solidus liquation mechanisms can be divided into three general categories, constitutional liquation of second phase particles, eutectic melting of terminal solidification constituent of a segregated cast structure and grain boundary liquation due to segregation of melting point depressing minor elements like boron and sulphur. Liquation cracks tend to occur as tiny intergranular microfissures. Besides the occurrence of cracking in the presence of liquid phase, localized melting may also produce a re-solidified material on cooling, which could be brittle and thus lead to subsequent cracking.

Weld-Metal Liquation Cracking: Weld-metal liquation cracking occurs in the underlying pass of a multi-pass weldment. The susceptibility of this type of cracking generally parallels that of the HAZ. However, the inherent microsegregation remnant from weld solidification, the presence of terminal solidification microconstituent that exhibit lower liquation temperatures and a coarse fusion zone grain size can promote a greater susceptibility to this form of cracking relative to HAZ liquation cracking particularly in wrought alloys. Baeslack III et al [54] reported an increased weld-metal liquation cracking susceptibility of Incoloy 903 using a double-weld spot-Varestraint technique. The greater susceptibility of the alloy was attributed to the lower constitution liquation temperature of Nb-rich Laves phase present in the weld-metal versus Nb-rich carbides in the base metal, and an appreciably larger grain size in the fusion zone.

Strain-age or Post weld heat treatment cracking (PWHT): This type of cracking is often found to occur during post weld heat treatment of precipitation hardenable nickel

base alloys. A PWHT is usually required to re-establish the properties of weldment and/or to relieve residual welding stresses. It normally consists of a solution anneal followed by a period of aging at about 700°C – 850°C. The temperature range at which stress relief begins to occur coincides with the range in which rapid precipitation of γ' phase occurs. The combination of the inability of the material to stress relief coupled with the fact it is gaining strength by rapid γ' precipitation leads to PWHT cracking. Cracking during PWHT mostly initiates in the HAZ but their length frequently extends through the weld metal or for a substantial distance into the parent metal. It has been reported to initiate mostly in regions that had liquated during welding operation [5]. It is widely believed that strain-age cracking is a cumulative effect of residual welding stresses, aging contraction stresses and thermal stresses acting upon the HAZ which has been embrittled by various possible metallurgical reactions. The factors that control the occurrence of strain age cracking (SAC) are not precisely established, nor are the means of alleviating it. The various factors reported in several investigations are discussed as follows:

(1) **Chemical Composition:** Nickel alloys having high levels of titanium and aluminium are generally prone to SAC due to the rapid precipitation of γ precipitate particles. The influence of minor elements is less established. Hughes et al [55] reported that lower levels of carbon content produce better resistance to SAC. However, Carlton et al [56] found that low carbon content is detrimental to SAC resistance and has been supported by other investigators [57,58]. Carlton et al [56] attributed their findings to the tendency of low carbon alloys to undergo grain coarsening. Hughes et al [55] generally conclude that SAC resistance could be improved by using high purity raw material low in iron, manganese, silicon

and sulphur. Silicon was found to be detrimental to SAC resistance by Carlton et al [56]. A statistical correlation has been found between boron content and SAC resistance [59]. Higher levels of boron were found to correlate significantly with improved resistance to this type of failure.

(2) **Grain Size:** Several investigations have shown that fine-grained alloys are more resistant to SAC that those that are relatively coarse. This may be due to a relative ease of stress relaxation by grain boundary sliding in fine-grained materials. Higher number of grain boundary triple points in fine-grained alloys could also be a contributing factor due to the effect of triple points in inhibiting void linkage on grain boundary facets.

(3) **Preweld Treatments:** The ductility of the base material is a major factor that influences its susceptibility to SAC. It has been found that overaging precipitation hardened nickel base alloys tend to reduce the occurrence of SAC. This may be due to the fact that the base metal remains weak and ductile while the HAZ becomes comparatively strong. Stress relaxation could then be forced on the weaker, more ductile and voluminous base metal than the HAZ, which has relatively little capacity to accommodate strain. In the case of Rene 41, a simple preweld solution anneal at 1080°C for 25 mins followed by water quench was reported to result in SAC resistance better than that of base metal overaging treatments [58]. However, no explanation as to why the solution treatment produced better result than overaging treatments. In addition, preweld heat treatments that produce serrated grain boundaries have also been reported to enhance resistance to SAC.

(4) **Post weld heat treatment cycle:** Rapid heating to post weld solution anneal temperature has been reported to reduce the occurrence of SAC in most heats of Rene 41 [57]. It is thought that rapid heating allows sufficient stress relief and reduces residual stresses to an innocuous level before the grain boundaries are embrittled by the aging reactions. Jordan et al [60] found that rapid heating rates could be used to avoid SAC in Ni-base superalloy with an Al + Ti content of about 4%. However, the technique was not successful with an alloy of significantly higher hardener Ti and Al, 9% content. Uniform heating rates could become difficult to achieve in the various sections of a massive weld assembly. Rapid heating in such cases may induce a high level of thermal stresses and may eventually be detrimental. A solution proposed [61] for this difficulty is a stepped – heating technique in which the component is slowly heated to about 500°C, soaked at this temperature to reduce thermal gradients throughout the component, and then rapidly heated through the mid-range ductility dip to the solution-treatment temperature. It has also been found that weld-bead contour could influence microfissuring tendency during PWHT [62-64].

(5) **Heat-treating Environment:** It has been determined that SAC can be significantly reduced by performing post weld heat treatment in a dry and inert atmosphere. Thompson et al [57] found that severe SAC occurred only in oxygen-containing atmospheres. The detrimental effects of oxygen were found to be active even at low concentration of 2 vol.%. SAC was eliminated in high purity dry argon, argon containing 0.5 vol.% oxygen and vacuum atmospheres. It was suggested of that the detrimental effects of oxygen-rich atmospheres could be due to the rapid diffusion

of oxygen along grain boundaries and the consequent formation of oxides, which are not able to resist plastic deformation.

(6) **The Midrange Ductility Minimum:** The ductility trough at temperatures around 700°C exhibited by a large number of nickel base superalloys is another factor that influences the occurrence of SAC. The ductility decline is thought to begin as a result of processes which cause deformation to be localized at the grain boundaries and which lead to unhindered crack initiation and propagation. Such processes may include formation of precipitate-free zone at grain boundaries, local ordering reaction and dislocation pining. This phenomenon is of considerable significance to SAC, since the ductility minimum occurs over the range of temperatures normally used for post weld aging treatments.

2.4 Weldability and Weldability Testing

Weldability as defined by the American Welding Society (AWS) is the capacity of a metal or combination of metals to be welded under fabrication conditions into a specific suitably designed structure and to perform satisfactorily in the intended service [65]. Two general types of weldability can be considered, fabrication weldability and service weldability. In the case of fabrication weldability, hot, cold and stress relief cracking must be avoided in the weldment along with other more common weld defects. From the service weldability point of view, the strength, toughness and creep resistance of the weld metal and the HAZ must match that of the base metal. The following quantitative measurements have been used for comparing fabrication weldability of a material under different welding procedures and/or metallurgical conditions.

Maximum Crack Length: Provided constant weld pool geometry is maintained, the maximum crack length can be used as a rapid screening technique during preliminary testing of materials. It is based on the theory that the crack length is proportional to the width of the cracking temperature range for a given welding procedure and microstructural conditions.

Total Crack Length: The total crack length produced in a weld by a given combination of welding procedure and microstructural condition has proved to be a good quantitative index of the cracking susceptibility of the fusion zone. Similarly, the total crack length for HAZ cracks provides a reasonable quantitative index of the base metal cracking sensitivity for a given welding procedure and microstructural conditions.

Average Crack Length: The average crack length in a particular specimen, obtained by dividing the TCL by the total number of observed cracks, is also sometimes used in addition to MCL and TCL as an index to compare fabrication weldability of a material.

These measurements, however, are reliable only for a given constant heat input. In situations of different heat inputs, the data is normalized by taking into account the area under the HAZ/FZ. In addition to the above quantitative measurements, other empirical weldability tests have been developed, with emphasis on determination of cracking susceptibility. Several reviews of weldability testing techniques have been presented elsewhere [66,67]. These techniques can be grouped into two major categories: representative and simulative. Representative test generally utilizes a less expensive mock-up to represent an actual welding condition and characterize welding discontinuities. A simulative test attempts to duplicate or approximate metallurgical and mechanical factors characteristic of actual welding conditions and discriminate between

materials and/or process variables. Two of the most frequently cited simulative tests in the literature; Varestraint test and hot ductility test are discussed next.

2.4.1 The Varestraint Test [68]

The Varestraint (Variable Restraint) test is a technique developed for testing base metal weldability and evaluation of the influence of a particular welding process and the associated welding parameters on hot cracking. It provides a reproducible means of augmenting the normal shrinkage strains and thus simulates the large shrinkage strains, which are characteristic of a highly restrained weldment in a laboratory specimen. The degree of restraint is simulated by the application of a controlled augmented strain to the specimen during welding. It utilizes a movable GTAW torch and a mechanical system for the application of stress to the sample.

One type of testing system utilizes a small, laboratory scale specimen supported by a cantilever beam as shown schematically in figure 2.16 [68]. A weld is made from left to right, as shown, using any combination of processes, joint geometry, welding parameters and microstructural conditions of interest. As the arc passes the point marked A in figure 2.16, a large, pneumatically controlled loading yoke bends the specimen downward suddenly to conform to the radius of curvature of the top surface of the removable die block, B. As the arc travels steadily onward, it is subsequently interrupted in the run-off area at point C. Since the specimen tends to bend preferentially at the location where the heat of the arc has reduced the strength of the material to a minimum, the addition of bending plates as shown in figure 2.16 forces the specimen to conform to the contour of the die black, creating a large tensile strain on the top surface of the .

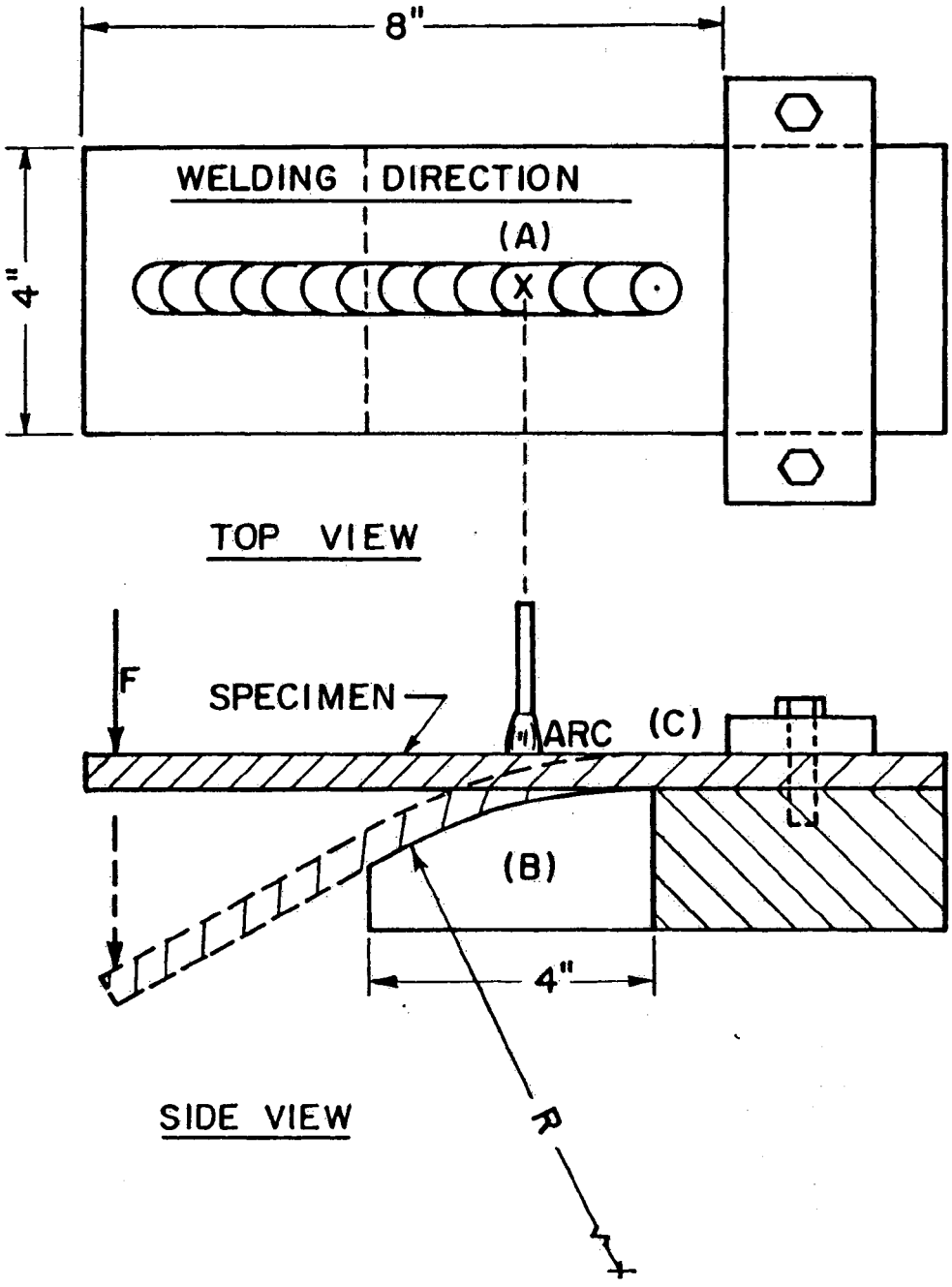

Fig 2.16: Simplified sketch of the operation of Varestraint testing device [68].

specimen. This result in the formation of fusion zone solidification cracks in a susceptible material and possible occurrence of liquation cracks in the HAZ. The resultant augmented strain (ε) can be estimated from the simple relationship;

$$\varepsilon = t / (2R) \qquad (2.13)$$

where t is the sample thickness and R is the radius of curvature of the die block. By using a die block with an appropriate R value, any desired augmented strain can be applied to the weldment at any pre-determined instant during the welding process. Since the magnitude of the total augmented tangential strain is independent of the welding parameters, the effect of welding process, weld composition and other parameters influencing microstructural features of the weldment, can be isolated from the mechanical effect of the externally imposed restraint. The effect of initial microstructural condition on hot cracking can, thus, be evaluated from the varestraint test. For a particular welding procedure, cracking occurs in those regions where the temperature of the material at the instant of straining is within the crack sensitive range and the augmented strain exceeds the strain tolerance of the existing weld microstructure. The hot cracking produced by the varestraint test is adjacent and usually contiguous with the location of the weld pool at the instant of the augmented strain (fig. 2.17 [68])

The inherent restraint provided by a simple rectangular block is essentially too low to cause cracking in the absence of augmented strain. Thus, the minimum augmented strain required to cause cracking with a given set of welding variables and microstructural condition provides a quantitative index of cracking sensitivity, which is referred to as a cracking threshold. Subsequent to testing, specimens are normally examined as-welded at approximately 50X magnification. Each crack is measured and

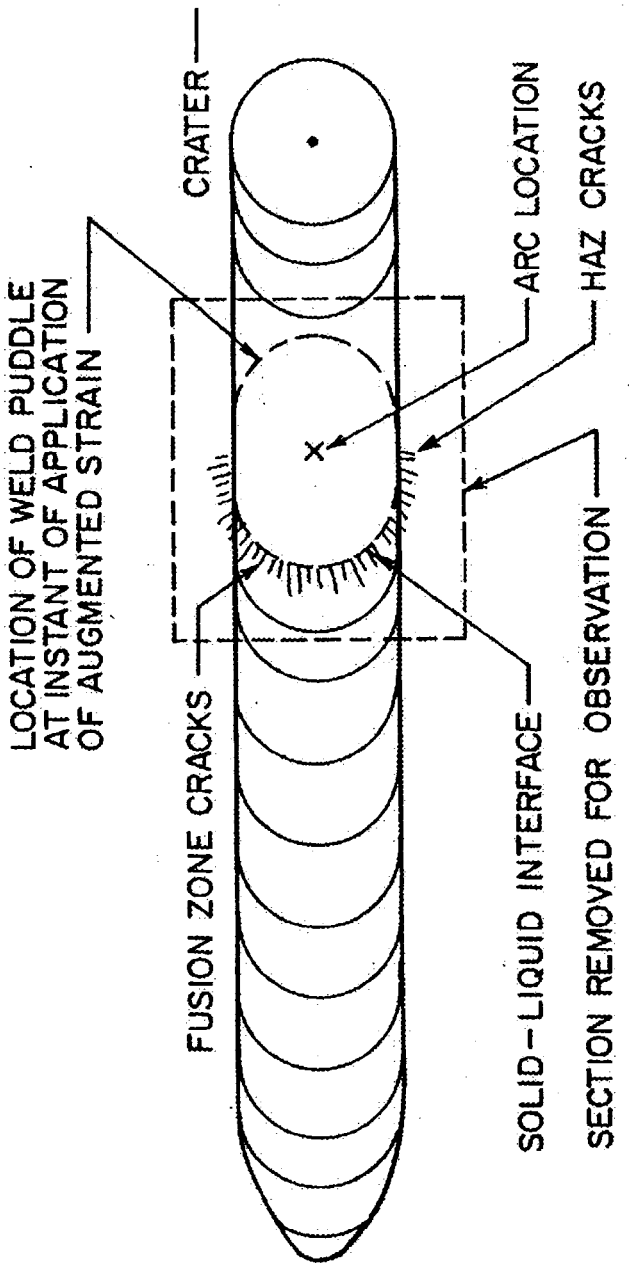

Fig 2.17: Schematic representation of the top surface of the weld showing location of the arc, weld pool and solid-liquid interface at the instant of straining [68]

the data is quantitatively represented as total crack length (TCL), maximum crack length (MCL) and average crack length (ACL). Plots of TCL, MCL or ACL against percentage of augmented strain are commonly used as an effective technique of data representation. Several modifications have been made to the original Varestraint test since its introduction, with most utilising a reduced sample size from the original 50 X 300 X 4.8 mm dimensions. The Spot-Varestraint test first used a reduced sample size for the testing of sheet materials [69]. This technique utilizes a stationary GTAW torch to create an autogenous spot weld in the centre of a coupon, with a controlled arc time sufficient to establish a relatively stable weld pool. After a short, predetermined delay time, a pneumatically actuated ram forces the sample to conform to the radius of a die block. The selection of delay time determines whether cracks are formed in the HAZ or FZ. Proper selection of delay time permits a reasonable evaluation of susceptibility of a material to HAZ liquation cracking [70]. Another variation of the original Varestraint test involves the addition of a movable GTAW torch to the spot-Varestraint test, making it effective for the evaluation of FZ solidification cracking [71]. This device is referred to as Subscale or Mini-Varestraint test and it also utilizes a reduced sample size. A third variation, the Trans-Varestraint test, strains the test specimen transverse to the linear weld axis and is an effective test for weld centreline cracking susceptibility [72].

2.4.2 Gleeble Hot Ductility Testing

"Gleeble" is equipment consisting of a time-temperature control device for evaluating the effects of thermal cycle on the hot ductility of materials. It reproduces in a cylindrical test bar the time-temperature cycle experienced by the metal adjacent to

fusion zone during welding operation. A typical hot ductility test utilizes a sample gripped between water-cooled copper jaws through which electric current is passed, and uses a thermocouple attached to the mid section of the specimen to provide feedback to the control system. The sample is heated rapidly by electric resistance heating, and at an appropriate time in the thermal cycle, a high strain rate load, simulating the force experienced by HAZ is applied to fracture the specimen at desired temperature on heating or on cooling. The thermal cycle, which the specimen had experienced, the ultimate tensile load for fracture and the amount of elongation to failure can be recorded by appropriate instrumentation attachment to the machine. After the test, reduction in area of the specimen at the failure region can also be measured.

The data obtained by testing a series of specimens at various points in the time-temperature cycle provide the basis for evaluating susceptibility of a material to hot cracking in the HAZ. Test results are often presented graphically as percent reduction in area (%RA) versus test temperature or ultimate tensile strength (UTS) versus test temperature. When tested on heating many alloys exhibits some level of ductility (and strength). On reaching a certain temperature during continuous heating, rapid loss of ductility ensues, which continues until the temperature where the material exhibits no ductility or zero ductility. The temperature at which zero ductility starts is referred to as nil ductility temperature (NDT). At a higher temperature, known as the nil strength temperature (NST), the material exhibits no strength or zero strength. Another important parameter obtained from the on cooling curve is the ductility recovery temperature (DRT). This is the temperature on cooling from above NDT or NST at which the material starts to recover some level of ductility.

In order to determine the susceptibility of a material to HAZ cracking, a number of criteria have been proposed by various investigators. The importance of the DRT was recognised when the test was first introduced [73]. Others have suggested that the extent of zero ductility range (ZDR) during heating i.e. the temperature range between NDT and NST as well as the amount and rate of ductility recovery are equally important [74]. A material, which recovers ductility quickly (i.e. DRT is close to NDT) and to a level comparable to that on-heating would be expected to be crack resistant. Muesch [75] proposed a cracking factor, (NST – DRT) / NST, based on the temperature range between NST and DRT. Donati et al [76] subsequently used this factor to predict cracking tendency.

Hot tensile strength in addition to ductility behaviour needs to be considered in determining cracking susceptibility since a material can accommodate strain either elastically or plastically [77]. A material with low ductility but high strength at elevated temperatures may be able to elastically accommodate the strain associated with welding and therefore resist cracking. Figure 2.18 [78] shows a typical behaviour of austenitic alloys considered to have good resistance to cracking. This behaviour is characterized by a good ductility when tested on-heating close to NDT, and when tested on-cooling from NDT the ductility is essentially comparable to that observed on heating. Figure 2.19 [78] illustrates the typical behaviour of alloys considered to be highly susceptible to cracking. Materials in this category may exhibit good on-heating ductility but a marked difference is evident during on cooling testing from NDT. They exhibit poor ductility on cooling from their NDT, by remaining at nil-ductility level for a considerable amount of time or show limited insignificant recovery. It has been considered that this loss of ductility in

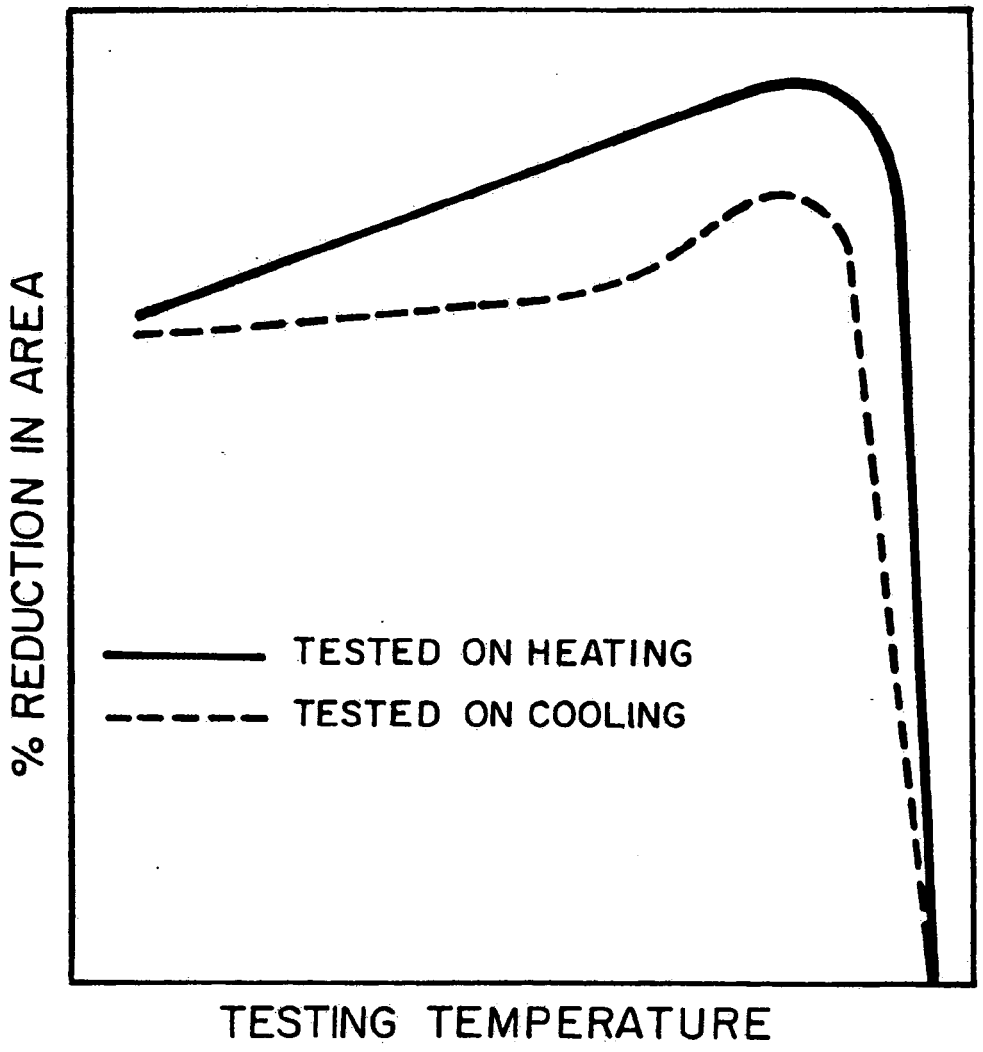

Fig 2.19: Schematic representation of the typical behavior of highly crack resistant materials [78].

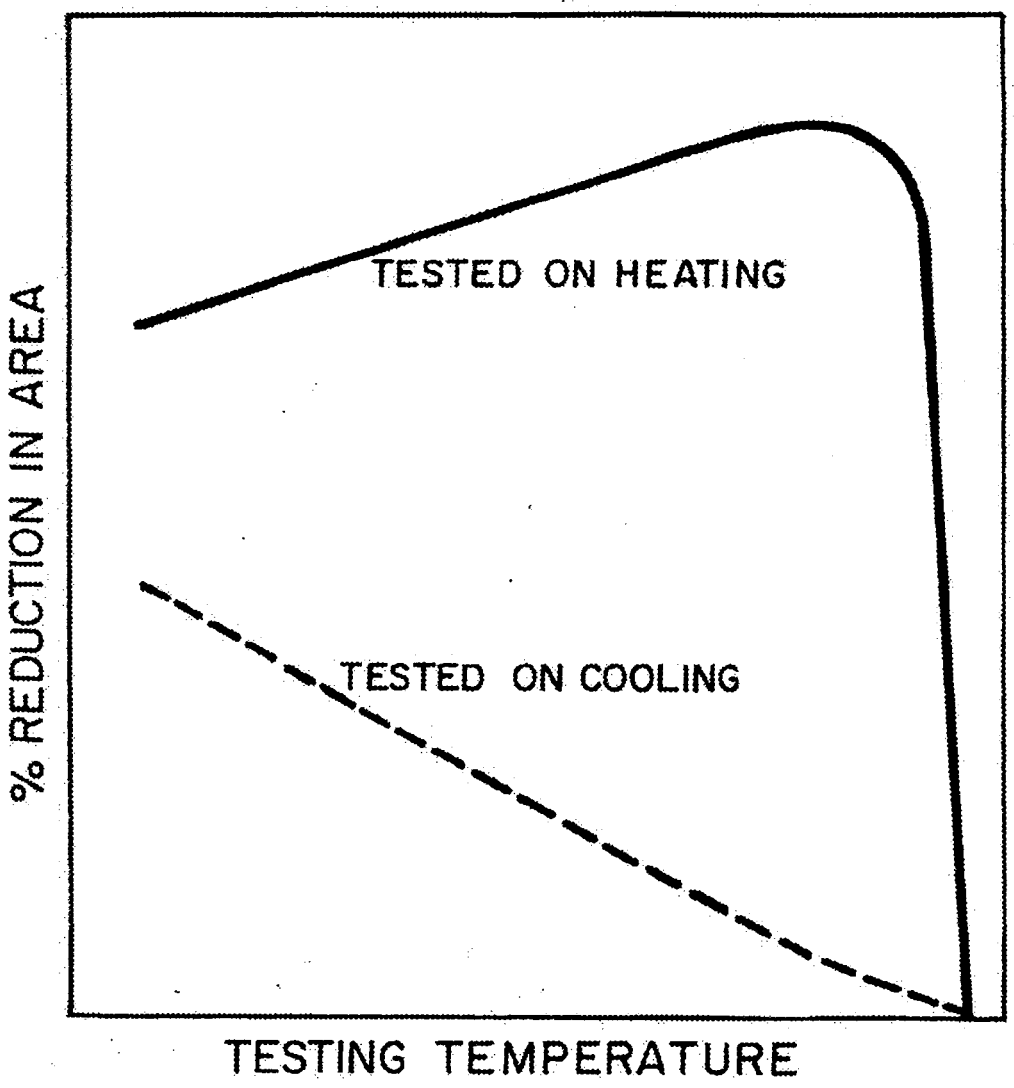

Fig 2.18: Schematic representation of the typical behavior of crack susceptible materials [78].

the HAZ regions close to the fusion line makes the regions susceptible to cracking during welding. Another factor that has received some attention in the literature is the relationship of partial or bulk melting to the various critical temperatures determined by hot ductility testing. It has been reported that liquation (partial melting) occurs at the NDT [77] while some have indicated that it occurs when ductility begins to drop on heating i.e. below NDT [79]. This, however, has been criticized by the argument that only a change in fracture mode from transgranular to intergranular occurs when ductility drops and that, liquation starts only at a temperature in excess of the NDT [80]. Extensive studies in the past have shown advanced austenitic alloys are prone to weld cracking due to grain boundary embrittlement by liquation reaction [81, 82]. The NST is believed to correspond to the temperature at which complete grain boundary wetting by liquid phase occurs and a small volume fraction of the microstructure is liquid [77, 79]. Owczarski et al [51] suggested that testing on cooling from a peak temperature above the NST was more appropriate for discriminating cracking resistance between materials. Testing parameters can have significant effect on hot ductility behaviour of a material and thus on evaluation of cracking sensitivity. Variations in peak temperature used for on cooling test and the time duration at peak and test temperatures can be particularly important. The effect of peak temperature is illustrated in figure 2.20 [83] where a three dimensional representation is made of a weld HAZ in Hastealloy X. It is seen that the peak temperature depends on distance from the fusion line decreasing with increasing distance from the fusion boundary. In addition, the zero ductility range during cooling, ZDRc, during which a material is susceptible to cracking becomes larger with increase in peak temperature. Consequently, the peak temperature used for on-cooling ductility test

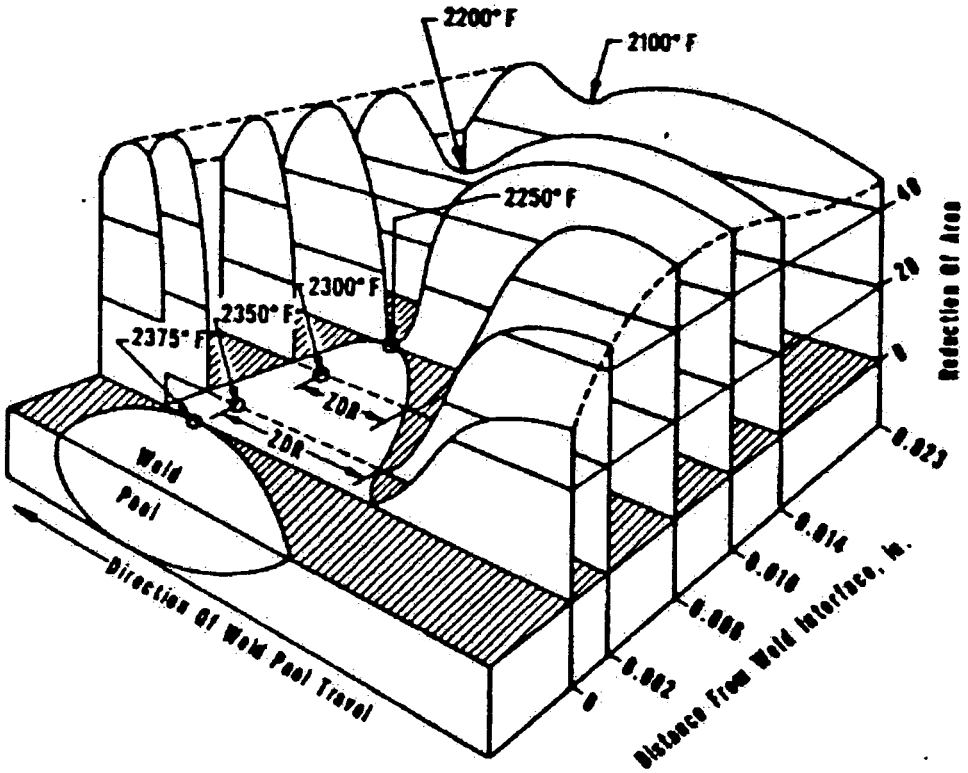

Fig 2.20: Three-dimensional representation of the effect of peak temperature on ductility behavior [84]

has a significant effect on the value of ZDRc used to evaluate cracking resistance. A study of hot ductility technique to better characterize the DRT and nil ductility region (NDR) during cooling, utilized actual thermal strain measurement from weldment correlated with fracture strain during testing [84]. Extrapolation of thermal strain to the hot ductility test temperature intersected the fracture strain curve at several percent reduction in area. This intersection was termed the "Critical Strain Temperature" (CST), which was very close to the DRT above which the material is susceptible to cracking. The temperature range between the NDT and CST was termed the 'Critical Strain Temperature range' (CSTR), which is very close to the temperature range between NDT and DRT. Besides the use of Gleeble for hot ductility test, the thermo-mechanical simulation system can also be used to freeze the microstructure from various temperatures during heating or cooling cycles by simply quenching the specimens. This approach can be used to study microstructural changes such as phase transformations and grain boundary liquid distribution resulting from rapid non-equilibrium heating and cooling.

2.5 Metallurgical Phenomena Associated with Formation of Hot Cracks

2.5.1 Solidification Cracking

The formation of weld cracking in materials that have been fusion welded is a major concern in the design and manufacture of welded assemblies. Solidification cracking frequently occurs between the weld-metal growing grains during the terminal stages of weld pool solidification and cooling, when the thermal strains exceed the ductility of the almost solidified system. There is no consensus as to the initiation

temperature of solidification cracks. Some investigators believe the cracks are wholly or almost wholly initiated and propagated above the solidus while the alloy is solidifying. The main factors causing solidification cracking are mechanical and metallurgical in nature. Mechanical factors include thermal strains caused by the dynamic expansion and contraction of the weld and heat affected zone, the weld joint design, thickness and size of adjoining material and shape of the weld bead.

The main metallurgical factors are the presence of a liquid phase at the interdendritic and/or grain boundaries during a specific temperature interval of freezing and the accompanying solidification microstructures. There are 3 major different theories that have been advanced to explain the occurrence of solidification cracking of weldments. These are (i) Shrinkage-brittleness theory [85] (ii) Strain theory of hot tearing [86] and (iii) Generalised theory of cracking [87,88]. In the shrinkage-brittleness theory [85], it is argued that the basic cause of cracking is the inability of the semi-rigid network of interlocked dendrites to withstand the shrinkage strains imposed upon it during cooling through a brittle temperature range. In the case of strain theory, it is believed that the cracks are formed during the last stages of solidification when a liquid film exists between solidifying grains in a region where solid-solid bridges have not been established. The generalized theory attempts to reconcile, modify and extend the shrinkage-brittleness theory and strain theory to explain how the quantity and distribution of liquid during solidification affects susceptibility of the weld to cracking. Boland [87, 88] suggested that the distribution of liquid is largely influenced by the solid-liquid interface and intercrystalline boundary energies. The generalized theory suggests that for cracking to occur it is not sufficient that a wide freezing range exists but liquid should

also be present over a relatively wide temperature range in a form that allows stresses to be built up between the grains.

2.5.1.1 Shrinkage-Brittleness Theory [87, 88]

Shrinkage-brittleness theory is based on the view that cracking occurs in the brittle temperature range (BTR). The upper temperature limit of the BTR is defined by the solidifying stages when the dendrites come to contact with each other and interlock thus preventing the liquid phase from circulating around them, also known as coherent temperature [87, 88]. The lower limit is defined by the temperature at which the strength of the grain boundaries is sufficient to absorb the loads imposed upon them. The lower limit is considered by some investigators to be the solidus. The mechanism of cracking is thought to be as follows:

At some time during the liquid-solid stage, the growing primary dendrites come into contact and interlock (the temperature at which this occurs is termed coherent temperature), thereby forming a coherent network. During subsequent cooling, contraction strains develop, and when the critical rupture stress has been exceeded, a rift will occur in the network. If there is insufficient liquid to heal the newly formed fissures, the rift will persist. Below the solidus, fissures are unlikely to form because it is assumed that the solid metal is ductile at sub-solidus temperatures. Cracking therefore is only likely to occur in the brittle temperature range [87]. The extent of brittle temperature range of an alloy is dependent on the composition of the alloy since it lies within the freezing range. The other main factors besides constitutional factor are the mode of liquid distribution and the factors that influence it. The coherent temperature at which a

coherent network forms during solidification of an alloy is dependent on the shape of the dendrites, which in turn is dependent on the temperature gradients within the cooling mass. Pumphrey et al [85] reported that an approximately linear relationship exists between the proportion of eutectic in Al-Si alloy that did not crack in a given set of circumstances and the average cooling rate over the solidification range. It appears that the slower the cooling rate, the higher is the proportion of the grain boundary liquid with a composition similar to that of the eutectic it solidifies into and, at very slow rates all the eutectic has an intercrystalline distribution. The influence of eutectic on shrinkage-brittleness depends on the fact that the coherent temperature is a function of the proportion of liquid between the dendrites, as opposed to the liquid between arms of a single dendrite. A minimum shrinkage-brittleness would be expected when there is no tendency for entrapment of liquid and when all the eutectic in the finally solidified alloy is situated along the grain boundaries. It has also been observed that the sensitivity to cracking within the brittle temperature range is dependent on grain size. Pumphrey et al [85] suggested that the degree to which liquid is entrapped between the dendrite arms during their formation is a function of the linear rate of crystal growth. A decrease in the rate of cooling could result in a decrease in the rate of advancement of the dendrite arm into the surrounding liquid. The slower the rate of dendrite growth the greater is the tendency for the liquid to be concentrated at the tips of the growing dendrites and, smaller is the tendency for entrapment between the dendrite arms.

Based on their experimental observations Pumphrey et al [85] concluded that, during the solidification of an alloy coherency is gained when the amount of interdendritic liquid (as distinct from liquid entrapped within the dendrite arms) falls

below approximately 5%. A eutectic alloy which contains 5% or more of interdendritic liquid will not gain coherence until the eutectic temperature is reached and consequently will possess no brittle range. This is confirmed by the fact that aluminium binary and ternary alloys show no tendency to cracking when the total alloy content exceeds a certain level. Tensile tests on Al-Si alloy have shown that for each alloy with a particular Si content there exists a temperature at which coherence is gained. This temperature is either between the liquidus and the solidus or coincident with the effective solidus.

Vero [89] introduced the concept of "healing" whereby incipient cracks are considered to be filled with liquid and their harmful effects are, thus, overcome. He postulated that if a solidifying metal mass contains more than a critical volume of eutectic liquid, any crack formed by the contraction of the primary crystals would be healed by the inflow of eutectic liquid. Pumphrey [85] later introduced the concept of "accommodation" and distinguished it from the concept of healing. He defined accommodation as the degree to which an alloy is able to withstand shrinkage strains by movement of grains within the solid-solid mass when the alloy is solidifying in the brittle range thus preventing cracking. They argue that in welds and small castings, accommodation is more usual than healing, because for healing to occur, there needs to be a critical volume fraction of liquid which may not be present in most cases.

Medovar [90] expanded these various ideas by stating that variation in hot cracking with alloying additions, which form continuous solid solutions is determined by the length of the freezing range. If the alloying elements are mutually soluble in either the liquid or the solid state, then cracking should not occur. In cases where the system forms

primary solid solutions, very small additions of second element may cause severe cracking, owing to the increase in the freezing range.

2.5.1.2 Strain Theory of Hot Cracking [86]

The proponents of the strain theory of hot tearing [86] suggest that hot cracking is caused by localized strains. These are set up by thermal gradients and tend to tear apart masses of solidifying material, which are separated by "essentially continuous liquid films". Cracking does not occur in the "mushy" stage of solidification since the shrinkage stresses are uniformly distributed. Cracking only takes place when the film stage is reached and localized strains are exceedingly high. In passing through the liquidus – solidus temperature range, irrespective of whether the process entails heating or cooling, the alloy develops a condition of essentially continuous liquid films. The strength and ductility of a mass of solid grains separated by liquid films is extremely low. The time/temperature period during which the "film" exists is important since it determines total cumulative strain applied to the film.

If the grain boundaries contain a continuous network of low melting segregated material, the liquid film should form at the solidus temperature of the segregate material. Fracture during the continuous liquid film stage has been observed to occur in an intergranular mode. If the network is not continuous, the fracture occurs at some intermediate temperature, which depends on the amount and distribution of the liquid films. As the composition of an alloy approaches that of a pure metal the amount of segregated material, which may be formed, is greatly reduced, hence its distribution becomes less continuous and less effective in lowering the film stage temperature. The

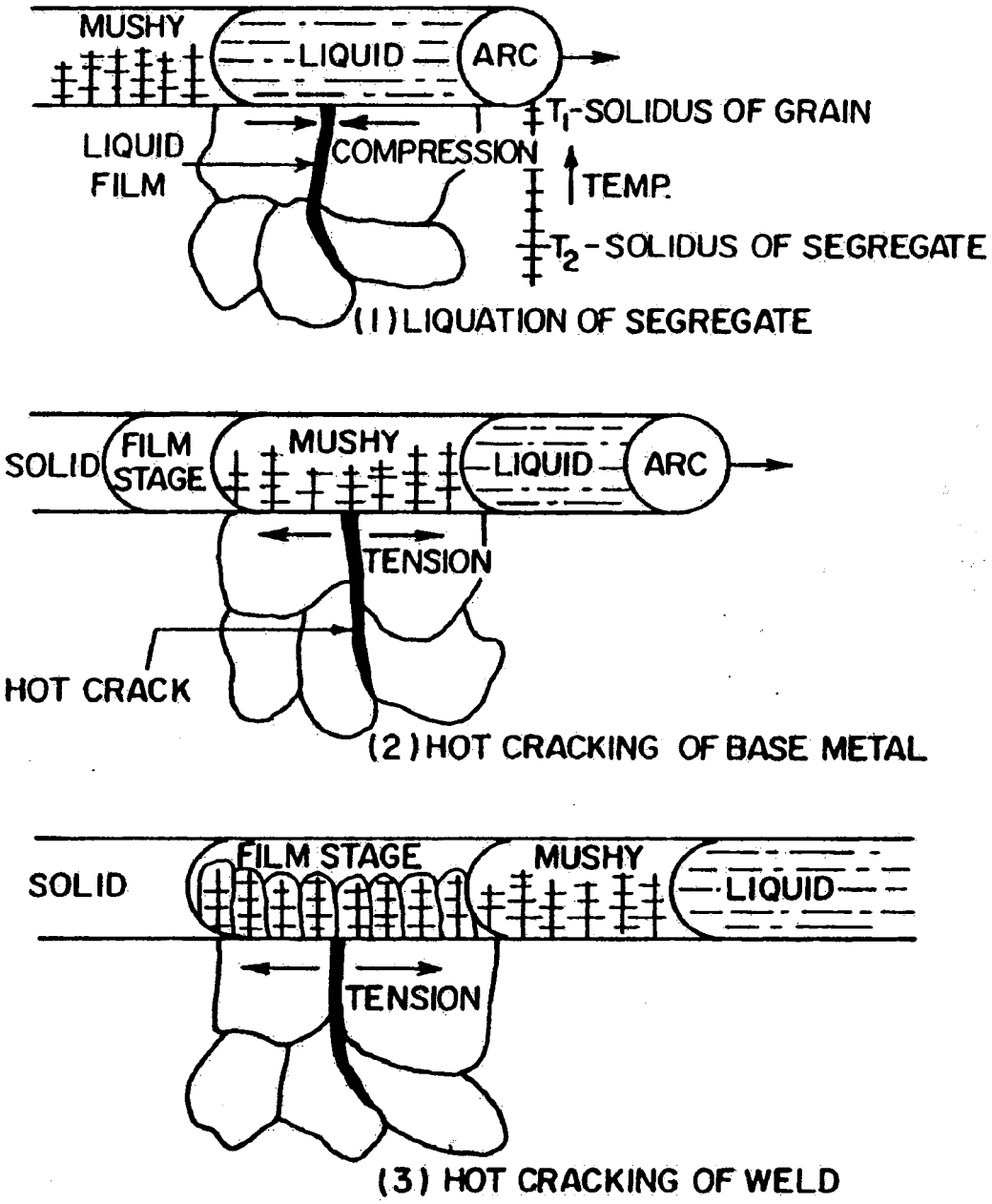

Fig 2.21: Schematic illustration of weld hot cracking process [86].

significance of the film stage is that separation can occur through the liquid films which exist either at the true solidus temperature of the metal or in the range of temperatures between the true solidus and the effective solidus of the segregated material. Figure 2.21 [86] illustrates schematically, the process of combined hot cracking of weld and HAZ. As the liquid pool behind the arc passes the segregate region, melting occurs between the grains; the lateral distance of regions from the weld that develops melting is determined by the thermal gradients perpendicular to the weld and, thus, by welding parameters. Figure 2.21 (a) shows that grain boundary melting occurs to the distance at which the gradient temperature corresponds to the solidus temperature of the segregate film. At this stage, the HAZ region is in a state of compression due to the thermal expansion of the hot metal near the fusion zone. As the arc passes on, the HAZ contracts on cooling resulting in the development of tensile stresses which cause parting of the film region and fissure forms in the HAZ. At this point, the weld metal is in a mushy condition and hot tearing is not possible. At a later time, however, the weld metal reaches the film stage and a strain concentration is developed at the HAZ crack position.

Therefore, the shrinkage strain developed by cooling of the weld is concentrated at the HAZ crack point with the consequent development of a hot tear in the weld, which is essentially a continuation of the HAZ hot crack. Hot cracks may also occur in the fusion zone alone because of the extension developed in the portion of the weld, which is at a film stage, by the contraction of colder regions.

Liquid film stage is the common element in various manifestations of hot tear near the complete solidification point of metals. There is a general agreement that segregates of melting temperature less than that of the matrix material highly accentuate

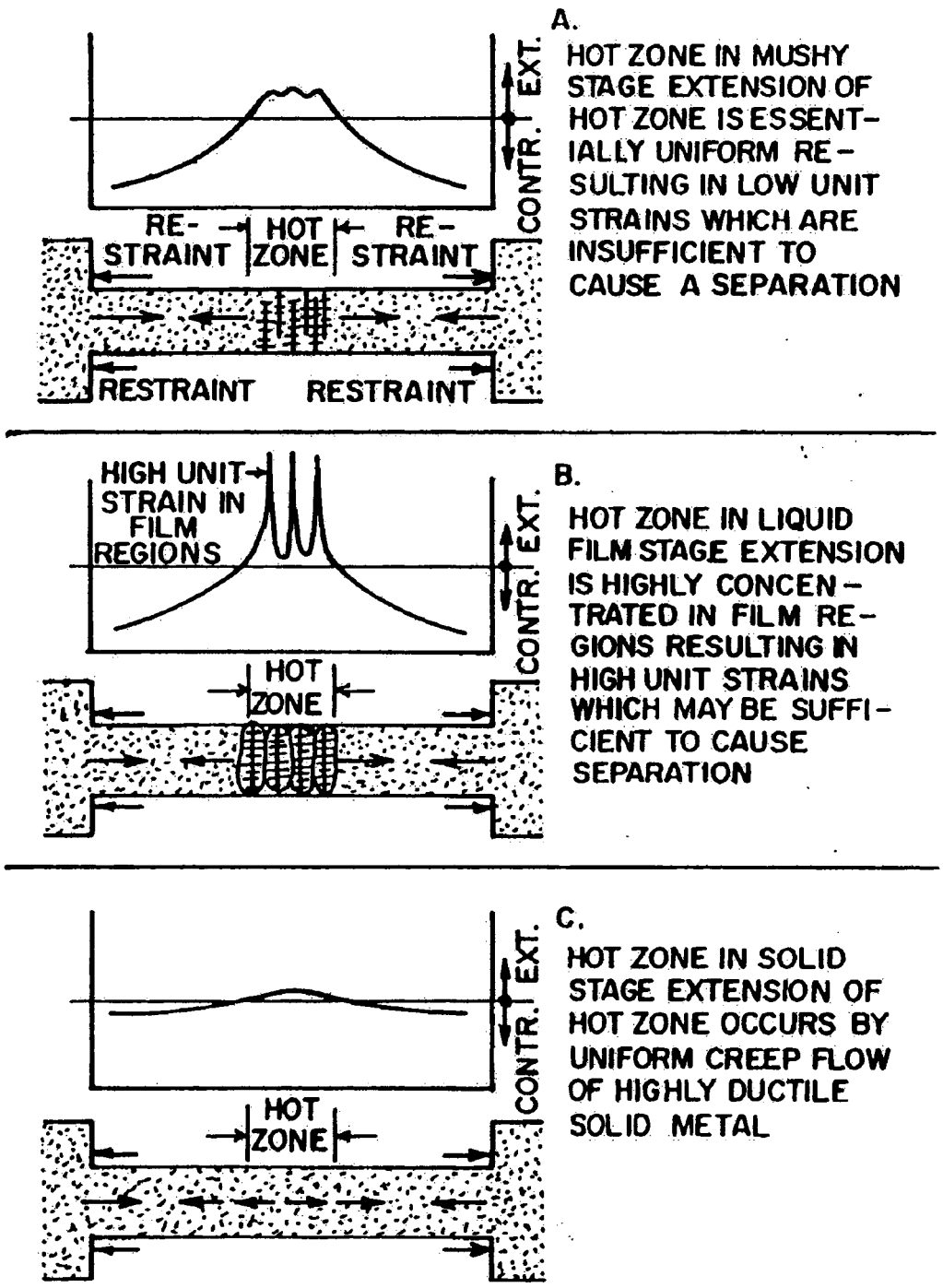

Fig 2.22: Schematic illustration of the various stages of solidification in a casting system containing hot spot [86].

the sensitivity to hot tearing. Segregated liquid films have been observed to be more effective than liquid films developed at the true solidus in promoting hot cracking. Pellini [86] used the strain theory to explain the effect of segregate liquid film in promoting cracking. The strain theory provides a generalized mechanism of hot tearing in terms of the time-rate of extension developed in the liquid film stages. Based on this theory, liquid film provides the metal a condition that permits hot tearing. The actual occurrence of hot tearing, however, is determined by mechanical factors inherent in the rate of extension per unit time imposed within the short time before the liquid film solidifies. In a non-segregated condition, the metal passes through the film stage over shorter times, while under segregated conditions the liquid film condition exists over a wider temperature range i.e. for a much longer time. Accordingly, the rates of extension which do not develop sufficient separation of the liquid film to cause fracture in shorter times may be very effective with longer times, since the separation developed in the films is additive with time. This is illustrated in figure 2.22. The strain theory rebuffs the assumption that hot tears may form when the metal is in the mushy zone, which exist at temperatures considerably above the solidus. It is believed that stresses are evenly distributed at this stage and also that stress relaxation occurs by general flow of the pasty mass. As the hot zone approaches the liquid film stage, the extension of the hot zone is necessarily forced into the narrow liquid films, which have no appreciable strength and ductility compared to the adjoining solid dendrites. The comparatively high value of unit strains developed in these regions at the liquid film stage is illustrated in figure 2.23 [86]. The several observations of interrelated effect of metallurgical and mechanical variables lead Pellini [86] to generalize the hot tearing problem to the following principal elements:

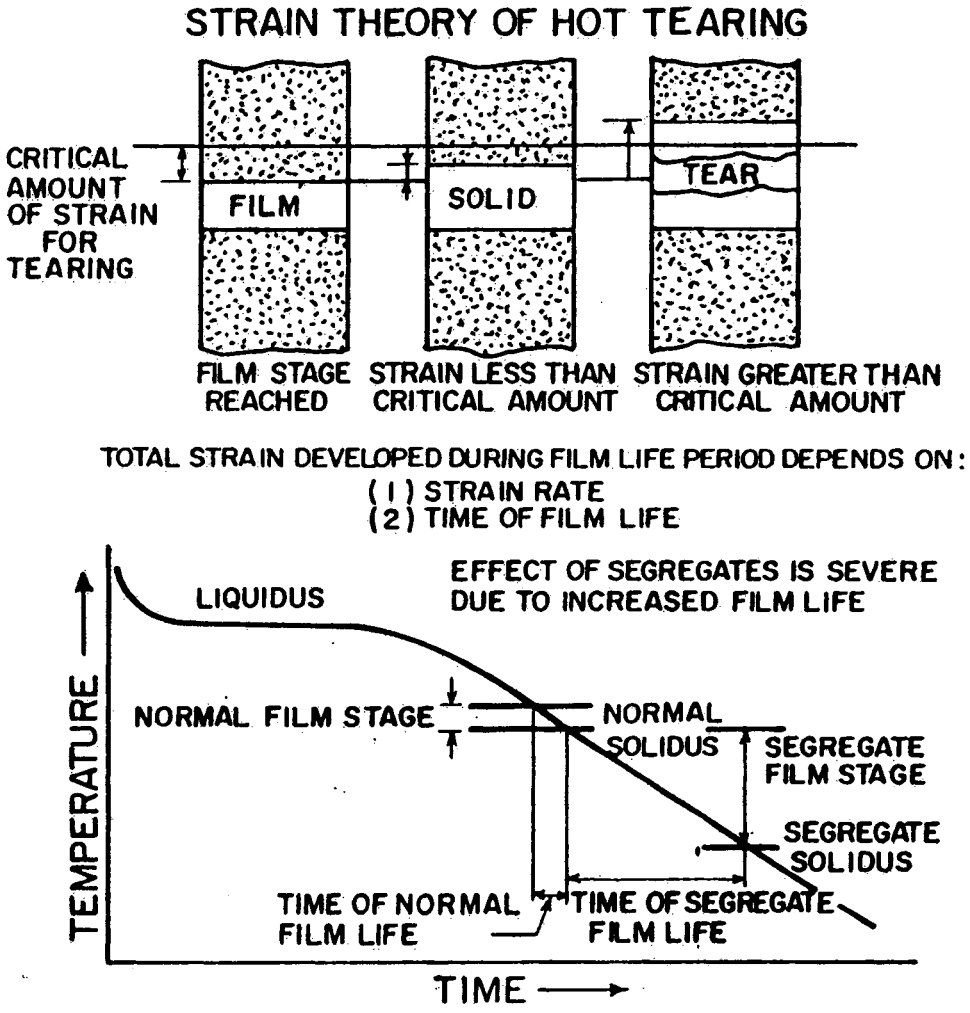

Fig 2.23 Schematic diagram illustrating strain theory of hot cracking [86]

(1) The primary mechanical factor, which determines hot tearing during liquid film stage of the hot zone, is the time rate of extension of the zone.

(2) The rate of extension acting on the liquid film is related to: (a) the overall extent of the hot zone (b) the amount of the mold restraint and (c) the length and rate with which the adjoining sections cool relative to the hot zone.

(3) The presence of melting point depressing elements such as sulphur extends the liquid film condition to lower temperatures and therefore increase the duration of the film stage.

(4) The longer the interval of the liquid film stage, the greater is the total amount of separation which develops in the films.

The presence of melting point depressant and surface active elements like sulphur, phosphorous and boron causes enlargement of hot tears which begin at the normal high temperatures, in addition to the effect of increasing susceptibility to cracking. The wider temperature range induced by these elements permits enlargement of initial cracks in true hot tear fashion.

2.5.1.3 Generalized Theory of Super-Solidus Cracking [87, 88]

Boland [87, 88] proposed a generalized theory of super-solidus cracking to explain the occurrence of solidification cracking in metals. According to this theory, cracking can occur in regions where high stresses can be built up between grains or where by reasons of lack of constraint, a parting of the liquid phase can occur as a result of the development of highly localized strains. Three different situations were recognised:

(1) Necking of liquid films exposed to external surfaces and subsequent crack formation, for example crater cracks and weld centreline cracks.

(2) Separation of highly stressed thin liquid films separating adjoining grains. A thick liquid film prevents cracking due to ability of liquid volume to accommodate strains.

(3) Breaking of solid-solid bonds in areas where liquid coverage of grain surfaces is sufficiently extensive to allow "breaking stresses" to be imposed on the solid-solid bridges.

The generalized theory is very close in concept to the strain theory except that it does consider the possibility of cracking occurring in the mushy stage as suggested by the shrinkage-brittleness theory. The main point of contention is whether cracking normally takes place during continuous liquid film stage or when some solid-solid bridge has occurred. The concept of generalized theory is that in most practical situations cracking takes place after a small amount of solid-solid bridging has occurred.

As indicated by shrinkage-brittleness theory, alloys with a wide solidification temperature range tend to be more prone to solidification cracking than alloys that solidify over a narrow temperature range. Boland [87, 88] attempted to establish a general quantitative method for comparing the effects of various solute elements on the melting temperature range of a given solvent element. Figure 2.24 [87] shows a schematic binary alloy phase diagram with linear liquidus and solidus lines. For an alloy of composition C_o, T_L is the liquidus temperature and T_S is the solidus temperature. T_M is the invariant melting temperature of the solvent element. The slope of the liquidus is m_L

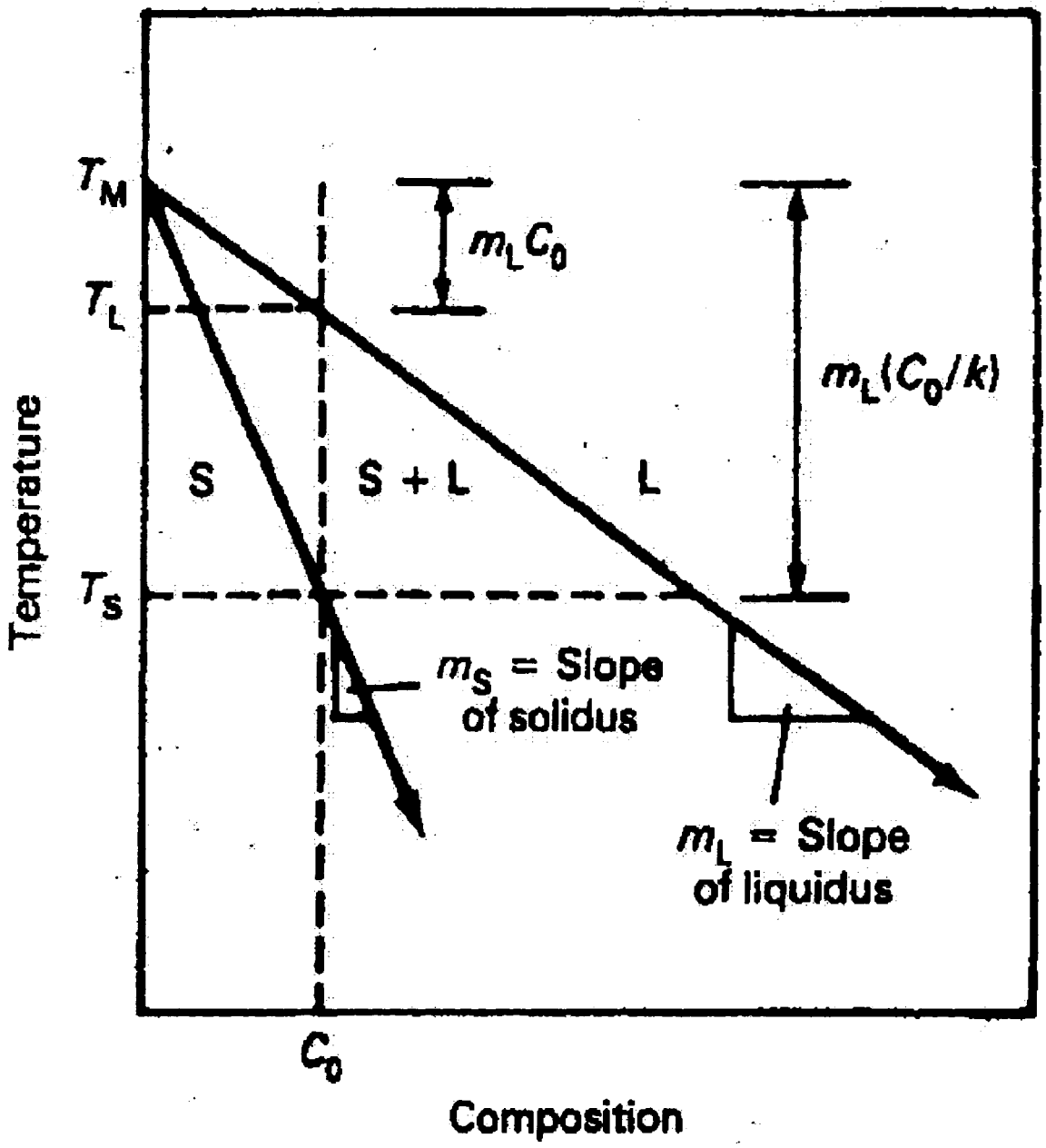

Fig 2.24: Hypothetical binary alloy phase diagram showing key parameters required to derive the relative potency factor (RPF) [87].

and the slope of the solidus is m_S and the equilibrium partition coefficient is given by k. A relative potency factor (RPF) was defined by Boland as the change in melting temperature range per weight percent of solute added and is given by:

$$RPF = (T_L - T_s) / C_o = m_L (k - 1) / k \qquad (2.14)$$

where for $k < 1$, $m_L < 0$; and for $k > 1$, $m_L > 0$. The larger the RPF, the wider the melting temperature range and the higher the solidification cracking susceptibility. This implies that alloy elements with small values of k i.e. those that preferentially partitions into the liquid will tend to increase RPF and thus, cracking susceptibility. Boland, however, indicated that for cracking to occur, it is not a sufficient condition that a wide freezing temperature range should exist but also, the liquid should also be present over a wide temperature interval in a form that will allow stresses to be built up between the grains.

Liquid distribution along grain boundaries is related to interfacial energies of the liquid and solid concerned. According to Smith [91], the interface and grain boundary energy are related to the dihedral angle θ by:

$$\gamma_{SL} / \gamma_{SS} = 1 / \{2\mathrm{Cos}(\theta/2)\} \qquad (2.15)$$

where γ_{SL} is the solid-liquid interface energy and γ_{SS} is the grain boundary energy. The ratio of $\gamma_{SL} / \gamma_{SS} = \tau$ is of particular importance. The dihedral angle is zero for $\tau \leq 0.5$. The relation between dihedral angle and τ for $\tau \geq 0.5$ is shown below:

$\theta = 0^\circ$ $\quad 1 / \{2\mathrm{Cos}(\theta/2)\} = 0.5 \Rightarrow$ Liquid forms as films on grain boundary

$\theta = 60^\circ$ $\quad 1 / \{2\mathrm{Cos}(\theta/2)\} = 0.5\ 7 \Rightarrow$ Liquid forms at grain edges

$\theta > 90^\circ$ $\quad 1 / \{2\mathrm{Cos}(\theta/2)\} = 0.7 \Rightarrow$ Liquid forms on grain corners

In alloy systems where solid solutions occur over an extended composition range, when the liquid is substantially of a composition similar to that of the previously frozen solid,

wetting of the grain faces and edges will almost be complete. If this condition exists in the weld pool over a relatively large temperature interval while it is freezing then it can be inferred that cracks could form easily, since only small areas of the grain faces will be joined. However, when metals are immiscible in the molten state and one metal solidifies τ will be much greater than 0.5, and the liquid will be largely confined to grain edges and corners thereby reducing propensity to cracking. Borland proposed that microfissuring can be prevented when the stresses imposed on the solid-solid bridges between growing dendrites does not exceed a critical value. This stress is a function of the grain boundary area that is joined and not separated by the liquid film. The distribution and quantity of the liquid is influenced by the grain size and shape, and the effect of temperature and cooling rate on the slope of the liquidus and solidus curves.

In practical welding applications, the actual solidification range can be significantly larger than the equilibrium melting temperature for a given alloy. Clyne and Davies [92] defined a more refined criterion in which the time interval spent by the mushy zone in the vulnerable region is considered. This region corresponds to the existence of a thin continuous film of interdendritic liquid in between the dendrite arms and thus also to a low permeability (0.9 – 0.99 volume fraction of solid). When thermal strains are induced in this region by the coherent solid underneath, and the film is unable to sustain the stresses an opening will form which could eventually lead to a crack.

2.5.1.4 Liquid Metal Embrittlement (LME)

This is another phenomenon that is sometimes invoked to explain hot cracking in metals. LME is the reduction in the elongation to failure that can occur when normally ductile

solid metals are stressed while in contact with liquid metals. In severe cases, the ductility may be so reduced that the normal ultimate tensile strength is not achieved and thus the load needed to produce failure is decreased. LME failures occur by the nucleation of a crack at the wetted surface of the solid and its subsequent propagation into the bulk. In its simplest form, LME is caused by the fact that the surface-free energy between liquid and solid at grain boundaries is sufficiently small that it is energetically easy to form liquid cracks. This is shown most clearly by Stoloff et al [93], who considered the relative surface energies and solubilities in nearly 50 solid metal/liquid metal systems, and correctly predicted whether they would be ductile or brittle. There are two necessary but not sufficient conditions that must be satisfied simultaneously for LME to occur;

(i) The applied stress should be sufficient to produce plastic deformation.

(ii) There should be direct contact on an atomic scale between the stressed solid and the embrittler, which implies that the liquid must flow into any crack that may form and propagate [94, 95].

LME failure is usually intergranular and hence it is to be expected that variations in grain size, microstructure, or the grain boundary chemistry should influence the susceptibility of stressed solids. Whether or not LME occurs on a particular occasion depends not only on the composition of the solid/liquid combination but also upon the metallurgical state of the solid and the exposure conditions. One of the interesting aspects of LME is its apparent specificity; i.e., certain liquid metals can embrittle only certain solid metals. Few empirical rules have been advanced to guess possible embrittling systems:

(i) If the two metals involved form stable high melting intermetallic compounds in the solid state, then its unlikely that they constitute an embrittling couple.

(ii) Embrittlement rarely occurs in systems in which two metals exhibit mutual solubility. Hence, the occurrence of LME must be determined by the chemical-electronic interactions between the solid and the liquid and the associated reduction in cohesion [95].

It has also been observed that the degree of embrittlement is related to the dihedral angle, which is a function of the relative surface energies of the solid grain boundaries and the liquid. In a study of the Al-Bi, Al-Cd and Al-Pb systems [96], it was found that, the less the dihedral angle, the greater the embrittlement by the liquid metal. This observation has also been made in Al-Sn system [97], whose dihedral angle depends on temperature. Two of the mechanisms that have been proposed for LME are

(i) Adsorption-induced reduction in cohesion model: embrittlement is associated with a localized reduction in the strength of the atomic bonds at the crack tip or at the surface of the solid metal by certain chemisorbed species.

(ii) Stress-assisted dissolution model: here, the crack is assumed to propagate by the solution of the solid in the liquid under the influence of an applied stress, with volume diffusion of the dissolved solid through the liquid controlling the propagation [98].

The most promising model appears to be the adsorption-induced reduction in cohesion. Unfortunately, it does not permit quantitative assessment of the embrittlement nor

provide insight into the detailed atomic mechanism. Kamdar [95] in his review on LME concludes that the stress-assisted model is an unlikely possibility. He reasons that the reduction in surface energy is obvious since embrittlement effects must originate at the solid-liquid metal interface and hence energy considerations are important. He however, points out that the experimentally determined values of total energy involved in crack propagation are several orders of magnitude greater than the surface energy of the solid. Minor alloying additions to embrittling liquid metal have also been shown to either reduce or increase the severity of LME [95]. However the role of the liquid metal and its solution in controlling the severity of embrittlement and the associated mechanism(s) are not well understood. None of the several theories that have been advanced and models described that attempt to account for the main characteristics of LME has been completely satisfactory.

2.5.2 Heat Affected Zone Liquation Cracking Theories

Heat affected liquation cracking is a general problem that affects a large number of advanced austenistic alloys such as, highly alloyed cast and wrought nickel base superalloys and stainless steels. While the problem of fusion zone cracking is also encountered in many of these alloys, it does not pose as great a challenge as HAZ liquation cracking because it can be essentially managed effectively by proper selection of filler materials and appropriate welding procedures. HAZ liquation cracking is, however, more insidious since the factors and phenomena contributing to its occurrence are often related to the composition of the material and its microstructure, both of which have been optimized to achieve desirable high temperature base metal properties.

HAZ liquation is known to occur either by non-equilibrium phase transformation below an alloy bulk solidus or by supersolidus melting above the equilibrium solidus of the alloy. Subsolidus HAZ liquation is generally considered more detrimental in relation to cracking resistance in that it does not only extend the effective melting range of an alloy but could also influence the nature of supersolidus melting by establishing non-equilibrium film at a lower temperature which alters the reaction kinetics during subsequent heating. There are 2 main mechanisms that are generally used to describe the occurrence of subsolidus liquation in the HAZs; grain boundary penetration mechanism and grain boundary segregation mechanism. Grain boundary penetration mechanism involves a phenomenon known as constitutional liquation of second phase particles in the HAZ during welding operation and subsequent penetration of the grain boundary regions by the resulting liquid film. This liquation is a consequence of the rapid dissolution of the constituent particle at elevated temperatures and the resulting reactions at the particle-matrix interface. The amount of liquid that forms along the interface depends on the heating rate, initial particle size and dissolution kinetics of the constituent particle at elevated temperatures. Since the HAZ cracking is an intergranular phenomenon, penetration of the grain boundary liquid film is requisite to the occurrence of cracking. This could occur by the interaction of a migrating HAZ grain boundary with liquating matrix particle or, if the liquating particles are already situated on the grain boundaries. The penetration of the grain boundary by the liquid at the particle-matrix interface either pins the boundary or significantly slows its rate of migration and allows uniform wetting by the liquid. Grain boundary segregation mechanism involves the segregation of surface-active elements, which in most cases are also melting point depressants, to the

grain boundaries leading to a localized composition with a lower melting point. This mechanism could be important in many single-phase materials that are comparatively free of intermetallic and constituent particles. In practise, both grain boundary penetration and segregation mechanisms could be active in the HAZs of a material. HAZ liquation microfissures form in a manner somewhat analogous to the formation of solidification cracks in the fusion zone. Cast microstructures appear to be more susceptible to HAZ liquation cracking than those present in wrought alloys due to the high level of inhomogeneity present in cast alloys that makes them susceptible to the formation of incipient melting below the alloys equilibrium solidus temperature.

2.5.2.1 Constitutional Liquation [99]

The theory of constitutional liquation was first proposed and published by Pepe and Savage with supporting experimentation on 18Ni Maraging steel [99]. The theory has gained wide acceptance since its introduction and it has been used to explain the occurrence of non-equilibrium melting in a variety of alloy systems. It describes the formation of liquid pockets and the subsequent intergranular liquid film by a eutectic-type reaction between a second phase particle and the surrounding matrix. Under conditions of slow heating (i.e. equilibrium heating) particles can be dissolved by diffusional processes before they have an opportunity to react with matrix. However, most welding processes are characterized by very rapid heating rates (non-equilibrium), which could preclude complete dissolution of the particle prior to reaching a temperature at which eutectic reaction occurs between the dissolving particle and the surrounding matrix.

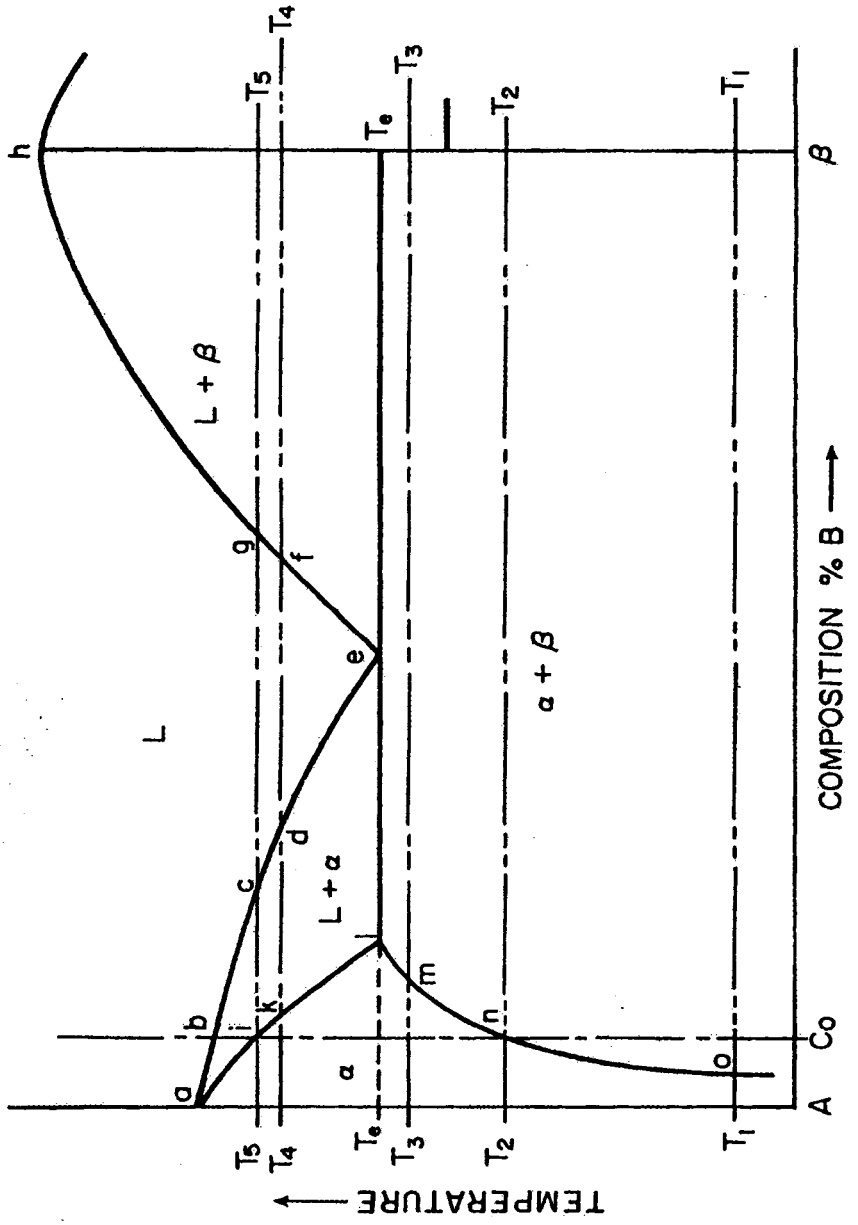

Fig 2.25: Schematic diagram of a portion of hypothetical phase diagram for an alloy system exhibiting constitutional liquation [99].

Constitutional liquation was illustrated by the use of a simple binary phase diagram for a hypothetical binary alloy system shown in figure 2.25 [99]. At temperature T_1 the alloy with composition C_o consists of a high melting point spherical β (A_xB_y) intermetallic particles distributed within the α phase matrix. As the temperature increases at an infinitely slow rate, the solubility of element B in the α matrix increases causing gradual dissolution of the A_xB_y particles until at temperature T_2 when complete dissolution should occur and the alloy becomes a homogeneous single solid solution phase. Continued heating at an infinitely slow rate from T_2 to just below T_5 would cause no further phase transformation in the alloy but rather the occurrence of normal grain growth and equilibrium grain boundary segregation. At T_5, the solidus of the alloy, melting begins with the formation of liquid of composition corresponding to point "C". The behaviour under a non-equilibrium rapid heating would, however, be different from the one just described above. Figures 2.26 shows schematically the changes expected in the vicinity of the β particles during rapid heating to temperatures T_3, T_e and T_4, also marked on the phase diagram in Figure 2.25. During heating to T_3, β begins to dissolve since it is unstable with respect to the α matrix at this temperature. Therefore, the β phase should shrink somewhat from its original size (represented by the dashed circle in fig. 2.26(a)) to a smaller size (represented by the solid circle in fig. 2.26(a)). The solute B atoms released from β particles should diffuse into the adjacent α matrix. However, as shown in figure 2.21, the β must be in contact with α phase of composition 'm' if the two phases are to coexist. Thus, a concentration gradient is set up in the α matrix with a maximum of 'm' at the β interface and a decrease towards the original matrix

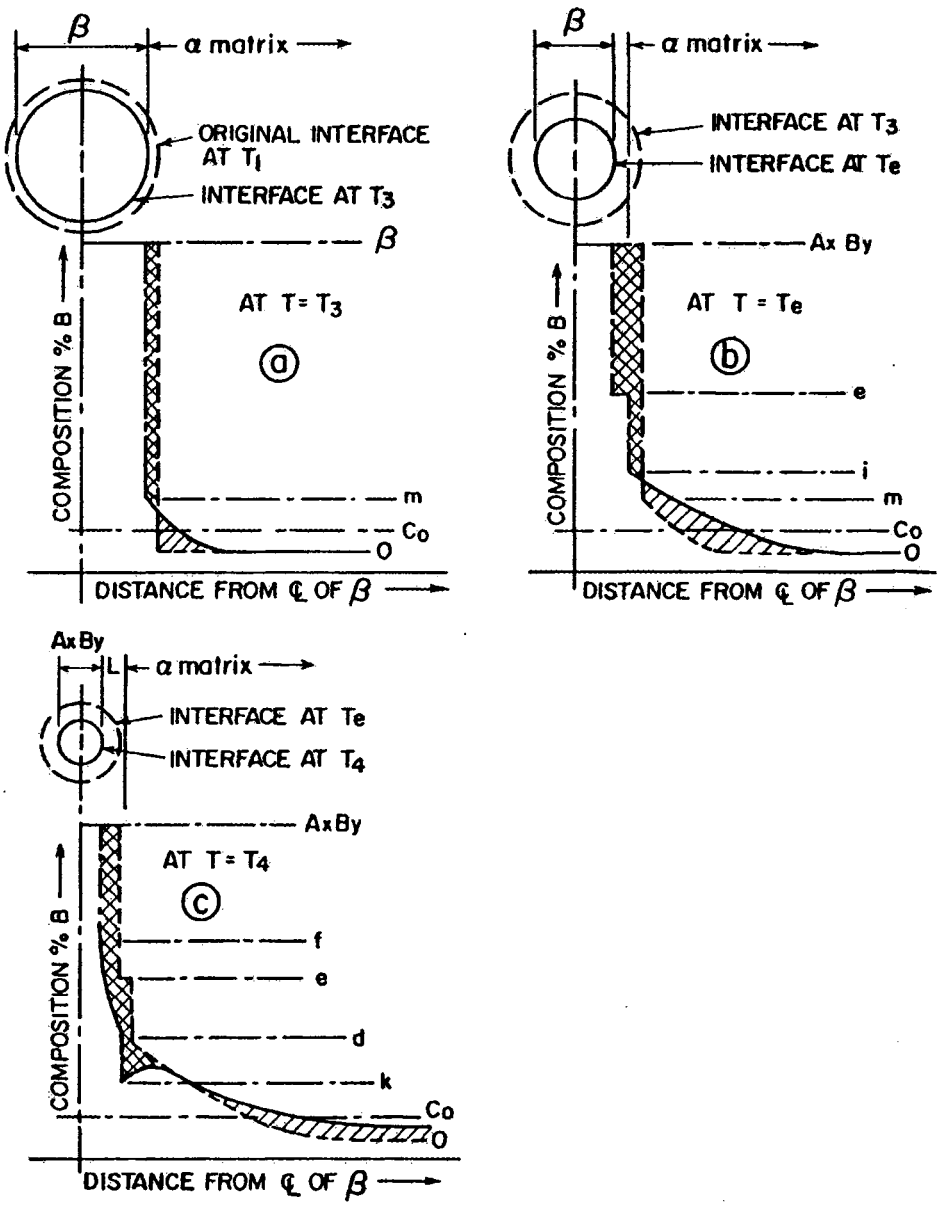

Fig 2.26: Schematic representation of the concentration gradients at various temperatures during formation of constitutional liquation [99].

composition (represented by point o) further away into the α phase. The slope of the concentration gradient produced would be dependent upon the following:

(1) Heating Rate: The faster the heating rate, the steeper should be the concentration gradient.

(2) Solute Diffusivity: The slower the diffusivity of the solute B atoms, the shallower would be the concentration gradient.

(3) Accommodation Factor: The relative ease with which each successive single-phase region in the diffusion zone accommodates the solute atoms would influence solute build up and thus the concentration gradient. The easier the accommodation the shallower the gradient.

Figure 2.26 (b) shows further changes, which should occur during continuous heating from temperature T_3 to T_e, the eutectic temperature. The dashed line represents solute distribution present at temperature T_3, while the solid line represents the modified solute distribution at T_e. During the time interval of heating the alloy from T_3 to T_e, β continues to dissolve as shown in fig. 2.26 (b) where the dashed circle represents the location of the particle interface at T_3 and the solid line when the temperature reaches T_e. At T_e, the composition corresponding to point 'e' permits formation of a liquid phase at the interface of the β phase. Thus, at the instant the temperature of the alloy reaches the eutectic temperature, the undissolved portion of β particle should be surrounded by a liquid phase of composition 'e' which, in turn, should be surrounded by the α matrix. The distribution of solute atom B in the three phases coexisting at T_e is shown in fig. 2.26 (b).

Additional heating to T_4 would allow more time for dissolution of the β phase. During heating above T_e, the equilibrium solubility of B atoms in the α phase decreases along the solidus line 'akl'. Therefore as the temperature rises above T_e, the concentrations of the solid solution and the liquid phase in contact with one another should correspond to 'k' and 'd' respectively (fig 2.25). This readjustment in composition would create an inverted region in the concentration gradient similar to that shown in fig 2.26 (c). The excess solute in the α phase would cause the α/liquid interface to move epitaxially into the α matrix until the excess solute is consumed by forming liquid of composition 'd', since a solid metal cannot be superheated above its liquidus temperature by more than an infinitesimal amount. The expected solute distribution at temperature T_4 can be represented by the solid line of fig. 2.26 (c).

At temperature T_4 each undissolved β phase should be completely surrounded by a liquid phase of variable composition ranging from 'f' at the β interface to 'd' at the interface with the α matrix. Hence, localized melting should be possible with rapid heating rates at temperatures below the equilibrium solidus temperature T_5. This phenomenon, which in theory could occur at all temperatures above T_e, is termed constitutional liquation. Evidence of constitutional liquation should be observable whenever an intermetallic compound and the surrounding matrix phase react to form a low melting liquid phase, provided that the heating rate is rapid enough to preclude complete dissolution of the compound prior to reaching the minimum liquidus temperature. It should however be mentioned that if the initial composition of the alloy is above the solubility limit 'l' (fig. 2.25), then occurrence of eutectic type melting at β/α

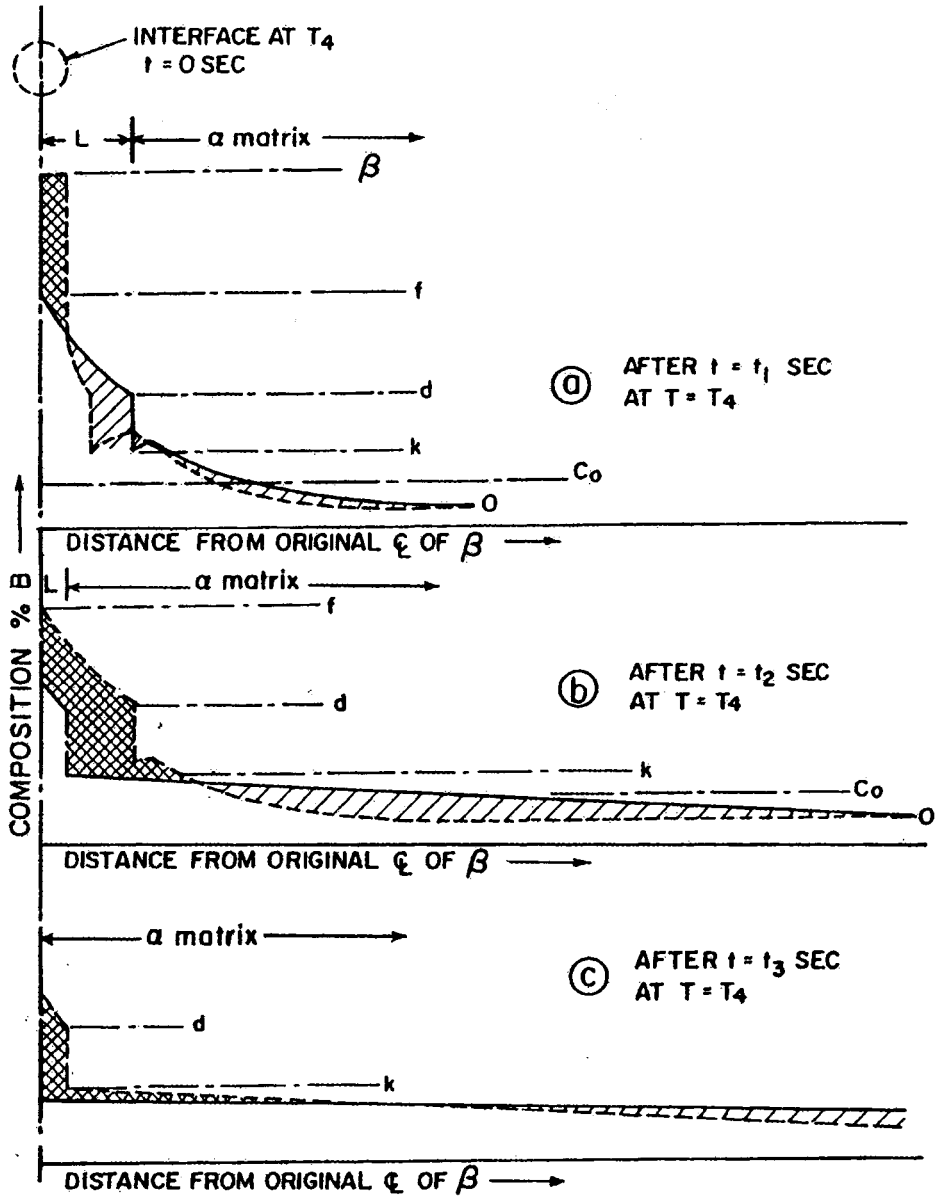

Fig 2.27: Schematic representation of the effect of holding time on stability of liquid film produced by constitutional liquation [99].

interface would be independent of heating rate as β would be thermodynamically stable up to the eutectic temperature T_e.

Figure 2.27 illustrates schematically, the changes in solute distribution that occur in a specimen exhibiting constitutional liquation when heated rapidly to temperature T_4 and then held isothermally for varying times. After sufficient holding time, nearly complete homogenisation occurs thereby permitting the liquid phase to dissipate completely diffusion-induced solidification. Subsequent to solidification of the liquid, the composition gradient of B atoms in α phase would exhibit a maximum corresponding to the composition represented by the point k (the maximum solubility of B atoms in the α phase at T_4) at the original centre position of β and decrease towards a composition corresponding to point 'o' at the interior of the α matrix. Therefore, the liquid films produced by constitutional liquation should experience gradual modification in composition once the β phase is completely dissolved and should ultimately disappear by solidification if subjected to a sufficiently isothermal holding at any temperature below the equilibrium solidus.

One important factor that significantly influences the occurrence of constitutional liquation in multi-component system is the solid-state dissolution behaviour of the second phase particle. The constitutional liquation of interstitial compounds such as Fe_3C, is unlikely, because of the ease of dissociation and rapid diffusion of the interstitial solute, like carbon. This was verified by Aronso [100] who studied constitutional liquation in plain carbon eutectoid steel and concluded that with a heating rate of 625°C/s, Fe_3C particles less than 2μm in diameter would dissolve completely prior to reaching the eutectic temperature of 1271°C. In contrast, a less readily dissolvable alloy carbides or

Table 2.3: Constitutional Liquation in Multicomponent Systems

Alloy System	Liquating Phase	Reference
Udimet 700	M_3B_2	Owczarski et al [51]
Inconel 600	Cr_7C_3, Ti (CN)	Weiss et al [101]
18% Maraging steel	Titanium Sulphide	Pepe and Savage [99]
Austenitic alloy A286	TiC or Ti (CN)	Brooks [102]
Hastelloy X	M6C	Duval et al [51]
Inconel 718	NbC and Laves Phase	Radhakrishnan et al [53]
Incoloy 903	MC and MNP Phosphides	Nakkalil et al [103]

intermetallic compounds involving substitutional type solute, makes constitutional liquation almost unavoidable, except for welding conditions producing extremely slow heating rates. Other investigators have also substantiated the occurrence of constitutional liquation in multi-component alloys. Some of the alloy systems in which constitutional liquation induced has been observed and the corresponding liquating phases are shown in Table 2.3.

2.5.2.2 Grain Boundary Segregation Mechanism

Grain boundary liquation resulting primarily from elemental segregation has been used to explain the occurrence of non-equilibrium subsolidus melting in alloys where constitutional liquation does not, or cannot occur. In its simplest form it provides for solute/impurity element segregation to grain boundaries, thereby reducing the melting temperature of the boundary regions relative to the surrounding matrix. Above a critical temperature during welding operation, preferential melting occurs along these boundaries in the HAZ subjecting them to the occurrence of liquation cracking.

Elemental segregation to base metal grain boundaries prior to welding can be induced during different thermal processes such as casting, hot forming and heat treatment. It is a diffusion-controlled process and can occur by two mechanisms, viz., equilibrium segregation [104] and non-equilibrium segregation [105-107]. Equilibrium segregation occurs when a material is held at a sufficiently high temperature to permit appreciable diffusion of the solute atom from inside the grain matrix to grain boundary where it is absorbed to reduce the interfacial free energy of the loosely packed region. The segregated atoms are localized to a few atomic layers at the boundary and the total

amount is usually of the order of a monolayer. The extent of this segregation increases with decreasing temperaure and increasing initial solute concentration in the matrix.

Non-equilibrium segregation occurs during cooling from elevated temperature and during annealing following plastic deformation. This type of segregation requires the formation of solute-vacancy complexes and a concentration gradient of these complexes between the grain interiors and grain boundaries. Annihilation of vacancies at grain boundaries during cooling produces a concentration gradient of complexes, which drives the complexes to diffuse from within the grain to the grain boundary regions. This would result in excessive concentration of solute atoms in the vicinity of grain boundaries. The degree of non-equilibrium segregation has been found to depend on the starting temperature, cooling rate, bulk concentration of solutes and the binding energy between solute atoms and vacancies [105-107]. For more complex alloys, like ternary systems, the different solutes may interact at the grain boundary and enhance or decrease segregation. This synergetic effect, which is the cause of most intergranular failures in engineering materials, has been studied in detail by Guttmann [108]. It has been proposed that the free energy of segregation of one species may be increased by the second if the interaction energy between the two species is negative (attraction) [108].

Grain boundary segregation can also take place during welding operation [109]. The occurrence of equilibrium segregation in this case might be dependent on the temperature to which the material is exposed and the diffusion time that is available. Thompson et al [110] examined grain boundary segregation in IN 718 superalloy using Auger spectroscopic analysis and reported that HAZ liquation and subsequent cracking was caused by segregation of sulphur to the grain boundaries during pre-weld heat

treatments. Huang et al [111] have also attributed HAZ liquation cracking to equilibrium and non-equilibrium grain boundary segregation of boron detected by Secondary Ion Mass Spectrometry (SIMS) analysis, after various pre-weld heat treatments of IN 718 alloy. Chaturvedi et al [112] compared the effect of S and B segregation on HAZ liquation cracking of IN 718-based alloys and found that B has much more detrimental effect than S, which supports earlier suggestion of Kelly [113]. Guo et al [114] investigated the interdependence of character of grain boundaries, intergranular segregation of boron and grain boundary liquation in IN 718 superalloy. They reported a close relationship amongst crystallographic character of grain boundaries, boron segregation and intergranular liquation in simulated weld HAZ in the alloy. The grain boundary character determined the level of segregation of boron, which in turn determined the liquation tendency during welding thermal cycle. They observed a high level of boron segregation on random boundaries by Secondary Ion Mass Spectroscopy (SIMS), which resulted in extensive liquation during welding simulated thermal pulse. Very low levels of boron segregation were found on the Coincident site lattice (CSL) boundaries and they exhibited a higher resistance to intergranular liquation. It was observed that as the Σ value decreased, the tendency for boron segregation and grain boundary liquation decreased.

A grain boundary sweeping mechanism has also been proposed to account for the segregation during welding [109]. It is suggested that, as grain boundaries migrate upon heating above the threshold grain growth temperature, solute and/or impurities are swept into the boundaries and are dragged along as the grain growth proceeds. It has, however, been questioned whether the solutes are swept into grain boundaries or the migrated grain

boundaries can actually escape the segregated solutes during their migration [115]. Romig et al [116] investigated the possibility of occurrence of grain boundary sweeping mechanism in simulated HAZ microstructures in alloy 800. They reported using analytical electron microscopy examination that no clear evidence for grain boundary enrichment via a sweeping mechanism could be detected in samples heated to liquation temperature range and then quenched in-situ. Instead, a microconstitutional liquation mechanism was detected whereby submicron Ti(C,N) particles reacted with the surrounding matrix and liquated. This liquation reaction resulted in localized liquation of the grain boundaries and a subsequent loss in ductility, thereby producing a crack susceptible microstructure. Another mechanism for HAZ grain boundary elemental segregation is described by the pipeline diffusion theory. Epitaxial nucleation and growth of fusion zone grains normally makes the grains in the weld metal zone to be continuous with those in the HAZ at the fusion fine. Solute partitioning (microsegregation) during weld metal solidification could result in solute/impurity enrichment along the grain boundaries in the fusion zone relative to those in the HAZ. This provides a diffusion pipeline for elemental segregation and subsequent enrichment of the HAZ grain boundaries. Since grain boundary diffusion is faster than lattice diffusion [117-120], this mechanism could contribute to grain boundary liquation in HAZ regions adjacent to the fusion line.

2.6 Previous Investigations of Nickel Based Superalloy Weldability

A great number of investigations have been carried out over the past 40 years on weldability of nickel base superalloys. Metallurgical problems associated with welding of

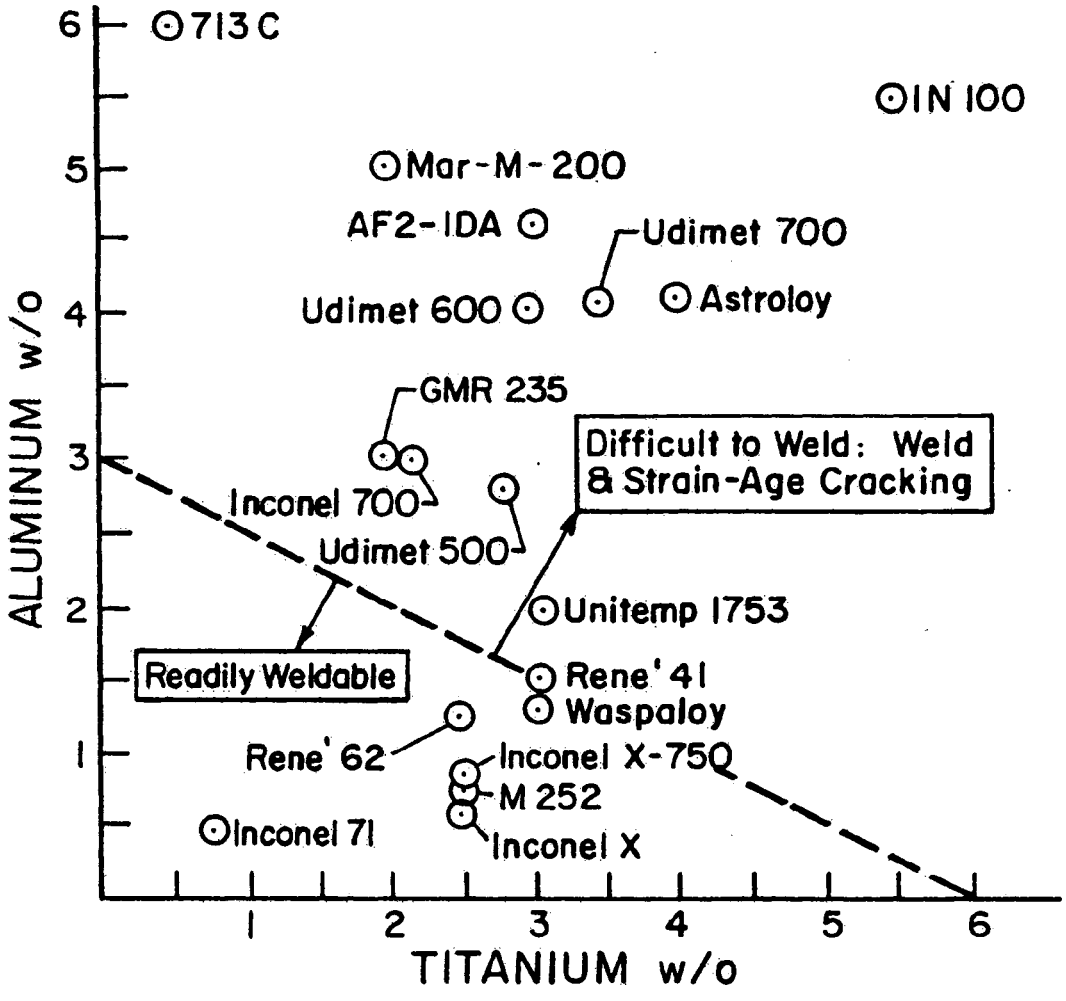

Fig 2.28: Separation between γ' strengthened alloys that are difficult to weld and those readily weldable [83]

nickel base alloys include porosity, fusion zone cracking, heat affected zone cracking, loss of corrosion resistance, embrittlement by trace element segregation and loss of mechanical properties due to grain boundary liquation and subsequent formation of re-solidified constituents. Post weld heat treatment (PWHT) is usually applied as a remedy to most superalloys weldments to modify the as-welded microstructures and relax residual welding stresses in order to impart optimum reliable properties. Nevertheless, not all superalloys can be readily post weld heat treated successfully due to the occurrence of post weld heat treatment cracking, which is also known as strain age cracking. The sensitivity of a particular alloy to fusion zone cracking, HAZ liquation cracking and PWHT cracking is primarily dependent upon the alloy composition, thermal history of the base alloy and the state of stress generated in the weldment during welding and heat treatments. The status of welding technology for nickel-base superalloys is shown in figure 2.28 [83]. Those with Al and Ti contents, shown below the dashed line in the figure are readily weldable. As combined Al and Ti content is increased, welding becomes more difficult. Alloys like Rene 41 and Waspaloy, which are on the borderline weld with relatively little difficulty but sometimes crack during PWHT [83]. Based on the criterion shown in figure 2.28, IN 738 can be considered to be a difficult to weld alloy. Some examples of previous investigation of weldability of some superalloys are summarized as follows:

Owczarski et al [51] used Gleeble to perform hot ductility testing and study the HAZ cracking behaviour of Udimet 700 and Waspalloy. The alloys were tested in the solution treated and aged conditions. In both alloys, liquation was found to initiate below the bulk solidus in the vicinity of MC – type carbides and, in Udimet 700 cracking was

enhanced by the presence of borides. They believed that the re-solidification of liquated grain boundaries embrittled them, causing subsequent solid-state cracking, or crack initiation in liquated areas and propagation along embrittled grain boundaries. Savage et al [121] investigated Hastealloy X, using a modified hot ductility specimen, which contained a GTA weld along the centre. Cracking was found in the fusion zone along the solute-rich grain boundaries. In the HAZ, cracks were associated with grain boundaries wetted by liquid film produced by constitutional liquation of carbides and with boundaries enriched in solute but not associated with discrete particles. The solute enrichment was attributed to grain boundary sweeping and pipeline diffusion.

Thompson and Genculu [122] used Gleeble to study the role of heat treatment on the HAZ hot cracking resistance of alloy IN 718. A modified HAZ simulation test was performed by heating samples to specific peak temperatures followed by quenching to preserve the high temperature microstructure for correlation with hot ductility tests. Their result showed that the solution annealed material was more resistant to HAZ cracking than age-hardened and as-received materials. HAZ cracking was attributed to the grain boundary liquation caused by constitutional liquation of NbC particles.

Nakkalil et al [103] performed microstructural study of Incoloy 903 weldment known to be susceptible to HAZ hot cracking, using analytical electron microscopy. The microstructure observed in the HAZ microfissures suggested grain boundary liquation and formation of low melting liquid films enriched in niobium and carbon. The liquid was reported to originate primarily from the constitutional liquation of MC carbides and MNP phosphides that were present on the grain boundaries of the alloy prior to welding. The observation of microfissuring on grain boundaries, which showed continuous, and/or

semicontinuous sheets of resolidified constituents was taken as an indication that HAZ microfissuring in this alloy occurs due to the presence of low melting liquid films.

2.7 Scope and Nature of the Present Study

As discussed earlier, the γ' precipitation hardened nickel base IN 738 is a very difficult to weld alloy due to its high susceptibility to HAZ cracking both during welding and post weld heat treatment. However, no detail study exists in open literature on the occurrence and nature of HAZ liquation in IN 738 weldment, despite the fact that liquation has been found to be the primary cause of low resistance of HAZ grain boundaries to microfissuring during welding of nickel base superalloys. Likewise, liquation occurring during welding has also been found as a fundamental cause of grain boundary embrittlement, which degrades material resistance to PWHT cracking. Furthermore, very limited information is also available about the as-weld fusion zone microstructures of this alloy, which is the basic metallurgical factor controlling response of the weld metal to PWHT. Adequate comprehension of the various liquation phenomena will undoubtedly aid the development of suitable and appropriate pre-weld heat treatment, which has been proven to be an effective means for eliminating or minimizing HAZ cracking in nickel base alloys. A pre-weld heat treatment has been developed at the University of Manitoba (UMT) [123], which resulted in considerable reduction in the HAZ cracking after welding. However, further study of the causes of HAZ cracking in IN 738 superalloy is considered imperative to optimizing pre-weld heat treatment for the alloy. Also, proper characterization of the fusion zone microstructure would contribute to the development of a more suitable PWHT schedule that would result

in minimal microfissuring and reliable microstructures and properties. Therefore, the objectives of this study were:

1. To study and gain a comprehensive understanding of the nature of grain boundary liquation in the HAZ of IN 738 superalloy and its contribution to microfissuring.
2. To study the microstructures that develop in the weld-metal zone of tungsten inert gas (TIG) welded IN 738 superalloy.

Investigations were performed to provide the following principal information about HAZ liquation cracking in IN 738 and the microstructures which develop in the weld-metal zone during autogenous TIG welding.

(a) Microconstituents in the as-cast, solution treated and overaged alloys that are contributing to the HAZ liquation.

(b) Liquation mechanisms involving different constituent particles during welding thermal cycle.

(c) Characteristics of intergranular liquid film affecting the alloys susceptibility to liquation cracking.

(d) Hot ductility data of the alloy in the solution treated and overaged conditions.

(e) Correlation between the HAZ liquation and alloys hot ductility data of the alloy in the solution treated and overaged conditions, to confirm the role of HAZ grain boundary liquation in reducing resistance to hot cracking.

(f) Characterization of microstructures which develop in the weld fusion zone of the alloy during TIG autogenous welding.

Chapter 3

Experimental Procedures

3.1 Materials and Processing

The base alloy for this investigation was IN 738 supplied by Hitchiner Manufacturing Co. Inc. in the form of cast plates of dimension 15 X 2.5 X 0.6 cm. The chemical composition of the as-received alloy is shown in Table 3.1. Some of the as-received plates were given two pre-weld heat treatments viz., (i) standard solution treatment at 1120°C for 2hrs followed by argon quenching (ST) (ii) solution treatment at 1120°C for 2hrs and subsequent overaging at 1025°C for 16hrs followed by water quenching (UMT). 7.6 x 2.5 x 0.3 cm rectangular plates on which 0.2 cm deep V groove had been machined were gas tungsten arc welded (GTAW) with IN 738 filler wire, using a current of 60A d.c. and 10V. The welding torch and wire speeds were maintained at 76mm/min and 304mm/min, respectively. Metallographic sections were cut transversely to the weld from the welded specimens by electro-discharge machining for subsequent microstructural examination.

3.2 Optical Microscopy, Scanning Electron Microscopy and Electron Probe Microanalysis.

All the microstructural conditions prior to TIG welding were studied by optical microscopy, scanning electron microscopy (SEM) and X-ray microanalysis (energy dispersive spectroscopy (EDS) and wavelength dispersive spectroscopy (WDS)). Metallographic sections from welded specimens and Gleeble thermally cycled specimens were likewise examined to study microstructural changes occurring during welding thermal cycle. An inverted-reflected light microscope equipped with a CLEMEX Vision

Table 3.1 Composition of IN 738LC Base Alloy used in the present Study

Elements	Wt%
Aluminum (Al)	3.46
Boron	0.012
Carbon (C)	0.11
Chromium (Cr)	15.84
Cobalt (Co)	8.50
Iron (Fe)	0.07
Manganese (Mn)	0.01
Molybdenum (Mo)	1.88
Niobium (Nb)	0.92
Silicon (Si)	0.01
Sulfur (S)	0.001
Tantalum (Ta)	1.69
Titanium (Ti)	3.47
Tungsten (W)	2.48
Zirconium (Zr)	0.04
Nickel (Ni)	REM

3.0 image analyzer system was used for qualitative and quantitative optical metallography. Polished samples were used to examine the morphology of cracking and level of pores and micropores in the base metal, fusion zone (FZ) and the HAZ. Polished samples were electrolytically etched in 12ml H_3PO_4 + 40ml HNO_3 + 48ml H_2SO_4 solution at 6V for 5s. This etchant revealed the dendritic microstructure of the alloy and enabled easy measurements of the dendrite arm spacing. The serrated nature of grain boundaries in the alloy was also appreciably revealed by the etchant.

SEM studies were undertaken on a JEOL 5900 SEM both under secondary emission mode (SE) and backscatter emission (BSE) on etched and polished samples respectively. Semi-quantitative chemical composition analysis of the different microconstituent particles in the base alloy, HAZ and FZ were conducted using ultra-thin window Oxford EDS system with INCA analyzing software attached to the SEM. Other SEM techniques viz SEM/line scanning and SEM/x-ray imaging were also utilized in the microstructural analyses. It should be mentioned that several etching techniques and solutions were attempted during this investigation to reveal microstructural details concerning the nature of HAZ microfissuring of welded samples in the SEM. Out of all the solutions and techniques used, it was only the electrolytic etching described previously combined with proper optimization of the several SEM operational variables that sufficiently revealed microstructural evidence of HAZ liquation, which is fundamental to the cracking mechanism. Microstructures of the FZ in SEM were captured by an attached CLEMEX Vision 3.0 image analyzer system, which was subsequently used to estimate the volume fraction of carbides and γ-γ' eutectic constituent.

Electron microprobe analysis was performed with a Cameca MBX electron microprobe machine. X-ray microanalysis in the electron probe microanalyser (EPMA) has become a valuable tool for the investigation of elemental microsegregation in castings as well as in fine microstructures of weld fusion zone. The salient characteristic of the EPMA is the ability to determine the chemical composition of very small volumes within a bulk sample. By using the smallest probe size available, composition of particles in a matrix as small as 1μm in diameter can be reliably analyzed with sufficient accuracy. In the present work, the EPMA was operated at 15KeV and a beam current of ~ 20nA. Under these conditions the volume of x-ray generation would be slightly less than 1μm in diameter [124]. These conditions were chosen to optimize the special resolution of the EPMA analyses. The surfaces of as-polished EPMA specimens were carbon coated prior to analysis. Microchemical analysis of the dendrite core and interdendritic regions and second phase particles were performed by x-ray wavelength dispersive spectrometry. Raw counting data were reduced to weight percentages using a

ϕ (p, z) correction algorithm.

3.3 Analytical Electron Microscopy

Analytical electron microscopy was performed on thin foils and on particles extracted by carbon extraction replica technique from the base metal and weld metal zone, using a JEOL 2000FX transmission electron microscope/scanning and transmission electron microscope. Carbon extraction replicas were made using mounted, polished and etched samples, which were subsequently carbon coated in Edwards Auto36 vacuum coater under a vacuum of about 1x 10^{-5} torr. The deposited carbon film was scored into

squares using a sharp edge before electroetching in a solution of 10% HCl + 90% methanol at a d.c. voltage of 20 volts for 12 secs. The carbon film was floated off in distilled water by lowering the sample slowly into the water at a shallow angle. Water surface tension pulled off the carbon film, which were gathered and dried on 3mm diameter, 200 mesh, copper grid disks for the succeeding TEM examination.

Thin foils were produced by twinjet polishing with 25% perchloric acid in 75% methyl alcohol at -20 to –40°C using a current of 1.8 – 3.5A. In cases where good polishing was not achieved by the electrolytic polishing, the samples were finish-polished by ion-milling for 15 to 45 minutes at 4.5KeV (Ar^+), 50mA, 12 degree glancing angle and ~ -130°C in a Gatan Duomill equipped with a liquid nitrogen cooled stage. Selected area diffraction was used to identify the crystal structure of various phases observed on the carbon extraction replicas and thin foils. Their lattice parameters were accordingly determined from the numerous reflections obtained from the selected area diffraction patterns (SADP). The camera length calibration was carried out using ring patterns obtained from thin films of evaporated high purity aluminum placed on a copper grid. A double-tilt holder with zero tilt readings was used.

Chemical microanalyses were performed on EDS spectra obtained from thin particles extracted on carbon extraction replica and those in thin foils with TEM operating with a tungsten filament at an accelerating voltage of 180kV. The acquisitions and analyses were performed with an ultra-thin window EDAX EDS equipped with Genesis thin-film analytical software. The program uses Kramer's law for background modeling but does not perform any deconvolution routine for assessment of any relative contribution of elements to overlapped peaks. Nevertheless, x-ray acquisition was mostly

from very thin areas and also from precipitates not aligned along strongly diffracting orientations. Raw x-ray data were converted to weight percentages using theoretical Cliff-Lorimer independent sensitivity factor k_{AB}, which is given by:

$$k_{AB} = (C_A/C_B) \times I_B/I_A \qquad (3.1)$$

where C_A and C_B are the weight percents of A and B respectively and I_A and I_B are the characteristic x-ray intensities.

3.4 Gleeble HAZ Simulation

The Gleeble testing apparatus, a computer-controlled high temperature thermo-mechanical simulator system, was used to simulate a relatively large HAZ area in ST and UMT specimens. Laboratory scale cylindrical specimens of 6mm diameter and 115mm length were rapidly resistance heated between water-cooled copper jaws to various peak temperatures ranging from 1120°C to 1245°C at a rate of 150°C and then held for 0.5s at all temperatures and water quenched. Some samples were also held for 4s at 1165°C before being water quenched. All the Gleeble HAZ microstructure simulation experiments were carried out in air. The sample temperature was controlled with a chromel-alumel thermocouple that was spot-welded at the sample's mid-section. After thermal cycling, the samples were sectioned transversely by electro discharge machining at the location of the spot welded thermocouple and prepared by standard metallographic techniques for microstructural examination. The transverse sections were taken within 0.5mm from the spot where the thermocouples were initially welded, so that any variation due to longitudinal temperature gradient was essentially eliminated. Likewise, in order to minimize the effect of radial temperature gradient, microstructures were

recorded mainly from locations, which were at a radial distance of 0.5mm from the sample surface. It was assumed that these locations were sufficiently far away from the periphery so that surface oxidation effects could be avoided and at same time, the temperatures were close to those measured at the surface. The result from this test should provide necessary information for the understanding of evolution of HAZ microstructures and therefore, the liquation cracking mechanism in IN 738 superalloy.

3.5 Gleeble Hot Ductility Tests

The concept behind hot ductility test is to characterize the ductility of a material at elevated temperatures and relate this ductility data to cracking susceptibility. Specimens similar in configuration to the one used for HAZ microstructure simulation, machined from ST and UMT samples were utilized for the hot ductility tests. Tests were performed in vacuum (2×10^{-5} torr) using a Gleeble 1500 system, which has been refurbished to Gleeble 3500. A specimen freespan (jaw spacing) of 25mm was used. The nil strength temperature (NST) was determined by preloading the samples with a force sufficient to just overcome friction in the movable jaw assembly and then heating the samples at a rate of 111°C/s. The temperature at which fracture occurred was designated as the NST. On-heating tests were conducted by heating the samples to peak temperatures at the rate of 111°C/s held for 0.03s for brief stabilization and then pulled at an extension rate of 25mm/s. On-cooling tests were performed by heating to 1245°C peak temperature held for 0.03s and cooled to the different temperatures at a rate of 19°C/s held for 0.03s then pulled to failure at the same extension rate of 25mm/s. A typical Gleeble thermal cycle

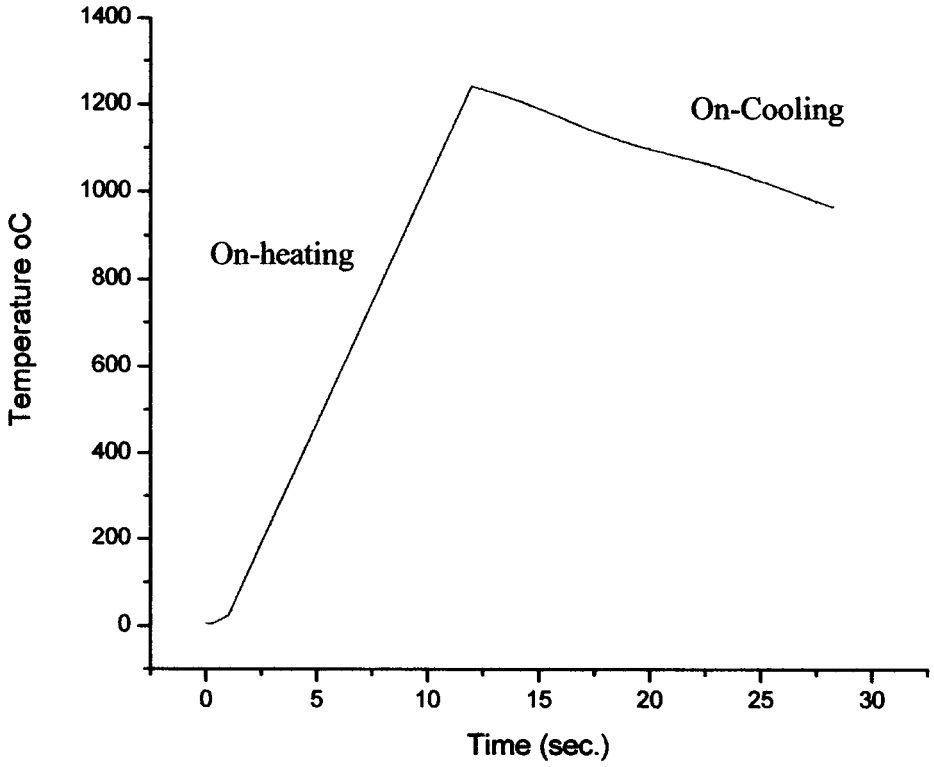

Figure 3.1 Typical On-heating and On-cooling Cycles used for Gleeble Hot Ductility Test

showing the heating and cooling cycles is shown in figure 3.1. This rapid stroke rate was selected to minimize the change in specimen temperature during fracture [125]. The cooling rate of 19°C/s was the maximum achievable with the material and specimen freespan utilized. A dummy sample heated to 1245°C was allowed to free cool to determine the most rapid cooling rate that could be programmed. This maximization of cooling rate allows for a more close representation of actual weld cooling conditions. The peak temperature of 1245°C, which is between the nil ductility temperature (NDT) and NST and specimen freespan chosen are in accordance with recommendations made by Lundin et al [125] in their report on standardization of Gleeble hot ductility test. Diameter of fractured test pieces was measured in several regions around the fracture surface with digital vernier calipers and with a calibrated low magnification microscope to allow for the calculation of reduction in area. The hot ductility testing parameters are summarized in Table 3.2.

Table 3.2 Gleeble Hot Ductility Test Parameters

Process Parameters	Values
Heating Rate	111°C/s
On-Cooling Peak Temperature	1245°C
Hold Time	0.03s
Cooling Rate	19°C/s
Jaw Spacing	25mm
Stroke Rate	25.4 mm/s
Atmosphere	2×10^{-5} torr

Chapter 4

Results and Discussion

4.1 Base Metal Microscopic Examination

4.1.1 Introduction

It is known that the base metal microstructure prior to welding plays an important role in weldability of metals, particularly in relation to microfissuring and other welding defects in the HAZ regions. Therefore, it becomes imperative to characterize the starting microstructure of alloy IN 738 in different conditions prior to welding. This section first describes the results of microstructural characterization of as-cast IN 738, followed by microstructural changes produced by the standard solution heat treatment (ST) and the University of Manitoba heat treatment (UMT).

4.1.2 Optical Microscopy

An optical micrograph of a polished as-cast IN 738 alloy is shown in figure 4.1. A small fraction of casting micropores can be observed within the grains of the alloy. Electrolytically etched samples revealed a cored dendritic microstructure, which is typical of a as-cast alloy, as shown in figure 4.2. The grains consisting of numerous dendrites were observed to be of considerably large size, about 1-2mm, with well rounded/curved serrated grain boundaries. The dendrites were widely spaced and irregular, exhibiting secondary and tertiary arms. The average secondary arm spacing λs was estimated to be 53μm with the values ranging from 50-66μm. The type of solidification microstructure developed in a casting is known to be influenced by two

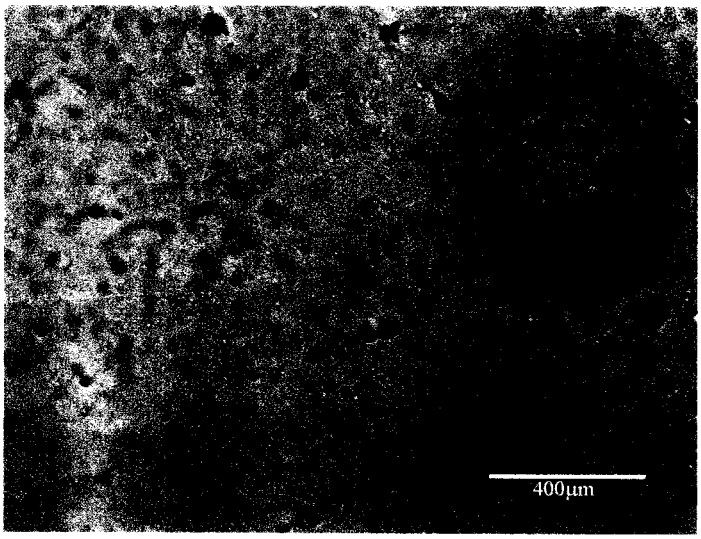

Figure 4.1 Optical micrograph of polished as-cast IN 738.

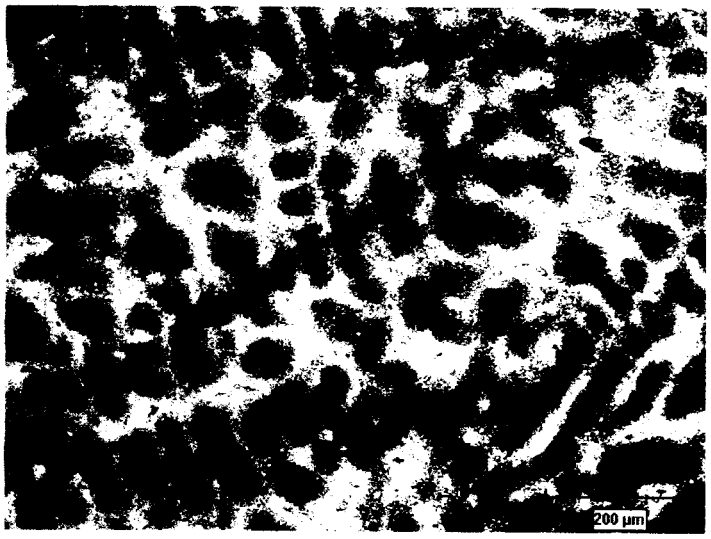

Figure 4.2 Optical micrograph of etched as-cast IN 738.

important solidification parameters, temperature gradient (G) and solidification rate (R). According to Tiller et al [126] a transition from a plane front to a cellular dendritic structure occurs when $G/R \leq \Delta T/D$ where ΔT is the melting range and D is the effective diffusion coefficient of atoms in the liquid. Mclean et al [127] found this transition to be occurring in IN 738 at 2.3 $Khmm^{-2}$. Dendrite arm spacings in castings are often correlated with the cooling rate GR. The following empirical relation has been developed between the secondary dendrite arm spacing and cooling rate in IN 738 alloy [128]:

$$\lambda s \propto (GR)^{-0.4} \qquad (4.1)$$

This shows that a corresponding refinement in dendritic microstructure of IN 738 can be expected with an increase in the cooling rate. Microconstituent particles were observed within the interdendritic regions and along the serrated grain boundaries.

4.1.3 Scanning and Transmission Electron Microscopic Examination

The as-cast alloy was further examined in an SEM to study the nature of microconstituents present in the as-solidified alloy. Second phase particles of different morphologies viz. blocky/cubic, Chinese-script, irregular shaped, and needle-like were observed dispersed within the nickel base γ austenitic matrix. It has been reported [1,16] that phases commonly present in IN 738 are intermetallic $\gamma'(Ni_3Al, Ti)$, MC type carbides, M_2SC Sulphocarbide and M_3B_2 boride in addition to γ-γ' eutectic constituent. A different eutectic-like constituent was observed in front of some of the γ-γ' eutectic in the interdendritic regions. This type of solidification product has not been previously reported by other researchers to be present in IN 738.

The chemical composition of various constituent particles was measured semi-quantitatively by EDS x-ray microanalysis. However, due to elemental resolution and analyzable particle size limitations of SEM/EDS, EPMA/WDS and TEM/EDS techniques were utilized for further microanalyses of the carbide particles and the eutectic constituent formed ahead of the γ-γ' eutectic. γ' precipitate particles, γ-γ' eutectic, MC carbides and M_2SC were identified by their unique characteristic morphologies and chemical composition. The microconstituents observed in the as-cast alloy can be generally classified in to two groups: (i) solidification product including γ-γ' eutectic, MC carbides, M_2SC and the eutectic-like constituent ahead of the γ-γ' eutectic and (ii) solid-state reaction product i.e. the γ' precipitate particles. Each of these groups is discussed in more detail in the following section. However, before proceeding, it is expedient to first discuss the elemental microsegregation pattern that ensued during the ingot solidification, which is an important factor influencing the formation and distribution of various secondary phases.

Dendritic growth during solidification of alloys is known to give rise to elemental partitioning / segregation between solidifying dendrites and the residual interdendritic liquid. The resultant microsegregation often leads to micro-inhomogeneties with local difference in composition producing different precipitate volume fraction, sizes, shapes and mechanical properties in the as-solidified material. The distribution coefficient of an alloying element may be determined by zone melting [129], plane front directional solidification [130] or dendritic solidification [131]. The principle behind all these techniques being the formation of a coarse microstructure (avoiding curvature effects and concentration gradients) by quenching the liquid during solidification and analyzing the

concentration at the interface in the homogeneous solid and in the quenched liquid. Considering the case of local equilibrium, this procedure gives the equilibrium distribution coefficient, k, which describes the direction and extent of microsegregation during solidification. Taha and Kurz [129] have used the method of zone melting, quenching of the melt and interface composition analysis to determine the equilibrium elemental distribution coefficient of the most important alloying elements in IN 738LC alloy. Their result and those of Nakao et al [132] on theoretical k values of B, S and C, as estimated from their Ni-X binary phase diagrams, are shown in Table 4.1 and will be used to discuss the microstructures observed in the present investment cast IN 738 alloy

It can be seen from Table 4.1 [129] that W, Al and Co with k values greater than unity will segregate to the axis of the dendrite arms while Mo, Ta, Ti, Nb & Zr with k values less than unity will enrich the interdendritic regions during solidification. Ni and Cr with k values approximately unity, will tend to be relatively uniformly distributed between the dendrite and interdendritic regions. In comparison with the corresponding distribution coefficient in binary nickel alloys, it can be seen that the general partitioning tendency is the same and that the values (except for Al and Cr) are quite similar. It should be mentioned, that the distribution coefficient may not necessarily be constant during solidification and may be influenced by solidification parameters, particularly the cooling rate. However, they explain reasonably well the observed segregation induced microconstituents in the as-cast alloy, as will be discussed next.

Table 4.1: Elemental Distribution Coefficients of Alloying Elements IN 738

Element	Experimental k [129]	Theoretical k [129] (Ni-X binary alloy)
Al	1.2	0.9
Co	1.1	1.1
Cr	1.05	0.5
Ni	1.05	1.0
Zr	0.06	0.07
Nb	0.4	0.4
Ti	0.6	0.8
Ta	0.7	0.8
Mo	0.85	0.7
W	1.4	1.6
Element		Theoretical k [132] (Ni-X binary alloy)
B	-	0.0082
S	-	0.01
C	-	0.3

γ' Precipitates and γ-γ' Eutectic Product

Figure 4.3 shows an SEM micrograph of the as-cast alloy. Extensive intragranular dispersion of γ' precipitate particles, which could not be resolved by optical microscopy, can be observed. The particles are essentially "ogdoadically" diced cube shape (clusters of cubes particles [133]), in the dendrite core regions and became coarser and more irregular at the dendrite arm boundaries. The "ogdoadically" diced cube morphology of the γ' particles was confirmed by TEM examination of particles extracted on carbon extraction replica (figure 4.4). A more complex dendritically and arrowhead shaped γ' particles were observed along some interdendritic regions (figure 4.5), in addition to the relatively coarser and irregularly shaped γ' particles formed along the grain boundaries. The occurrence of extensive dispersion of discrete γ' particles in the alloy is known to be due to solid-state precipitation reaction involving nucleation and growth of coherent precipitates. Many investigations on nickel base superalloys have shown that γ' precipitates first form as coherent spheres, which change into cubic shape as growth proceeds due to a reduction in strain energy by the formation of low energy (001) interfaces. The development of cluster like γ' morphology is attributed to phenomenon associated with solid-state dendrite growth. Ricks et al [134] investigated the development of solid-state dendritic instabilities in γ' precipitates in a number of nickel base superalloys. The sequence of morphological changes observed during the isothermal treatment at temperature 20°C below the solvus temperature in the alloys was found to be: sphere → cubes → arrays of cubes/ogdoadically diced cubes → solid-state dendrites. The early stages of γ' dendrite formation from cuboidal particles was interpreted to be due to a preferential growth in <111> minimum compression directions. They proposed

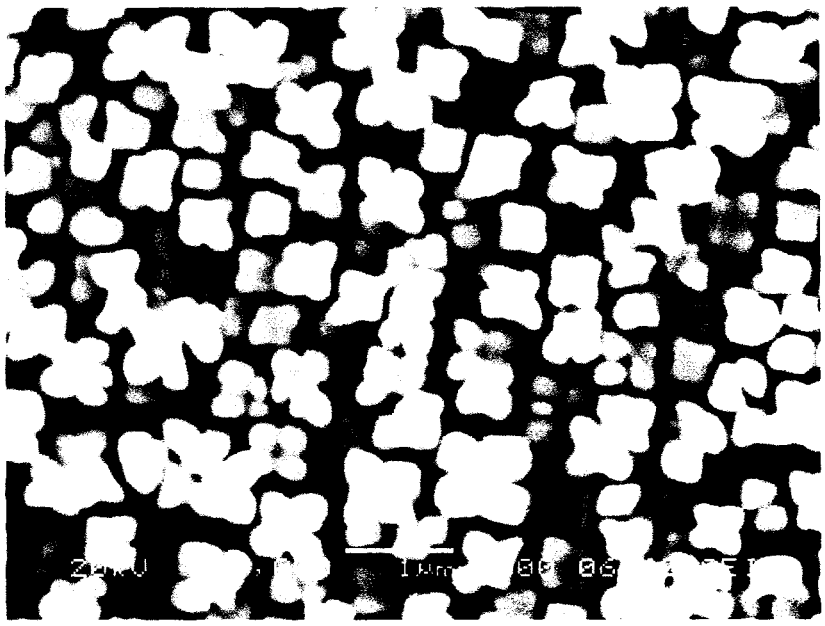

Figure 4.3: SEM micrograph of γ' particles in as-cast IN 738

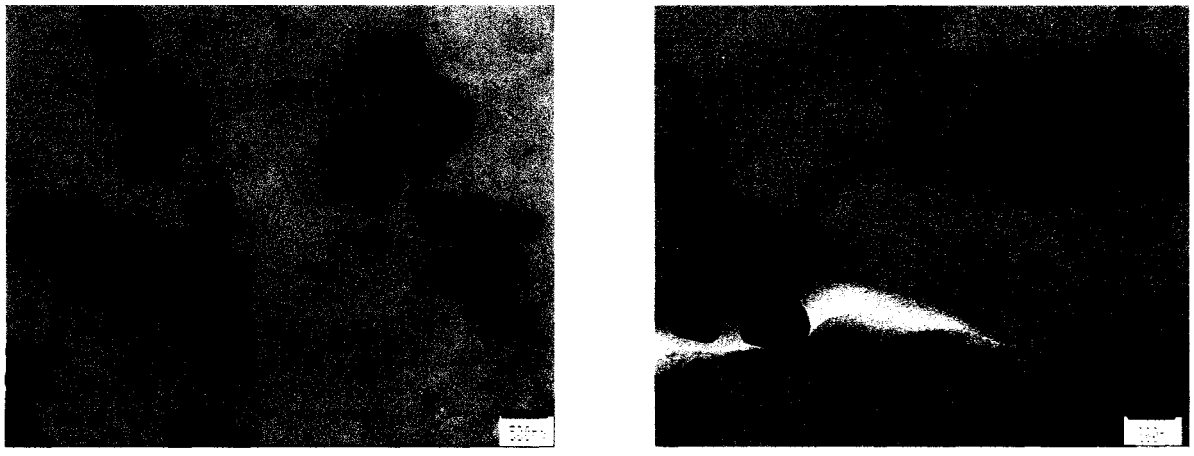

Figure 4.4: TEM micrographs of γ' particles extracted from as-cast IN 738 on carbon extraction replica.

that the anisotropy of the system favored the development of {001} planar facets of the ogdo-cubes. On continued growth, a stage is reached where the protrusions are constrained to adopt a cuboidal morphology, leading to cluster formation. After a longer period, "arrowhead" shapes appear as individual cubes in the clusters which have developed a preferential <111> growth direction. The process of evolution of γ'morphological features from spheres to complex clusters or dendrites is favored by a decrease in cooling rate. More time available for diffusional morphological changes increases the possibility of obtaining complex clusters and dendritic and arrowhead shaped γ'particles in a given alloy system. The observations, in the present work, of variation in γ'morphology from the dendritic core to the interdendritic regions, which contain more complex clusters with dendritic and arrowhead shaped γ' particles, suggests that γ' particles nucleated at different temperatures/time in these regions during continuous cooling of ingot solidification. An earlier γ' nucleation and growth during the continuous cooling process could allow sufficient time for diffusional solid-state transition into complex clusters and dendritically shaped particles in the interdendritic regions and/or areas close to the dendrite arm boundaries compare to the dendrite core regions.

It has been observed [17,18, 135] that in IN 738 alloy there is a considerable difference between the solvus temperature of γ'particles within the dendrite core regions and those at the dendrite arm boundaries and interdendritic zones. Rosenthal et al [135] reported the γ' particles in the interdendritic regions of IN 738 to have a higher solvus temperature, in the range of 1165-1170°C, compared to 1120-1130°C for those within the dendrite core regions. The variation in the γ' solvus temperature was attributed to

microsegregation induced enrichment of interdendritic zones with γ' forming elements, particularly, Ti with k value < 1, during solidification. McColvin [17] observed the dendrite core regions of IN 738 alloy to be surrounded by rings of coarser γ' particles in samples which were heat treated at 1120°C for 2hrs, and attributed it to higher Al and Ti contents. Higher solvus temperature could be responsible for the possible early nucleation and growth of γ' particles in the interdendritic regions into a more complex clusters with dendritic and arrowhead morphology.

In addition to γ' precipitate particles, γ-γ' eutectic was observed along the interdendritic regions of the as-cast IN 738 alloy (figure 4.6). The eutectic consisted mainly of γ' phase separated by thin lamellae of γ phase. Formation of γ-γ' eutectic in most nickel base superalloys is known to be due to the dendritic microsegregation during solidification. Supersaturation of interdendritic liquid with γ' forming elements, caused by continual solute enrichment, at temperatures approaching the equilibrium solidus often results in the subsequent formation of γ-γ' eutectic. In IN 738 alloy, the temperature of γ-γ' eutectic reaction occurring towards the end of solidification process was reported by differential thermal analysis (DTA) to be around 1230°C [136] and 1198°C [137]. However, metallographic examination by Rosenthal et al [135] of directionally solidifying IN 738 from above the liquidus temperature to different on-cooling temperatures followed by water quenching, has shown that γ-γ' eutectic reaction in this alloy occurs over a range of temperatures which could be as low as below 1180°C. Formation of γ-γ' eutectic over a range of temperatures has been also reported by other investigators in other nickel based superalloys [138, 139].

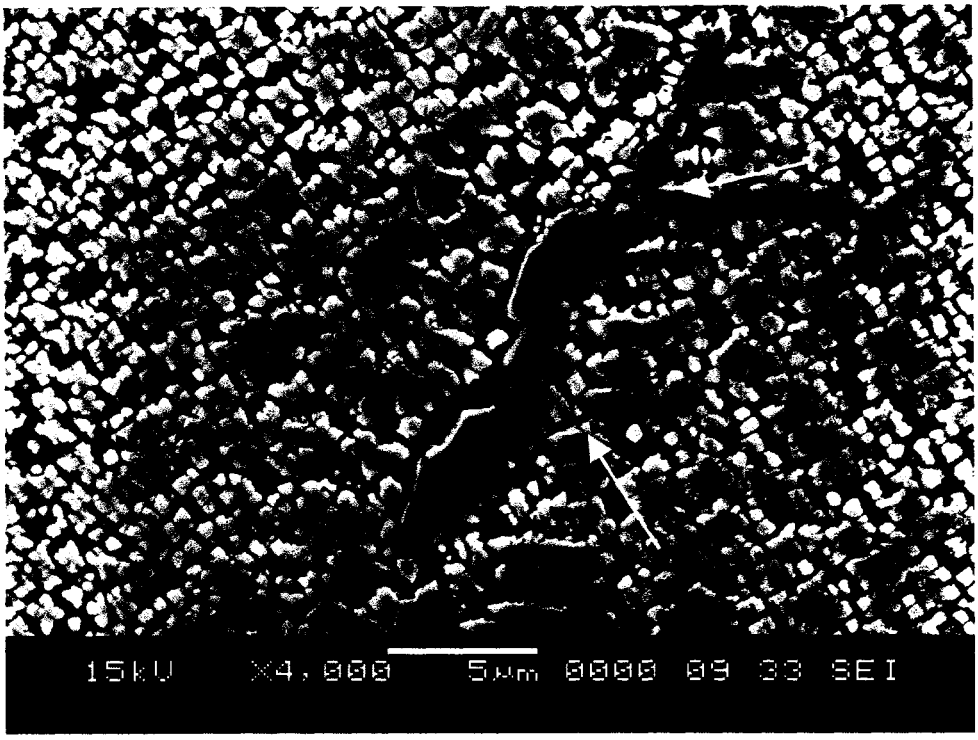

Figure 4.5: SEM micrograph showing dendritically and arrowhead shaped γ' particles

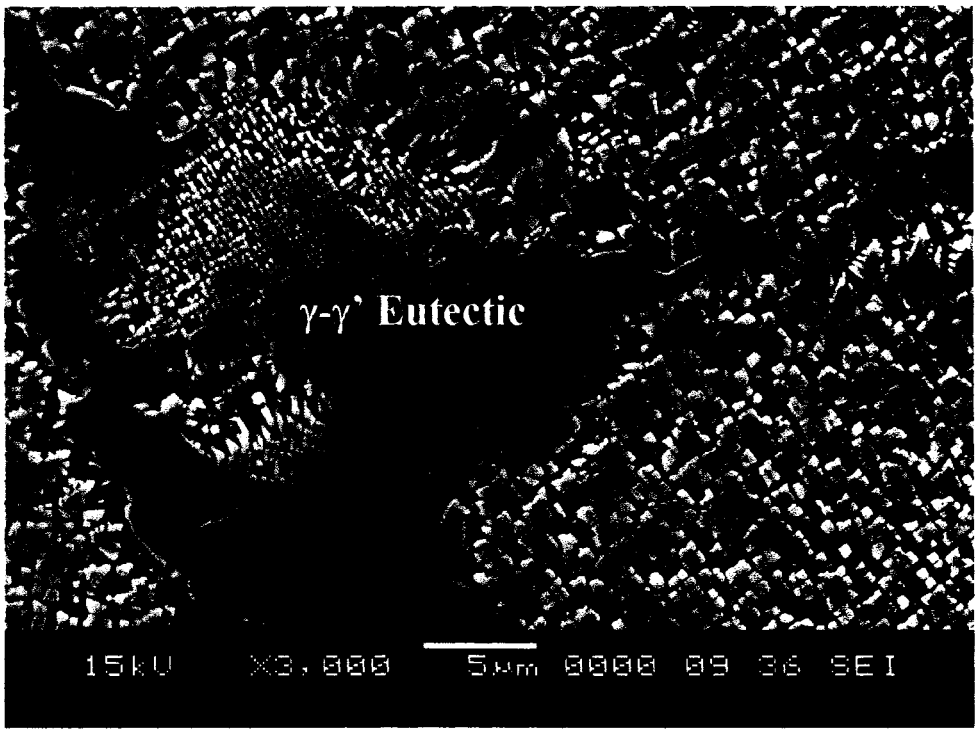

Figure 4.6: γ-γ' eutectic constituent in as-cast IN 738

In their analysis of γ-γ' eutectic formation involving nucleation and coupled growth of γ and γ' phases by movement of the solid-liquid interface, Zhu et al [140] indicated that the eutectic formed at higher temperatures is finer in structure than that formed at lower temperatures, which consists of massive γ' at the "cap" region of the eutectic. In the present work, both types of γ-γ' eutectic were observed. Rosenthal et al [135] studied the influence of solidification parameters G and R on γ-γ' eutectic formation in the directionally solidified IN 738 alloy. They noted that at a very slow cooling rate GR, corresponding to the plane front solidification mode, formation of γ-γ' eutectic was completely suppressed. As the cooling rate increased producing cellular dendritic and dendritic microstructure, γ-γ' eutectic volume fraction increased to a maximum of 2%. This shows that the formation of γ-γ' eutectic in IN 738 is a non-equilibrium product induced by dendritic microsegregation during solidification. γ-γ' eutectic constituent is undesirable in superalloys since it retains large amount of alloying elements that otherwise would have been available for strengthening the material. Being a non-equilibrium solidification product, γ-γ' eutectic may be removed in a casting by appropriate solution heat treatment. It has been shown that γ-γ' eutectic can be dissolved completely by solution heat treatment at a temperature at which incipient melting of the alloy could occur [141].

Another γ' morphology, in the form of a rod-like cell was observed along some regions of the as-cast grain boundaries which also consisted of γ-γ' eutectic colony (figure 4.7). These fan like cells with elongated γ' rods and planar front are larger in size compared to the γ-γ' eutectic. The interfaces of the γ' rods could be seen to have

generally developed 'dendritic' type instabilities. Similar observations have been reported in DS IN 738 [142, 143]. It was described to be the product of a discontinuous γ' precipitation reaction initiated by the migration of grain boundaries activated by impingement of fine γ-γ' eutectic, which are often found adjoining the discontinuous cells [143]. It was reported [143] that chemical composition of the discontinuous γ' rods, as determined by STEM/EDS x-ray microanalysis, is close to that of the continuous and eutectic γ' particles.

M_2SC Sulphocarbide

Needle-like elongated Ti-Zr sulphocarbide particles (M_2SC) were observed in close association with some γ-γ' eutectic constituent in the as-cast alloy, as shown in the backscatter electron micrograph of figure 4.8. SEM/EDS x-ray mapping showed that the M_2SC particles were enriched in Ti, Zr, Nb, S and slightly in C, but depleted in Al, Cr, Co and Ni (figure 4.8b). Sulphur is one of the main residual non-metal of concern in superalloys. Its presence in solid solution has been recognized to be detrimental to superalloys' high temperature properties due to the embrittlement of grain boundaries by its segregation on them [144]. Studies on a model Ni-Ta-Al superalloy by Doherty et al [145] have shown that sulphur embrittlement of grain boundaries can occur at bulk sulphur levels of 40 at ppm. Using Auger spectroscopy, Johnson et al [146] showed that the sulphur concentrations at grain boundaries could be up to 12at% in alloys containing 0.006 at% S. The addition of elements such as Ti, Zr, Nb, Hf and La, having a low solubility in the γ phase and a high affinity for sulphur were found to prevent such embrittlement by reducing the amount of sulphur, available for grain boundary

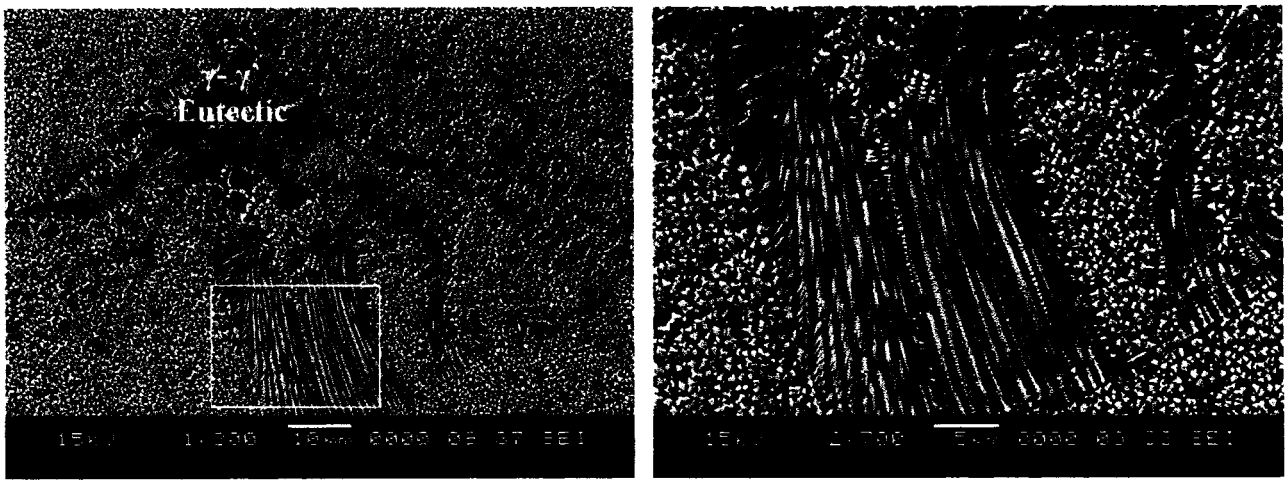

Figure 4.7: SEM micrographs showing discontinuous γ' cell in the as-cast alloy

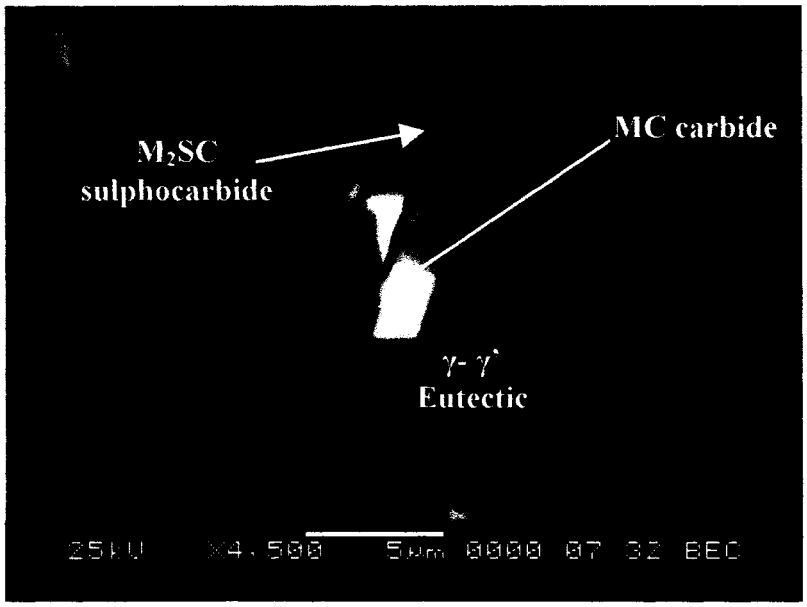

Figure 4.8: SEM backscatter electron image showing M_2SC associated with γ- γ' eutectic.

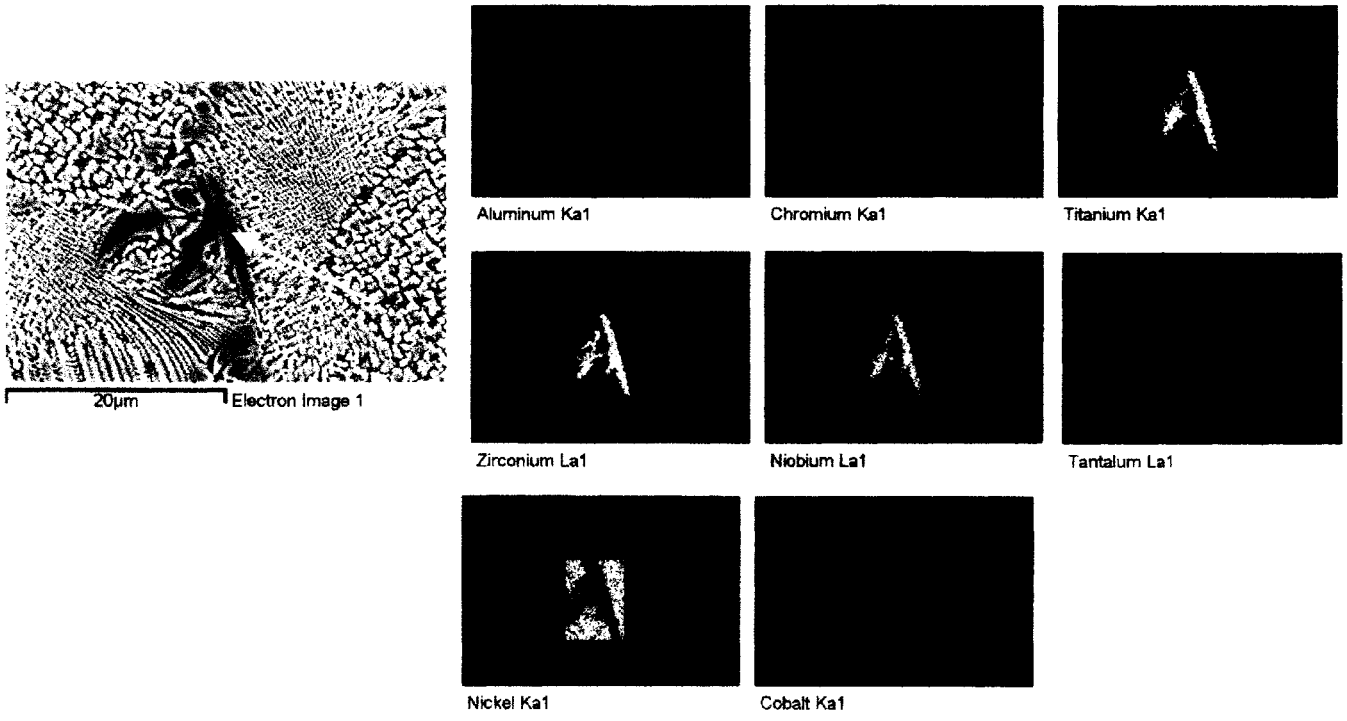

Figure 4.8b: SEM/EDS x-ray imaging of the M_2SC phase.

segregation due to the formation of second phase particles rich in sulphur. A number of sulphur-containing inclusions have been observed in nickel base superalloys and found to be crystallographically and chemically similar to the τ-$M_4C_2S_2$ phase observed in ferrous alloys. Ti and Zr rich sulphocarbides of the M_2SC type have been reported in commercial cast or powder fabricated nickel base superalloys [144, 147]. The M radical in the particles in IN 100 superalloy was found to be composed mainly of Ti with minor amounts of Zr and V [147]. In IN 713LC the particles had a high Zr content and minor concentrations of Nb and Ti. C and S were detected in particles present in both the alloys [147].

In the present work, the presence of M_2SC in close association with γ-γ' eutectic suggests that the particles formed from residual interdendritic liquid during the later stages of solidification. This may constitute a thermodynamically and microstructurally viable mode of relieving supersaturation of the interdendritic liquid enriched by the microsegregation of S, C, Nb, Zr and Ti, during the growth of γ dendrites. It is evident from the literature [148] that there is a general tendency for several group 4A, 5A, 6A and 7A transition elements to react preferentially with, and therefore to act as scavengers for S both in steels and in superalloys. Therefore one important function of Ti and Zr in IN 738 lies in their microsegregation into the interdendritic liquid phase and their scavenging of residual S in this liquid through the formation of M_2SC particles.

A notable observation in the present work was that MC type carbides formed on some of the M_2SC particles (figure 4.8). The M_2SC phase has been reported [149] to be crystallographically and chemically similar to the MC phase, with the alternate octahedral layers of S in M_2SC being replaced by layers of C. The small lattice mismatch between

the closed packed planes of the two phases often causes MC to precipitate epitaxially and coherently on M_2SC plates with a (111)//(0001) orientation relationship [149].

MC Carbides

The discrete interdendritic and intergranular particles observed under optical microscope were further examined and analyzed in SEM and EPMA (figure 4.9). They were of blocky, Chinese-script and eutectic-like (coarsely lamellar with γ phase) morphology with sizes ranging between 2-8μm. SEM/EDS semi-quantitative and EPMA/WDS x-ray microanalysis of these particles suggested them to be based on MC-type carbides. This was confirmed by electron diffraction and TEM/EDS microchemical analysis on particles extracted on carbon extraction replica (figure 4.10). The analyses indicated the particles to be cubic (FCC) MC carbides rich in Ti, Ta and Nb with a lattice parameter of 4.37Å. The nature of carbide phases that are desirable in polycrystalline nickel-base superalloys for high temperature grain boundary strengthening, depends on the composition of the superalloy. In the as-cast condition these carbides are usually of the MC-type where M is Ta, Nb, Zr, Ti, or Mo [150, 151]. Multicomponent carbides of the MC type encountered in many nickel-base superalloys are metastable with a tendency towards dissolution or dissociation after long term exposure to elevated temperatures.

It has been observed that the near equilibrium growth morphology of MC carbides in superalloys is faceted octahedral blocks, which minimizes their interface energy [152]. The octahedral shape could transform to Chinese-script morphology as the cooling rate increases [153]. Solidification processing parameters such as solidification front shape and cooling rate are important factors, which govern the growth morphology, size,

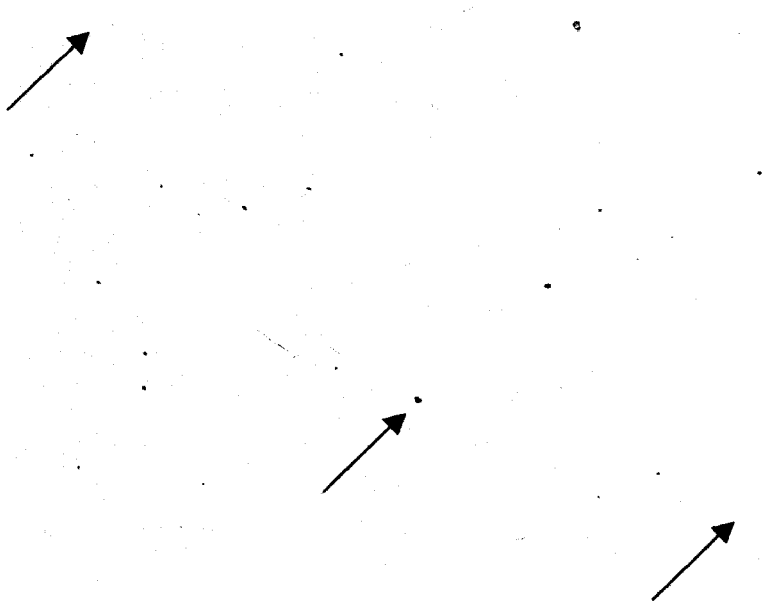

Figure 4.9: SEM backscatter electron image showing MC type carbides dispersed with the γ matrix

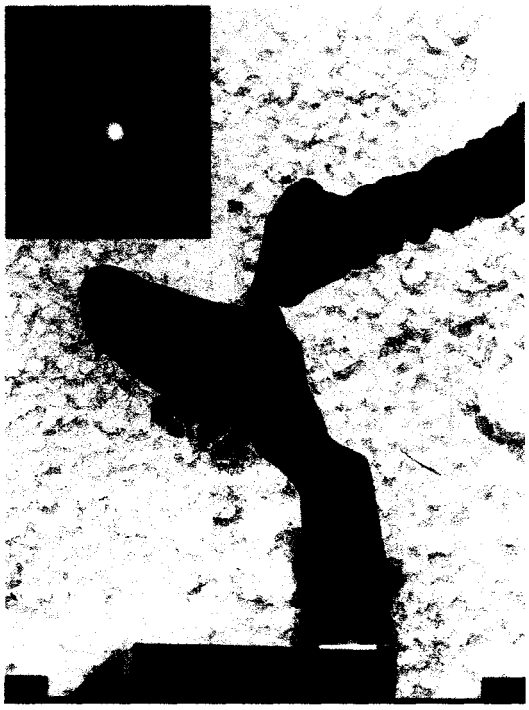

Figure 4.10: (a) TEM image of MC type carbides extracted from the as-cast alloy on carbon extraction replica (b) SADP from a carbide particle at [001] zone axis.

distribution and composition of MC carbides. Different types of MC carbides based on chemical composition were observed in the present work. It is a generally accepted view that MC carbides in IN 738 alloy form by crystallization from liquid melt above 1290°C [136, 137]. However, observations of this study suggest that they evolve over a range of temperatures, which could be appreciably below 1230°C, by eutectic type reactions. This inference is based on morphology, location and compositions of the MC carbide particles. Most of the carbides exist as discrete particles, however, a number of them were observed to have formed with a coarsely lamellar eutectic-type morphology (figure 4.11), while some were prominently connected to γ-γ' eutectic (figure 4.12), which could have formed by a solidification reaction involving formation of γ-γ' eutectic at the later stage of solidification. The occurrence of MC carbide in close association and in some cases ahead of γ-γ' eutectic, as well as on M_2SC (as discussed earlier) strongly suggests that the range of temperature of formation of MC carbides in this alloy extends from around 1300°C, as determined by DTA [136, 137], to much lower temperatures close to γ-γ' eutectic transformation temperatures. This suggestion is further supported by the results of EPMA/WDS x-ray microanalysis of the different carbide particles, which showed that they could be generally classified into 3 groups as shown in Table 4.2.

Titanium was the predominant metallic component in most of the carbides except in those few particles which were located in front of γ-γ'eutectic, and which were Zr rich. The Ti based carbides can be categorized into two main types. The atomic ratio of Nb/Ta in type 1 is less than 1 and they also contain more W atoms than Mo with very small amount of Zr,< 1at%. In type 2 carbides, however, the Nb/Ta ratio is greater than 2, with smaller amount of W than Mo and an appreciable concentration of Zr,> 2 at% and up to

Table 4.2: WDS Chemical Composition Analysis of MC Carbide Particles.

Elements (At.%)	Type 1 High Temperature MC	Type 2 Low Temperature MC	Zr Based Low Temperature MC
Ti	56.2	47.9	13.6
Cr	2.18	1.6	2.0
Co	0.6	0.7	-
Ni	3.42	4.11	8.5
Zr	0.19	1.61	53.3
Nb	12.4	26.3	20.0
Mo	2.9	3.6	-
Ta	18.1	11.9	2.7
W	4.0	2.5	-
Nb/Ta	~ 0.7	~ 2.2	~ 7.4

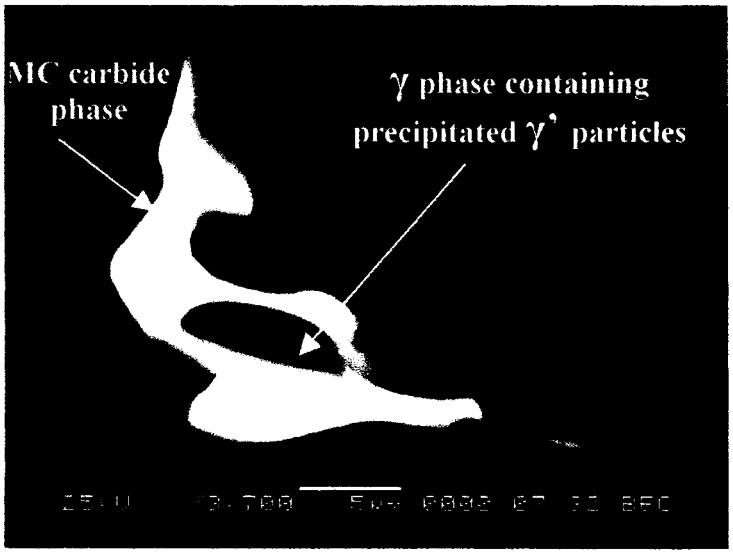

Figure 4.11a: SEM backscatter electron image showing MC carbide formed in γ-MC eutectic-like morphology.

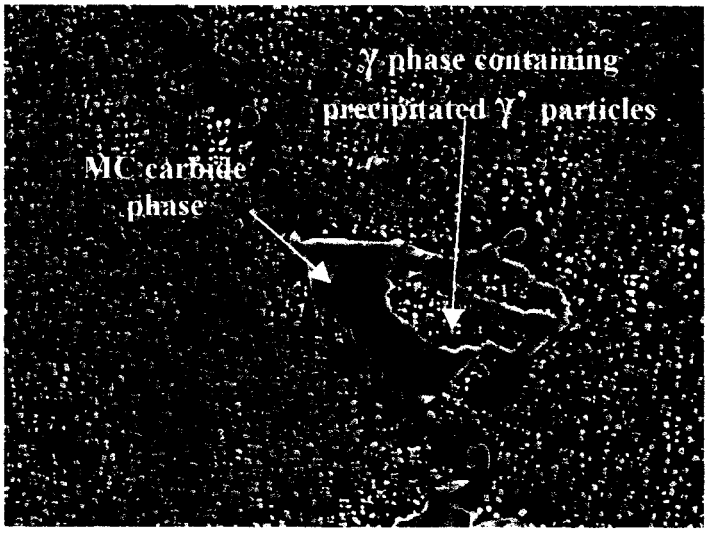

Figure 4.11b: SEM secondary electron image showing MC carbide formed in γ-MC eutectic like morphology.

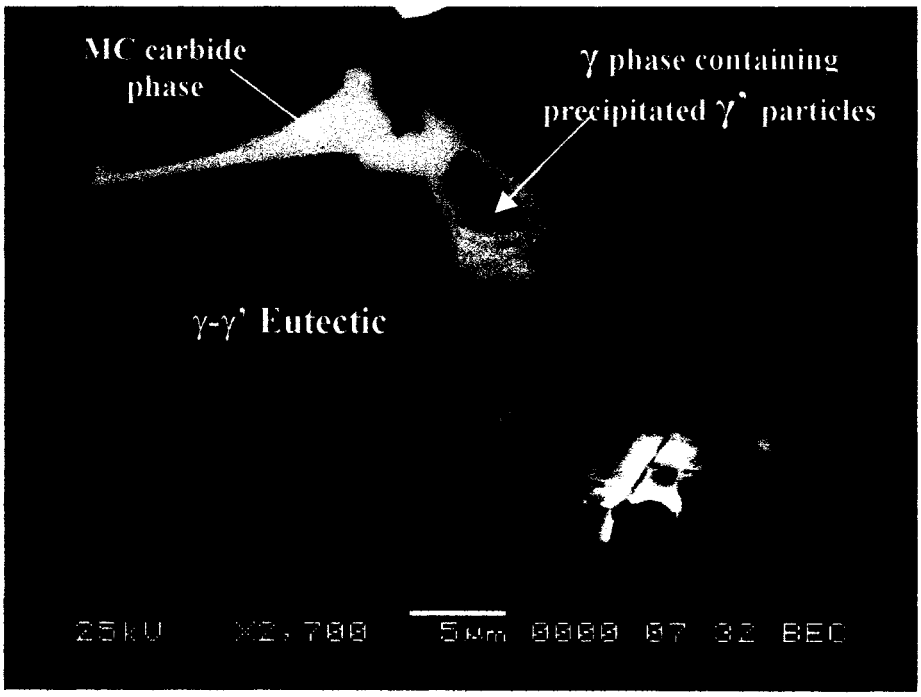

Figure 4.12a: SEM backscatter electron image showing eutectic like γ-MC associated with γ-γ' eutectic.

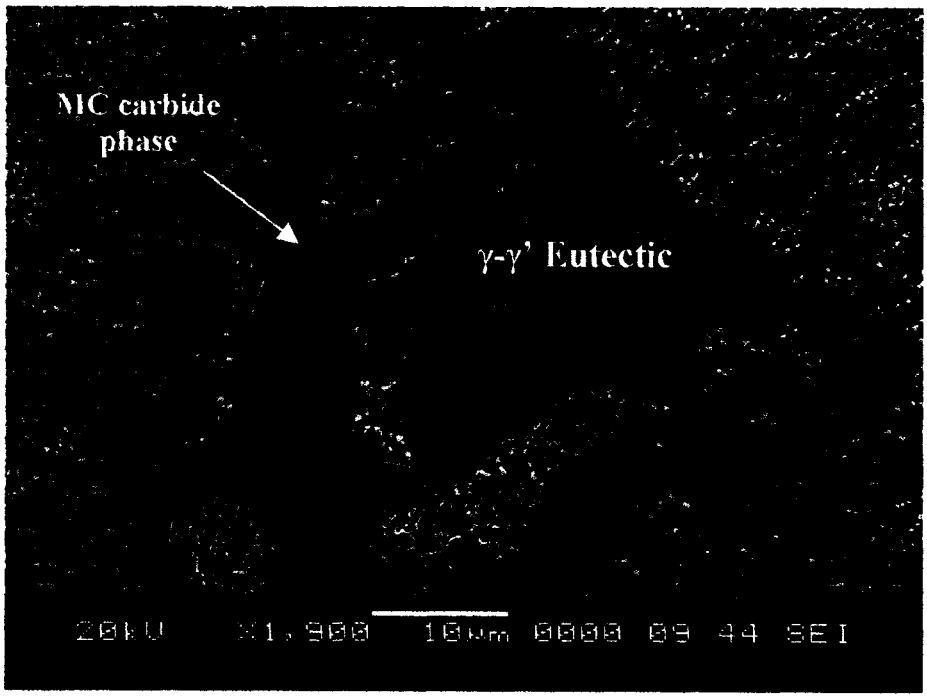

Figure 4.12b: SEM secondary electron image showing large MC type carbide particle associated with γ-γ' eutectic

5 at%. It was observed that most of the carbides formed in close proximity to γ-γ' eutectic and those which formed on M_2SC were of type 2. The type 2 carbides are also termed low temperature carbides as compared to type 1, which are termed high temperature carbides, as they are believed to have formed at higher temperatures. This classification into low and high temperature carbides, based on their composition and location, correlates with the segregation behavior of carbide forming elements during solidification. Carbide particles which formed at higher temperatures around 1300°C, as determined by DTA [136,137], can be expected to be leaner in severely positive segregating elements with lower k values like Zr and Nb as compared to Ta and W which exhibit higher values of k. Likewise, carbides that formed towards the later stages of solidification are expected to be enriched with Nb and Zr atoms. Formation of Zr based carbides containing more than 50 at% of Zr ahead of the γ-γ' eutectic, as mentioned earlier, can be attributed to two different solidification occurrences. The severe positive dendritic segregation of Zr (k = 0.06) into interdendritic liquid during cooling and secondly, its further rejection together with carbon atoms into residual liquid pool during γ-γ' eutectic transformation (due to their low solubility in both γ and γ' phases). Hence, the Zr based carbide is also classified as a low temperature carbide.

During the solidification process, the growth of the γ dendrites, which form from the melt prior to MC carbide formation, causes the carbide forming elements, mainly Ti, Nb, Ta, Zr and C all with k values < 1, to enrich the interdendritic liquid. If the interaction among these elements can be neglected, the composition in the interdendritic regions may be described by the Bower-Fleming's equation [154].

$$C_L = C_o [a / (k-1) + 1 - (a\,k / (k-1)) \times f_L^{(k-1)}] \qquad (4.2)$$

$$a = [D_L G_L (1-k)] / (\Delta T k R) \qquad (4.3)$$

where D_L is the diffusion coefficient in the liquid, C_o is the initial composition of the liquid, k is the solute distribution coefficient and ΔT is the freezing range of the alloy. It can be seen from these equations that the concentration of solutes with k values < 1 in residual interdendritic liquid C_L, will increase with a decrease in liquid fraction f_L. When the concentration of these elements reaches the necessary supersaturation for carbide formation, the nucleation and growth of carbides could commence via a monovariant $L \rightarrow \gamma + MC$ eutectic-type reaction.

The observations of this work are in agreement with some published work on nickel base superalloys. Lecomte-Beckters [155] in his study of solidification behavior of some nickel base superalloys reported that composition of MC carbides in these alloys changes as solidification progresses, thus affecting the composition of the residual interdendritic liquid. Carbides formed during the final solidification stages were more enriched in highly positively segregating elements. It has also been recently recognized that nickel base superalloys that contain Hf together with the addition of Ti generally contain two or more MC type carbides with different compositions [156]. Starink et al [156] indicated that a wide miscibility gap in MC carbide phase resulted in the formation of MC carbides with a broad range of composition in Mar-M002 superalloy. MC carbides formed at the initial stages of solidification were Hf lean as compared to the Hf rich carbides formed at the later stages.

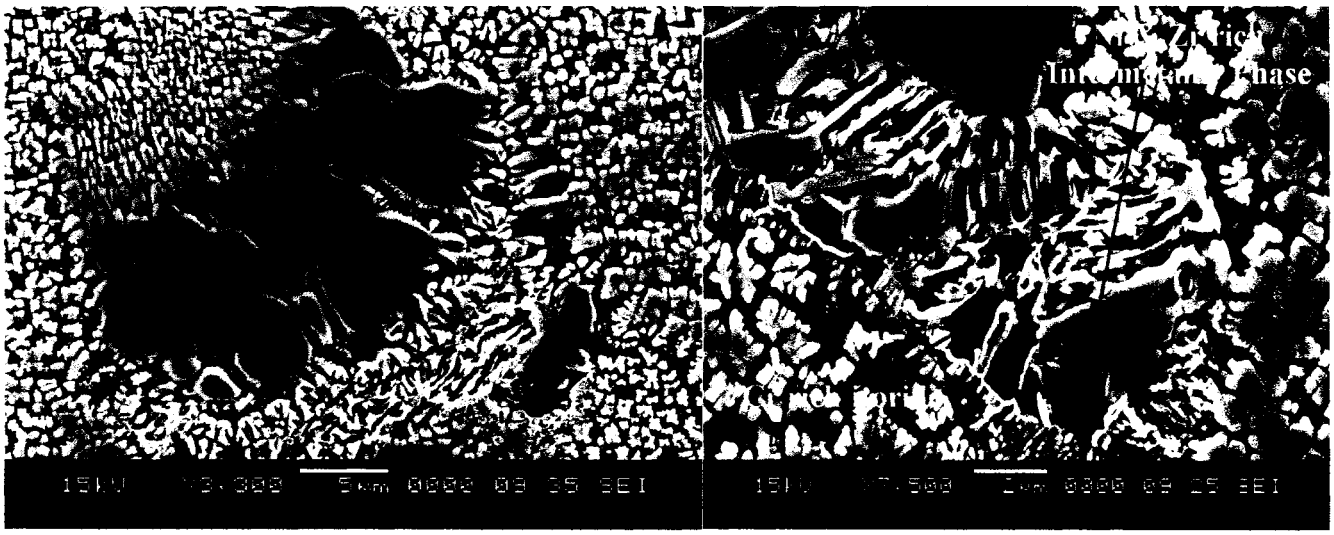

a b

Figure 4.13(a &b): SEM secondary electron image showing eutectic like constituent in front of γ-γ' eutectic.

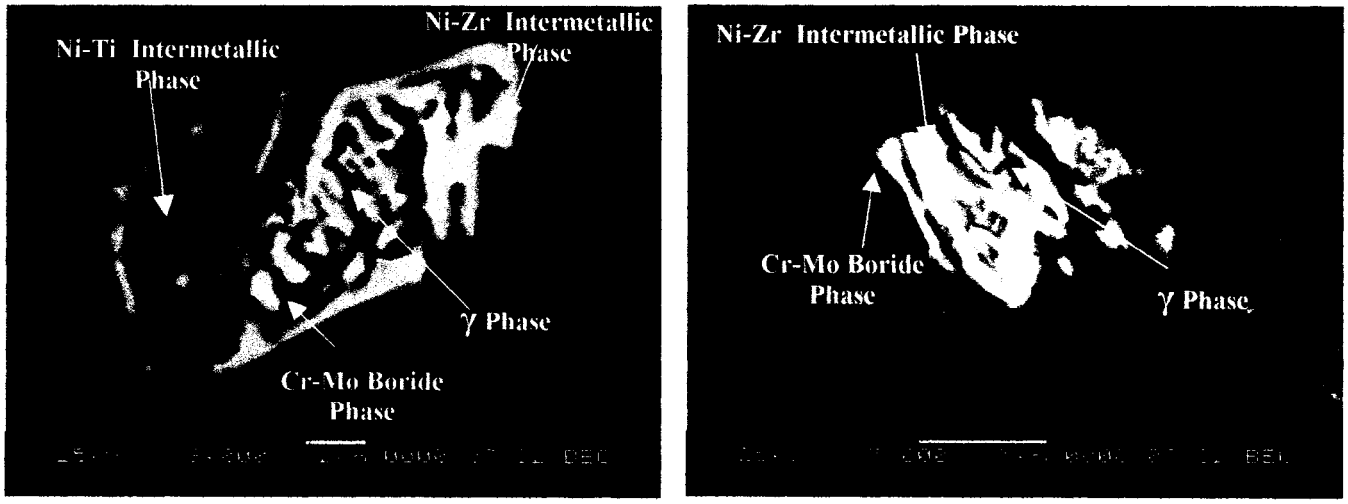

c d

Figure 4.13; SEM backscatter electron image of (c) quaternary eutectic-like constituent and (d) ternary eutectic-like constituent

Low Melting Terminal Solidification Constituents

Careful microstructural investigations using backscatter and secondary electron imaging modes in SEM revealed the occurrence of different solidification products in front of some of the γ-γ' eutectic in this alloy (figure 4.13). The lamellar morphology of the solidification product suggests that it formed by eutectic transformation involving at least ternary and quaternary eutectic reactions. The constituent phases of the eutectic-like product are delineated by the atomic number based backscatter electron contrast in an SEM (figure 4.13). Chemical composition of the two main phases, and that of another phase which was occasionally observed in association with gamma within the eutectic-like products, as determined by energy dispersive X-ray microanalysis are shown in Table 4.3. Significant boron concentration was detected in the Cr - Mo rich particle by the ultra thin window EDS detector. Strong Cr and Mo peaks observed in the EDS spectra in this work (figure 4.14) are noted to be characteristic features of M_3B_2 boride phase in other Ni base superalloys [157]. TEM examinations showed that these particles formed in dendritically shaped morphology suggesting that they formed by a solidification reaction, most likely to be a eutectic-type reaction (figure 4.15a). TEM diffraction and x-ray microanalysis were performed on these to confirm the nature of the phase. Analysis of selected area diffraction patterns from these particles showed them to be based on M_3B_2 phase with a tetragonal crystal structure and lattice parameters of a= 5.71Å and c = 3.05Å (figure 4.15b). M_3B_2 boride has been reported in heat treated IN 738 by X-ray diffraction analysis [16]. The present work indicates that the particles are actually present in the as-cast alloy as a solidification product, which is consistent with observations in other boron containing cast nickel base superalloys [158].

Table 4.3: Chemical Composition of Terminal Solidification Constituent

Elements	Ni-Zr Inter. (At.%)	M_3B_2 Boride (At.%)	Ni-Ti Inter. (At.%)
Al	0.7	-	4.7
Ti	2.5	2	11.7
Cr	3.2	67.9	5.1
Co	7.4	1.73	6.6
Ni	67	4.6	66.3
Zr	16	0.9	2.18
Nb	2.5	2.4	1.8
Mo	-	16	0.28
Ta	0.8	-	0.95
W	-	4.45	0.34

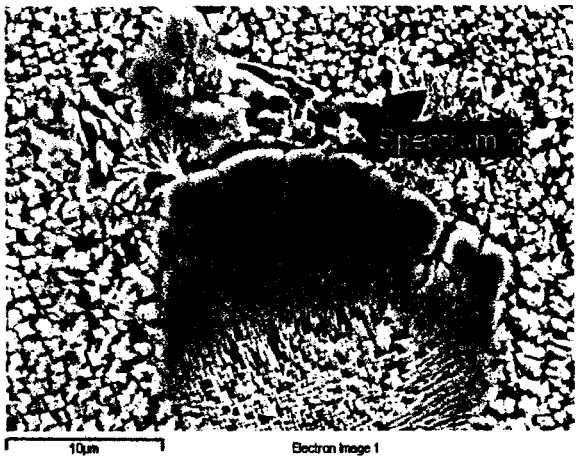

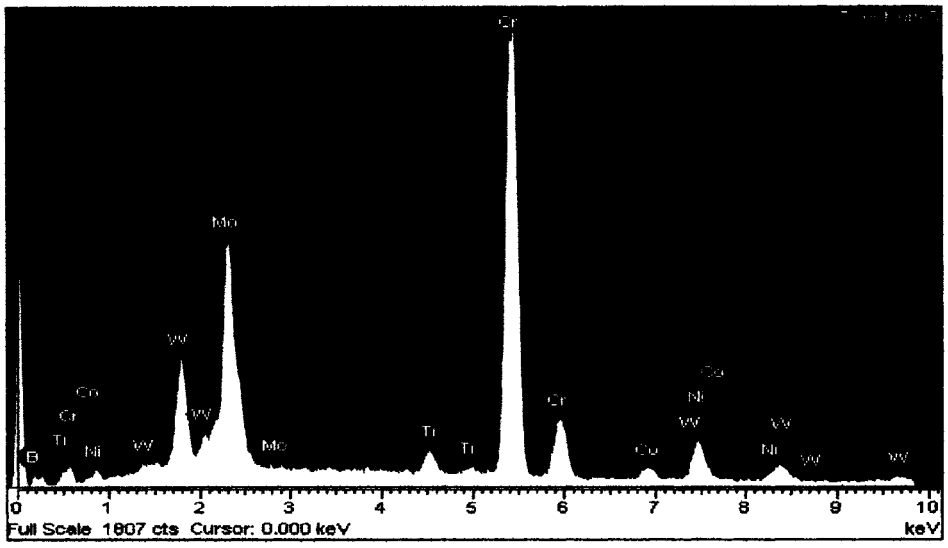

Fig. 4.14: SEM/EDS Spectrum from Cr-Mo Boride

The composition of Ni-Zr and Ni-Ti rich intermetallic phases suggests them to be based on Ni_5Zr and Ni_3Ti, respectively. Ni_5Zr has been reported to be formed during directional solidification of Zr doped Ni based MAR-M200 superalloy [159].

By differential thermal analysis (DTA), it has been suggested that ingot solidification of IN 738 is completed by the γ-γ' eutectic transformation at around 1230°C [136] and 1198°C [137]. Rosenthal et al [135], however, indicated that the γ-γ' eutectic reaction in this alloy occurs over a range of temperatures, which could be as low as below 1180°C. Zhu et al [160] in their study of solidification behaviour of some Ni base superalloys reported that in an alloy, which is close to IN 738 in composition, 90% of the liquid had solidified before 1230°C but the remaining liquid did not solidify until the temperature was about 1120°C. Zou et al [161,162] in a separate work, to study the solidification behaviour of another derivative of IN 738 using a slow heating rate of 0.28°C/s in DTA reported, that the terminal eutectic reaction temperature in the alloy was 1094°C. The nature of such terminal eutectic was, however, not discussed. The results of these investigations [160-162] thus suggest that, contrary to the generally accepted view that solidification of IN 738 ingot is completed by the γ-γ' eutectic reaction at around 1180 – 1198°C, a different eutectic transformation could be occurring in this alloy at a significantly lower temperature. During solidification, the first solid to form from the liquid is in the form of gamma dendrites. As these dendrites grow during cooling, dendritic microsegregation occurs with interdendritic liquid getting enriched with positively segregating elements ($k < 1$). Supersaturation of the liquid with these solutes due to continual enrichment on cooling, would invariably result in the formation of secondary solidification constituents such as MC carbides, M_2SC sulphocarbide and γ-γ'

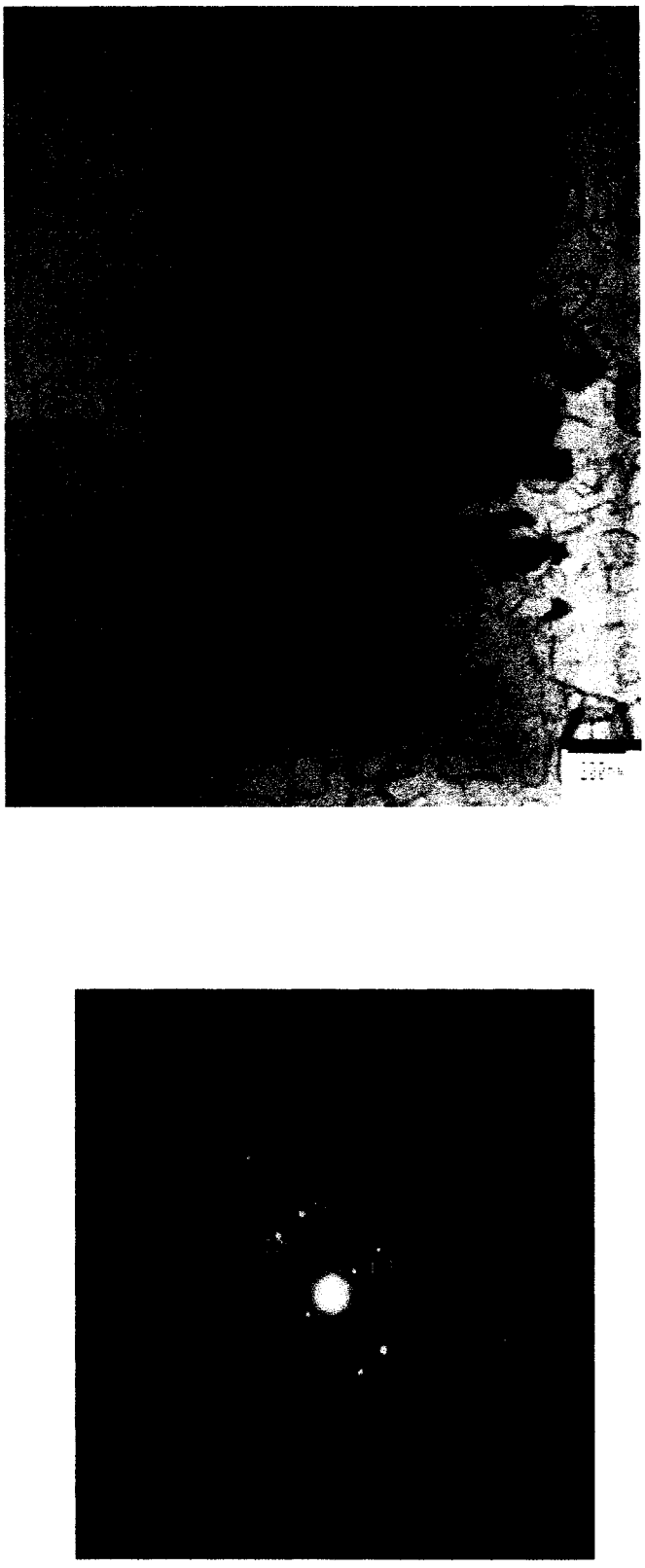

Fig. 4.15: TEM image and SADP from Cr-Mo Boride particles extracted on carbon taken at $[\bar{1}12]$ Zone axis.

eutectic in the interdendritic regions. During the formation of γ-γ' eutectic at the later stages of solidification, which has been reported to occur over a range of temperatures [135], solute partitioning occurs with elements having low solubility in γ and γ' phases being rejected into the residual liquid pool ahead of the γ-γ' eutectic. Zr and B are known to have low solubility in γ and γ' phases and as such would partition into the residual liquid pool. Increase in concentrations of the these elements, which are also known to be melting point depressants in Ni, would result in further lowering of the solidification temperature of the residual liquid. Cr and Mo, which have high affinity for boron have also been found to exhibit positive segregation ($k<1$) into the liquid during γ-γ' eutectic formation [140]. On continuous cooling to the invariant terminal solidification reaction temperature of the alloy, i.e. the effective solidus temperature, high concentration of solute elements in the final liquid would invariably result in the formation of terminal solidification product, which is most likely by eutectic-type reaction involving multiple constituent phases. This could then explain the formation of ternary eutectic-like product containing Ni-Zr intermetallic and Cr - Mo rich boride observed in the present work.

In addition, it is known that once the ratio of Ti/Al exceeds 3:1, Ni_3Ti would be preferentially formed, which could also account for the formation of what appears to be Ni_3Ti based intermetallic in the quaternary terminal eutectic-like product, considering the positive segregation behaviour of Ti ($k = 0.6$) versus negative segregation of Al ($k = 1.2$). The Ni-Ti-Al ternary phase diagram data [163] shows that η phase Ni_3Ti forms at the titanium rich portion of the system. Earlier work on η phase in superalloys was mainly concerned with the transformation of γ' to η phase during heat treatment and long-term service exposure. The chemical stochiometry of η phase is usually written as Ni_3Ti, but it

has solubility for Mo, W, Al and Cr [164]. Its occurrence has been reported in some cast nickel base superalloys such as IN 792 + Hf, IN 6230 DS and DS GTD111 [165, 166]. Sun et al [165] have recently shown that formation of Ni_3Ti in cast IN 792 + Hf is significantly influenced by the degree of microsegregation of Ti, Hf, Ta and W during the solidification of the alloy.

Cast alloys are typically given a homogenisation heat treatment prior to service, at temperatures between γ' solvus and the bulk equilibrium solidus temperature to obtain optimum properties. In a complex casting alloy like IN 738, the character of γ' precipitate particles is likely to be significantly variable due to dendritic microsegregation that occurs during ingot solidification. The dendritic core γ' particles in IN 738 are richer in negatively segregating Al atoms ($k>1$) and exhibit a solvus temperature of 1120 – 1130°C as compared to interdendrite particles, which are enriched with positively segregating Ti atoms, ($k<1$) and have a higher solvus of 1170 – 1180°C [135]. In addition, γ-γ' eutectic product also forms along the interdendritic regions. Solution heat treatment at temperatures high enough to dissolve the entire volume of primary γ' precipitates and homogenize the alloy for subsequent γ' re-precipitation in the form of uniformly distributed fine γ' precipitates has been severely restricted in this alloy due to the occurrence of incipient melting [167]. Consequently, the standard solution heat treatment generally adopted for this alloy has been limited to 2hrs at 1120°C, which results only in a partial homogenization by exclusive dissolution of dendrite core γ' particles.

The low melting temperature of the terminal eutectic was confirmed by heating a cylindrical as-cast sample of diameter 6mm and length 115mm in a Gleeble thermo-mechanical simulator system to 1155°C (15°C below 1170°C, the quoted solvus

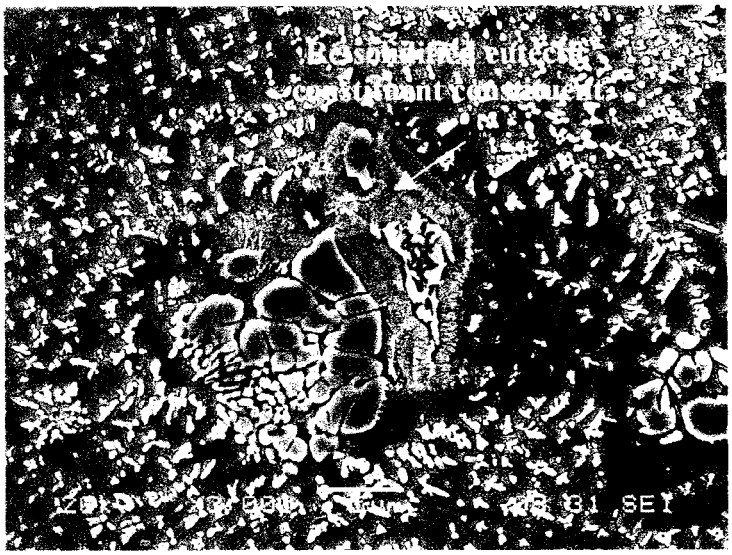

a

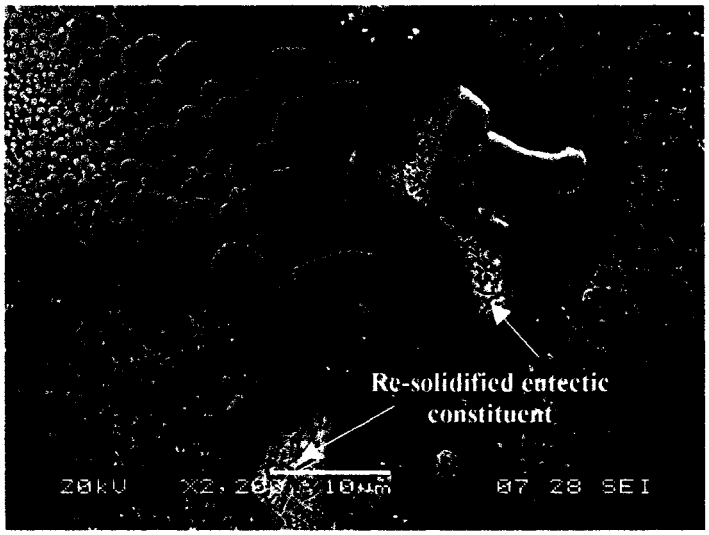

b

Fig. 4.16: Melting of terminal solidification constituents at 1155°C

temperature for interdendritic γ' precipitates) at a rate of 38°C/min, held for 1sec and then water quenched. Evidence of melting of the terminal solidification constituents was observed, as shown in figure 4.16. As can be seen from this micrograph, the terminal solidification constituent liquated prior to the dissolution of γ' precipitate particles. This nature of incipient melting in IN 738 alloy has not been reported in the literature prior to this work. Incipient melting of the terminal solidification product as observed in this work at 1155°C, could thus be an important factor limiting efficient higher solution heat treatment (> 1170°C) needed to dissolve interdendritic γ' precipitates as well as eutectic γ' particles in cast IN 738 superalloy.

Microstructure After ST and UMT Heat Treatments

The standard solution heat treatment (ST) at 1120°C for 2 hrs results in almost complete dissolution of primary γ' within the dendrites with little, if any dissolution of the particles in the interdendritic regions. The microstructure after this heat treatment consists of fairly regular coarse cuboidal 0.6-0.8μm size primary γ' in the interdendritic regions and fine (~ 0.1μm) spheroidal dispersion of secondary γ', predominantly in the dendrite core as well as within the interdendritic regions (figure 4.17). Figure 4.18 is a thin film TEM bright field image of a ST material, showing primary cuboidal γ' precipitate and spheroidal secondary particles. Superlattice reflections in the SADP shown in figure 4.18b confirm them to be ordered intermetallic γ' phase with its usual orientation relationship $\{100\}_{\gamma'}$ // $\{100\}_{\gamma}$ and $<100>_{\gamma'}$ // $<100>_{\gamma}$ with the γ matrix. The secondary γ' particles apparently formed during cooling from the solution treatment temperature.

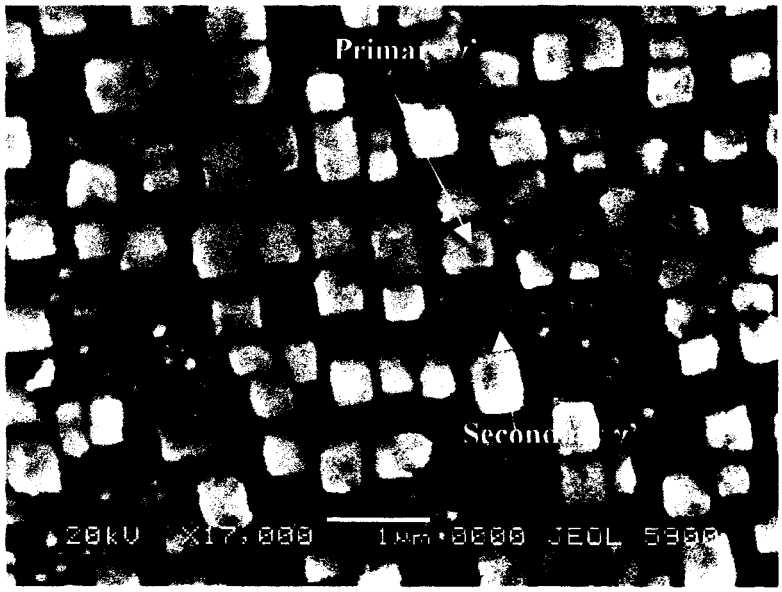

Fig. 4.17: γ' particles in solution heat treatment (ST) sample.

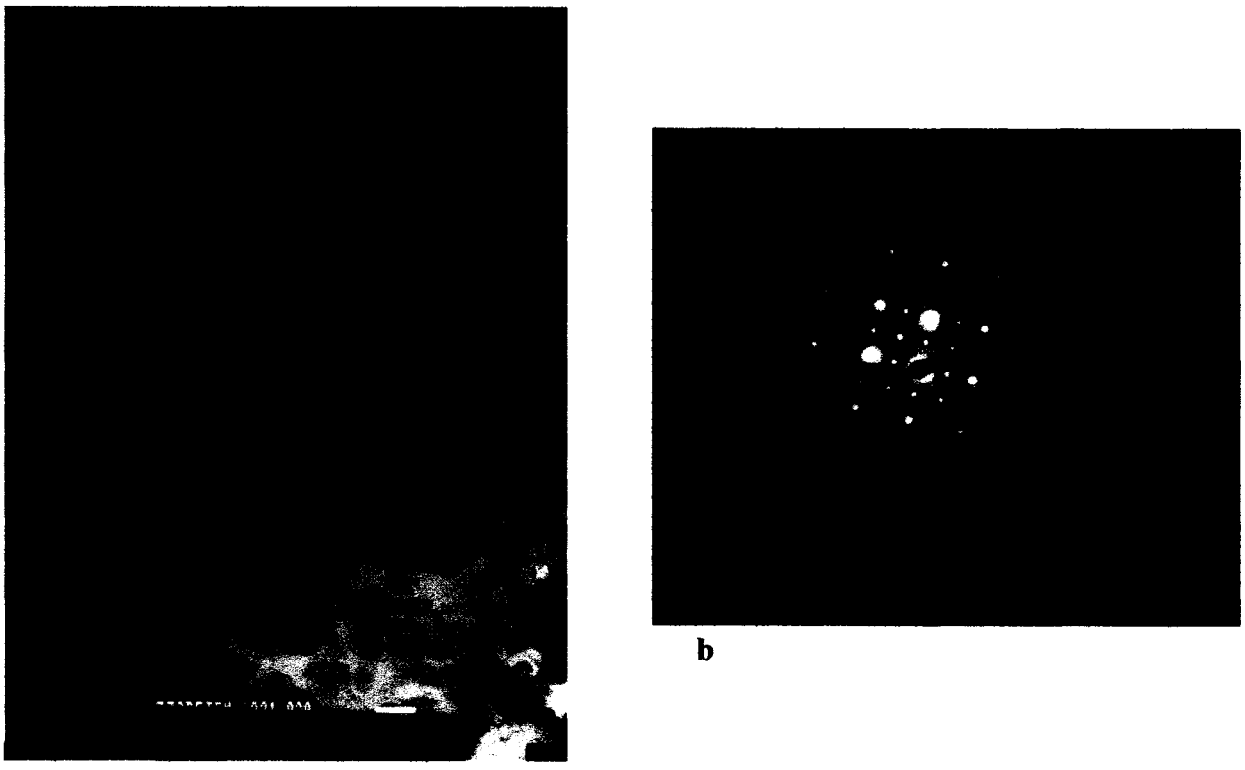

a **b**

Fig. 4.18: (a) TEM micrograph showing γ' particles in solution heat treated (ST) thin foil and (b) SADP from [001] zone axis

The UMT treatment caused coarsening of both the primary and secondary γ'. The microstructure after this treatment consisted of bimodal distribution of large cuboids and smaller spheroids of size range of 0.5-1μm (figure 4.19). Large γ' particles of average size 1.8μm were observed along the grain boundaries after the two heat treatments. Solidification constituents MC carbides, γ-γ' eutectic, M_2SC sulphocarbide and M_3B_2 boride were also observed in the ST and UMT samples. Nevertheless, the terminal solidification product ahead of γ-γ' eutectic in the as-cast material was found to consist mainly of the M_3B_2 boride and Zr and Nb rich carbide particles. There was no evidence of the presence of the Ni-Zr intermetallic in any of the ST and UMT samples. It has been reported that in DS MAR-M200 annealing at 1130°C for 3 hrs results in a solid-state dissolution of Ni_5Zr intermetallic with concomitant formation of Zr based MC carbides. It is possible that such a reaction could be also occurring in the present alloy. A network of chromium rich particles encased in γ' phase were observed along the grain boundaries which were connected to γ-γ' eutectic and at the interface of γ-γ' eutectic, as well as at the MC-γ interface in samples given the UMT heat treatment (figure 4.20). It has been widely reported that chromium rich $M_{23}C_6$ particles precipitate along the grain boundaries and at the interface of MC-γ during the aging heat treatment of IN 738 at temperatures below 1050°C.

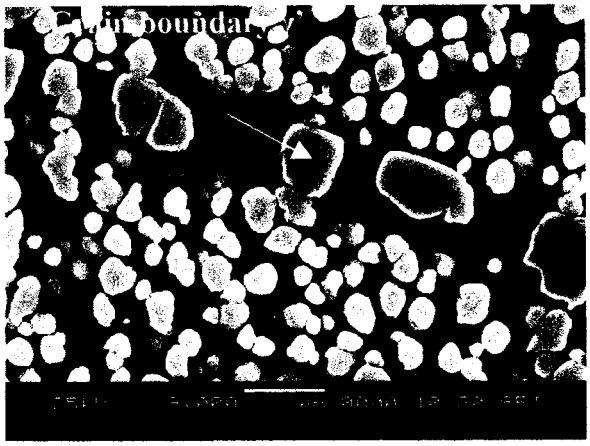

Fig. 4.19: SEM micrograph of a sample given the University of Manitoba heat treatment

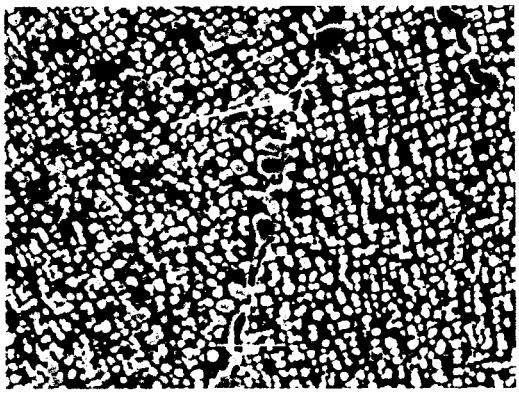

Fig. 4.20a

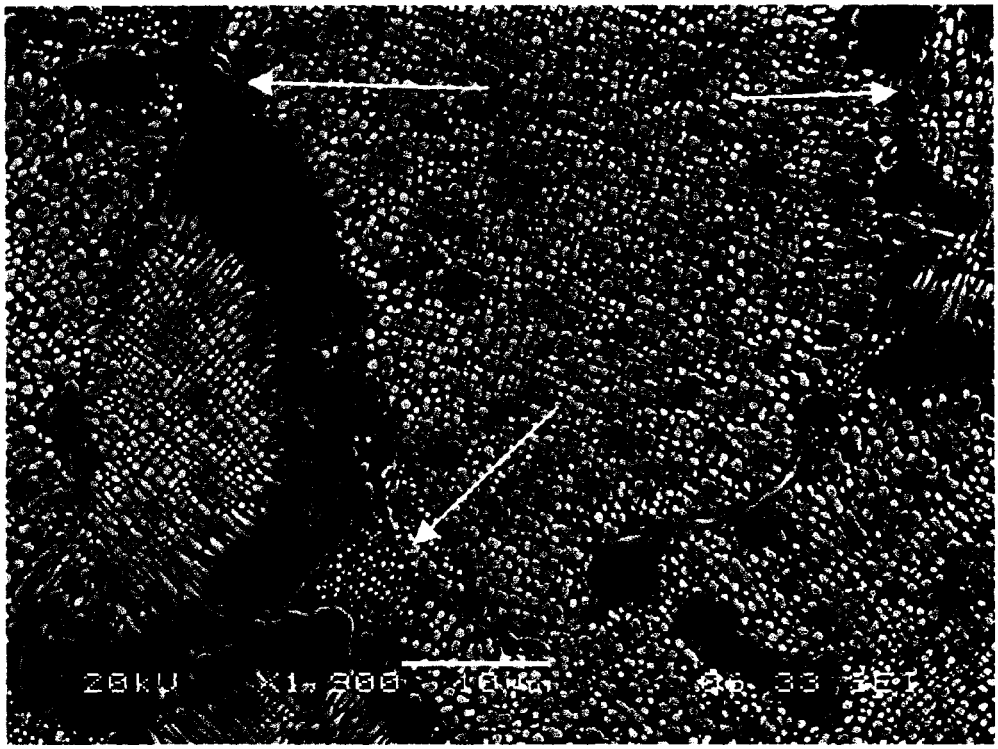

Fig. 4.20b

Fig. 4.20a&b: SEM micrograph showing a network containing Cr rich particle in UMT sample

4.2 Characterization of Fusion Zone Microstructure

4.2.1 Introduction

Microstructural development in superalloy welds, which invariably controls properties and reliability of the weldments, can be significantly influenced by the microsegregation and non-equilibrium phase transformation that occur during solidification. Apart from the formation of secondary solidification constituents along dendrite interstices, microsegregation often leads to extension of solidification temperature range in castings and welds. The presence of a liquid phase from which terminal solidification product form at a lower temperature has been shown by several investigators [168, 169] to be responsible for hot cracking. The result of a study of microstructure that develop in the weld-metal zone of IN 738 alloy is presented and discussed in this section.

4.2.2 Optical Metallography and Electron Microprobe Analysis

Figure 4.21 shows an optical micrograph of the fusion zone consisting of cellular-dendritic microstructure. No evidence of exclusive fusion zone solidification cracking was observed in any of the welded samples. The average secondary dendrite arm spacing within the fusion zone was about 3.75μm with the values ranging from 3.3-4.5μm. Secondary dendrite arm spacing λs is known to generally follow an equation of the type [128]:

$$\lambda s = k_s(GR)^n \qquad (4.4)$$

where GR is the cooling rate, k_s and n are constants. Using the values of $k_s = 4.7 \times 10^{-2}$ $mmK^{1/3}s^{-1/3}$ and n = -0.4, as experimentally determined by Quested et al [128] for IN 738

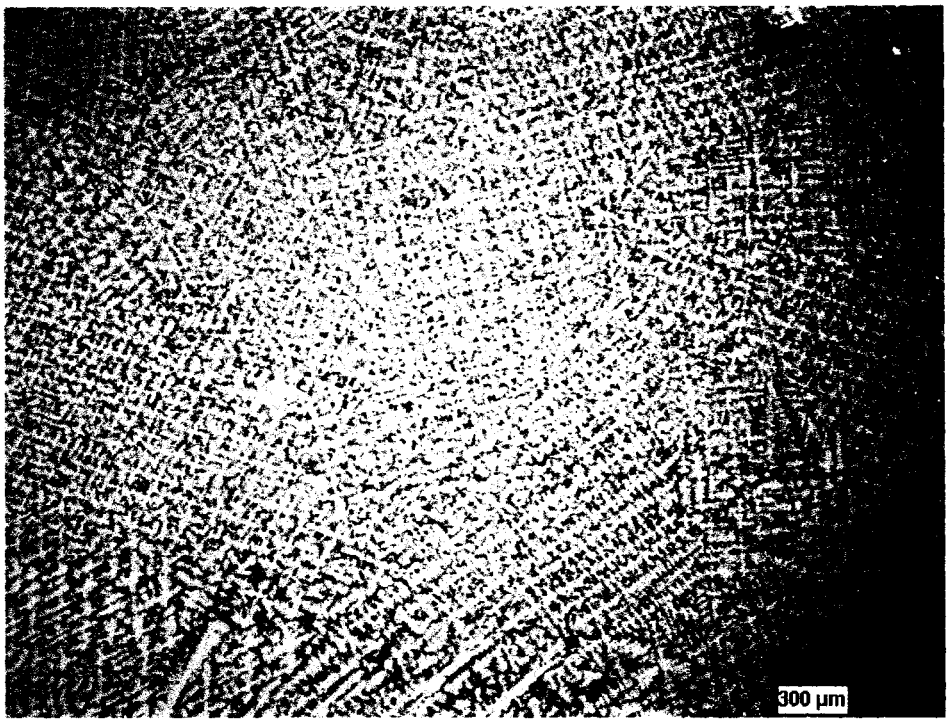

Fig. 4. 21: Optical micrograph of the fusion zone

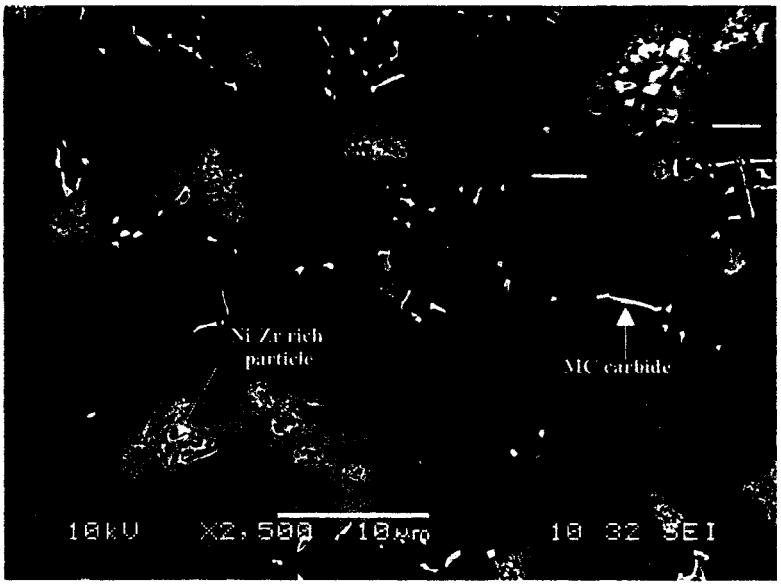

Fig. 4.22: SEM micrograph of the F fusion zone.

within the fusion zone is found to be around 556°C/s, which falls within the range of 300 – 1000°C/s that was computed for 12% Cr steel welds by solving Rosenthal's heat conduction equation [170]. This is a considerably more rapid cooling rate compared to those experienced during conventional investment casting of an alloy ingot, which is typically less than 5°C/s.

The chemical composition within the dendrite core regions as determined by x-ray microanalysis using EPMA/WDS is given in Table 4.4. A fundamental solidification parameter that can be determined from this data is the distribution coefficient of the alloying elements during the weld-metal solidification. According to solute redistribution model developed by Brody and Flemings [154], solute concentration in the solid at the solid-liquid interface (C_s) for a parabolic dendritic growth rate is given by:

$$C_s = k\,(C_o\,[1-(1-2\alpha k)\,f_s]^{(k-1)/(1-2\alpha k)} \qquad (4.5)$$

$$\alpha = D_s t_f / L^2 \qquad (4.6)$$

Here, k is the equilibrium distribution coefficient, C_o is the nominal solute concentration, f_s is the fraction of solid, D_s is the diffusivity of solute in the solid (assumed constant), t_f is the local solidification time and L is half the dendrite arm spacing. α is a dimensionless back-diffusion parameter, which is dependent on the diffusion distance L, the time available for diffusion and the diffusivity of solute in the solid D_s. For a constant solute diffusivity and a given dendrite arm spacing, it can be seen that α is simply a function of the cooling rate. In the case of negligible solid-state diffusion such that $\alpha << 1$, Brody and Fleming's equation reduces to the well known Scheil equation [171], i.e.

$$C_s = k\,C_o\,[1-f_s]^{(k-1)} \qquad (4.7)$$

Table 4.4 Chemical composition of Dendritic core and various Phases present in the Fusion Zone

Elements	Ni	Cr	Co	Al	Ti	Ta	Nb	Mo	W	Zr	C	B
Dendrite Core (wt%)	63.16	15.52	9.28	3.19	2.43	1.24	0.48	1.64	2.81	0.005	-	-
k	1.03	0.98	1.09	0.92	0.69	0.74	0.52	0.87	1.13	0.13	0.3 [132]	0.008 [132]
MC Carbide (at%)	2.4	9.1	0.6	-	40.9	17.8	18.2	4.8	6.2	-	-	-
M_3B_2 Boride (at%)	4.2	63.9	2.3	-	1.3	-	3.4	18.9	4.3	1.7	-	-
Ni_7Zr_2 (at%)	63.1	2.6	5.4	-	1.6	4.0	2.3	-	-	21	-	-

As discussed earlier, the cooling rate within the fusion zone in the present work was estimated to be about 556°C/s. Such a rapid cooling rate could appreciably limit the extent of solute back-diffusion during the weld-metal solidification. It has been recognized that the diffusion of substitutional alloying elements in γ austenite during solidification conditions typical of fusion welding is negligible [172]. Therefore, equation 4.7 can be reasonably used to estimate the solute distribution coefficients. At the start of solidification, $f_s = 0$, under local equilibrium conditions and by neglecting undercooling at the dendrite tips, the first solid to form from the liquid, which is the dendrite will have a composition of kC_o. The ratio of dendrite core composition and the nominal composition will thus yield the distribution coefficient of an element at the beginning of the weld solidification process. The initial partition coefficients at the start of solidification of the metallic alloying elements were calculated and are listed in Table 4.3. The results indicate that W and Co with $k > 1$ segregate to the dendrite core while Mo, Ta, Ti, Nb, Zr and Al with $k < 1$ enrich the interdendritic regions. Ni and Cr having k values approximately equal to unity tend to exhibit uniform distribution between dendrite core and dendrite interstices.

The microsegregation pattern of the alloying elements observed in the present work is in close agreement with those reported in other superalloy welds [173-175]. The reverse segregation behavior of Al in the fusion zone as compared to their negative segregation during casting of IN 738, as reported by Taha et al [129], could be due to back-diffusion effect. It is known that during dendritic solidification, the extent of segregation can be significantly reduced by solid-state diffusion [38] which would be more pronounced with slowly cooled casting compared to the rapidly solidified weld-

metal. Another possible cause of the reverse segregation pattern could be due to a change in the nature of solute interactions in the liquid, which can also be influenced by rapid cooling through higher undercooling and limited back-diffusion effects. The partition coefficient of B and C could not be determined in the present work due to the difficulty in quantifying these light elements with sufficient accuracy and the fact that the effect of back-diffusion of interstitial elements can be significant during solidification. It has, however, been mentioned by Knorovsky et al [176] that the distribution coefficient of carbon in alloys similar to IN 625 is approximately 0.2. Thompson et al [177] in their study on IN 718 have experimentally confirmed by auger electron spectroscopy that carbon segregates into interdendritic liquid. Moreover, the binary Ni-X phase diagrams indicate that C and B exhibit $k<1$ in nickel. Hence, it is reasonable to assume that in IN 738, during solidification, an extensive segregation of C and B atoms would occur into the interdendritic liquid. It should be noted that the partition coefficients are not necessarily constant during the solidification process, but they explain well the formation of interdendritic microconstituent, as would be discussed shortly. In addition, in the case of solute buildup at the dendrite tips, the initial solid to form will have a higher concentration of solutes (compared to the case of no solute buildup as assumed in the present approach) and lead to a higher measured value of k. Hence, the obtained k values reported here provide an upper bound when $k<1$.

4.2.3 Scanning and Analytical Transmission Electron Microscopic Examination

Figure 4.22 shows a typical SEM micrograph of the fusion zone. No evidence of centerline solidification cracking was observed in any of the welded samples, however,

occurrence of microporosity mainly associated with isolated eutectic regions was observed at higher magnifications. The interdendritic region consisted of discrete second phase particles (blocky, rod-like and Chinese-script like morphologies) and isolated γ-γ' eutectic constituent with its usual characteristic mode of formation consisting of the "crown" region protruding into the last liquid to solidify [140] (inset of figure 4.22). Preliminary SEM/EDS microchemical analysis of the interdendritic discrete particles suggests them to be based on MC type carbides, however, TEM was used for their positive identification. Based on areal fraction analysis, the volume fraction of γ-γ' eutectic islands was estimated to be between 2 and 3% while that of the discrete interdendritic particles was between 1.5 and 2%. Different types of second phase particles some of which were enriched in Ni and Zr and others in Cr and Mo were observed in front of some of the γ-γ' eutectic (figure 4.22). In addition, careful SEM examination at higher magnification suggests that the observed variation in the light etching contrast in interdendritic regions, which is most prominent around the γ-γ' eutectic, could be due to precipitation of closely spaced fine γ' precipitates which could not be resolved appropriately by SEM.

TEM/EDS x-ray microanalysis of interdendritic constituents extracted on carbon extraction replicas showed that most of the particles have composition similar to those of MC type carbides observed in the base metal (Table 4.4). Analysis of electron diffraction patterns confirmed them to be cubic (FCC) MC carbides with a lattice parameter of 4.36Å. TEM examination revealed that the morphology of some of the MC carbides was of coarsely lamellar and dendritic shape (figure 4.23). The inset in fig. 4.23 shows the diffraction pattern of the carbide particle with a [001] zone axis. Apart from the carbides,

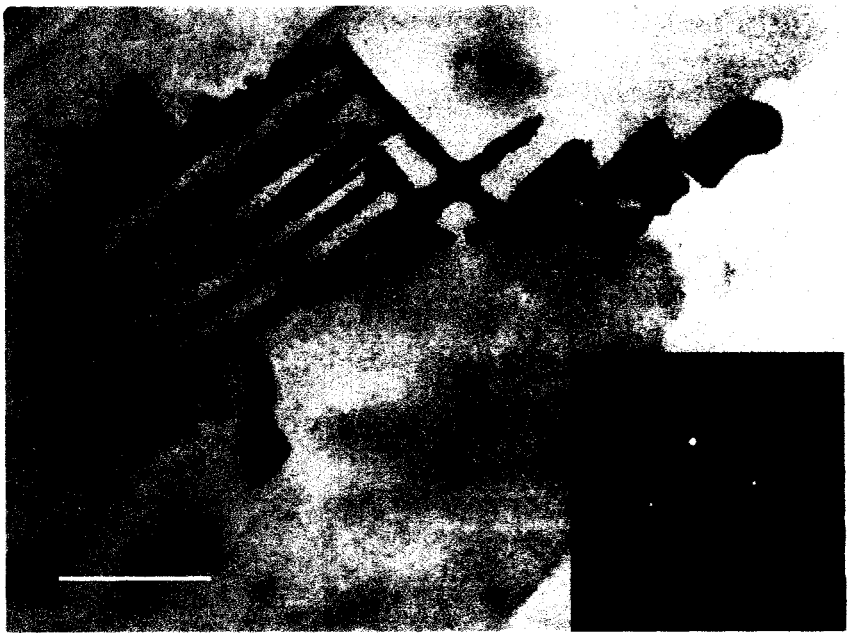

Fig. 4.23: TEM image of coarsely lamellar and dendritically shaped MC carbide with SADP from [001] zone axis

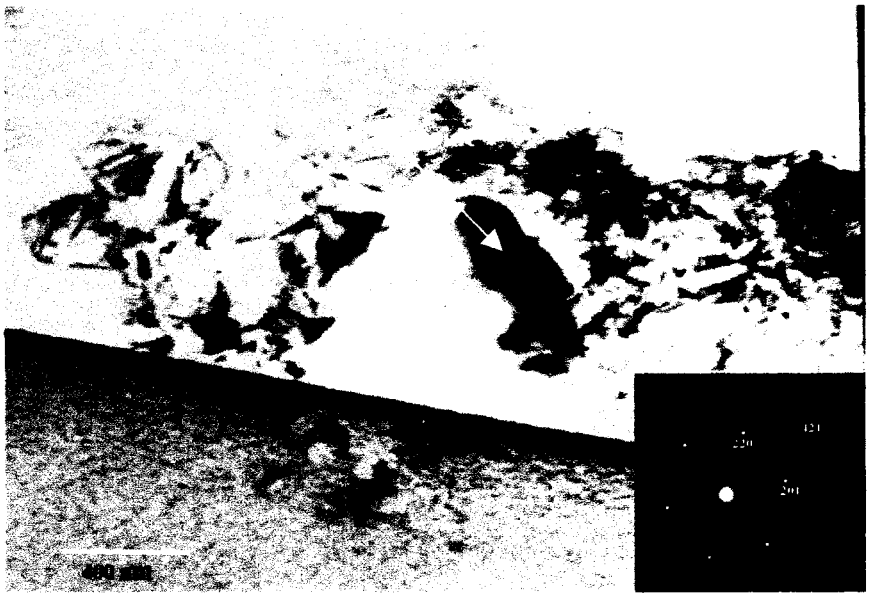

Fig. 4.24: TEM image of M_3B_2 boride extracted on carbon extraction replica with SADP from $[\bar{1}12]$ Zone axis.

the only other phase observed in smaller amounts on carbon extraction replicas was Cr-Mo rich particle, occurring mostly in regions having impressions of γ-γ' eutectic constituent (figure 4.24). Thin foils examination likewise showed the presence of similar phase associated with γ-γ' eutectic regions (fig. 4.26). Selected area diffraction pattern (SADP) analysis and TEM/EDS x-ray microanalysis indicated the phase to be tetragonal M_3B_2 boride with lattice parameters of a = 5.71Å and c = 3.05Å (figure 4.24 & Table 4.3). Figure 4.25 shows a typical TEM/EDS spectrum from a boride particle. As can be seen, boron was detected by the ultra thin window TEM/EDS. The spectrum also has the strong Cr and Mo peaks, which have been found to be characteristic of M_3B_2 boride in other Ni base superalloys [157].

In addition to M_3B_2 boride, the Ni-Zr rich phase observed in SEM was also found in thin foils by TEM examination (figure 4.26). The average chemical composition of this phase, as determined by TEM/EDS, is given in Table 4.3. This type of Ni-Zr intermetallic phase has not been previously reported in IN 738 alloy. The Ni-Zr binary phase diagram [178] suggests that two intermetallic phases Ni_5Zr and Ni_7Zr_2 form at Ni rich corner of the Ni-Zr system ($Ni_5Zr \rightarrow$ 14.85–18.4at%Zr and $Ni_7Zr_2 \rightarrow$ 22.2at %Zr). Likewise the phase diagram data for the Ni rich corner of Ni-Al-Zr ternary system show that both Ni_5Zr and Ni_7Zr_2 are possible intermediate phases that could be formed by the solidification reaction. Chen et al [179] have reported, based on their x-ray diffraction analysis, the formation of Ni_5Zr in a nickel aluminide alloy doped with Zr. They mentioned that the formation of Ni_5Zr in this alloy was dependent on the cooling rate. In contrast, Samuelsson et al [180] reported by EPMA analysis that Ni_7Zr_2 rather than Ni_5Zr

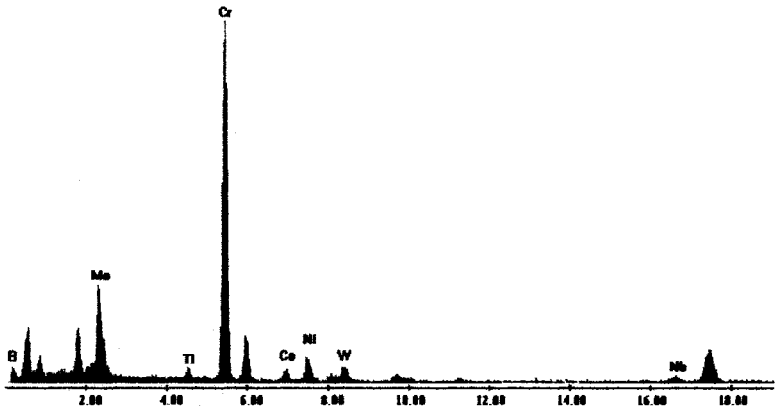

Fig. 4.25: TEM/EDS spectrum from a M_3B_2 boride particle.

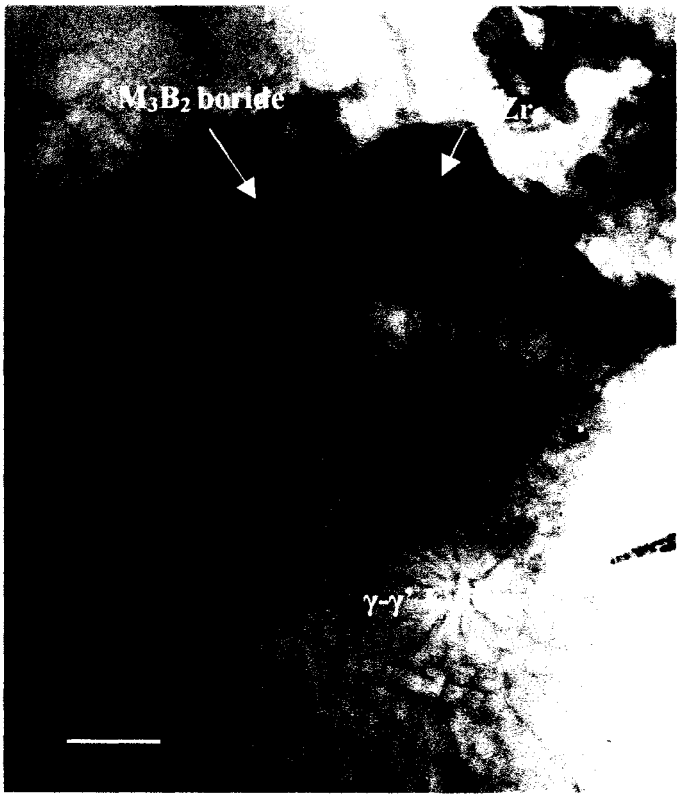

Fig. 4.26: TEM micrograph of a thin foil from fusion zone showing M_3B_2 & Ni_7Zr_2 associated with γ-γ' eutectic region.

crystallized from the residual interdendritic liquid in another nickel aluminide base alloys. They stated that the reason for the formation of Ni_7Zr_2 in this alloy instead of Ni_5Zr, which would be expected for an alloy containing 1.8 wt% Zr, was not fully understood. They suggested that perhaps strong interaction between nickel and aluminum leads to a decreased activity of nickel in the interdendritic liquid. A review of the literature shows that both Ni_5Zr and Ni_7Zr_2 are reported in cast nickel base superalloys containing Zr [159, 181]. Similarly, Ni_5Hf and Ni_7Hf_2 have been reported in interdendritic zones of Hf bearing cast nickel base superalloys Mar-M200 and DS200 single crystals [182, 183]. The intermediate phases Ni_5Hf and Ni_7Hf_2 are known to be isostructural with Ni_5Zr and Ni_7Zr_2 respectively. Identification of the phases in these reports was based on the chemical composition as determined by EPMA.

The chemical composition given in Table 4.3 suggests the phase observed in the present work to be based on Ni_7Zr_2 with some substitution of Ni by Cr and Co atoms, while Ti and Al replacing some Zr atoms. This suggestion was confirmed by selected area diffraction pattern analysis of the particles which indicated them to be based on monoclinic Ni_7Zr_2 with lattice parameter of a = 4.82 Å, b = 8.22 Å, c = 11.13Å and β = 96.7°. Figure 4.27 shows a SADP from a particle of this phase with [101] zone axis.

In addition to interdendritic microconstituents mentioned above, precipitation of γ' particles was observed in all the thin foils from fusion zone. Figure 4.28 shows a TEM dark field image obtained using a superlattice reflection from γ' precipitate particle with $[\bar{1}12]$ zone axis. However, the morphology and size of the γ'phase were observed to vary depending on their location. Regions around the interdendritic γ-γ' eutectic were found to contain the coarsest γ' precipitates (fig. 4.29).

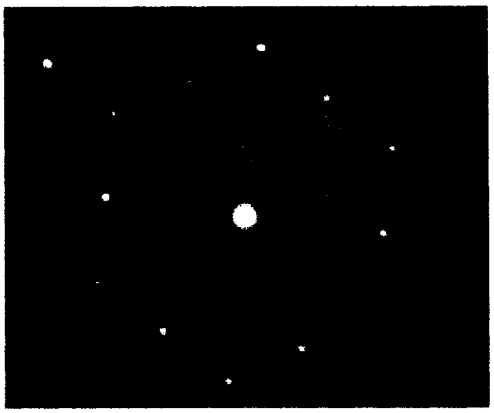

Fig. 4.27: SADP from a Ni_7Zr_2 particle at [101] Zone axis

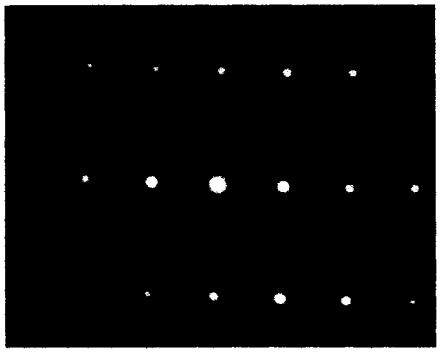

Fig. 4. 28(a): SADP at $[\bar{1}12]$ Zone axis

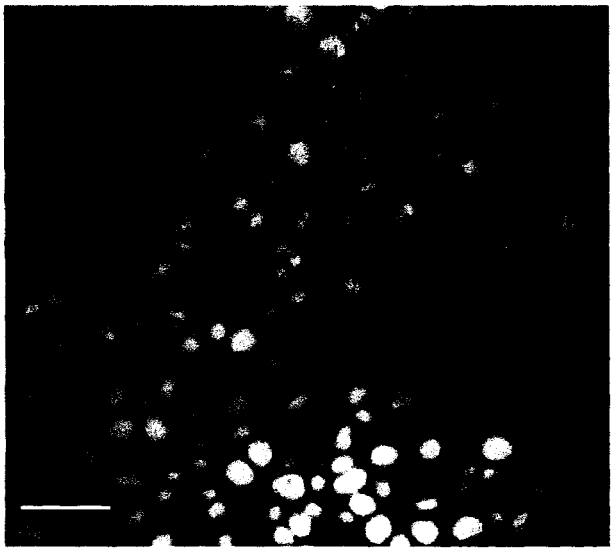

Fig. 4. 28(b): TEM dark field image of γ' precipitate particles taken with superlattice reflections at $[\bar{1}12]$ Zone axis

4.2.4 Fusion Zone Solidification Behavior and Microstructural Constituents

The microstructural development in the fusion zone of a weld is largely dominated by two interrelated solidification occurrences, dendrite formation and solute partitioning. The first solid to form from the weld pool in IN 738 is in the form of γ dendrites. During the continued formation of γ dendrites, solute elements with partition coefficient $k < 1$ were rejected into interdendritic liquid at the dendrite/liquid interface. Continual solute enrichment of the interdendritic liquid could cause the solubility limit of the primary solidification phase, γ matrix, to be exceeded, such that secondary solidification constituent are formed between the dendrites. In nickel base superalloys, several secondary solidification constituents are possible including carbides, borides, eutectic γ' and a number of other intermetallic phases. In IN 738 alloy, substantial positive dendritic microsegregation of strong carbide forming elements, Ti, Nb, Mo and Ta along with C, which also exhibits limited solubility in Ni, would eventually result in the formation of interdendritic MC carbides. It is most likely to occur via a monovariant $L \rightarrow \gamma + MC$ eutectic-type transformation, as supported by the observed lamellar and dendritically shaped carbide particles (figure 4.23). Coupled growth of MC and γ in a eutectic-like fashion is more pronounced in the fusion zone than the coarsely lamellar type observed in the base alloy. This may be due to a larger degree of undercooling during weld-metal solidification aiding such growth.

Generally the carbides were much finer than those observed in the as-cast base alloy, mostly less than 1μm in size. Nonetheless, some coarse MC particles with sizes approaching twice the secondary dendrite arm spacing were observed located mainly within the dendrite core (figure 4.30). Occurrence of these coarse carbide particles within

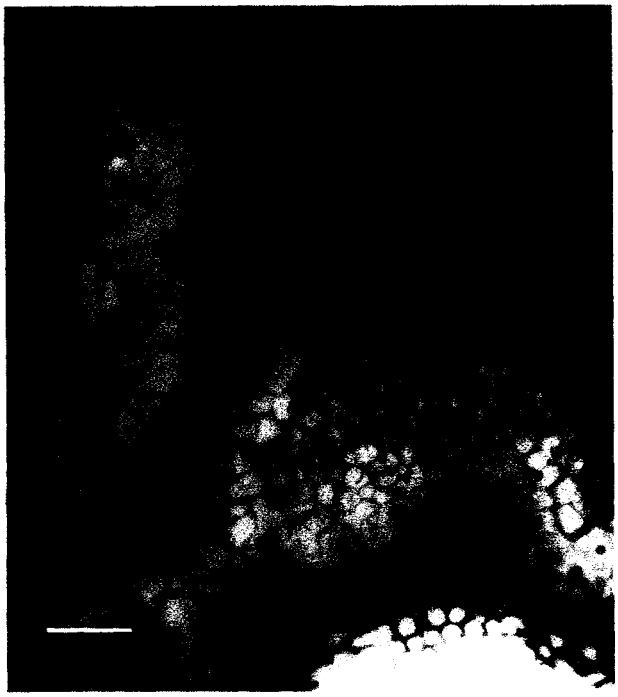

Fig. 4.29: TEM image showing inhomogeneous γ' distribution within interdendritic region.

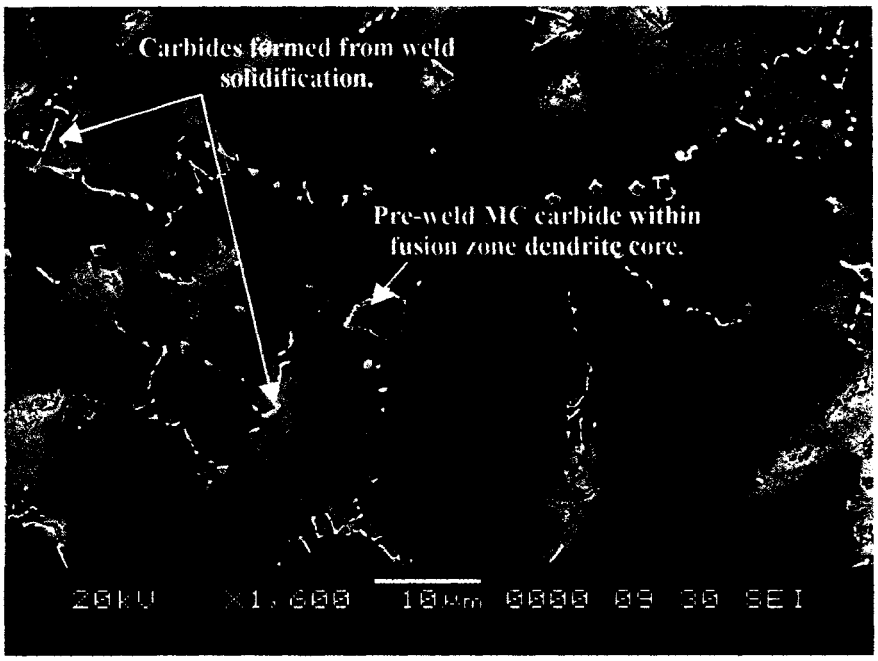

Figure 4.30: Weld fusion zone showing the presence of pre-weld MC carbide and those formed along interdendritic regions (light etching regions) during weld solidification.

the dendritic core regions is possible under two conditions: (i) the particles were present in the pre-weld alloy but did not dissolve completely in the weld pool (ii) the particles nucleated and grew from the weld pool prior to nucleation of the γ dendrite. In either case, particles could serve as nucleation site for the dendrites during solidification or they could be entrapped within the dendrites if the cooling rate is high and growth rate exceeds the critical velocity for particle entrapment. DTA analyses, however, have established that solidification sequence of IN 738 starts by nucleation and growth of γ dendrite rather than MC carbide. This, in addition to the fewer number of these particles, thus, suggests that the coarse MC carbides observed within the γ dendrites are most likely the residual MC particles that dissolve completely in the weld pool. Liu et al [184] have reported that some primary MC carbides in IN 738 can be stable and remain in the melt above the liquidus temperature of the alloy, of up to 1550°C, for 5-10 minutes.

On cooling, supersaturation of remaining interdendritic liquid with γ' forming elements Ti, Al, Nb and Ta due to continual enrichment would eventually be relieved through the formation of γ-γ' eutectic. $L \rightarrow \gamma + \gamma'$ eutectic-type reaction has been reported to occur over a range of temperatures in IN 738 alloy [135]. A combination of limited space between the smaller dendrites and shorter cooling times might be the reason for a finer size of γ-γ' eutectic within the fusion zone interdendritic regions as compared to that present in the as-cast base metal. As discussed earlier, based on the DTA experiments it is generally believed that solidification of IN 738 alloy is completed by γ-γ' eutectic transformation around 1200°C. However, as was shown in the present work, there exists a different type of terminal solidification reaction product in front of some γ-γ' eutectic in the as-cast alloy. It is suggested that a similar solidification events could be responsible

for the formation of Cr-Mo rich M_3B_2 boride and Ni_7Zr_2 based intermetallic compound observed ahead of the interdendritic γ-γ' eutectic in the fusion zone of the alloy. It is also possible that the M_3B_2 boride and Ni_7Zr_2 formed together with γ-γ' eutectic by the following complex eutectic type reaction suggested by Babu et al [185]:

$$L \rightarrow \gamma + \gamma' + M_3B_2 \text{ and/or } Ni_7Zr_2$$

Reported observations of a different γ- M_3B_2 eutectic reaction several tens of degree below the γ-γ' eutectic transformation temperature in boron containing nickel base superalloy [158,186] tend to support the first suggestion.

The γ' precipitate particles would start forming from supersaturated solid γ matrix when the temperature is sufficiently lower than the γ' solvus temperature to initiate nucleation. Segregation of γ' forming elements during solidification would cause γ' precipitation to occur in the interdendritic regions at higher temperatures compared to that within the depleted dendrite core, as an increase in Al and Ti concentration is known to increase γ' solvus [187]. This would explain the formation of coarser γ' precipitates within the interdendritic regions. Such, inhomogeneous γ' distribution does not appear to provide a reliable high temperature performance and is one of the main factors that normally necessitate the use of PWHT to homogenize and restore properties of superalloy weldments. A potential cause of problems during PWHT of the present alloy, particularly during the initial stage of common PWHT cycle involving rapid heating to solution heat treatment temperature, could be the presence of the low melting terminal solidification constituent M_3B_2 and Ni_7Zr_2 in association with γ-γ' eutectic in the fusion zone. Incipient eutectic melting of these constituents either during the heating cycle or during solution treatment could reduce the resistance to PWHT cracking and/or degrade the final

properties of the weldment. A DTA study of nickel base superalloys [187] has shown the occurrence of eutectic melting of Ni-Zr intermetallic at 1154 – 1184°C. This temperature range is close to the interdendritic γ' solvus in IN 738 superalloy (1170 -1180°C) [135]. A Ni-Zr intermetallic compound of composition similar to that observed in the present work has been reported to cause low temperature incipient melting and reduction in strengthening efficiency of Zr in cast Mar-M200 superalloy [159]. In the same context, rapid heating to temperatures just above γ - M_3B_2 eutectic, which was below the γ' solvus have been also reported to cause incipient melting in IN 100 superalloy [186]. As mentioned earlier, incipient melting of the terminal solidification constituents during heat treatment of as-cast IN 738 alloy at 1154°C was observed in the present work. Besides, significant amount of Zr and B, which are grain boundary strengthening elements in IN 738, might be tied up in the Ni_7Zr_2 and M_3B_2 particles, respectively. Consequently, the presence of fusion zone terminal solidification products, identified in this work, appears to be an important factor that requires appropriate consideration during the development of optimum PWHT for reliable microstructure and properties of IN 738 weldments. Furthermore, in the case of multipass welding process, the presence of low melting terminal solidification constituents may reduce resistance to weld-metal liquation cracking in the underlying pass of the weldment. Susceptibility to this type of weld cracking generally parallels that of HAZ liquation cracking. The inherent microsegregation, which is remnant of weld solidification, presence of terminal solidification constituents that exhibit lower liquation temperature, and a coarse fusion grain size could interact to promote susceptibility to this form of weld cracking.

4.2.5 Development Of a Pseudo-Ternary Diagram For IN 738 Alloy

The solidification sequence for IN 738, as determined by DTA experiments [136,137], has generally been found to be:

$$L \rightarrow L' + \gamma$$
$$L' \rightarrow L'' + \gamma + MC$$
$$L'' \rightarrow \gamma + \gamma' \text{ (eutectic)}$$

The formation of MC carbide from the liquid has been indicated to take place isothermally at around 1300°C [136]. Likewise, the terminal solidification reaction was shown to be an invariant $L \rightarrow \gamma + \gamma'$ eutectic transformation. The sequence agrees with that determined by the method of metallographic examination of interrupted directionally solidified IN 738 alloy [135]. However, in contrast to the DTA report, the metallographic examination indicated that formation of the γ-γ' eutectic occurred over a range of temperatures. Likewise, microstructural observations made in the present work also suggest that the MC carbides in IN 738 formed by a monovariant eutectic-type reaction. For the purpose of buttressing the discussions already presented in the present work on microstructural development in as-solidified IN 738 alloy, a solidification diagram has been adapted for IN 738 alloy based on a pseudo-ternary consisting of (i) γ_o, an FCC solid solution of the substitutional elements, which make up the matrix of IN 738 alloy (ii) MC carbide and (iii) γ'. The simplification of the diagram is based on the knowledge of the Ni-Ti-C ternary diagram, which shows a solidification sequence similar to that of IN 738, for alloys of composition close to the nickel corner of the composition triangle.

The solidification of these Ni-rich alloys in Ni-Ti-C system can be studied by considering the composition triangle of Ni, TiC and Ni_3Ti, shown in figure 4.31. The liquidus projection for the Ni-TiC- Ni_3Ti triangle has been estimated by Backerud et al

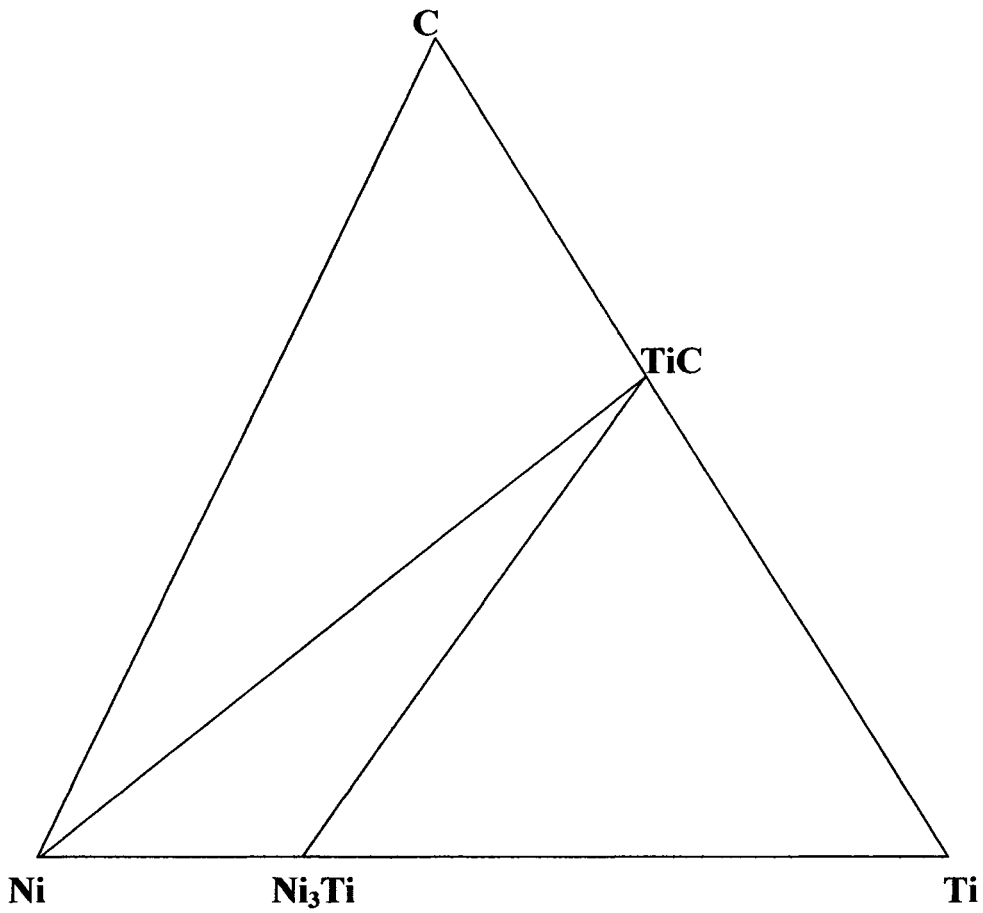

Figure 4.31: Ni-Ti-C ternary showing the composition triangle of interest, Ni-TiC-Ni_3Ti.

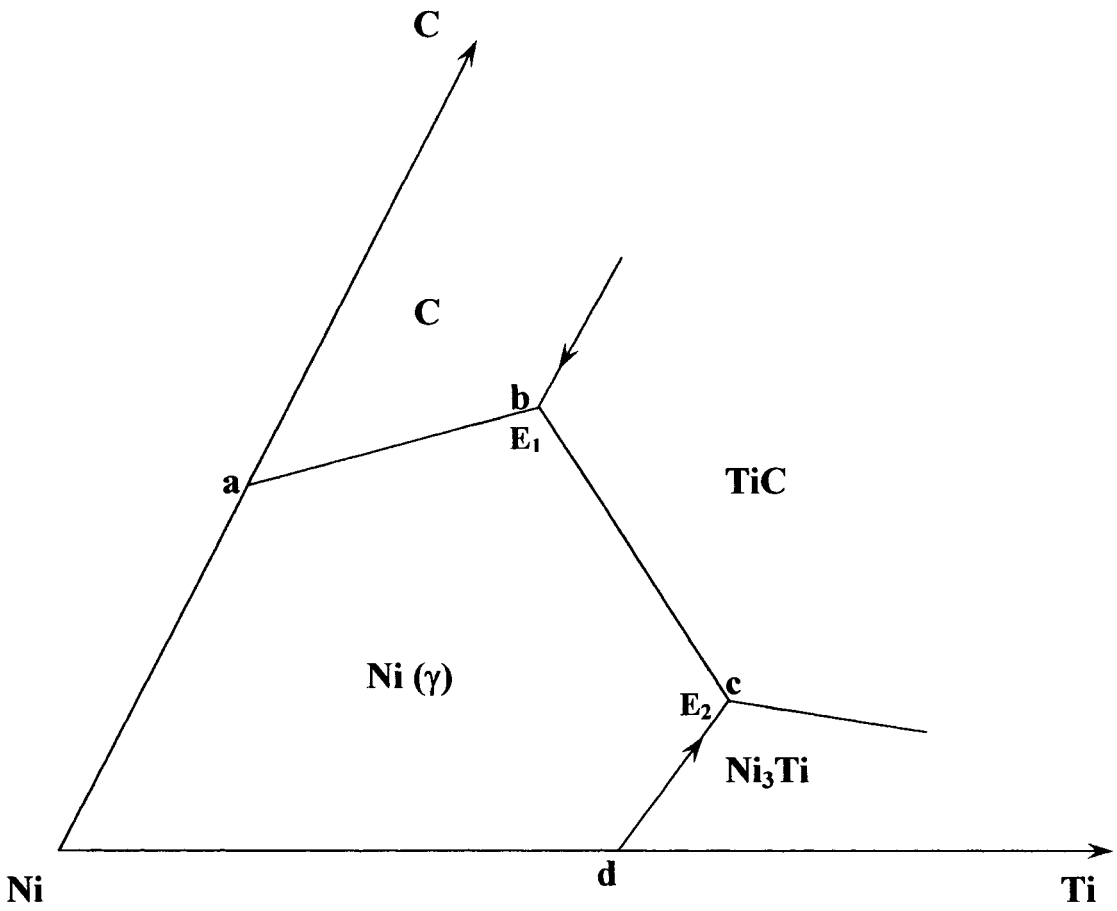

Figure 4.32: Basal projection of the liquidus surfaces of the nickel rich corner of Ni-Ti-C system [188]

[188] and is redrawn in figure 4.32. The primary phases are γ phase, i.e. nickel with titanium and carbon in solid solution, graphite (C), TiC (which has a wide homogeneous interval) and the intermetallic phase Ni_3Ti. The primary C (graphite) phase field which exists at high carbon contents is not of interest here. The intersection between the three liquidus surfaces for γ phase, graphite and TiC results in a ternary reaction E_1, where the equilibrium;

$$L \Leftrightarrow \gamma + C + TiC$$

is established. The other ternary eutectic reaction E_2 occurs at the intersection between the liquidus surfaces for γ, TiC and Ni_3Ti, where the reaction;

$$L \Leftrightarrow \gamma + TiC + Ni_3Ti$$

takes place. The eutectic valley between E_1 and E_2 has a rather flat maximum and slopes downwards in the neighborhood of E_1 and E_2. The quasi-binary monovariant eutectic between γ-C, γ-TiC and γ-Ni_3Ti are represented by ab, bc, and cd, respectively in figure 4.32.

If we consider the solidification of alloys of composition close to the Ni corner shown in figure 4.33, the first solid to form will be γ dendrite. During solidification, composition of the γ phase changes continuously rejecting Ti and C into the liquid phase. The corresponding liquid becomes enriched in both Ti and C and intersects either the line representing equilibrium between L, γ and TiC or the line representing equilibrium between L, γ and Ni_3Ti, depending upon the Ti and C content of the alloy. Depending on whether the former or the latter equilibrium line is reached, either γ + TiC or γ + Ni_3Ti will form simultaneously from the liquid by the following monovariant eutectic-type reaction:

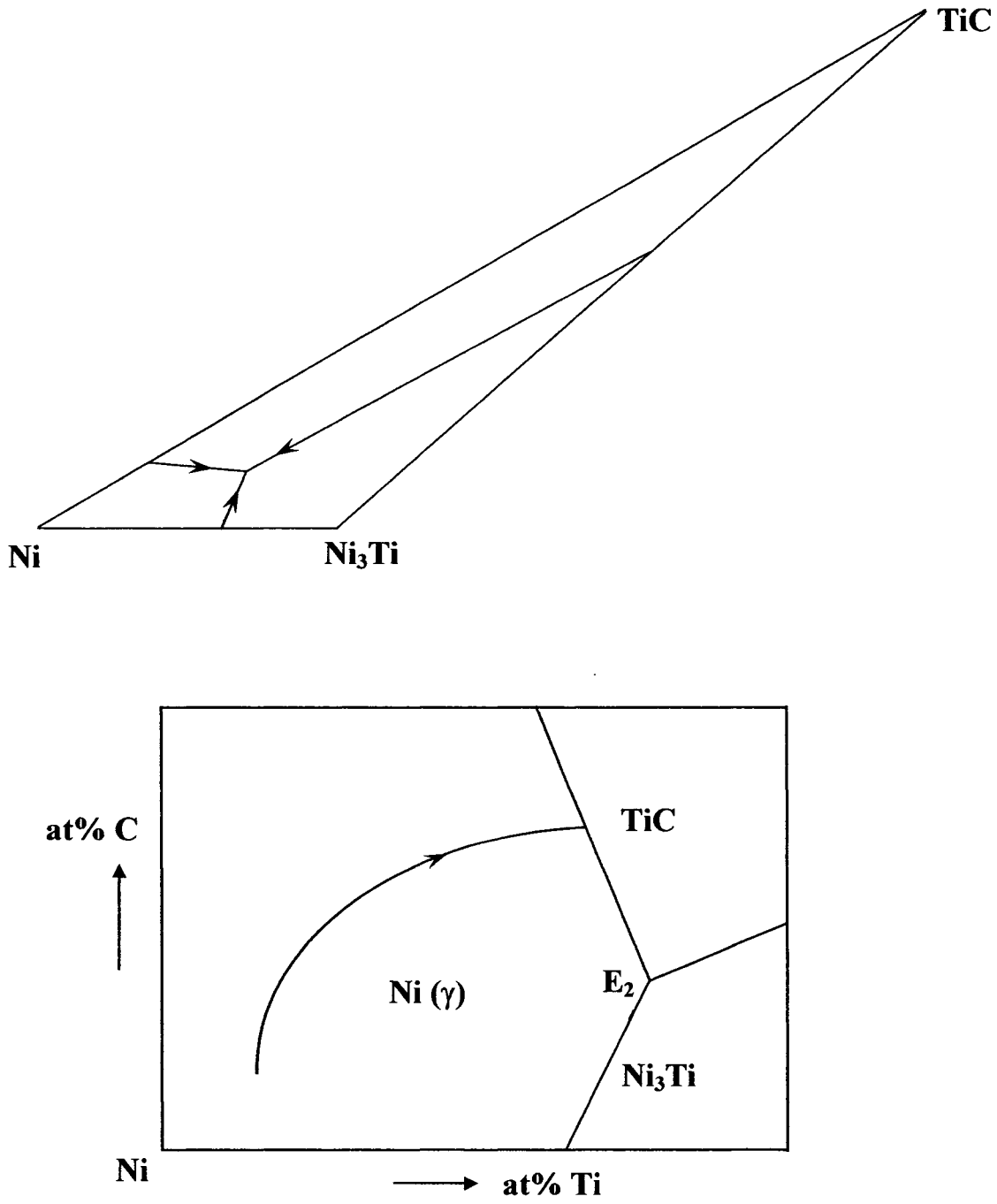

Figure 4.33: Sequence of solidification for alloys close to the Ni-rich corner of the Ni-TiC-Ni_3Ti .

$$L \Leftrightarrow \gamma + TiC \quad \text{or} \quad L \Leftrightarrow \gamma + Ni_3Ti$$

as the liquid composition travels down the line of two fold saturation until the terminal eutectic temperature E_2 is reached. At E_2, the remaining liquid will complete solidification by a ternary eutectic reaction:

$$L \Leftrightarrow \gamma + TiC + Ni_3Ti$$

It is interesting to note that the solidification of IN 738 follows a similar sequence, if we replace Ni_3Ti by γ', Ni (γ) by γ_o and TiC by MC carbides. The composition of γ_o is such that the addition of Al, Ta, Mo, W and Nb leads to the formation of γ' and MC carbides. It is known that ternary and quaternary additions of γ' forming elements to Ni-Ti system promote the formation of γ' phase at the expense of Ni_3Ti [163]. Also, a wide miscibility gap is known to exist between binary carbides of the carbide forming elements in Ni-based superalloys [156].

The solidification sequence developed for Ni (γ) - TiC - Ni_3Ti alloys can thus be applied reasonably to IN 738 to obtain the following sequence. During solidification, initial dendrites of γ_o form and cause the liquid to be enriched in Ti and other carbide forming elements together with C. This enrichment continues during cooling until the composition reaches the line representing equilibrium between γ_o, MC and liquid. At this point, MC carbide and γ_o form and continue to form over a range of temperatures i.e.

$$L \Leftrightarrow \gamma_o + MC$$

until at the ternary eutectic temperature E_2, where the eutectic transformation:

$$L \Leftrightarrow \gamma_o + \gamma' + MC$$

occurs. This solidification diagram approach for the solidification of IN 738, which shows $L \Leftrightarrow \gamma_o + MC$ forming over a range of temperatures is in agreement with the

observations of the present work, as discussed earlier. According to this proposed pseudo-ternary diagram which is based on Ni-Ti-C liquidus projection, where solidification is shown to terminate by the ternary eutectic reaction $L \Leftrightarrow \gamma + TiC + Ni_3Ti$, the ternary γ_o-γ'-MC eutectic constituent in IN 738 should be intermixed. This type of microstructure was not observed in the as-cast alloy nor in the fusion zone of IN 738 alloy. Instead γ_o-MC and γ_o-γ' eutectic type constituents are essentially separate. However, there is another possibility if the three binary eutectics of figure 4.33 lead to a class II type reaction within the Ni-TiC- Ni_3Ti composition triangle instead of Class I ternary eutectic [189]. The liquidus projection for this is shown in figure 4.34 with replacement of Ni (γ) by γ_o, Ni_3Ti by γ' and TiC by MC. In this case, after primary γ_o nucleation and growth, the liquid composition on reaching the line of twofold saturation separating the γ_o and MC carbide would follow this monovariant line forming γ_o – MC eutectic until reaching class II reaction isotherm E_2, where the peritectic reaction:

$$L + \gamma_o + MC \Leftrightarrow L + \gamma_o + \gamma'$$

occurs. The remaining liquid then continues to form γ_o-γ' eutectic over a range of temperature until solidification is completed. This mechanism would result in the formation of γ_o-γ' eutectic near MC carbides at the peritectic isotherm followed by monovariant

$$L \Leftrightarrow \gamma_o + \gamma'$$

eutectic transformation. Large MC carbides were observed near some γ-γ' eutectic in the present work as shown in figures 4.12a and 4.12b. In addition, as mentioned earlier, Rosenthal et al [135] have observed formation of γ-γ' eutectic over a range of temperatures in IN 738 rather than by isothermal transformation. This, thus, suggests that

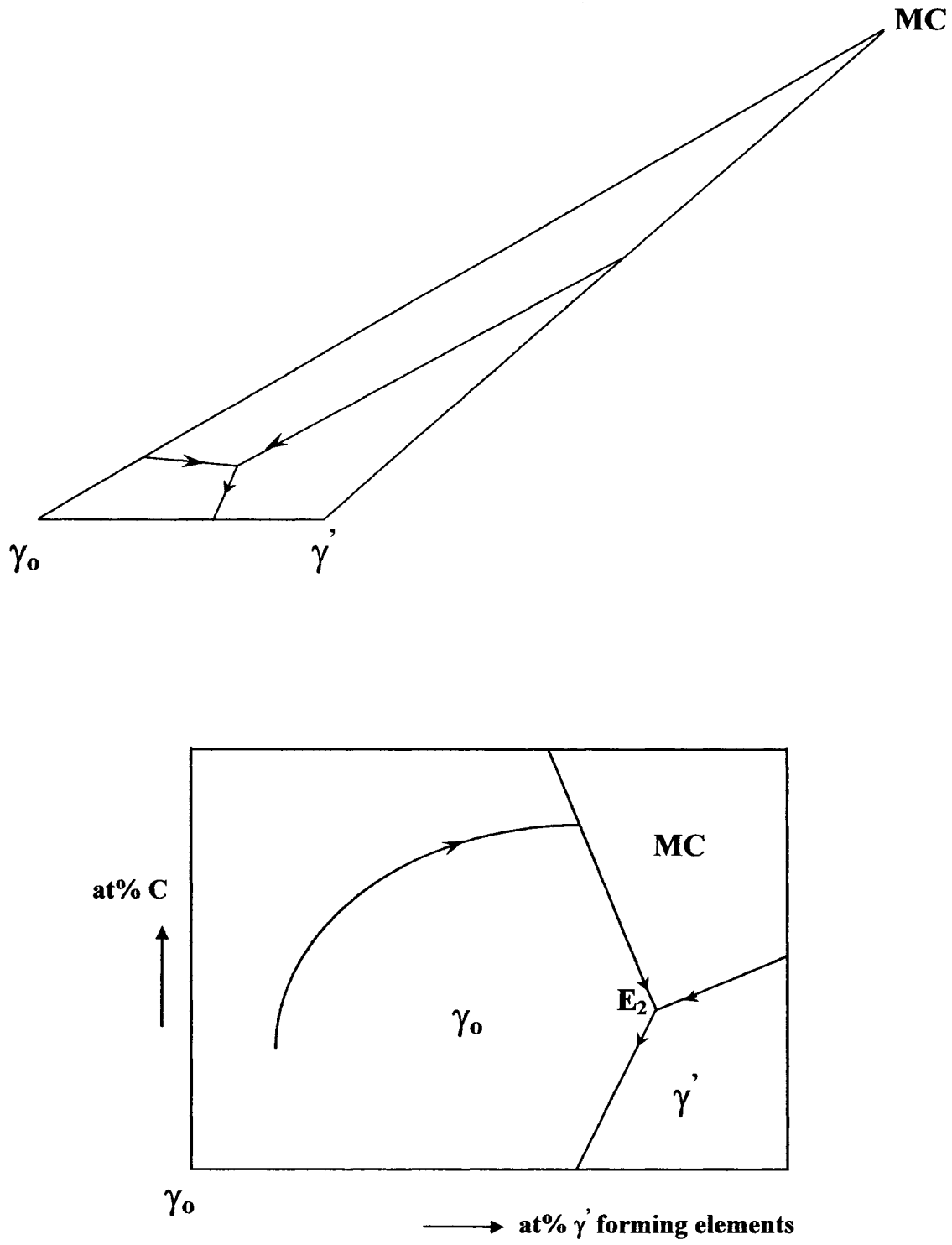

Figure 4.34: Liquidus projection for the case where the γ-γ'-MC shows a class II reaction instead of a class I reaction

the solidification behavior of IN 738 can be more properly represented by a class II reaction of the proposed pseudo-ternary diagram. It should, however, be noted that the multicomponent IN 738 simplified into a pseudo-ternary system consists of minor amount of severely segregating and melting point depressants Zr and B. As such, actual terminal solidification reaction could involve formation of other microconstituents in front of the γ-γ' eutectic due to continual rejection of solutes such as Zr and B into the residual liquid during the monovariant γ-γ' eutectic transformation. This would explain the occurrence of terminal solidification constituents in this alloy involving Ni_7Zr_2 and M_3B_2, as discussed earlier. The psedo-ternary representation developed here reasonably describes the solidification behavior of IN 738, especially as determined by the reported DTA analyses [136, 137] and microstructural examination [135]. It is interesting to note that the simplified psedo-ternary representation developed here appears to be generally applicable to other cast γ' precipitation hardened nickel base superalloys with carbon additions [155, 158, 190].

4.2.6 Defect Formation in the Weld-Metal Zone

The apparent absence of exclusive solidification cracking in the fusion zone of the present work merits some comment. Formation of cracks during solidification can occur in ingots, castings and welds. In general, cracks can form in certain alloy systems during the terminal stages of solidification when a liquid film is distributed along the interdendritic and solidification grain boundaries. At this stage, shrinkage across the primary grain boundaries of the solid can be appreciable. If the terminal liquid is distributed along the boundaries as a continuous thin film, the degree of local strain that

can be accommodated is limited and the boundaries may separate to form a crack if a critical strain level is exceeded. In terms of material factors, the solidification temperature range ΔT and amount and morphology of the interfacial liquid that exists at the terminal stages of solidification are primary factors that control solidification cracking susceptibility.

The ΔT controls the level of stress/strain under a given cooling rate that could be accumulated during cooling before the alloy completely solidifies and develops resistance to cracking. Generally, the larger the solidification temperature range, the higher is the propensity to cracking. The degree of elemental microsegregation observed in as-solidified IN 738 alloy normally extends ΔT, nonetheless the alloy is known to be relatively resistant to solidification cracking. It has been recognized that mere occurrence of a large ΔT is not sufficient to cause cracking in a given alloy system, as cracking susceptibility cannot be correlated with ΔT alone. For cracking to occur, the amount and distribution of interfacial liquid must be such that ease of crack formation and/or propagation is favored appreciably. The distribution of liquid near the end of solidification is in turn controlled by the amount of terminal liquid and solid-liquid surface tension. A small amount of low melting liquid existing in the form of isolated globules has been suggested to reduce susceptibility to solidification cracking by promoting the formation of solid-solid bridge along the boundaries.

The observation of isolated interdendritic γ-γ' eutectic in the fusion zone of this work suggests that the residual liquid, from which the terminal solidification constituents formed, was also isolated within the interdendritic regions during weld cooling. This mode of liquid distribution as opposed to continuous/semi-continuous thin interfacial

liquid film could, thus, be an important factor contributing to the alloys appreciable resistance to solidification cracking. This factor could be associated with the effect of carbon addition on solidification behavior of IN 738 alloy. In γ' precipitation hardened nickel base superalloys free of residual non-metals like C, S and B, solidification is normally completed by the formation of γ-γ' eutectic. In these alloy systems, the amount and distribution of γ-γ' eutectic, which generally depends on the nominal concentration of γ' forming elements, tends to control susceptibility to solidification cracking. It has been found that addition of carbon to these alloys substantially decreased their susceptibility to solidification cracking. This beneficial effect of C addition in γ' precipitation hardened nickel base superalloys can be discussed using the psedo-ternary diagram developed in the present work. As can be seen from figure 4.32, the point of intersection between the primary solidification path and the line of twofold saturation will vary, depending on carbon content. This is illustrated in figure 4.34b. As the nominal carbon content is increased, the interdendritic liquid becomes more highly enriched in carbon and the intersection point occurs at a higher C content (path 1 in figure 4.34b). Consequently, the liquid composition must 'travel' a long distance down the L $\Leftrightarrow$ γ + MC line of twofold saturation, forming γ and MC before reaching the class II isotherm E_2, subsequent to which the γ-γ' eutectic constituent starts to form. In this case, much of the liquid is consumed and converted to γ and MC, thus, reducing the amount of liquid available for γ-γ' eutectic transformation during the final stages of solidification. In this process, much of Ti, Nb and Ta which are also γ' forming elements are consumed by the formation of MC carbides.

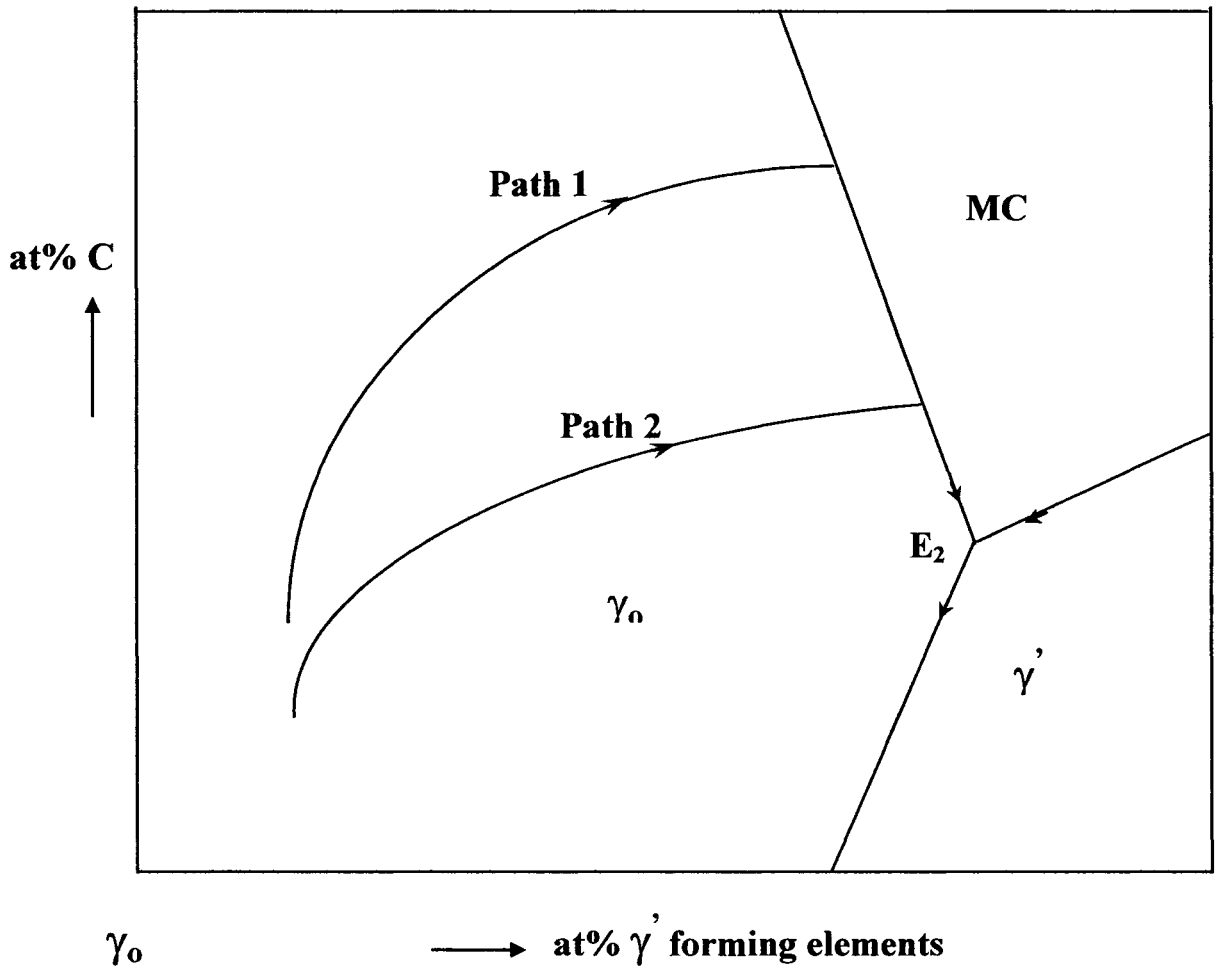

Figure 4.34b: Illustration of influence of C content on solidification behavior.

In alloys consisting of high C/(Ti+Nb+Ta) ratio, it is possible for almost, if not, all the liquid to be consumed during the L $\Leftrightarrow$ γ + MC monovariant reaction so that little or no γ-γ' eutectic forms. This could be the case in continuous cast IN 713C where MC carbide formation was reported to start close to the liquidus temperature and solidification was completed without the formation of γ-γ' eutectic [190]. In contrast, however, when the C content of the alloy is low, the primary solidification path 'travels' very close to the γ-Ti 'binary' edge of the solidification surface because the interdendritic liquid never becomes substantially enriched in C (path 2 in figure 4.34b). Under this condition, very little liquid is consumed and converted to γ and MC constituent as the liquid 'travels' only a short distance down the twofold saturation line before reaching the class II peritectic isotherm, where composition conditions required for the start of γ-γ' eutectic forms. Therefore, there will still be a relatively large amount of liquid available for γ-γ' eutectic transformation, which might cause the low melting liquid to form in a continuous/semi continuous fashion along the boundaries during the final stages of solidification. This could be the case in the γ' precipitation hardened nickel base superalloys containing little or no C addition. Weld solidification cracking in carbon-free PW1480 single crystal has been related to the formation of γ-γ' eutectic constituent along interdendritic regions during the last stages of solidification of electron beam weld-metal zone [138]. It is also to be noted that the distribution of interdendritic liquid during the last stages of solidification will not only depend on the wetting properties of the liquid but also equally important is the amount of the liquid. It has been found that even in a system containing interdendritic liquid with excellent wetting properties, a certain

minimum amount of liquid phase is required to produce continuous/semi-continuous liquid distribution [191].

The IN 738 alloy used in the present investigation contains 0.11 wt% of carbon. This can be considered to be on the high side compared with other nickel base superalloys and will act to reduce the amount of interdendritic liquid during the last stages of solidification, as explained for high carbon content alloys above. Accordingly, formation of small volume fraction (~ 2 %) of isolated globules of γ-γ' eutectic observed in the present work, which apparently enhanced resistance to solidification cracking, may be related to the effect of C in reducing the amount and also the distribution of interdendritic liquid during the last stages of the weld solidification.

Apart from susceptibility to fusion zone hot cracking, formation of MC carbides in the interdendritic regions, could affect microstructure of as-solidified superalloys by influencing the formation of microporosities. In principle, microporosity formation can arise from shrinkage and gas evolution during solidification. With the current state of vacuum technology, however, maintaining a high vacuum during remelting and casting can effectively eliminate gas porosity. It can then be generalized that microporosities are mostly due to solidification shrinkage. Since alloys solidify in a mushy manner, mass feeding stops when about 70% of the alloy is solidified [192]. Capillary (i.e. interdendritic and intergranular) feeding then becomes the only operative feeding mode. Microporosity formation in castings and weld, thus, occurs during the last stages of solidification when capillary feeding becomes insufficient. It has been found from basic fluid flow considerations that susceptibility of an alloy to form microporosity in a casting increases with decreasing permeability of the mushy zone during feeding [158]. It has

been indicated that interdendritic carbide particles could reduce permeability during capillary feeding and thus increase propensity to microporosity formation [193]. As was mentioned earlier, dispersed microporosity was observed in the fusion zone of the present alloy which was mainly associated with γ-γ' eutectic. This could be related to the above effect of interdendritic MC carbide particles and may also be due to a higher inherent solidification shrinkage associated with γ-γ' eutectic transformation. Lower solidification shrinkage has been reported to accompany γ-MC eutectic transformation as compared to that of γ-γ' eutectic due to lattice expansion at the final solidification stages [194].

Finally, though carbide formation may enhance resistance to fusion zone solidification cracking, it could, in contrast promote susceptibility to HAZ cracking, as will be discussed in the following section.

4.3 HAZ Microstructure And Microfissuring

4.3.1 Introduction

During the past decades, numerous investigations have shown that fully austenitic Fe and Ni-base alloys that contain Nb and Ti can be highly susceptible to HAZ liquation cracking [6]. This form of cracking involves the formation of a liquid film at the HAZ grain boundaries during weld heating cycle and the inability of this film to accommodate thermally and/or mechanically induced stresses experience during cooling. It has, however, been recognized that mere occurrence of liquation is not sufficient to induce cracking. For cracking to occur, continuous or semi-continuous grain boundary liquid should persist until a time when sufficient thermal and mechanical restraint have developed during cooling. Therefore, important characteristics of intergranular liquid that affect its amount, distribution and stability control an alloys susceptibility to HAZ liquation cracking. In this section, the results of examination of microstructure of HAZs in welded samples and those of Gleeble simulated materials are presented and discussed. The characteristics of the intergranular liquid contributing to the alloys low resistance to HAZ cracking are then discussed.

4.3.2 Weld HAZ Microstructure

Microcracks were observed in HAZs around welds made after both the pre-weld heat treatments (ST & UMT). An example is shown in figure 4.35. The microstructural examination of HAZs of welds in both the heat-treated conditions showed that microcracks originated mainly in the HAZ region slightly removed from the fusion boundary, and in some cases they extended as much as 300μm into the base material and

partly into the fusion zone. The cracks were intergranular and displayed a relatively irregular and zigzag morphology that is typical of liquation cracks (figure 4.36). A closer and careful examination of cracked boundaries at higher magnifications by SEM, operating in secondary electron as well as in backscatter electron imaging mode, revealed the presence of re-solidification constituents along the crack paths (figure 4.37 a & b). The re-solidification constituents, which formed mostly on one side of the microfissures, suggest the origin of microfissuring to be liquation cracking in the HAZ of this alloy. This suggests that in liquid film stage, while the liquated phase is still liquid, the HAZ microfissuring generally occurs by decohesion across one of the solid-liquid interfaces when on-cooling welding tensile stresses exceed the local strength at such an interface. Evidence of extensive grain boundary penetration by liquid film, even down to the lower sub-solidus temperature HAZ regions where primary γ' particles had essentially undergone little solid state dissolution, was observed in the form of resolidified intergranular eutectic constituents (figure 4.38). Samples given the ST pre-weld heat treatment were observed to exhibit higher degree of cracking compared to the UMT samples. This is in agreement with previous investigation [123]. However, more liquated but seemingly uncracked grain boundaries were observed in the UMT samples. Likewise more resolidified constituents were observed in the UMT HAZ regions than in the ST samples. Intergranular liquid film, from which complex eutectic-like constituent (figure 4.38) formed along some UMT HAZ grain boundaries, appeared to have been of considerable thickness as the eutectic width was found to be over 2.5μm.

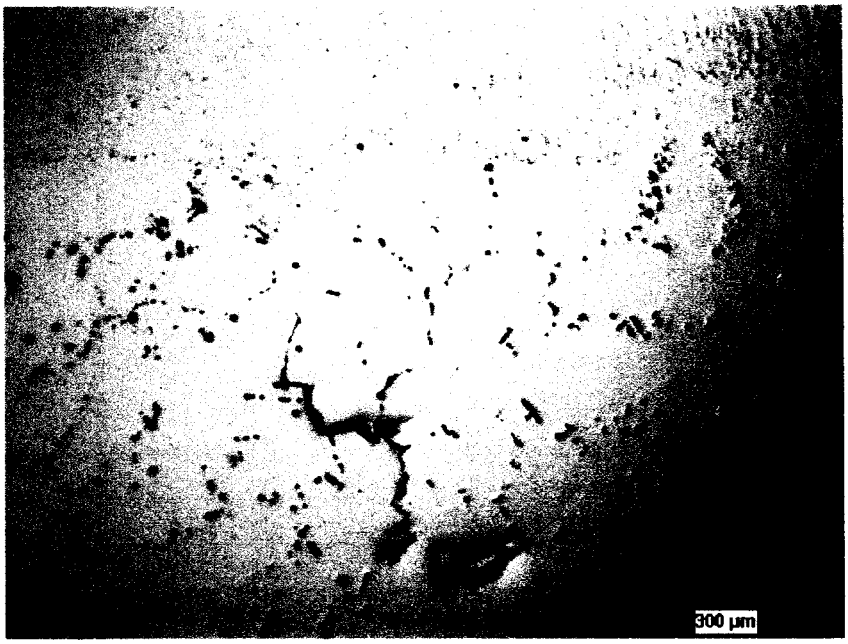

Figure 4.35: Optical micrograph of a HAZ Crack.

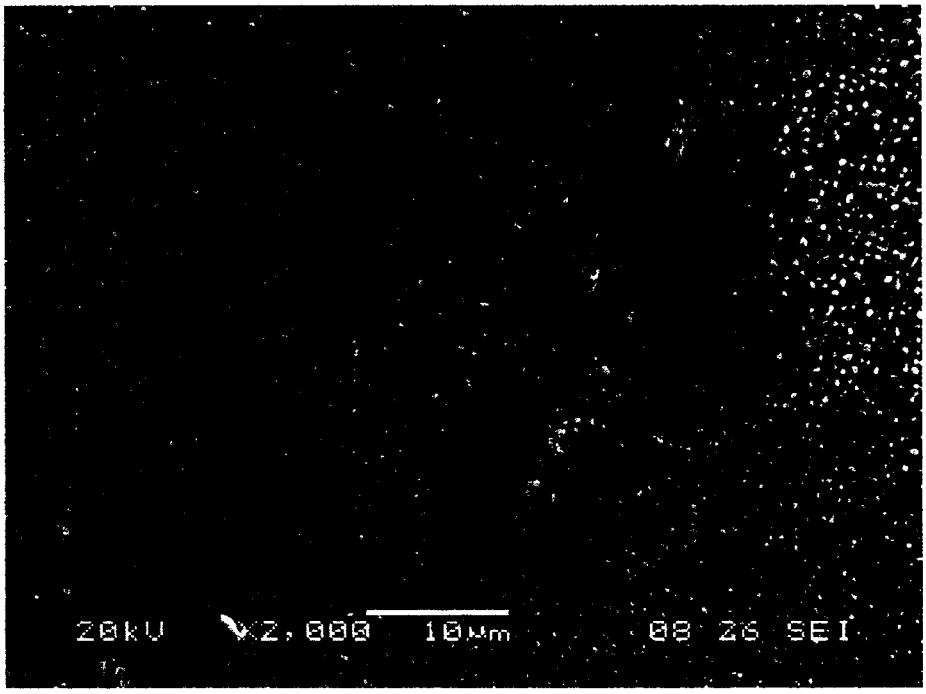

Figure 4.36: SEM image of HAZ crack in sample welded in solution treated condition.

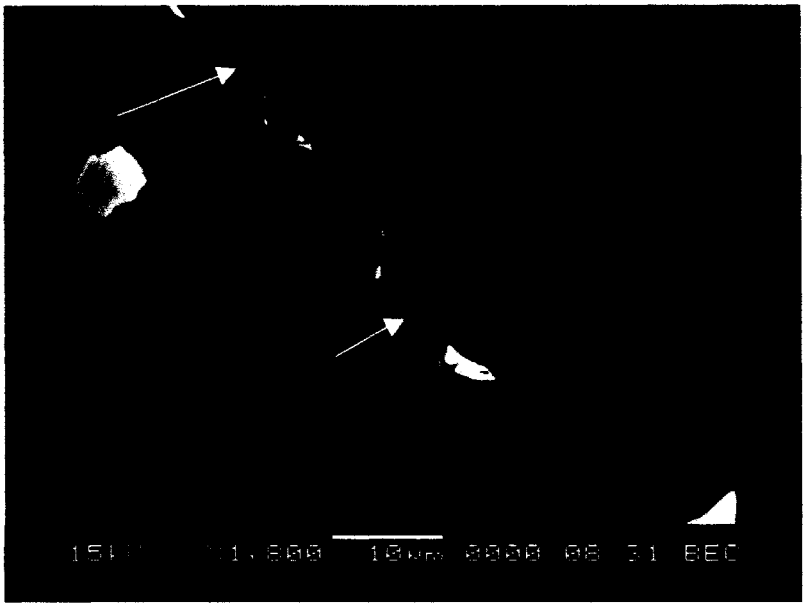

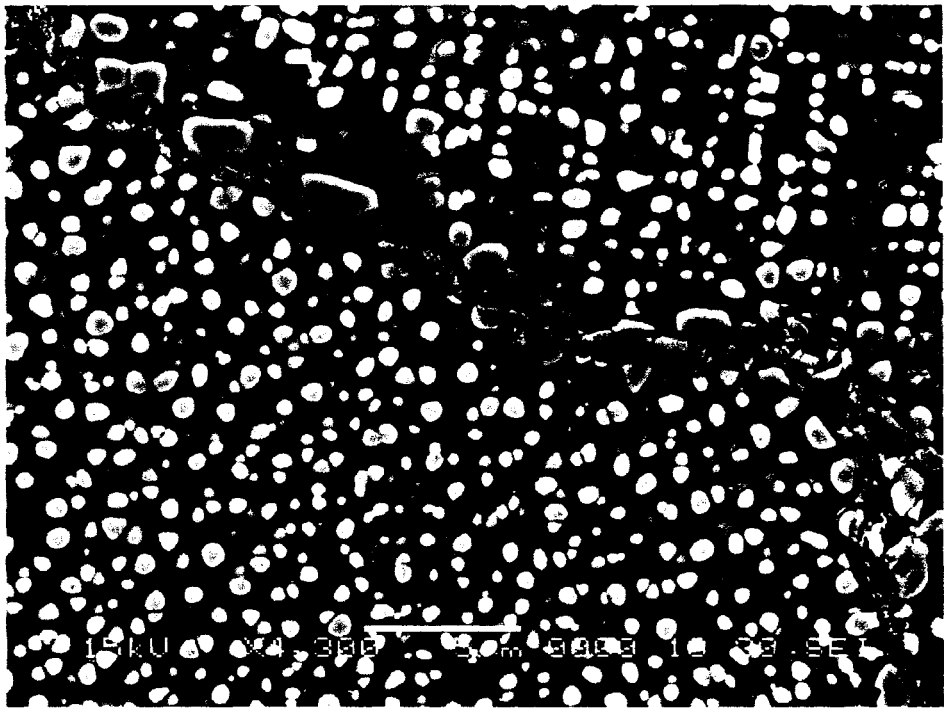

Figure 4.37: SEM (a) backscatter electron image (b) secondary electron image showing presence of re-solidification constituent along HAZ crack.

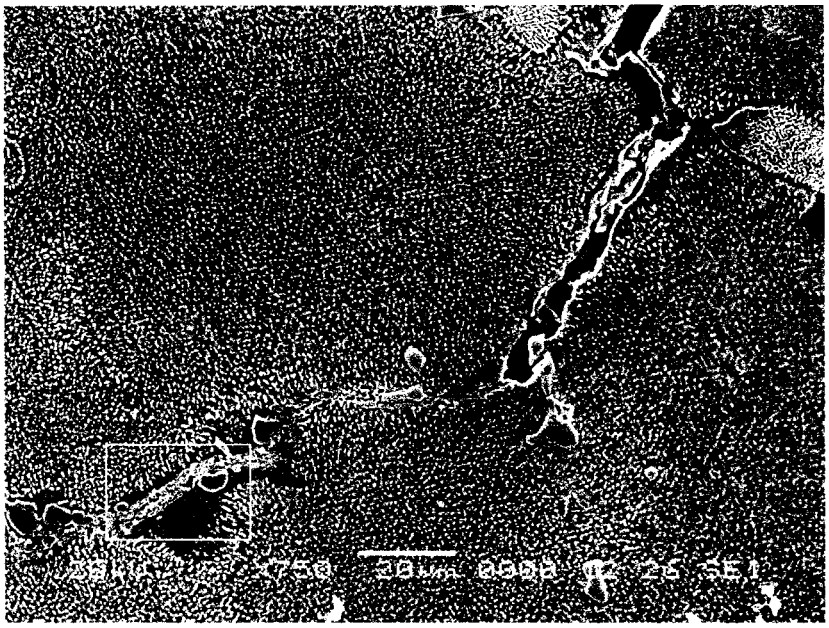

a

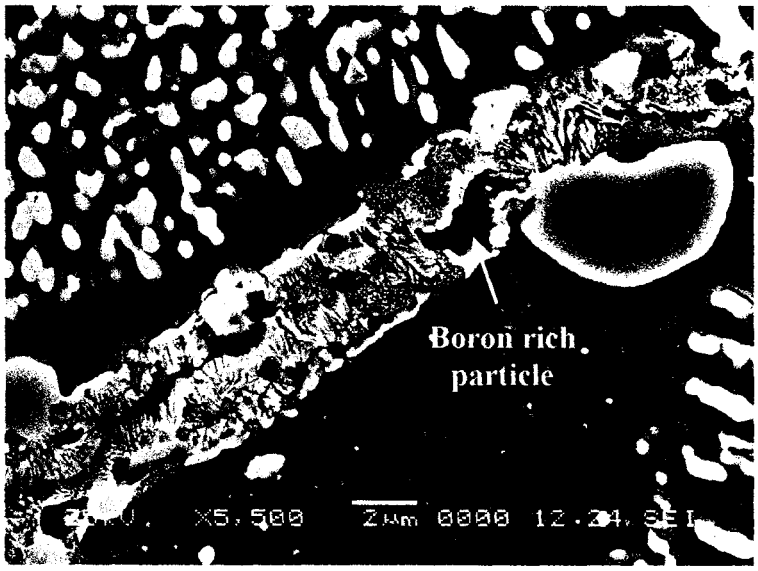

b

Figures 4.38a & b: (a) Thick intergranular re-solidified eutectic within sub-solidus region of the HAZ of a UMT sample (b) Enlarged image of area marked in 3a.

Apart from super-solidus melting which is expected to occur in all weldments due to heating above the equilibrium solidus temperature, sub-solidus liquation of solidification products and of γ' precipitate particles present in the pre-weld alloy, were observed to be contributing to the liquation phenomena and, thus, affecting the HAZ microfissuring. Microstructural variations over a relatively short distance in the weld HAZ owing to a steep temperature gradient, often cause difficulty in a detailed microstructural analysis, especially in relating microstructural changes to the temperatures of transformation. In order to understand the liquation behavior of different microconstituent particles in the alloy, a Gleeble system was used to simulate HAZs microstructure in the two pre-weld heat-treated conditions.

4.3.3 Microstructure of Gleeble Simulated Materials

4.3.3.1 Solution Heat Treated Condition

Figure 4.39 shows SEM micrograph of a ST sample rapidly heated to 1135°C, held for 0.5s and then water quenched. As can be seen from the micrograph, the secondary γ' particles observed in the ST specimens (figure 4.17) before thermal cycling have apparently dissolved completely during this thermal cycle. The primary cuboidal γ' particles, discrete coarse grain boundary γ' and other solidification constituents appeared to be not affected by the thermal cycle. Samples simulated at 1150°C showed similar microstructures to that observed in the specimen heated to 1135°C except that isolated melting was observed in regions ahead of some γ-γ' eutectic, as shown in figure 4.40. SEM/EDS composition analysis of resolidified constituents within the isolated regions showed the presence of Ni- Zr intermetallic phase and Cr-Mo rich boride particles

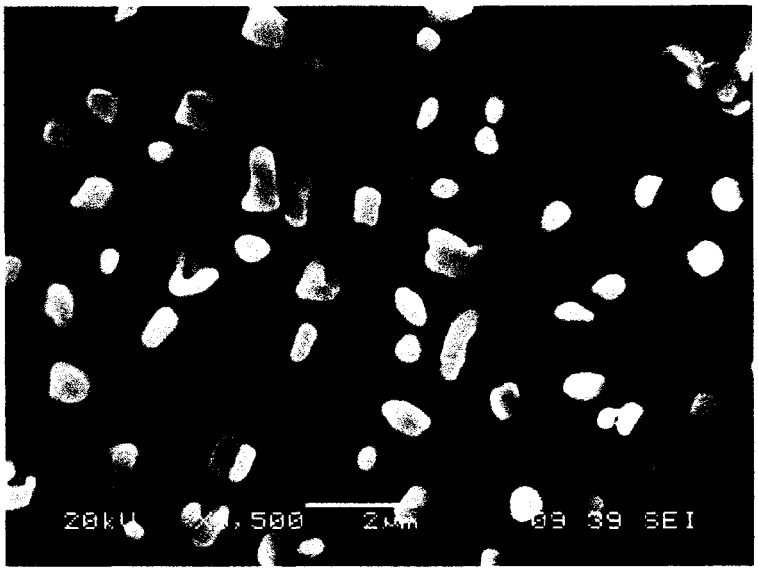

Figure 4.39: SEM image of ST Gleeble simulated sample at 1135°C and held for 0.5s.

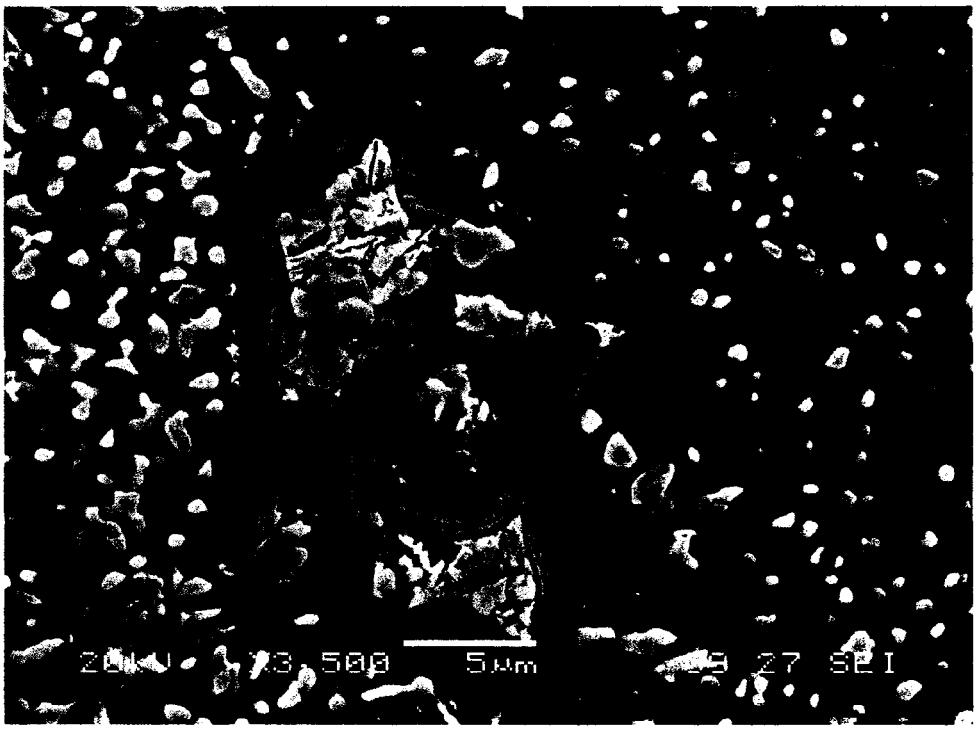

Figure 4.40: SEM image of ST Gleeble simulated sample at 1150°C and held for 0.5s.

(figure 4.41). On increasing the simulation temperature to 1165°C, a differentially etching thin film connecting the intergranular γ' was observed to have formed along the grain boundaries (figure 4.42). In addition, differentially etching seams were observed around the intragranular γ' precipitate particles, eutectic γ' and the discontinuously precipitated γ' particles. Quenching cracks were observed to have propagated preferentially along the continuous thin intergranular film along some grain boundary regions (figure 4.42b &C). Energy dispersive x-ray line scan across the thin film showed that it was enriched in γ' forming elements Al and Ti and depleted in essentially matrix elements Cr and Co (figure 4.43). In samples simulated at 1180°C clear evidence of liquation of intragranular and intergranular γ' particles was observed. The grain boundaries in this sample showed features that are typical of liquid film migration (LFM) process. Segments of these boundaries exhibited curvature that changed sign at several points along the boundary facets resulting in a zig-zag grain boundary pattern as shown in figure 4.43. In optical micrograph the concave side of these boundary segments appeared to be differentially etched (figure 4.44). When examined at higher magnification in SEM, they were found to be essentially precipitate-free solid solution phase as compared to the adjacent precipitate bearing grains (figure 4.45). Energy dispersive x-ray line scans across the grain matrix and this newly formed region showed noticeable enrichment of the newly formed region with γ' forming elements Al, Nb and Ta as compared to the grain matrix (figure 4.46). A closer examination of both the frontal and rear interfaces of the freshly formed regions showed intimate connection with the liquid film produced by constitutional liquation of intragranular γ' precipitate

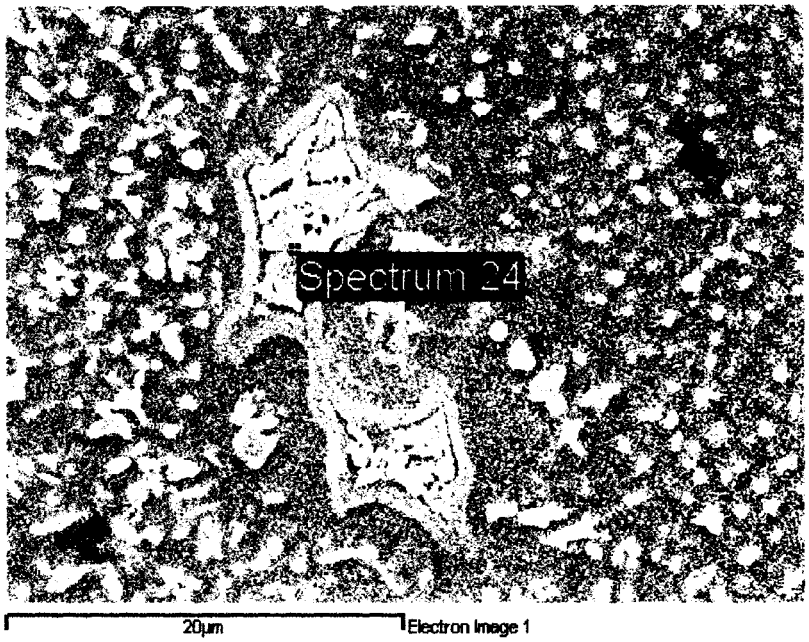

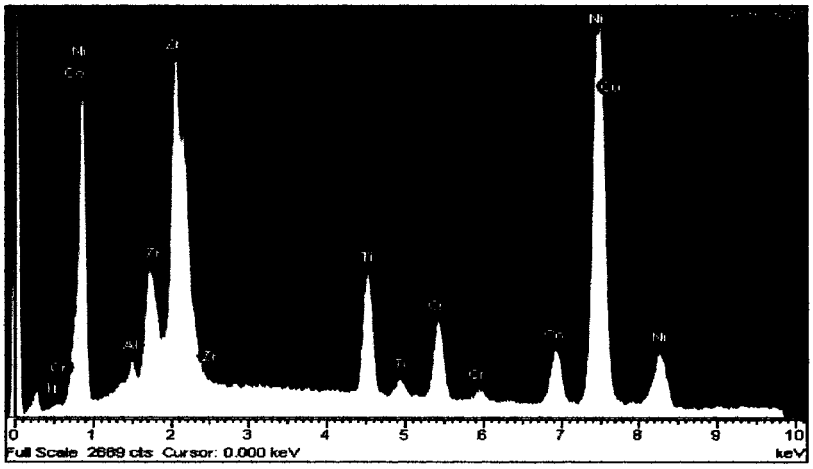

Figure 4.41: SEM/EDS of resolidified constituent particle in ST Gleeble simulated sample at 1165°C and held for 0.5s

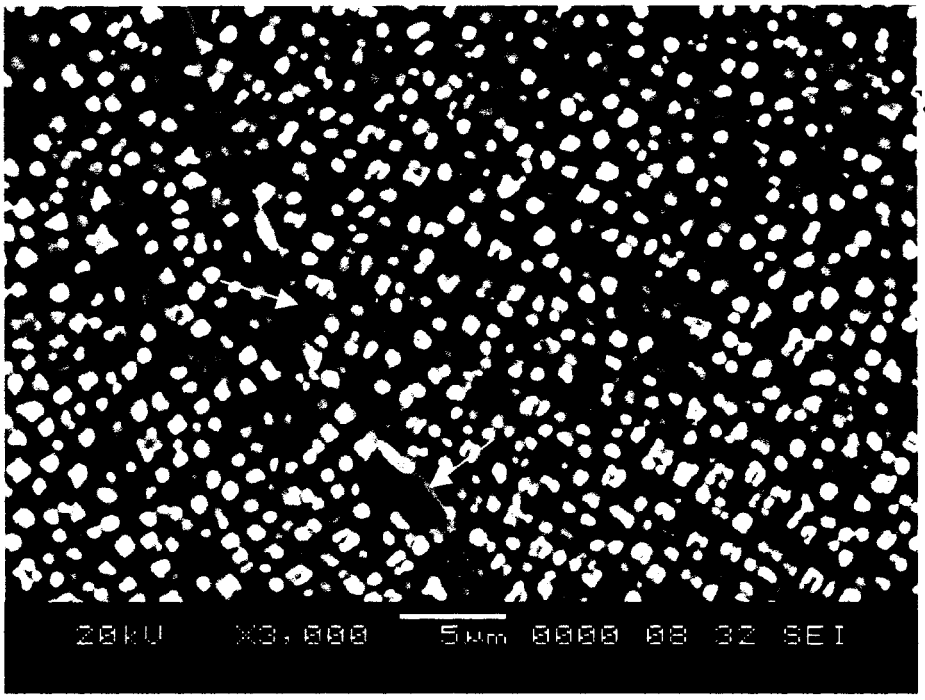

a

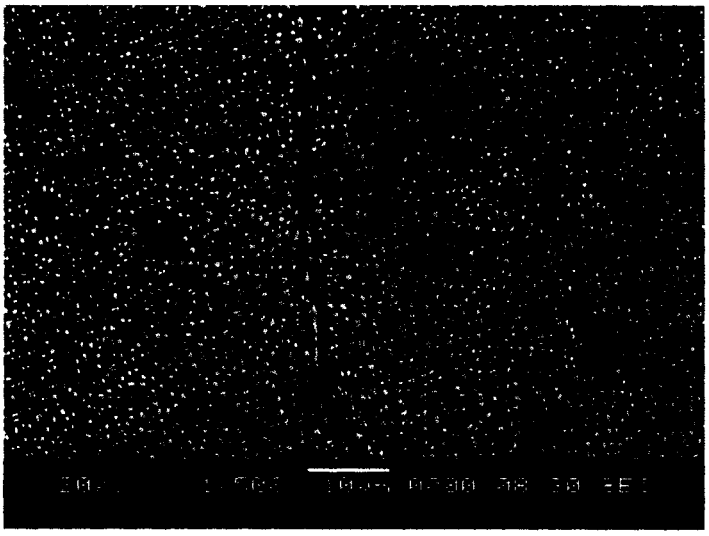

b

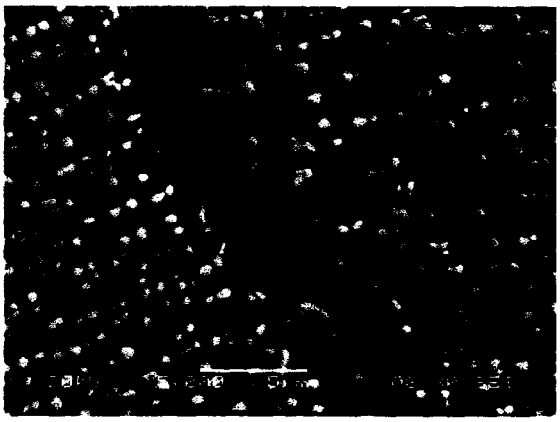

c

Figure 4.42: ST Gleeble simulated sample at 1165°C and held for 0.5s

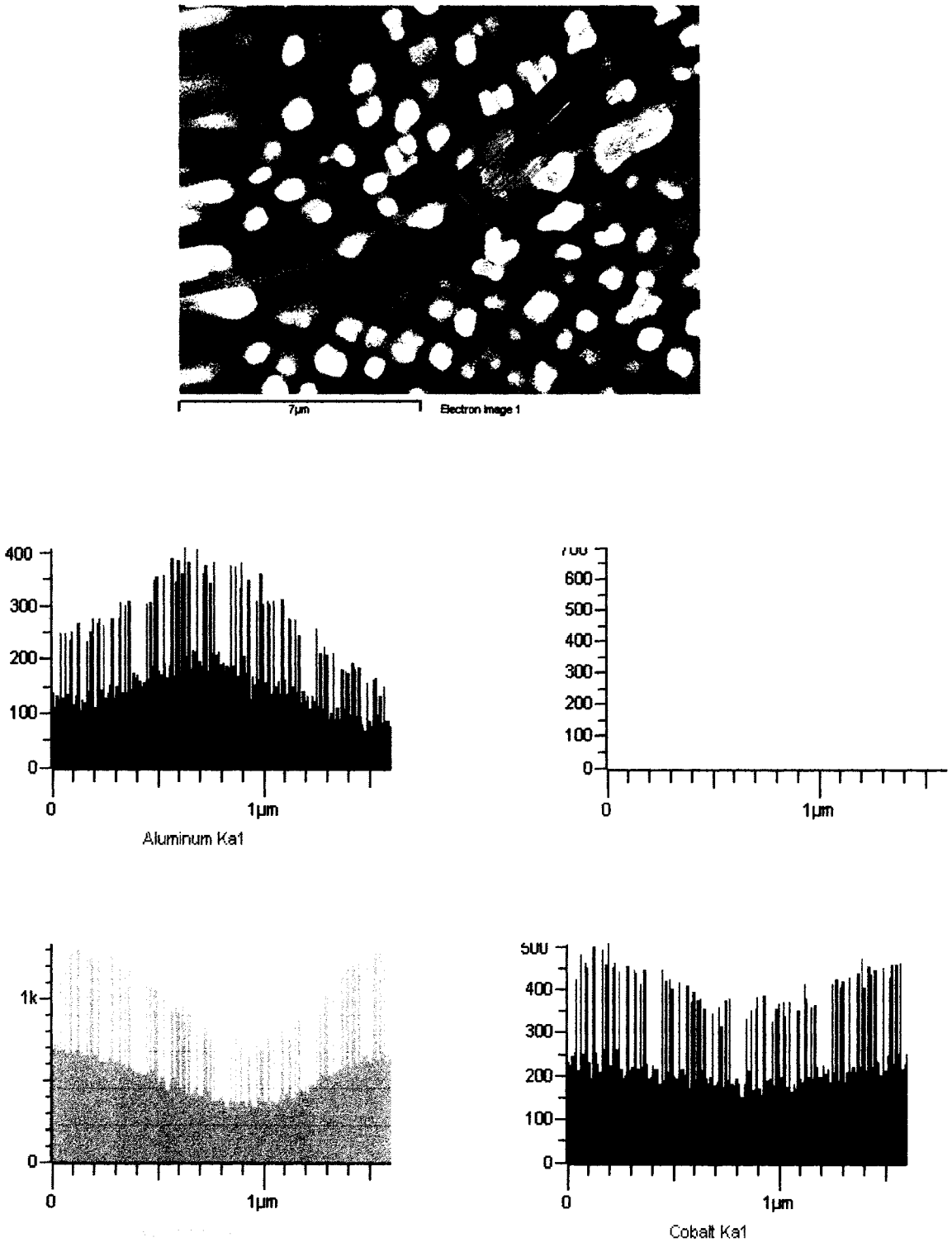

Figure 4.43: SEM/EDS Spectrum of intergranular thin film in ST simulated sample at 1165°C and held for 0.5s

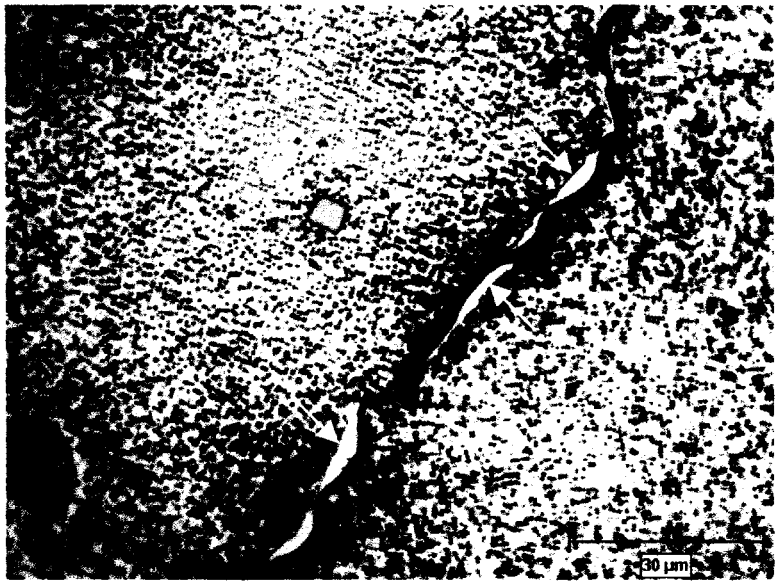

Figure 4.44: Optical micrograph of simulated HAZ at 1180°C for 0.5s showing migration zones

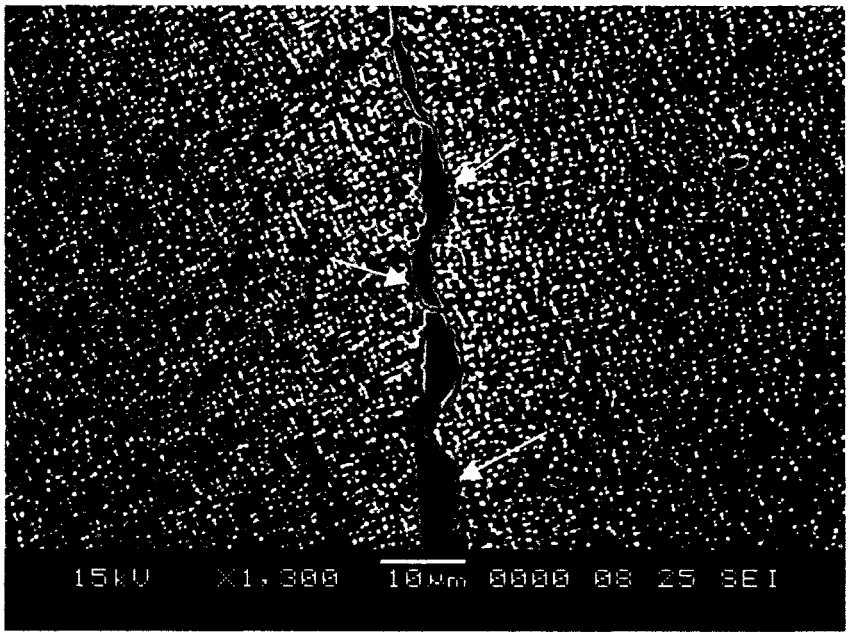

Figure 4.45: SEM micrograph of simulated HAZ at 1180°C for 0.5s showing crack ahead of migration zones

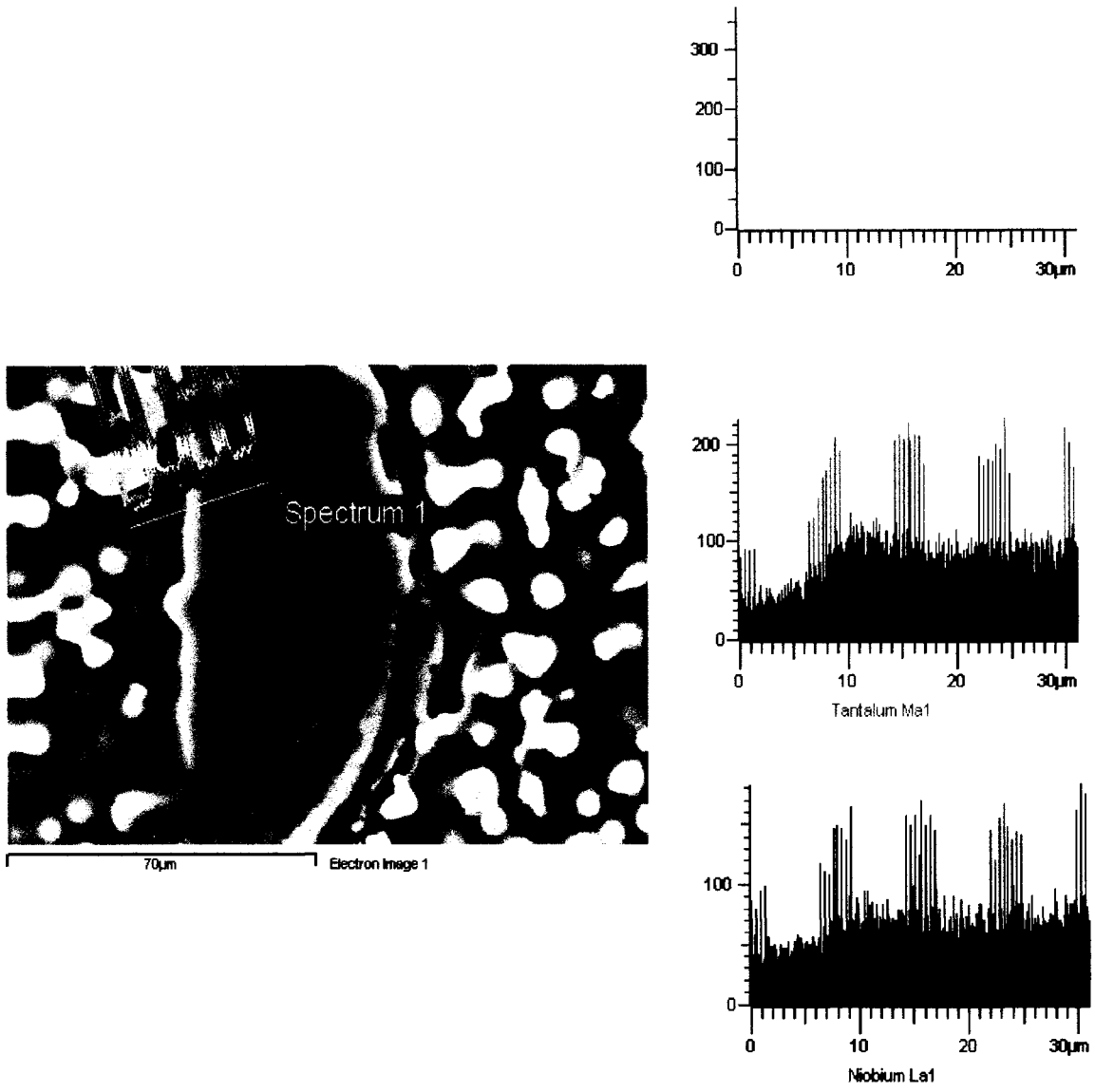

Figure 4.46: EDS line scan grain matrix and across migration zone in 1180°C for 0.5s sample

particles (figure 4.47). Constitutional liquation of γ' particles in IN 738 will be discussed later in section 4.3.4.2. Eutectic constituents were observed ahead of these newly formed zones, indicating a prior presence of liquid film. Quench- cracks in this sample were observed to have formed preferentially along liquated regions ahead of the freshly formed and alloyed zones (figures 4.44, 4.45 & 4.47). These observations suggest that the intergranular liquid film produced by constitutional liquation of γ' particles migrated during the thermal cycle leaving behind the newly formed alloyed regions.

In order to confirm the nature of the thin continuous grain boundary film observed in the sample held at 1165°C for 0.5s, another sample was held for 4s at 1165°C and then water quenched. The microstructure of this sample showed extensive intragranular γ' liquation with the grain boundaries exhibiting the aforementioned LFM features (figure 4.48). This indicates that the thin film observed after 0.5s hold was due mainly to constitutional liquation of grain boundary γ' particles and a 4s hold resulted in complete liquation of these intergranular γ' along with substantial liquation of the intragranular γ' particles. When the simulation temperature was increased to 1200°C, microstructures similar to those observed in 1180°C samples were observed in the samples with an increase in the extent of intragranular γ' liquation. Indication of complete liquation of some intragranular γ' particles was observed in this sample as shown in figure 4.49. In samples simulated at 1225°C, almost complete liquation of all the γ' precipitates occurred including the eutectic γ' phase. Increase in temperature up to 1225°C also produced a corresponding increase in the extent of LFM process. Liquation of M_2SC sulphocarbide particles and some MC carbides were also observed to be occurring in 1225°C sample

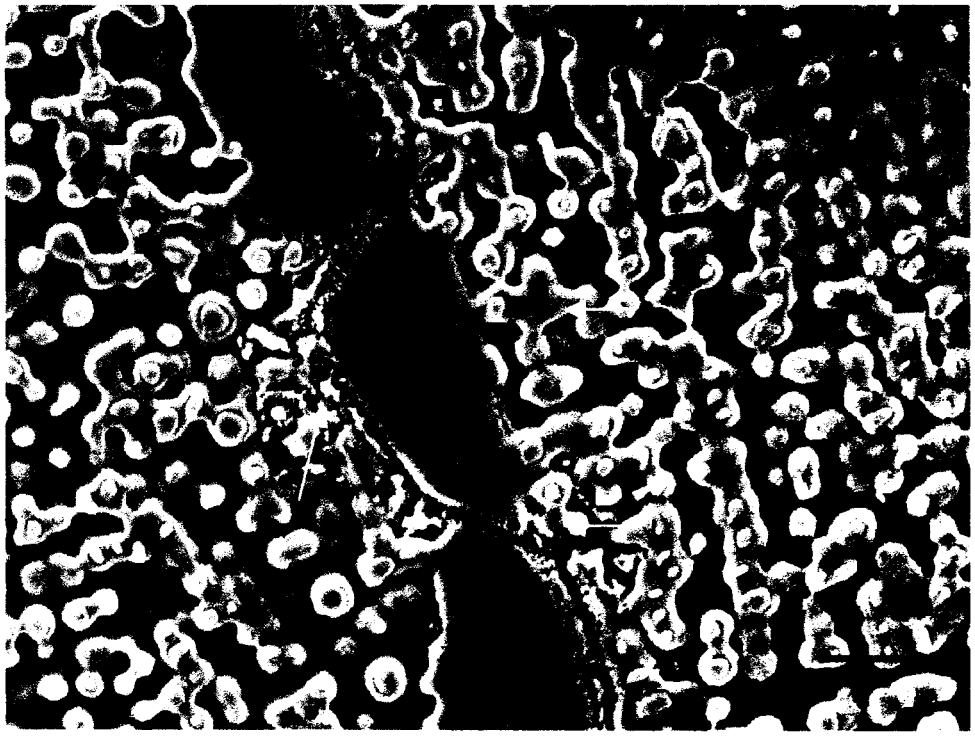

Figure 4.47: ST Gleeble simulated HAZ at 1180°C for 0.5s showing migration zones

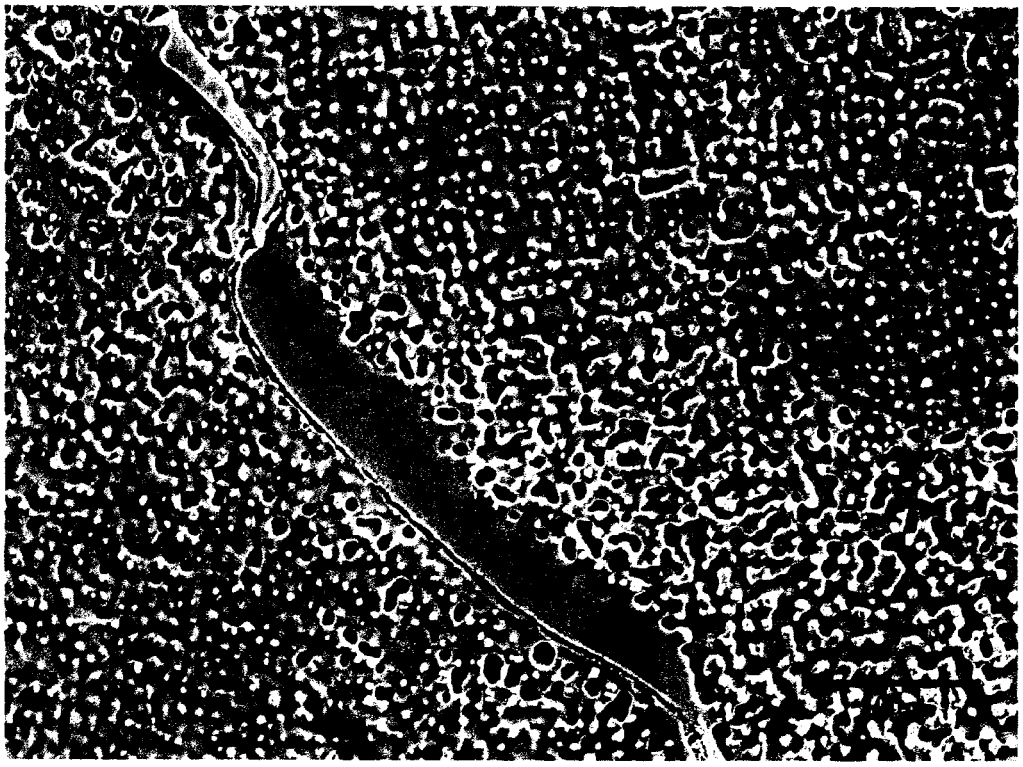

Figure 4.48: ST Gleeble simulated HAZ at 1165°C for 4s

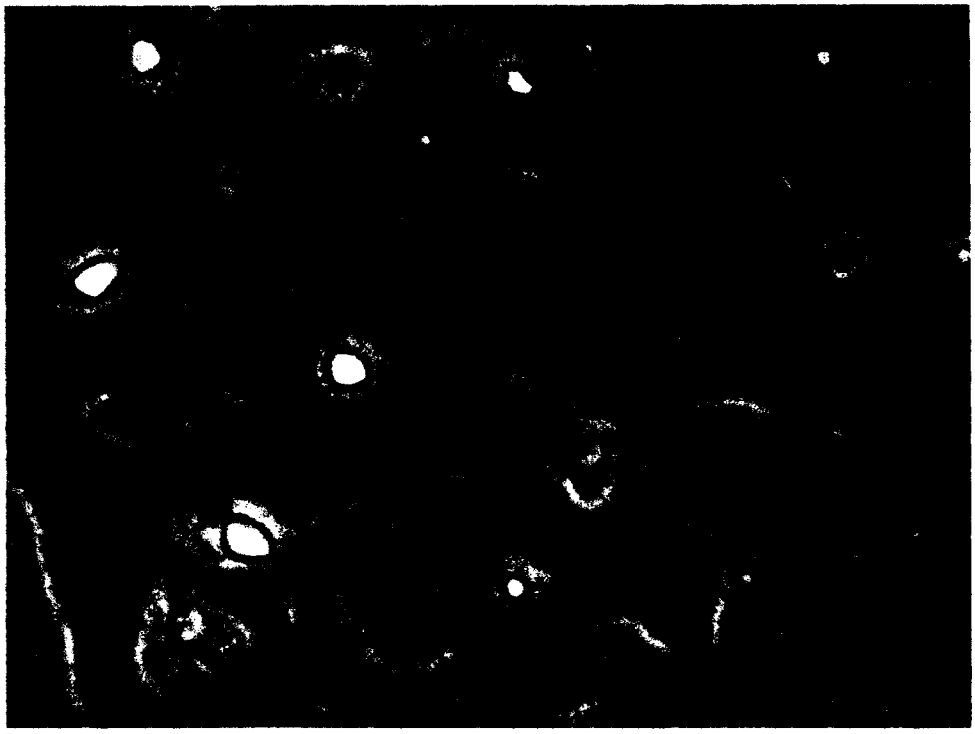

Figure 4.49: ST Gleeble simulated HAZ at 1200°C for 0.5s

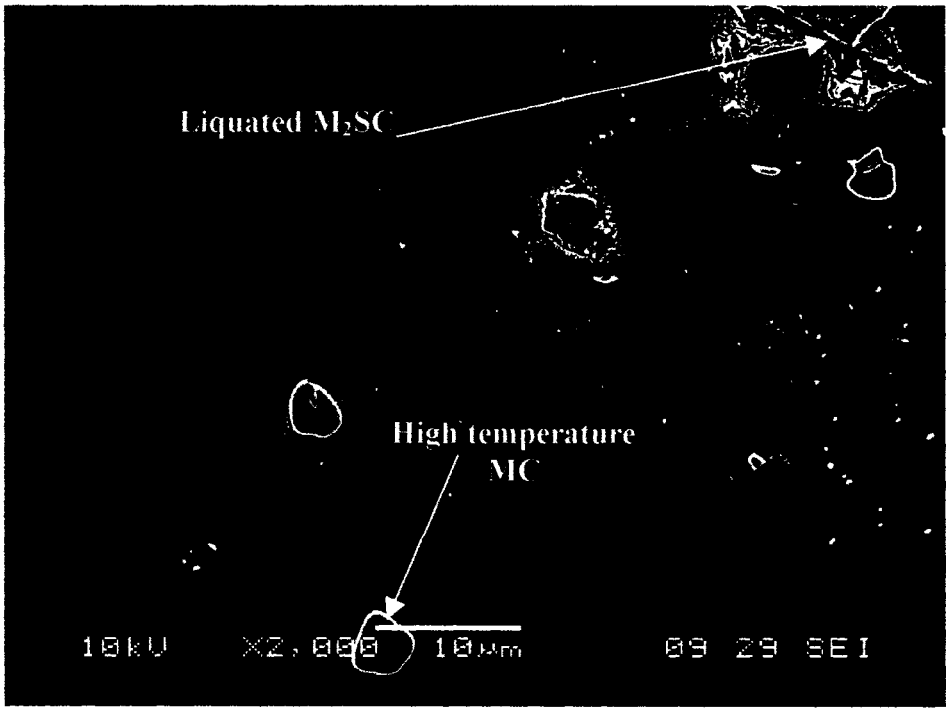

Figure 4.50: ST Gleeble simulated HAZ at 1225°C for 0.5s

(figure 4.50). Indication of liquation was observed around the low temperature MC carbides, while the high temperature particles appeared generally unaffected by the 1225°C thermal cycle (figure 4.50). On further increasing the simulation temperature to 1245°C, which is above the alloys equilibrium solidus temperature, a wider liquation of the bulk microstructure with coarser resolidified product occurred including liquation of some high temperature MC carbides (figure 4.51).

4.3.3.2 University of Manitoba Heat Treated Condition

The microstructure of a UMT sample heated to 1135°C and held for 0.5s followed by water quenching showed that the γ' particles and other solidification constituents in the sample appeared not to be affected by the thermal cycle. In samples simulated at 1150°C, substantial amount of liquation occurred in a continuous fashion along the interface of γ-γ' eutectic and adjoining grain boundaries, as well as at the interface of MC carbides associated with these regions (figure 4.52). SEM/EDS chemical composition analysis of the resolidified constituents showed the presence of Cr-Mo rich boride particles (figure 4.54). On increasing the simulation temperature to 1165°C, an increase in the intergranular liquation with LFM features were observed (figure 4.53). Boride particles were observed to form as part of the eutectic constituent ahead of grain boundary liquid film migration zone, as shown in figure 4.53. Liquation of intragranular γ' particles was also observed in this sample. Further increase in the simulation temperature to 1180°C, 1200°C, 1225°C and 1245°C resulted in concomitant increase in liquation broadening of the grain boundary regions involving liquation of γ' particles, MC carbides and M_2SC sulphocarbide particles.

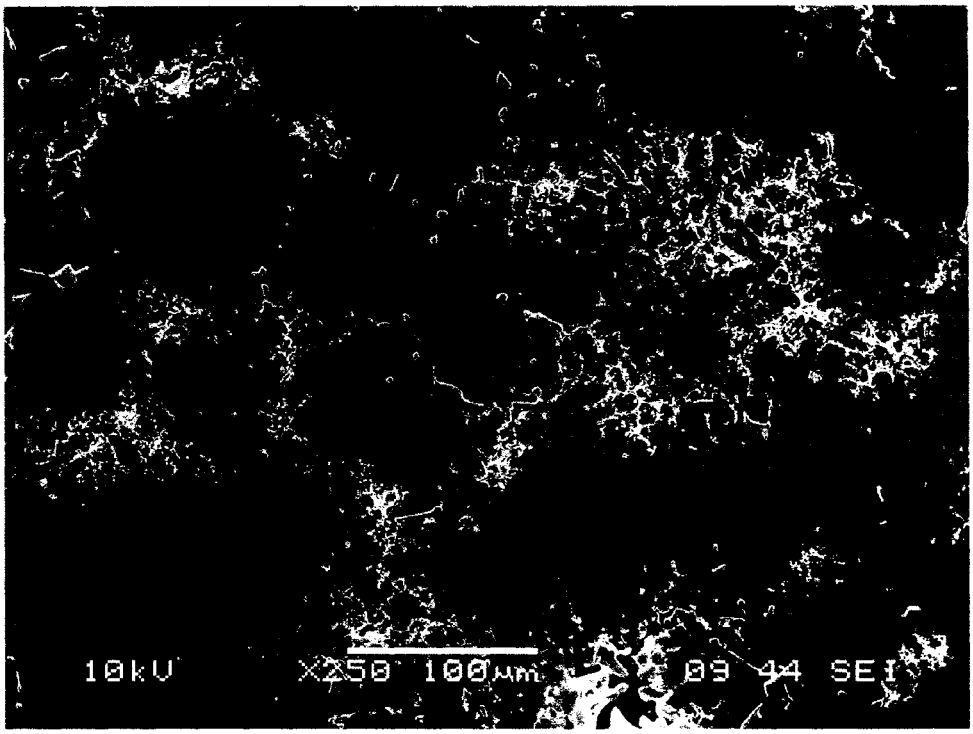

Figure 4.51: ST Gleeble simulated HAZ at 1245°C for 0.5s

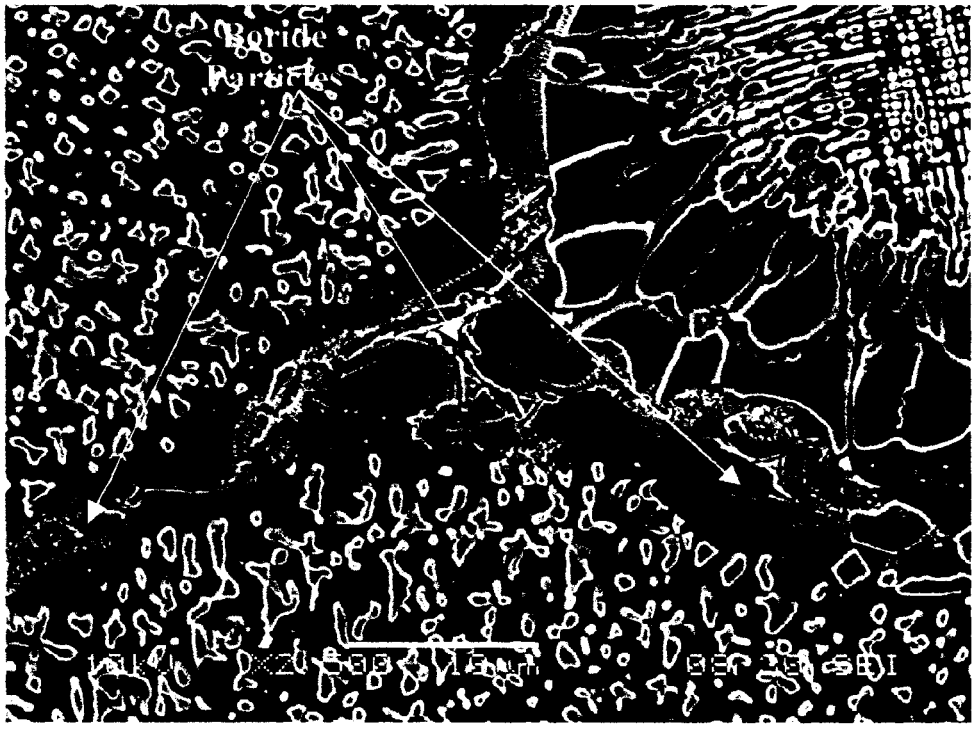

Figure 4.52a: UMT Gleeble simulated HAZ at 1180°C for 0.5s

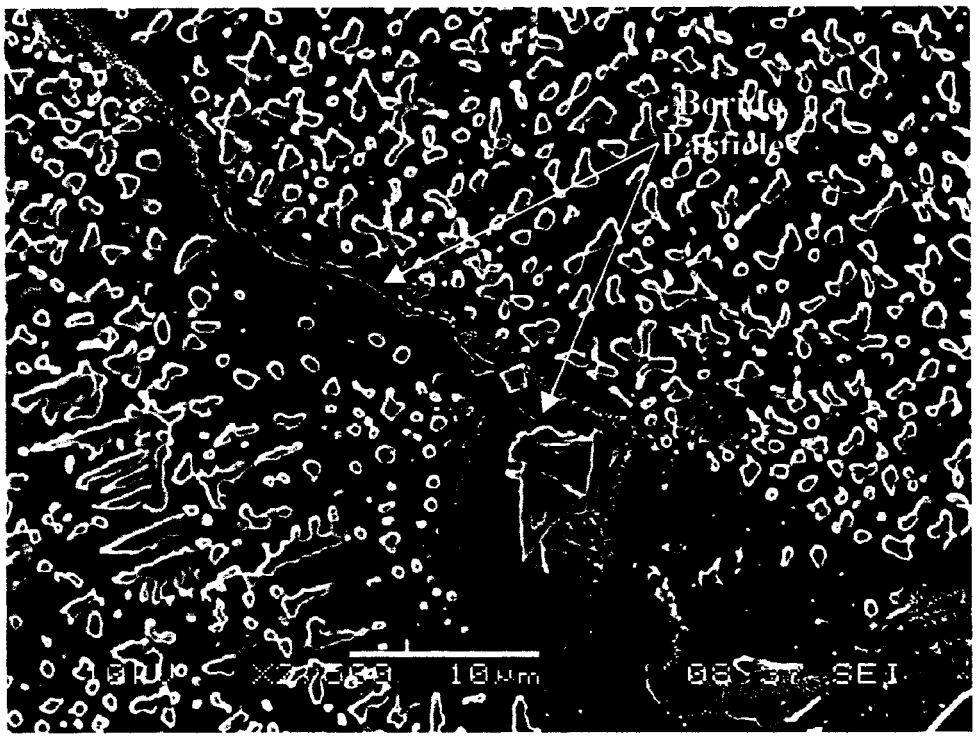

Figure 4.52b: UMT Gleeble simulated HAZ at 1150°C for 0.5s

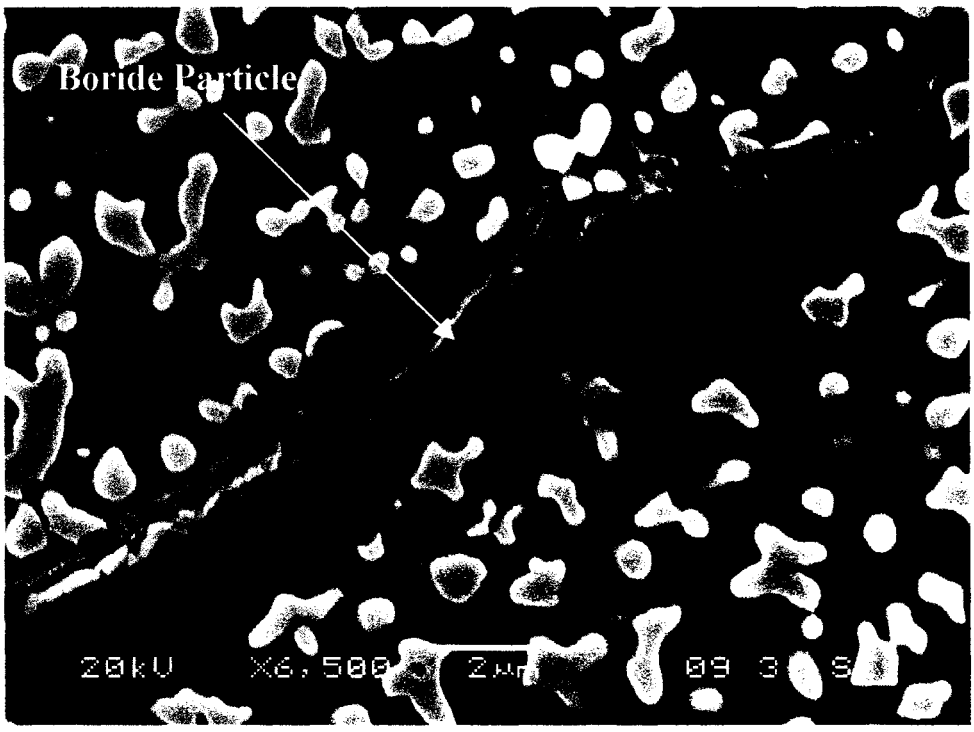

Figure 4.53: UMT Gleeble simulated HAZ at 1165°C for 0.5s

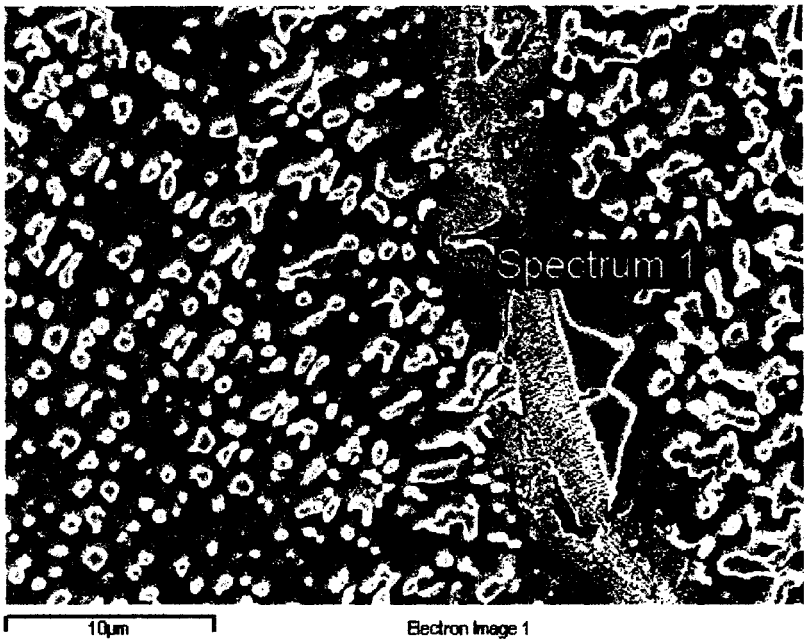

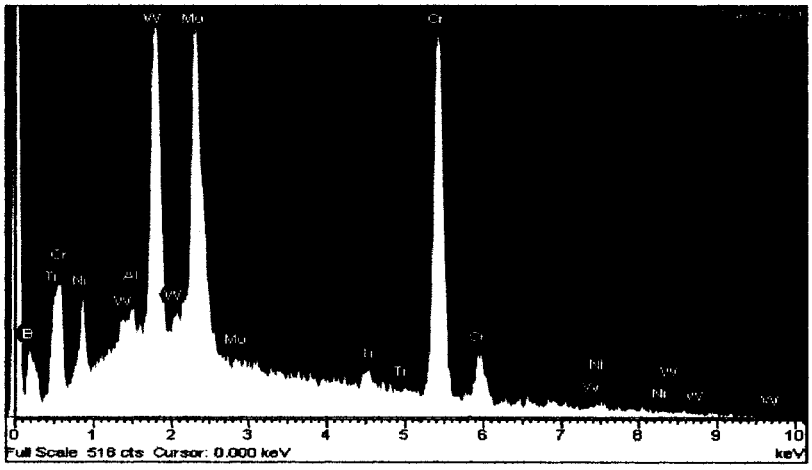

Figure 4.54: SEM/EDS showing boron peak in a resolidified constituent particle in UMT sample simulated 1150°C for 0.5s

4.3.3.3 Comparison of Microstructural Response of ST and UMT Samples

A significant difference in microstructural response of ST and UMT samples to the Gleeble thermal simulation, primarily in terms of amount and distribution of intergranular liquid was observed. This can be recognized by comparing the microstructure of the two materials simulated at 1150°C and 1165°C (compare Figures 4.42 and 4.52). It can be seen that while melting occurred mainly in isolated regions in the vicinity of γ-γ' eutectic colonies with apparently no grain boundary liquation in 1150°C ST sample, more liquation distributed in a continuous fashion along the interfaces of γ-γ' eutectic, associated MC carbides and adjoining grain boundary regions occurred in the corresponding 1150°C UMT sample. On increasing the simulation temperature to 1165°C, a more extensive grain boundary liquation with LFM features occurred in UMT sample, while only a thin intergranular film was observed in ST sample. After thermal simulation at subsequent temperatures above 1165°C, more grain boundary liquation was observed in the UMT samples at every temperature as compared to ST samples.

4.3.4 Liquation Behavior of Different Microconstituents in the Base Alloy

4.3.4.1 Initial Melting Occurrence

As mentioned earlier, the initial melting in the ST samples occurred in the form of isolated liquated pockets in the vicinity of γ-γ' eutectic. This location is known to be the region in which terminal solidification products, Ni-Zr intermetallic and M_3B_2 boride phases, form in the as-cast alloy. Even though the 1120°C/2hrs heat treatment modified the terminal solidification constituents by dissolving the Ni-Zr intermetallic particles,

these regions can be expected to be still enriched in Zr atoms capable of causing eutectic melting in conjunction with M_3B_2 boride during heating. Analysis of resolidified product in the 1150°C ST sample seems to support this idea, as boron and Zr rich particles were detected. It has been reported [195] that in boron bearing ($\gamma + \gamma'$) nickel aluminide alloy IC-218, an annealing heat treatment that dissolved Zr-rich eutectic resulted in incipient melting at a lower temperature during subsequent re-heating.

In UMT samples, the initial melting at 1150°C cannot be attributed only to the eutectic melting of terminal solidification constituents, as extensive liquation was observed to have occurred in a continuous fashion not only in the γ-γ' eutectic colonies but also along grain boundary regions. Such a high degree of grain boundary liquid penetration and relatively large liquid volume at this temperature could be related to the effect of grain boundary segregation of boron during the aging heat treatment of the UMT cycle. As mentioned earlier, boron rich particles were observed in the resolidified product along the liquated grain boundaries in the 1150°C UMT sample. An important microstructural difference in the ST and UMT before thermal cycling was the occurrence of a continuous grain boundary network containing chromium rich particles engloved in γ' phase, often described as $M_{23}C_6$ carbide particles. $M_{23}C_6$ carbides have been reported to form in nickel base superalloys during aging heat treatment (750°C - 1055°C) that follows solution heat treatment by two possible mechanisms [196]. The first mechanism involves precipitation of $M_{23}C_6$ from carbon-supersaturated γ matrix mainly on stacking fault and other lattice defects by the following reaction:

$$\gamma \Leftrightarrow M_{23}C_6 + \gamma$$

The second mechanism involves degeneration of primary MC carbides by reacting with γ matrix to produce $M_{23}C_6$ through the following reaction:

$$\gamma + MC \Leftrightarrow M_{23}C_6 + \gamma'$$

The $M_{23}C_6$ particles are said to be encased in γ' phase, which is the second reaction product. This is similar to the morphology observed in the present work figures 4.19 and 4.20.

The true nature of the Cr rich particles, however, requires some discussion. It has been proposed that the addition of boron to nickel base superalloys can influence the structure and chemistry of grain boundary precipitates [197]. The solid solubility of boron in austenitic γ alloy is very low and Goldschmidt [198] reports, for example, a maximum solubility of 97 ppm at 1125°C in 18% Cr – 15% Ni stainless steel. The solubility decreases rapidly with decreasing temperature becoming less than 30ppm at 900°C. Furthermore, the size of boron atom is larger than common interstitial elements in nickel (e.g. C) and smaller than substitutional elements (Co and Cr). This large size misfit of boron atoms in both substitutional and interstitial sites of austenitic lattice implies that it would be energetically favorable for boron atoms to segregate to loosely packed regions like interfaces. Considering the low solubility of boron and its strong tendency to segregate, it can be expected that boron affects the precipitation behavior at the grain boundaries. The segregation and precipitation of boron particles during heat treatments have been studied by several investigators in nickel and iron base austenitic alloys [107,199-201]. It was found that during isothermal holding at intermediate temperatures, segregation induced precipitation of boron containing particles occurred in alloys containing > 50 wt ppm boron. Kruger et al [199] observed by electron energy loss

spectroscopy analysis, that boron rich $M_{23}X_6$ precipitated in Ni-16Cr-9Fe-0.03C containing 50 ppm of boron during heat treatment at 1100°C for 20mins. Hu et al [201] used neutron-activated microradiography to study boron distribution in a cast nickel base superalloy. They reported that after a 1150°C/4hrs/AC heat treatment of the as-cast material, boron was uniformly distributed within the γ matrix of the alloy, with no evidence of intergranular segregation. However, after subsequent aging at 760°C/16hrs/AC, boron was found to have segregated to the grain boundaries. High concentration of boron was detected in locations containing $M_{23}C_6$ type carbides that precipitated during the aging heat treatment. By performing microchemical and x-ray diffraction analysis on electrolytically extracted carbide residue, they showed that the secondary carbide particles that precipitated along the grain boundaries was $(CrCoMo)_{23}(CB)_6$, containing 0.0011-0.0013 wt% of boron, with lattice parameter of 10.7Å. The increase in lattice parameter compared to pure $M_{23}C_6$, was suggested to be due to more carbon atoms being replaced by larger boron atoms in the $M_{23}(CB)_6$ particles.

It has been known for long that boron can substitute for carbon in $M_{23}C_6$ crystal lattice [202]. Delargy et al [203] reported using field ion microscopy analysis that significant concentration of boron was detected in the $M_{23}C_6$ that precipitated during aging heat treatment of cast IN 939, which is similar in composition to IN 738 alloy. Therefore, based on the aforementioned and considering the relatively high boron concentration of 120 wt ppm in IN 738 used in the present study, it is not unreasonable to expect that boron will segregate to the interface regions (grain boundaries, γ-γ' eutectic interface and MC-γ interface) during the 1025°C/16hrs aging treatment of the UMT heat treatment cycle. The boron segregation might thus cause the surrounding of $M_{23}X_6$ type

particle that is often referred to as $M_{23}C_6$ in IN 738, to be enriched with B atoms and/or the particle itself to contain significant amount of boron. The small size of these particles and the inherent limitations of conventional electron optical techniques made it difficult to carry out satisfactory quantitative SEM/EDS compositional analysis on the particle observed in the present work. An indirect indication of the presence of B in Cr-Mo rich particles is provided by the observation of fine γ' particles in the surrounding of a network containing Cr-Mo rich particles (figure 4.20b) as it has been suggested that boron stabilizes fine γ' precipitates in nickel base superalloy [204]. By SEM/EDS analysis, boron peak in some of these particles was detected as shown in figure 4.55.

It has been mentioned [196] that the reaction of MC carbides producing secondary $M_{23}C_6$ carbide particles i.e.

$$\gamma + MC \Leftrightarrow M_{23}C_6 + \gamma'$$

can be reversible, suggesting that pure $M_{23}C_6$ may dissolve by solid-state reaction upon heating to a sufficiently high temperature. Similarly, Owczarski et al [5] in their study of weldability of nickel base superalloys indicated that $M_{23}C_6$ particles would undergo solid-state reaction well below the solidus temperature and would not liquate during welding. In the present work, after rapidly heating to 1150°C and holding for 0.5s followed by water quenching, the grain boundary network of $M_{23}X_6$ was no longer observed in the UMT samples. Instead, resolidified constituents were observed along the grain boundaries and boron was detected in some of the constituent particles. Apart from being a melting point depressant in nickel, boron is known to enhance liquid wetting of grain boundary by lowering the solid-liquid interfacial energy. In this context, the extensive grain boundary liquation in UMT sample simulated at 1150°C appears to be due to boron

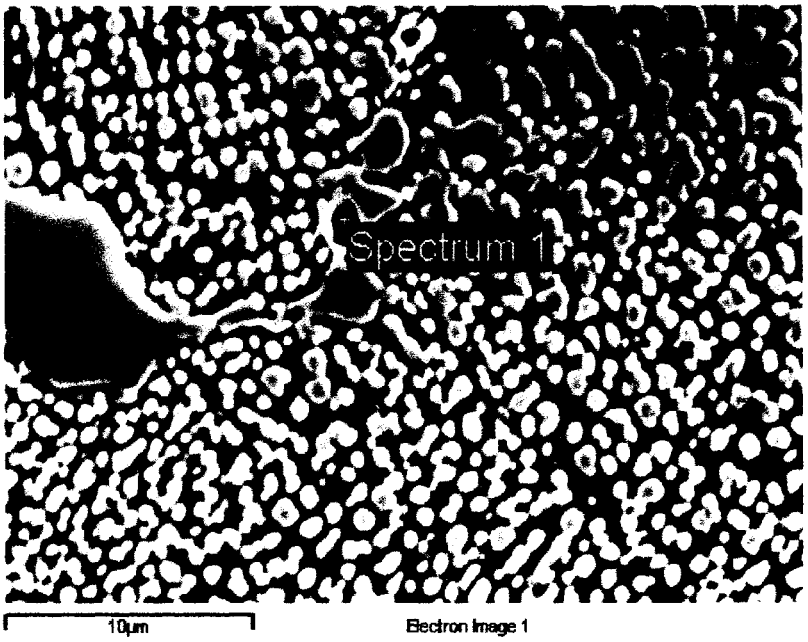

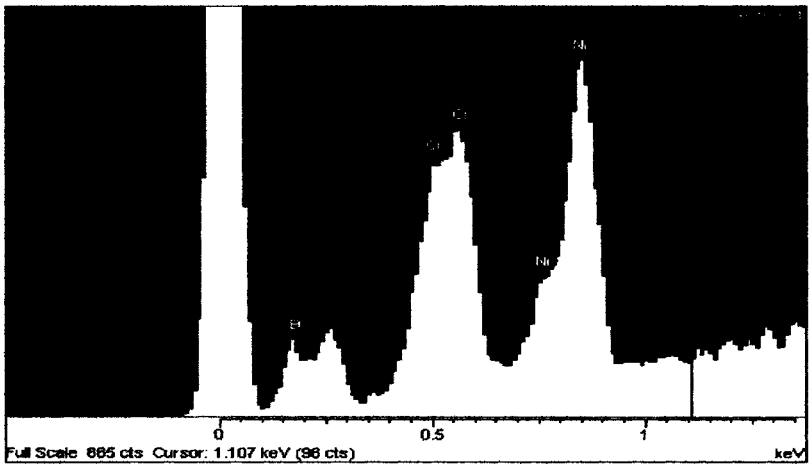

Figure 4.55: SEM/EDS showing boron peak in Cr rich particle of the network.

segregation at interfaces in this alloy during the UMT aging treatment. Interface segregation of boron during heat treatment of IN 718 has been reported to produce low temperature grain boundary liquation in the HAZs during welding [205].

4.3.4.2 Constitutional Liquation of γ' Phase

A very intriguing phenomenon observed in the present investigation was that apart from incipient melting in this alloy due to B and Zr enrichment, γ' precipitate particles, which are the main strengthening phase of the alloy, liquated and contributed significantly to the HAZ microfissuring (fig. 4.56). Until now, the main reported mechanism through which γ' precipitates contribute to poor weldability of nickel base superalloys has basically been due to their rapid re-precipitation creating large shrinkage stresses and inhomogeneous strain distribution during weld cooling, and due to contraction stresses due to their precipitation during post weld heat treatment. Nevertheless, it has been found that an increase in concentration of Al and Ti (main γ' forming elements) in nickel base superalloy, lowers the solidus as well as the liquidus temperature. This suggests that local enrichment of the γ' forming elements could lower the melting temperature, resulting in constitutional liquation. Constitutional liquation of carbides, borides and sulphides has been reasonably well discussed in other nickel base superalloy weldments [53, 99, 103, 4], but constitutional liquation of γ' precipitates in any alloy system has not been reported by other investigators.

The basic requirement for the occurrence of constitutional liquation of an intermetallic compound A_xB_y in an alloy is the existence of A_xB_y particles on heating of the alloy to temperatures equal to or above its eutectic temperature [99]. Consequently,

the susceptibility of an A_xB_y type second phase to constitutional liquation in the weld HAZ must primarily be related to its solid-state dissolution behavior, as a complete dissolution prior to reaching the eutectic temperature will preclude the occurrence of liquation. Solid-state dissolution of γ' and its liquation behavior is discussed in more detail in section 4.4 of this thesis, and only a brief comment about it will be made here. The terminal eutectic temperature in IN 718 above which constitutional liquation of A_2B-type Laves phase and NbC particles were observed was found to correspond to the terminal reaction peak temperature during thermal analysis [206]. In IN 738, the temperature of γ-γ' eutectic reaction occurring towards the end of solidification process was determined to be around 1198°C by differential thermal analysis [137], though Rosenthal et al [135] later reported that the eutectic reaction takes place over a range of temperature which could be as low as below 1180°C. What is evident is that the γ-γ' eutectic temperature is below 1200°C in this alloy, which is below the quoted equilibrium solidus temperature of IN 738, which is around 1232°C. During welding, dissolution behavior of γ' precipitates is expected to deviate from equilibrium due to rapid thermal cycling involved. Depending upon the initial particle size and heating rate, limited integrated time available for homogenisation by diffusion process during rapid heating of welding can cause γ' precipitate particles to survive to temperatures well above their solvus and the γ-γ' eutectic reaction temperatures of the alloy. In a differential thermal analysis of nickel base superalloys, Sponseller [187] reported that the temperature for complete dissolution of γ' particles depended on the heating rate (0.03 – 0.16°C/S), with an increase in complete dissolution temperature with increasing heating rate. In fusion welding process, like the one used in the present work, typical heating rates normally

exceeds 150°C/s and as such, variations in dissolution behavior of γ' particles can be expected to depend on the particle's location and size, with the possibility of some coarse particles remaining undissolved above 1200°C resulting in their constitutional liquation.

It may be argued that liquation of intergranular γ' particles can not be used to conclude the occurrence of constitutional liquation of the precipitate, considering that other liquation mechanisms may also be operative at grain boundaries, such as constitutional liquation of MC type carbides and possibly liquation due to segregation of low melting point depressing elements like boron. Consequently intragranular particles located up to 15μm away from HAZ grain boundaries and distinctly separated from other liquating phases were closely examined. Evidence of γ/γ' interface liquation was observed not only along the grain boundaries but more importantly within the grains of the HAZ (figure 4.57). The solute rich liquid pool adjacent to liquating particles is expected to commence solidification first as gamma and then on reaching the eutectic temperature transform to γ-γ' eutectic product. On further cooling, γ' could precipitate out of the newly formed supersaturated γ phase resulting in a resolidified region consisting of coarser γ' precipitate versus adjacent unmelted matrix and fine γ-γ' eutectic protruding into the last area to solidify. The microstructure that forms depends on volume and composition of liquid present at the peak temperature. These two types of resolidified morphology were observed in this work with the intragranular particles having fine resolidified morphology. Higher magnification SEM images (figure 4.57) suggested that some of these resolidified regions contain fine γ-γ' eutectic which formed at the terminal stage of the solidification process. This suggestion was further supported in instances where a complete liquation of the intragranular precipitates occurred. Fine γ-γ' eutectic

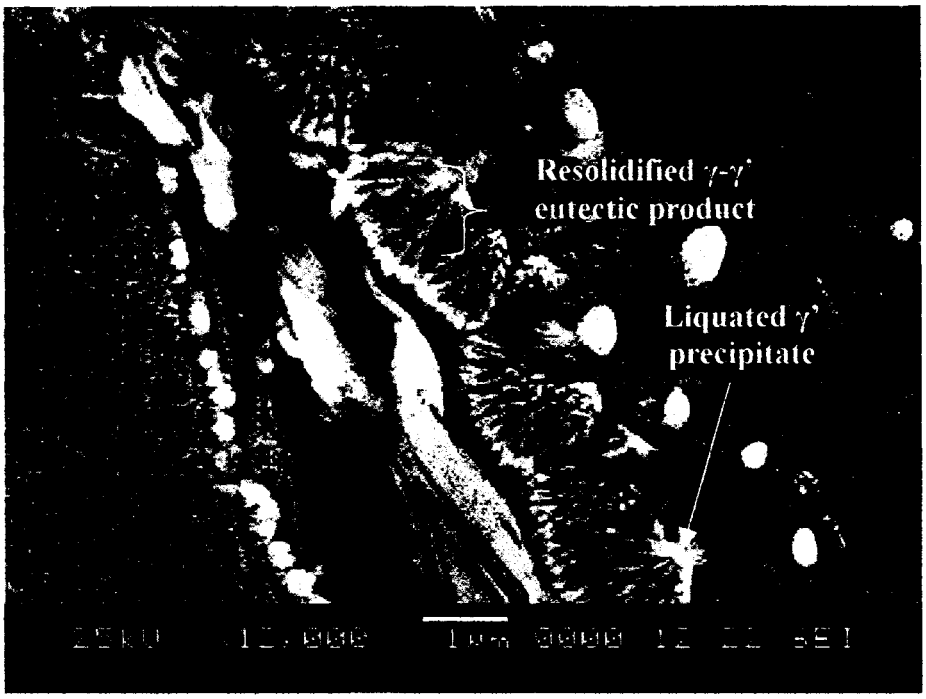

Figure 4.56: Liquated γ' particles along crack path in weld HAZ

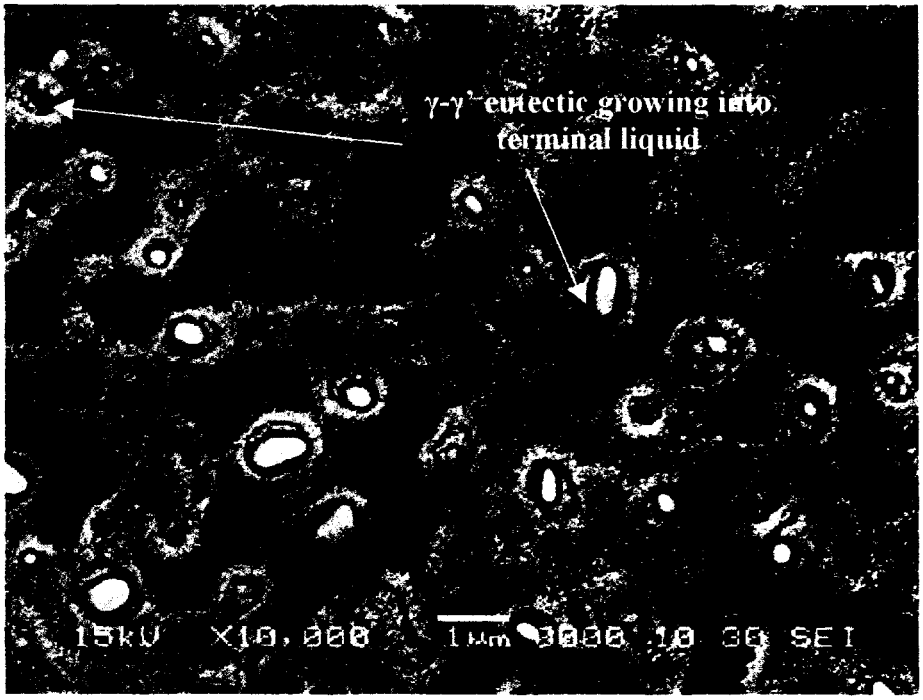

Figure 4.57: Liquation of Intragranular γ' precipitates

colonies were oriented with their "crown" region protruding into the last liquid to solidify, which is the typical mode of formation of γ-γ' eutectic [140]. An additional indication of γ/γ' interface melting was the observation of what appeared to be voids or cavities in the immediate vicinity of extensively liquated intragranular particles (figure 4.57). It is known that voids and cavities often form in melted and resolidified regions in superalloys owing to the expansion and contraction accompanying solidification.

Similarly, microstructural examination showed evidence of liquation at the interfaces of intragranular γ' particles of sample rapidly heated by Gleeble simulation system to 1180°C as compared to sample heated to lower peak temperature of 1135°C (figures 4.39 & 4.47). It is to be noted that atom probe field ion microscopy (APFIM) study of nickel base superalloys showed that there was no boron segregation to the interfaces of intragranular γ' particles [207]. Consequently, the occurrence of liquid film surrounding the intragranular γ' precipitates which are away from other liquating phases can only be reasonably attributed to constitutional liquation of the intermetallic particles [99]. It was observed that the closer these particles were to the fusion line, where they experienced a higher peak temperature, the more pronounced the liquation. This indicates that the coarse particles that did not completely dissolve before reaching the eutectic temperature constitutionally liquated, with the extent of liquation increasing in the HAZ regions which experienced higher temperatures i.e. regions closer to the fusion boundary. It should be mentioned that the γ-γ' eutectic in the alloy, which formed during ingot solidification and was also observed to liquate in the HAZ, is a non-equilibrium solidification product and as such can be removed by appropriate pre-weld thermal treatment. In contrast, however, the γ' precipitates are an essential strengthening phase

which are considered better to be in coarsened form in the pre-weld material to induce enhanced ductility in it so that it can withstand welding strains better. The detection of constitutional liquation of γ' precipitates in this alloy is considered crucial and significant due to it's inevitable presence as the main strengthening phase, high volume fraction and the lower eutectic temperature relative to the alloy's equilibrium solidus. Apart from contributing to the volume of grain boundary liquid, constitutional liquation of γ' phase in this alloy will also influence the nature of melting at super-solidus temperatures by pre-establishing local heterogeneities and altering reaction kinetics during subsequent heating.

4.3.4.3 Liquation of M_2SC Sulphocarbide and MC-Type Carbides

The M_2SC sulphocarbide particles in the alloy liquated in the HAZ of welded samples (figure 4.58) and in the Gleeble samples simulated at 1225°C and 1245°C. Abrupt decomposition of these particles by rapid heating could release S atoms, which is known as a melting point depressant in nickel alloys, thereby lowering local melting temperature of the surrounding area. TiS particles have been found to be a source of intergranular liquation in HAZ of 18-Ni Maraging steel weld [99].

Constitutional liquation of MC type carbide particles have been recognized as one of the causes of intergranular liquation in the HAZ during welding of a number of superalloys [53,103,4]. In the present work, the degree of their liquation depended on their type and location relative to the fusion boundary. Away from the boundary, carbide liquation appeared mostly due to constitutional liquation of low temperature carbides as compared to the regions closer to the fusion line, where liquid film from high temperature

carbides were observed to have contributed to intergranular liquation and the attendant cracking (figure 4.59). The low temperature carbides richer in Nb and Zr seem to be more susceptible to liquation than the high temperature particles leaner in these elements but richer in Ta. Some of the high temperature carbide particles apparently survived the liquidus temperature (~1332°C), as they were observed within the fusion zone (figure 4.30). These carbides could be distinguished from those that formed during weld solidification by their larger size, shape and location. They existed mainly within dendritic core regions where they possibly could have served as nucleation sites for γ dendrites as discussed earlier. Similar behavior was also observed in the Gleeble simulated samples. Figure 4.50 shows microstructure of the sample heated to 1225°C. Evidence of liquation can be seen around low temperature carbides, which are associated with a γ-γ' eutectic colony, while high temperature carbides appeared almost unaffected. In the same micrograph, considerable amount of liquation is shown to have taken place around the M_2SC particle, on which low temperature carbides often form. It is possible that there is synergetic effect between M_2SC and the MC carbide particles resulting in higher degree of liquation. At higher simulation temperature 1245°C, liquation of high temperature carbides was apparent. This observation, which is in agreement with a previously published work [208] that Ta modified MC carbides are less susceptible to liquation than the Nb rich carbides, is further supported by the fact that the eutectic reaction temperature of binary Ni alloys decreases in the following order: Ni-Ta > Ni-Nb > Ni-Zr.

A very important microstructural feature was noticed in Gleeble simulated samples, which was also observed in welded samples and further verified by isothermal

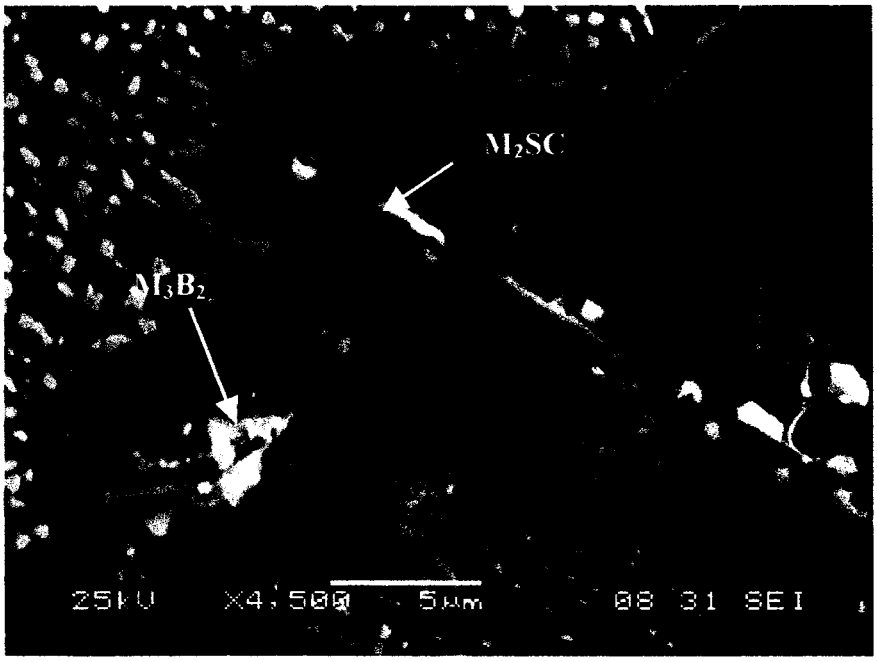

Figure 4.58: Liquation of M_2SC in weld HAZ

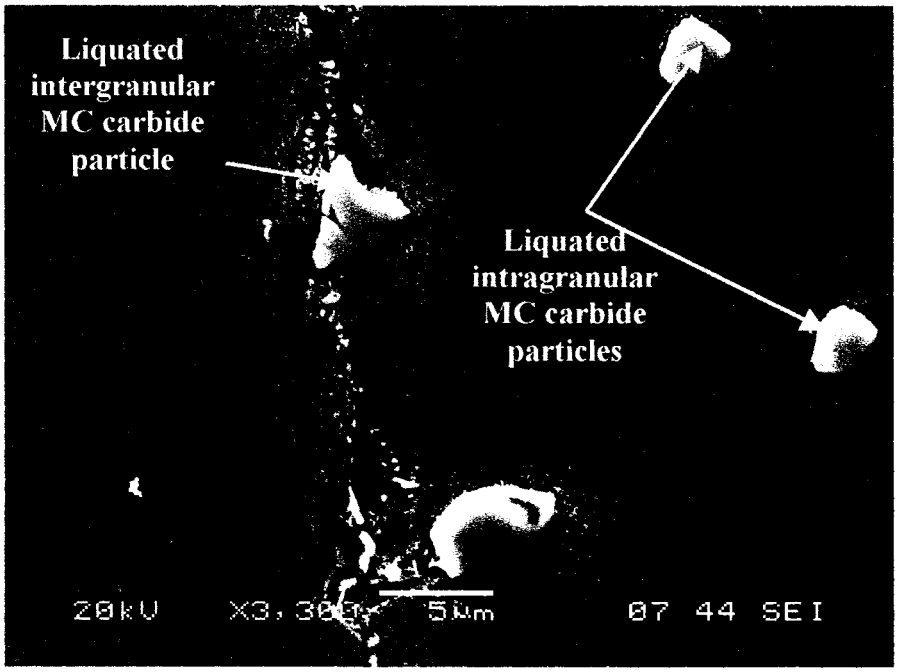

Figure 4.59: Liquation of MC type carbides in weld HAZ

heat treatment at temperatures above and below the bulk solidus temperature of the alloy. It was observed that a complete re-solidification of the liquid phase produced by liquation reaction(s) during rapid heating cycle in areas containing MC carbide always occurred directly adjacent to the surface of carbide particles. This can be seen in figure 4.60a&b (inter and intra) where fine resolidified γ-γ' eutectic constituent formed directly on the surface of both intergranular and intragranular MC carbide particles. This implies that this region will tend to be more susceptible to initiation and/or propagation of liquation cracking by sustaining liquid phase to a much lower temperature during weld cooling. This was observed in all welded samples (e.g. figure 4.59) and Gleeble simulated samples e.g. (figure 4.61), where liquation cracking occurred across MC carbide interface. This type of solidification behavior of the HAZ liquid can be understood by the aid of pseudo-ternary diagram developed for IN 738 and discussed in section 4.2.5.

The liquid that formed at 1225°C would be highly enriched in Ni and Ti due to prior constitutional liquation of γ' and lean in C due to limited dissolution of the MC carbide. As was discussed earlier, such liquid starts solidification by forming γ. During this process C, Nb, Ta and Ti will be rejected into the residual liquid, which will drive the solidification path toward γ-γ' 'pseudo binary edge' and toward the invariant temperature E_2 (figure 4.34), because the liquid never becomes significantly enriched in C. When the composition of the liquid reaches that corresponding to E_2, it can then complete the solidification process by two possible mechanisms, viz; (i) by terminal ternary eutectic reaction involving,

$$L \Leftrightarrow \gamma + \gamma' + MC$$

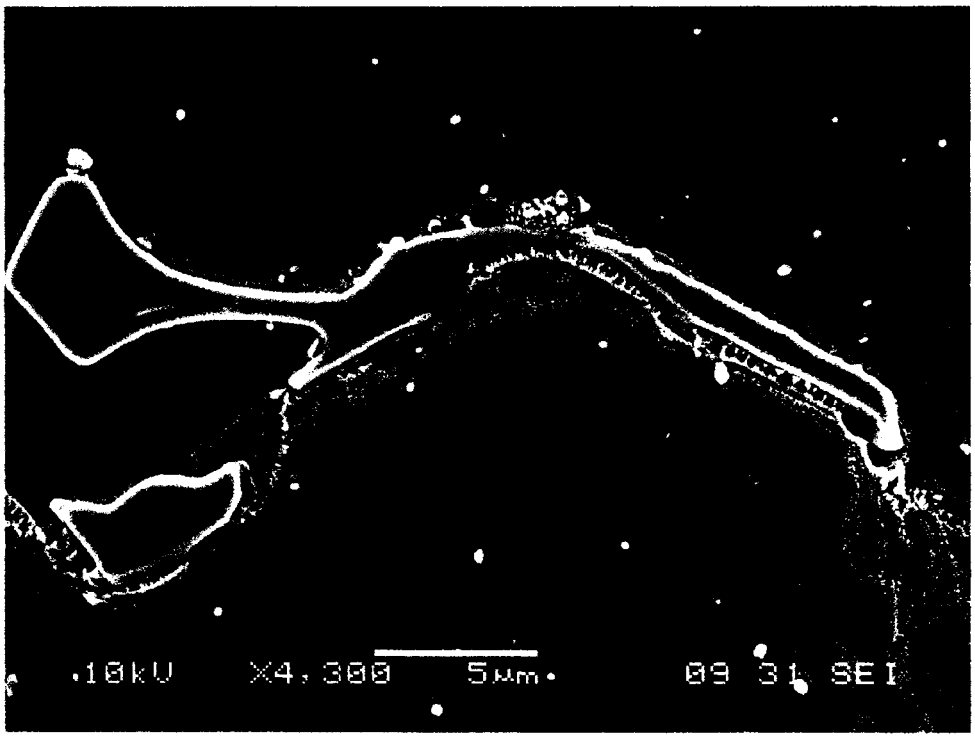

a

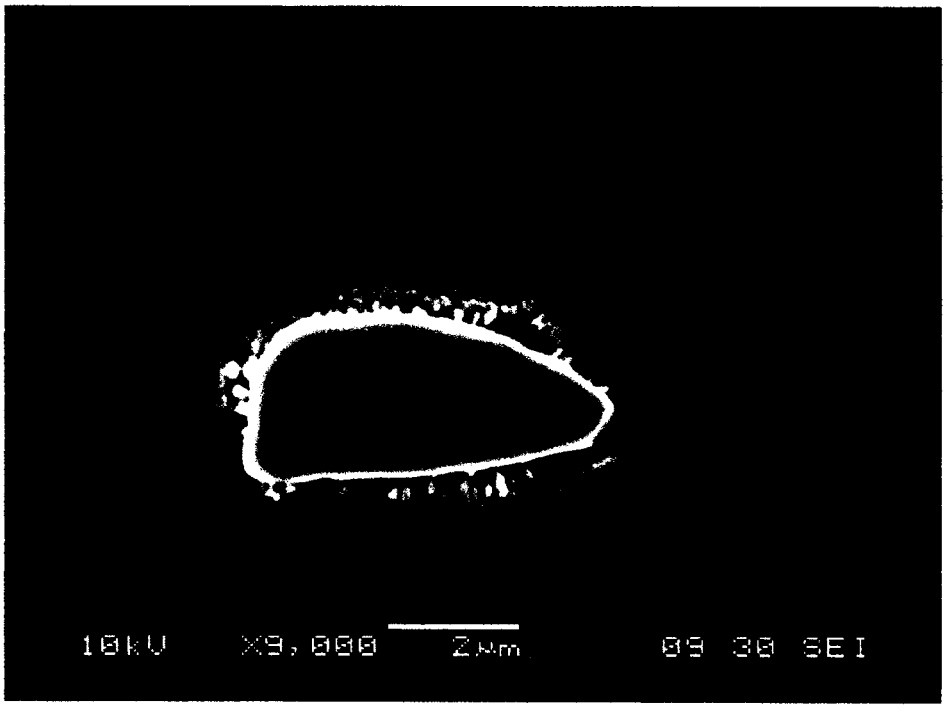

b

Figure 4.60: Re-solidification of (a) intergranular (b) intragranular liquid phase terminating at the surface of MC carbide particles.

or (ii) by class II peritectic reaction involving,

$$L + MC + \gamma \Leftrightarrow \gamma + \gamma' + L$$

followed by the monovariant eutectic transformation:

$$L \Leftrightarrow \gamma + \gamma'$$

In the first case, due to the low content of carbon, it might be more energetically favorable for the ternary eutectic transformation to occur by divorced eutectic reaction, in which the carbides form epitaxially on already existing carbide particle and surrounded by γ-γ'eutectic constituent. In the second case the already existing MC particle could take part in the peritectic reaction, thereby causing γ-γ'eutectic to form around it. In either case, the liquid will tend to solidify in a pattern with final solidification taking place adjacent to existing MC carbide particle.

Another important point can also be inferred from the possible reversible nature (heating and cooling processes) of the reactions represented by the above equations. Firstly, considering case 1, it can be seen that formation of the initial liquid phase during heating requires a eutectic reaction between γ, γ' and MC carbide at the terminal ternary eutectic temperature i.e. $\gamma + \gamma' + MC \Leftrightarrow L$. In the second case, however, the initial liquid phase during heating will occur by eutectic reaction between γ and γ' i.e. $\gamma + \gamma' \Leftrightarrow L$. The liquid produced by the monovariant eutectic reaction will, on reaching the peritectic isotherm react with γ and γ' to produce $\gamma + L + MC$ by a peritectic type reaction i.e. $\gamma + \gamma' + L \Leftrightarrow \gamma + L + MC$. The liquid produced by this peritectic reaction during heating should

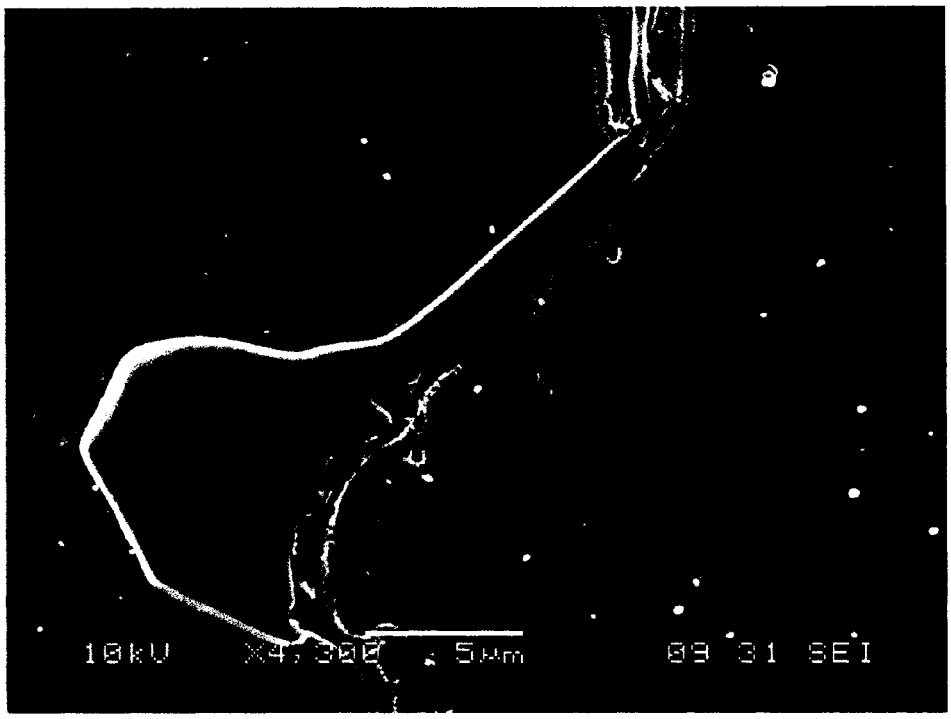

Figure 4.61: Crack propagating across the surface MC carbide particle.

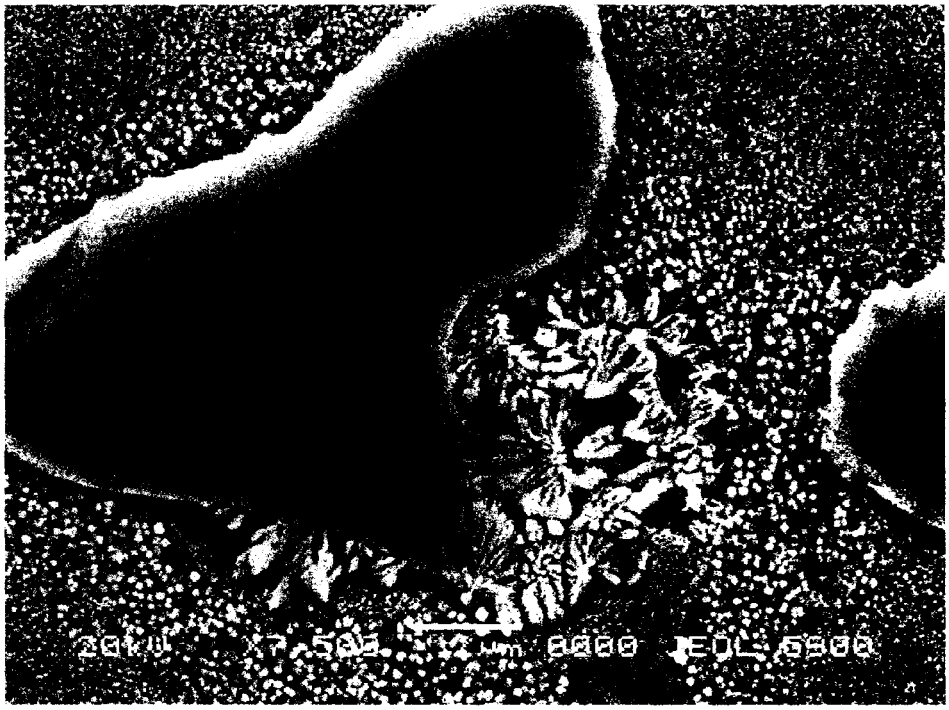

Figure 4.62: Sample heat treated at 1235°C for 4hrs

then be at equilibrium with γ and MC phases. In order to verify this possibility, IN 738 alloy was heat-treated at 1235°C for 4hrs then air-cooled. The microstructure of this sample (figure 4.62) shows formation of fine γ-γ'eutectic adjacent to the surface of dispersed MC carbide particles. This implies that the liquid phase, which completed the re-solidification process by γ-γ'eutectic transformation during the air-cooling, was at equilibrium with γ and MC carbides during the 4 hrs hold at 1235°C. The observation of exclusive formation of liquid phase by constitutional liquation of intragranular γ' (which are not connected with MC carbides) via a γ-γ'eutectic-type reaction indicates that formation of initial liquid phase during heating does not require involvement of MC carbides via a ternary eutectic type reaction. This supports mechanism (ii) above where the liquid completes solidification by monovariant γ-γ'eutectic reaction as opposed to mechanism (i), which indicates termination of solidification process by ternary eutectic reaction involving MC carbide. This again supports the idea that solidification behavior of IN 738 alloy is more properly represented by class II type reaction instead of class I reaction of the pseudo-ternary solidification diagram developed in this work.

The realization that liquation during rapid heating of IN 738 alloy during welding would necessarily occur via constitutional liquation of γ' particles before contribution from liquation of MC type carbides, underscores the unique role of γ' in the HAZ liquation cracking of this alloy. Considering the inevitability of presence of γ'phase in most nickel base superalloys as the main strengthening phase, more detailed discussion of solid-state dissolution of this phase, which is fundamental to its liquation behavior is given in section 4.4.

4.3.5 Characteristics of Intergranular Liquid Affecting Susceptibility to HAZ Cracking.

Having identified the liquating phases in IN 738, the characteristics of intergranular liquid film produced in the HAZ, which would influence its resistance to liquation cracking, will be discussed next.

Intergranular Liquid Film Thickness: The thickness of grain boundary liquid film can affect an alloy's resistance to liquation cracking through its influence on (i) the level of stress required to cause microfissuring at a given temperature during weld cooling and (ii) the re-solidification temperature range. According to Chadwick's calculations [209], the tensile stress required to overcome surface tension γ_L on a grain boundary containing liquid film of thickness h, is given by:

$$\sigma = 2\,\gamma_L / h \qquad (4.8)$$

which indicates that an increase in intergranular liquid film thickness would lower the stress required to cause decohesion at such a solid-liquid interface. Concerning re-solidification temperature range, in a relatively large volume of intergranular liquid, solute segregation may occur during re-solidification, which usually tends to lower the terminal re-solidification temperature with an attendant build-up of higher welding stresses across the grain boundaries during cooling. However, this does not necessarily mean that actual occurrence of liquation cracking will monotonically increase with increase in liquid film thickness in a given alloy system. For a given alloy and specific eutectic constituent, hot cracking susceptibility will most likely increase with increase in intergranular liquid thickness up to an amount, where the phenomenon of liquid healing begins. Liquid healing occurs when a large enough amount of intergranular liquid is

present to effectively backfill and heal incipient cracks as they form. Many braze and solder alloys implicitly use the phenomenon of liquid healing and thus are virtually immune from the problem of hot cracking during solidification. The amount of liquid necessary to fully affect liquid healing can be alloy dependent. Clyne and Davies [92] suggest that at least 10 vol.% is required, which is supported by the work of Arata and coworkers [210]. Consequently, any parameter, which contributes to an increase in the grain boundary liquid film thickness, would tend to influence the alloys resistance to liquation cracking. The high volume fraction of liquating phases in the present alloy which included γ' precipitate particles (21% in ST and 30% in UMT conditions), γ-γ' eutectic constituent (~ 2%), MC type carbides (~2%), M_3B_2 and M_2SC (<1%) and the large grain size of the cast alloy (500 - 800μm) are factors that could increase intergranular liquid film thickness and thus affect susceptibility to HAZ liquation cracking.

Grain Boundary Wetting: The ability of a liquid phase to effectively wet and spread out along grain boundaries and form a continuous or semi-continuous film has been recognized to directly control an alloy's propensity to liquation cracking during welding [87]. To a first approximation, intergranular liquid's distribution could be treated in accordance with the relationship proposed by C. S. Smith [91]:

$$\gamma_{gb} = 2\,\gamma_{SL}\,\mathrm{Cos}\,\theta \qquad (4.9)$$

where θ is the wetting angle, γ_{gb} is the grain boundary energy and γ_{SL} is the solid-liquid interface energy. From equation 4.9, it can be seen that for a given grain boundary energy, lower the solid-liquid interface energy, lower will be the wetting angle and more easy it will be for such a liquid to wet and spread on the grain boundary. Since the

classical study of Bailey and Watkins [211], it has been recognized that a relation exists between mutual solubility and/or the formation of intermetallic compounds and solid-liquid interfacial energy and, thus, with wetting properties. The greater the solubility of metals in the solid state, the lower will be the interfacial energy when these metals are brought into contact with one another in liquid state. Hence, it is probable that a solid metal will be wetted by a liquid metal, if the two are at least fairly soluble in each other. In the IN 738 alloy, it is known γ' has a high solid solubility in γ while MC carbide also exhibits some solubility in the γ matrix. In addition, intermetallic γ' and MC carbide particles are formed along the grain boundaries during solidification of the alloy. Therefore, in IN 738 the interface energy between γ grains and the liquid phase produced by constitutional liquation of γ' and MC carbide, can be expected to be relatively low, thereby exhibiting good wetting behavior and penetration of the grain boundary regions. This was observed in the microstructures of weld HAZs and Gleeble simulated samples. Besides, segregation of S and B to interphase interfaces, such as grain boundaries and MC/γ interface, has been detected by Kny et al [212] in IN 738, Delargy et al in IN 939 [203] and Guo et al in IN 718 superalloy [114]. Absorption of such segregated atoms and/or those released by decomposition of M_3B_2 and M_2SC particles by intergranular liquid, could substantially aid wetting behavior of the liquid through the influence of surface active elements in lowering solid-liquid interface energy along the grain boundary. Boron rich particles were observed in the present investigation to be a part of the resolidified eutectic constituents, especially in UMT samples, which formed along some liquated boundaries (figure 4.38). Furthermore, the metastable liquid produced by constitutional liquation of intergranular second phase particles always reacts with

adjacent solid grain through back diffusion of solute atoms across the solid-liquid interface. Therefore, in these situations the non-equilibrium solid-liquid interfacial energy is extremely low [213], which would make the liquid to effectively wet the grain boundary and exhibit extensive penetration. A recent model [214] developed for describing penetration of liquid phase along grain boundary has also shown that grain boundary penetration requires an under-saturated solid. This is essentially the situation prevalent in the HAZ during non-equilibrium rapid heating and cooling of welding operation.

In an alternate and/or complementary case, which is apparent from equation 4.9, is that for a given solid-liquid interfacial energy, the higher the grain boundary energy higher is the tendency for it to be wetted and penetrated by liquid phase. It has been found that grain boundaries in cast IN 738 alloy are more of a "random" nature with higher order of "Σ" values, than special boundaries [215]. Random high angle grain boundaries are inherently of higher energy than the special boundaries, including twin boundaries, and as such this character could be a factor aiding extensive grain boundary wetting and penetration by liquid film in IN 738 as observed in this work. Guo, H. et al [114] and Kokawa et al [216] have confirmed that liquid penetration at grain boundary was greatest at high angle boundaries and was relatively insignificant at low angle boundaries.

Re-solidification Behavior of Intergranular Liquid: The rate at which grain boundary liquids are eliminated prior to occurrence of sufficient welding stresses directly influences resistance to liquation cracking. There are 3 main mechanisms through which intergranular liquid film could be relieved of its excess solute concentration, and thus

solidify during welding thermal cycle. These are, (i) solute back-diffusion into the adjacent solid grain matrix, (ii) rapid solidification through liquid film migration (LFM) and (iii) by normal solidification involving solute partitioning. Exclusive solidification via solute back-diffusion is likely to be extremely limited in HAZ of cast IN 738 weldment due to two reasons.

(1) Solute rich interdendritic zones due to microsegregation in the pre-weld alloy, which could reduce solute concentration gradient expected to drive such diffusion process.

(2) Limited surface area available for diffusion flux due to the large grain size of the alloy.

LFM is a fundamental mechanism by which a metastable grain boundary liquid film can be effectively removed through rapid solidification, thereby promoting resistance to liquation cracking. Nakkalil et al [217] have shown that occurrence of LFM is enhanced in wrought Incoloy 903 alloy with smaller grains as compared to that observed in coarser grains. Intuitively, therefore, occurrence of LFM in a large grain cast IN 738 alloy may be expected to be less favored. Microstructural examination in this work has revealed an extensive occurrence of LFM in IN 738. Nonetheless, even though LFM occurred extensively in the alloy, it is still susceptible to liquation cracking. The possible driving forces for LFM in IN 738, and the likely reasons why the alloy still exhibits liquation cracking despite the occurrence of extensive LFM are discussed in section 4.6. Re-solidification of HAZ intergranular liquid by solute partitioning, which often terminates with the formation of eutectic and extension of solidification temperature range, was observed to be prevalent in the present work. In such a situation, terminal eutectic

reaction temperature during cooling is known to be dependent on chemical composition of the intergranular liquid. The chemistry of HAZ grain boundary liquid may not be much different from that of the interdendritic liquid present during the final stages of solidification of castings. This is due to similarity in solute partitioning during the later stages of solidification of a casting and that associated with the HAZ liquation of secondary solidification constituent. It has been found that terminal solidification temperature in IN 738 type casting alloy [160] and in another alloy GTD-111, (similar in composition to IN 738) [161], can be considerably below 1180°C. Persistence of intergranular liquid film to temperatures below this value could in effect promote susceptibility to HAZ liquation cracking.

4.4 Solid-State Dissolution and Liquation of γ' Phase

4.4.1 Introduction

Nickel base superalloys containing high volume fraction of γ'precipitates have long been known to be very difficult to weld, due to the occurrence of HAZ cracking. The main reported contribution of γ' precipitates to cracking in the HAZ of these alloys during welding has been through the effect of rapid re-precipitation of γ' on large shrinkage stresses [3]. In general, these reports have been implicitly based on the assumption that γ'particles undergo complete solid-state dissolution in the HAZ regions which experience peak temperatures above γ' equilibrium solvus temperature during welding cycles. However, a very important possibility, that these particles could persist during heating to a temperature at which they could react with the γ matrix producing a liquid phase by a eutectic-type reaction has, along with its concomitant consequences apparently, eluded due consideration. This section aims at discussing the possibilities of γ' particles surviving to temperatures well above the equilibrium solvus temperature during continuous heating to temperatures where liquation could occur by eutectic-type reaction in nickel base superalloys and the attendant effects. Due to perceived broad applicability of this concept, attempt is made to extend this discussion to other types of γ'strengthened superalloys.

4.4.2 Non-Isothermal Solid-State Precipitate Dissolution

Most of the microstructural transformations (grain growth, precipitate coarsening and dissolution) induced by heating cycle in alloys are diffusion controlled. As such, it has been shown by different investigators that these microstructural changes can be

reasonably represented by appropriate analytical and numerical mathematical models. Over the years, several analytical models have been developed, which describe the kinetics of particle dissolution in metals and alloys at high temperatures. None of these solutions are exact, since they use different approximations to represent the diffusion field around dissolving particles. Nevertheless, it has been shown that at least some of them are sufficiently accurate to capture the essential physics of the problem and to give valuable quantitative information on the extent of particle dissolution during welding thermal cycle. One of the most widely accepted analytical models for particle dissolution in metals is that due to Whelan [218]. Based on the assumption that the particle/matrix interface is stationary and has constant diffusivity, Whelan [218] has been able to show that dissolution rate of a spherical precipitate at a constant temperature can be represented by:

$$dr/dt = k\,[D_m/r - (D_m/\pi t)^{1/2}] \qquad (4.10)$$

where r is the radius of the particle, t is time, D_m is solute bulk diffusivity and k is given by:

$$k = 2\,(C_i - C_o) / (C_p - C_o) \qquad (4.11)$$

C_i, C_o and C_p are the solute concentration at the particle/matrix interface, in the particle and at infinity, respectively. The 1/r term on the right hand side of equation 4.10 comes from the steady state part of the diffusion filed, while the $1/t^{1/2}$ term arises from the transient part. By neglecting the transient segment, i.e. conforming to the solution after long times, it is possible to obtain a simple expression for the particle radius as a function of time [218].

$$r^2 = r_o^2 - 2kD_m t \qquad (4.12)$$

where r_o is the initial particle radius. Equation 4.12 is similar to the so called invariant-field solution developed independently by Aaron et al [219] and is valid after a certain period of time, provided that there is no impingement of diffusion field from neighboring precipitates. Equation 4.12 thus gives a simplified description of the dissolution kinetics of spherical precipitates under isothermal conditions. The time required for a complete dissolution of the particle can be obtained from equation 4.12 by setting r = 0 [220] to obtain:

$$t_f = r_o^2 / kD_m \qquad (4.13)$$

Application of the above model to non-isothermal conditions involving continuous heating, typical of welding process, requires numerical integration of equation 4.12 over the weld thermal cycle [221] i.e.

$$r^2 = r_0^2 - 2\int_{t1}^{t2} kD_m t \ \mathrm{dt} \qquad (4.14)$$

Another approach of utilizing equation 4.12 for non-isothermal conditions is by following the isokinetic concept described by Christian [222]. The isokinetic concept can be used if the increments of transformation in infinitesimal isothermal time steps are additive. In such a case the shape of the diffusion field ahead of dissolving particle can be neglected and an incremental scheme derived, where particle dissolution Δr in time increment Δt is given only by the temperature and particle size r. Bjorneklett et al [223] have been able to show that the particle dissolution reaction is additive during continuous heating. They developed a dimensionless form of equation 4.12 by introducing the scaled particle volume fraction $f/f_o = (r/r_o)^3$ and a time constant t* for the reaction to obtain:

$$f/f_0 = (1 - t/t^*)^{3/2} \tag{4.15}$$

The time constant t* contains all material and temperature dependent parameters and is defined as:

$$t^* = t_r^*(k_r/k)(D_{mr}/D_m)(r_o/r_o^r) \tag{4.16}$$

where, the index r refers to a chosen reference condition and t^*_r is based on equation 4.13. By differentiating equation 4.15 with respect to time and substituting for t, they obtained the following for the rate of particle dissolution:

$$df/dt = -3/2\{\frac{f^{1/3}}{2t^* f_o^{2/3}}\} \tag{4.17}$$

which after integration yields:

$$f/f_0 = (1 - \int_0^{t^2} dt/t^*)^{3/2} \tag{4.18}$$

The form of equation 4.18 shows that the reaction is additive in the general sense defined by Christian [222]. During continuous heating, the radius of the particle can be expected to start deceasing when the temperature reaches the equilibrium solvus temperature of the particle, T_{SL}. Considering an additive dissolution reaction process, depending on the heating rate and the initial particle size, the actual time spent at T_{SL} and at some temperatures above T_{SL} may not be up to that required to achieve a complete dissolution (i.e. the time predicted by equation 4.13). Hence, it is apparent that, during continuous

heating the temperature at which the particle will dissolve completely can be significantly higher than T_{SL} depending on heating rate and the initial particle size.

Bjorneklett et al [223] compared their analytical solutions based on isokinetic and additivity concept with a more exact control volume numerical calculations. They reported good agreement between the results of the two models for continuous heating process. Soucail et al [224] in a separate work, studied dissolution of γ' phase in a nickel base superalloy at equilibrium and under rapid heating. Following a different analytical approach developed by Ashby and Easterling, they derived a particle dissolution model, which they verified with experimental results. Their analytical results, which are reported to be in good agreement with the experimental results, are qualitatively consistent with those of Bjorneklett et al [222]. They showed that there is a significant departure from equilibrium under rapid heating condition, in that the temperature of complete solid-state dissolution increased with increasing heating rate and this departure is dependent on the initial particle size. This increase in complete dissolution temperature was found to be more pronounced with increase in particle size. An increase of about 120°C in complete dissolution temperature at a heating rate of 8°C/s was reported for γ' precipitates with an initial size of 0.8μm. They also indicated that the delay in γ'dissolution was more pronounced during the early stages of dissolution than during close to the end of dissolution process. No reasons were given for the apparent increase in the rate of dissolution towards the terminal dissolution stage.

Therefore, under rapid continuous heating process, γ' particles can be expected to persist to temperatures considerably above their equilibrium solvus temperature depending on heating rate and the initial particle size. Savage et al [99] have proposed

that existence of such second phase intermetallic particles at a temperature where they could react with the matrix by a eutectic-type reaction may result in consequential constitutional liquation. It then follows that, the important considerations are (i) the size of temperature interval that the particle requires to overcome before reaching the eutectic reaction temperature, since this will determine the minimum heating rate required for a given particle size to survive to such critical temperature (ii) the liquation kinetics i.e. whether liquation will occur almost immediately on reaching the eutectic temperature or a significant time delay is required for such reaction to take place. These factors will be discussed separately next.

4.4.3 γ-γ' Eutectic Reaction in Nickel base Superalloy

It is generally known that γ-γ' eutectic reaction occurs during solidification of most γ' precipitation hardened superalloys. It has been shown in the present work by the pseudo-ternary diagram developed for IN 738 alloy, which appears to be applicable to other γ' strengthened nickel base alloys containing carbon, that γ-γ' eutectic transformation occurs over a range of temperatures in this multicomponent alloy. Similar occurrence can be shown for carbon-free γ' strengthened nickel base alloys especially most single crystal superalloys. Ni-Al-Cr and Ni-Al-Ti are the two ternary systems mostly used to represent these type of superalloys. The configuration for low Ti contents in Ni-Al-Ti is similar to that of Ni-Al-Cr system [225]. Therefore from a more theoretical point of view, the Ni-Al-Ti system is a good reference for the discussion of γ-γ' equilibria and solidification path for this class of superalloys. Willemin et al [163] have studied liquid-solid equilibria in the nickel rich corner of the Ni-Al-Ti system and have proposed

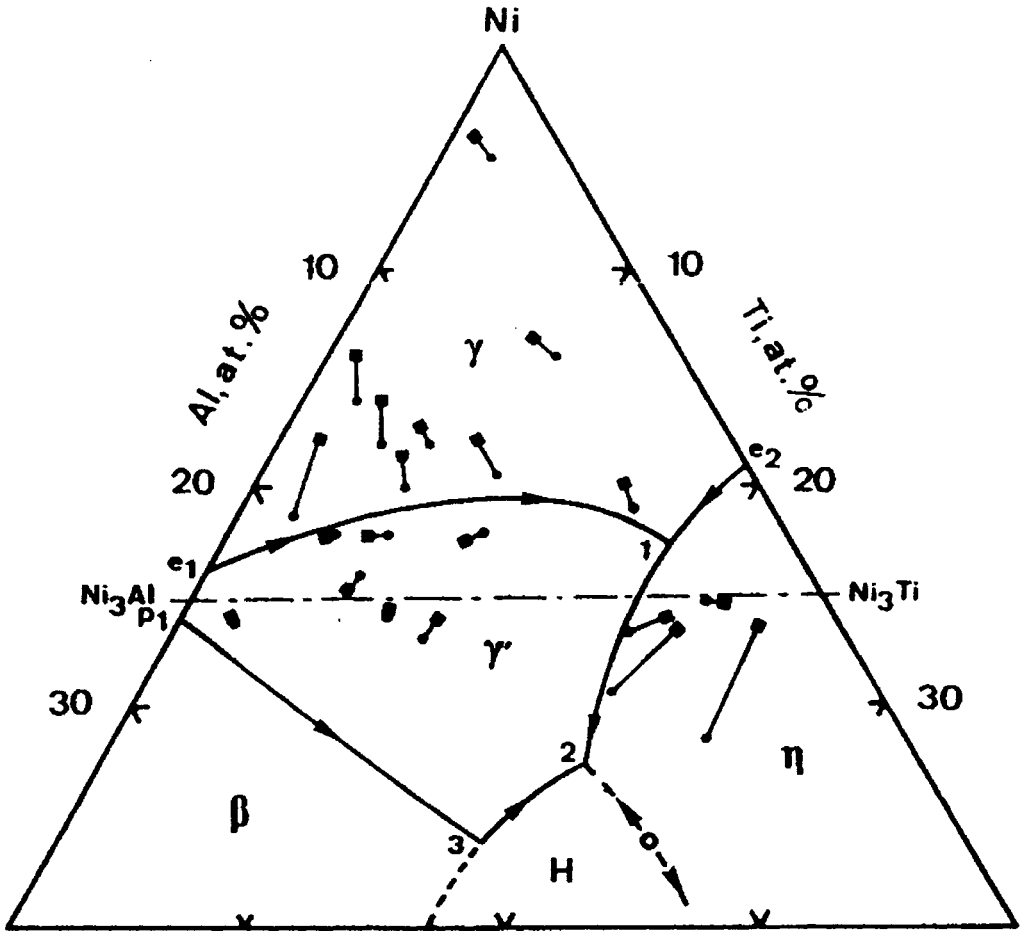

Figure 4.63: Projection of Liquidus surface of the Ni rich corner of Ni-Ti-Al Ternary System [163].

a projection of the liquid surface, which is shown in figure 4.63. The γ nickel base solid-solution region is bordered by γ' and η phases. The boundaries between the different phases are represented by monovariant lines. The three points 1, 2, and 3 represent invariant ternary reactions involving 3 solid phases and the liquid. Point 1 and 3 are peritectic since solidification does not terminate there, while point 2 is a eutectic isotherm. The equilibrium between γ, γ' and liquid is found to be of monovariant eutectic in nature for low titanium concentrations. It is suggested that the equilibrium could change to peritectic for alloys containing more than 5% Ti and in such a case the primary γ field can end solidification with the formation of β phase, since the solidification path can cross the peritectic line.

The solidification behavior of nickel base alloys represented by this diagram will start with the formation of γ dendrites, which upon forming reject Al and Ti to the liquid. As the solidification proceeds the liquid composition moves away from the nickel corner becoming progressively richer in Al and Ti, (particularly Ti since it exhibits lower partition coefficient) until the uninvariant line of twofold saturation between γ and γ'is reached. At this stage, the maximum solubility of (Ti + Al) in the γ dendrite is reached, causing coupled solidification of γ and γ' phases by a eutectic-type reaction, which continues on further cooling as the liquid composition follows the monovariant line. Solidification in most of this class of nickel base superalloys, especially those that are free of non-metal radicals like B and S, is reported to be completed by the γ-γ'eutectic transformation. γ' precipitate particles would start forming from the solidified alloy by solid-state precipitation reaction once the temperature is sufficiently below the solvus temperature. This could start at different temperatures in different regions of the alloy due

to inhomogeneity in composition caused by dendritic microsegregation during solidification.

DTA studies of superalloys solidification process are sometimes reported indicating isothermal γ-γ'eutectic transformation, followed by solid-state precipitation of γ'particles. According to the Gibbs phase rule, it is expected that γ-γ'eutectic formation in multicomponent nickel base alloys would occur over a range of temperatures as indicated by the Ni-Ti-Al ternary phase diagram. The apparent omission in the DTA reports could be due to limitation of DTA in detecting the remaining liquid eutectic reaction temperatures owing to slow freezing rate and low latent heat of solidification during the later stages of solidification process. Through careful DTA investigations, David et al [138] and Tewari et al [139] have reported formation of γ-γ'eutectic over a range of temperatures in PWA 1480 single crystal superalloys. As can be seen from figure 4.63, the monovariant line is curved with reaction direction towards the Ti rich region. This indicates that more γ-γ'eutectic forms as the liquid gets enriched in Ti during cooling. This is consistent with several experimental studies that have found that an increase in Ti content of γ' strengthened superalloys under a given cooling condition produced an increase in the volume fraction of γ-γ'eutectic, with concomitant decrease in terminal solidification temperature [155, 187]. An extension of temperature range over which γ-γ'eutectic forms with increase in nominal content of γ' forming elements especially Ti, could result in the solid-state precipitation of γ'particles in some regions of the alloy prior to completion of γ-γ'eutectic transformation. DTA analysis of nickel base superalloys, figure 4.64 [187], have shown that increase in γ' forming elements results in an increase in γ' solvus temperature T_{SL} with an attendant decrease in temperature interval between

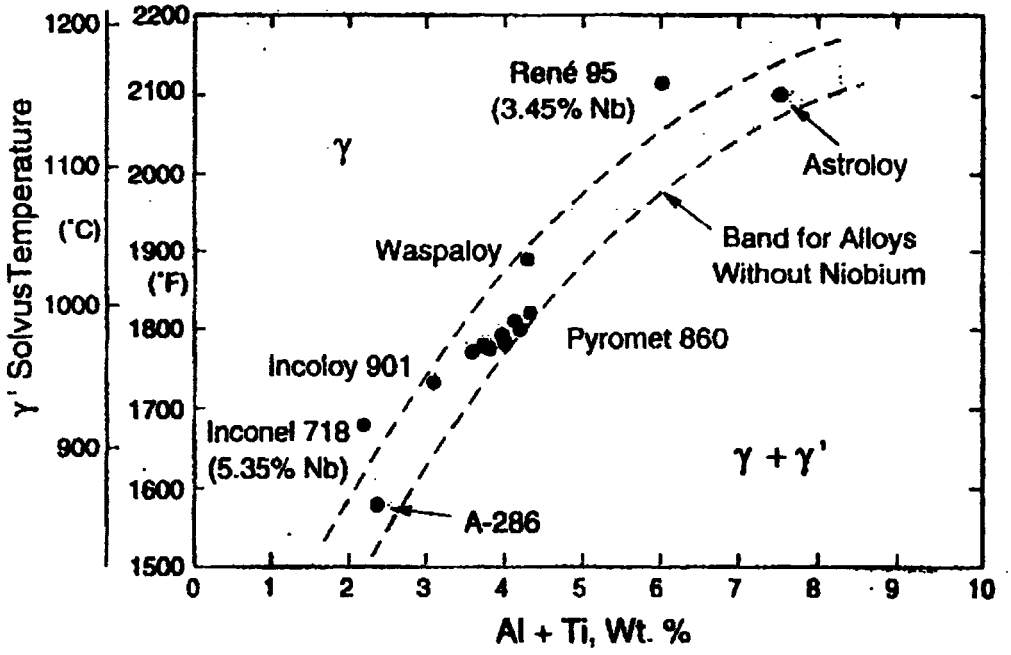

Figure 4.64: Variation of γ' solvus temperature of seven superalloys with Al + Ti content as determined by DTA [187].

γ-γ' eutectic reaction temperature (as detected by DTA) and the T_{SL}. Considering that actual γ-γ'eutectic transformation would occur over a range of temperatures, the eutectic reaction temperature could extend below T_{SL} in some alloy systems. Microstructural examination of directionally solidified and quenched IN 738 at different temperatures on cooling, have been reported to show that solid-state precipitation of γ' particles occurred prior to completion of γ-γ'eutectic transformation [135]. A more serious situation appears to be the case of single crystal superalloys, where γ'solvus temperature could be well above the γ-γ'eutectic transformation temperatures. A review of the literature shows that γ' solvus temperature in PWA 1480 (1287°C [225]) is above the eutectic transformation temperature range of 1287 - 1232°C [138] and 1280 - 1275°C [139].

Therefore, as the amount of γ' forming elements increases in nickel base superalloys, not only does the volume fraction of γ' particles increase but also the temperature range between γ' solvus temperature and γ-γ'eutectic reaction temperature reduces. This will in effect lower the minimum heating rate required for a given γ' particle size to persist to a temperature where it could react with γ matrix to produce liquation via a eutectic-type reaction (i.e. the minimum heating rate required to cause constitutional liquation of γ' particles).

4.4.4 Interface Reaction and Liquation of γ' Phase

It is implicitly assumed during the development of theory of constitutional liquation by Savage et al [99] that thermodynamic equilibrium exists at the precipitate-matrix interface during precipitate dissolution and at the precipitate-liquid and liquid-matrix during liquation. This implies that the precipitate dissolution and liquation

reactions are diffusion controlled. It has, however, been suggested that in a situation where the solid-state dissolution is fully interface controlled (such as in coherent precipitates) enrichment of solutes at the particle-matrix interface required for constitutional liquation might be significantly restricted [226]. This was based on the argument that interface controlled dissolution involves movement of the particle-matrix interface. Since driving force is required to move an interface, then there has to be an activity or free energy gradient for the components at the interface, which implies deviation from thermodynamic equilibrium. Under a local thermodynamic equilibrium condition at particle-matrix interface, the activities of the components in the precipitate will be equal to those in the matrix at the particle-matrix interface and hence, there will be no driving force required for transferring the atoms across the interface. In diffusion-controlled transformations where a near-thermodynamic equilibrium exists at the interface, virtually all of the available free energy of transformation is used up for solute transfer into the matrix by diffusion. This will increase concentration gradient in the matrix and thus promote solute build up at the particle-matrix interface to reach the equilibrium concentration.

Fully interface controlled transformation can occur when the interface mobility is extremely small and a significant portion of the available free energy of transformation is expended in moving the interface. This could result in a small solute concentration gradient in the matrix and thus reduce solute build up at the interface to a level below the equilibrium value. The mobility of precipitate-matrix interface is in general related to structure of the interface [227]. In certain alloy systems, the lattice mismatch between the precipitate and the matrix may be so small that the particle-matrix interface may remain

coherent even for coarser precipitates, such as γ' phase in some nickel base γ matrix of superalloys. This type of interface has been termed sharp or atomically smooth, with very few ledges or kinks. The movement of a coherent interface in a direction normal to the interface requires a coordinated or a simultaneous movement of a large number of solute atoms across the interface to nucleate a ledge, which then rapidly migrates in a direction parallel to the interface. It has been shown [228] that such a uniform detachment and attachment of solute atoms across the interface requires a driving force, which results in the precipitate dissolution being interface controlled in certain alloy systems.

Based on this argument, it was suggested that if an alloy containing coherent precipitates is rapidly heated to a temperature where the precipitates are thermodynamically capable of liquating, reduction in solute concentration at the particle-matrix interface due to interface controlled solid-state dissolution could prevent or significantly delay such a liquation occurrence. It was mentioned that although a bulk of the weld thermal simulation work has been carried out for multicomponent alloys, there have been no attempt made to detect the existence of interface-controlled dissolution limiting constitutional liquation. Nevertheless, the work of Romig et al [116], where coherent Ti(C, N) precipitates were reported to have liquated at a higher temperature as compared to the incoherent Nb rich precipitates of Nb,Ti(C, N) and (Nb,Ti)C, was cited as a possible case where this phenomenon could have occurred. Considering that γ' particles are coherent with γ matrix in most nickel base superalloys, it is useful to consider, if the dissolution behavior of these particles could limit their liquation by reducing the solute concentration at the particle-matrix interface to below the equilibrium

value, when these particles are heated to a temperature where they are thermodynamically capable of liquating.

It is commonly assumed that in superalloys the γ' phase precipitates are fully ordered up to their solutionzing temperature and that dissolution is accompanied with migration of the interface between the ordered γ' phase and γ matrix. In such a situation, the above deviation from equilibrium solute concentration at the particle-matrix interface during dissolution can be expected. However, a recent high temperature x-ray diffraction study of dissolution behavior of γ' phase in AM1 single crystal nickel base superalloy, has shown a significant variation from the above assumption [229]. It was reported that partial structural disordering of γ' phase occurs at γ/γ' interface at temperatures above 800°C. As the temperature increases, the layer of disordered γ' increases in thickness from the γ/γ' interface inwards within the γ' particle, reducing the volume fraction of the ordered phase without changing the composition enough to transform the γ' to γ phase. It was indicated that dissolution of the γ'particle occurred by partial disordering reaction before transformation to γ phase i.e.

$$\text{Ordered } \gamma' \rightarrow \text{disordered } \gamma' \rightarrow \gamma$$

A similar observation has been also reported in other single crystal nickel base superalloys by high temperature x-ray diffraction investigation [230]. It was reported that transformation of γ' to γ phase occurs by first formation of disordered phase enriched in γ' forming elements within the γ' particle above 600-800°C prior to a complete transformation to γ phase. It has been previously found that binary γ' phase with stoichiometry composition Ni_3Al is perfectly ordered with $L1_2$ type long-range order (LRO) up to 1330°C [231]. Above this temperature the LRO starts decreasing until it

melts into a partially ordered state [232]. Royer et al [229] in their work compared the degree of structural order in γ' phase in the multicomponent AM1 superalloy with those in a specimen of Ni_3Al γ' phase of pure stoichiometric composition. The disordering reaction was observed only in the superalloy in an experiment conducted up to 1300°C. They suggested that the structural disorder of γ' in the diphasic superalloy could be related to diffusion induced disorder reaction at the γ/γ' interfaces.

On a different premise, an investigation of Ni/Ni_3Al diffusion couple interface by analytical electron microscopy and high resolution electron microscopy has indicated the dissolution behavior of γ'phase in γ to be similar to that described just above [233]. It was reported that annealing of Ni/Ni_3Al diffusion couple resulted in the transformation of the original γ' phase in to a new γ phase with an orientation almost identical to that of the γ' phase. Based on their observations, they proposed a model for reaction of γ/γ' interface during heat treatment. Figure 4.65 [233] shows schematic illustrations of the interface before and after the annealing heat treatment. Heat-treating leads to the formation of a new γ phase in the original γ' phase, while the orientation relationship of the new γ phase with the γ' phase remains unchanged and coherency is conserved at the interphase boundary. It was mentioned that contrary to the view of epitaxial growth of γ phase on the γ' phase, which would involve migration of the ordered γ/γ' interface, the γ phase resulted from the transformation of the γ' phase. The formation of a new γ phase in the original γ' phase is also consistent with optical microscopy observations of Janssen [234] and scanning electron microscopy observations of Dupeux et al [235]. They further concluded from their microchemical composition analysis that solute composition at the

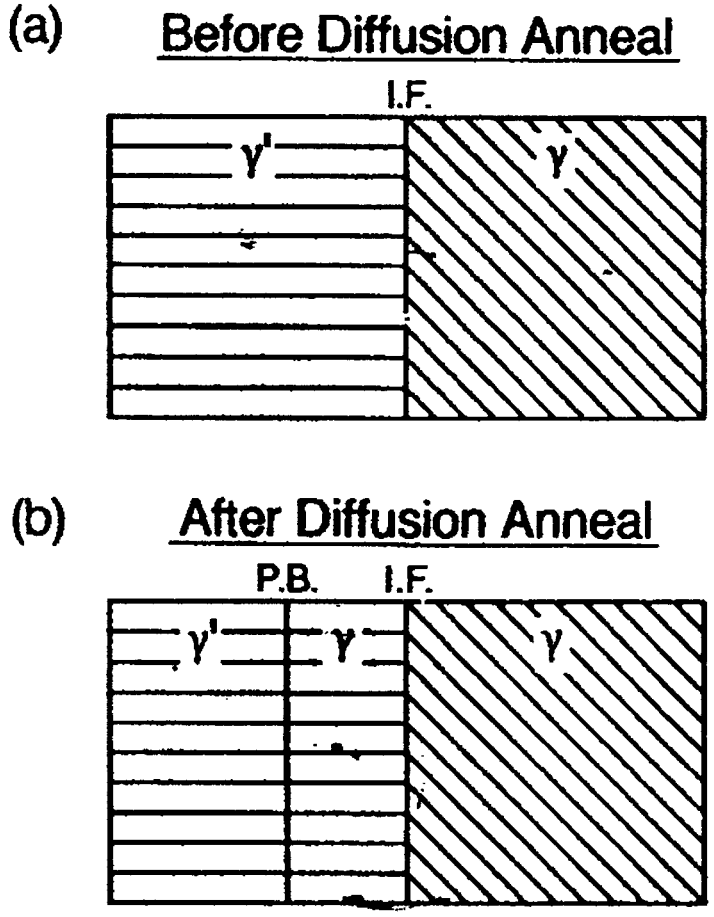

Figure 4.65: Schematic illustrations of interface (a) before and (b) after, diffusion annealing [233].

γ/γ' phase boundary at each annealing temperature was in an equilibrium condition. Reed et al [236] have recently indicated that local equilibrium is indeed adopted at the migrating γ/γ' interface during high temperature annealing of γ/γ' couple in the nickel-rich Ni-Al-Ti system. Therefore, the concept of solid-state dissolution behavior of γ' in which the ordered γ' phase is surrounded by solute rich γ phase transformed directly from it and the reports indicating local equilibrium at migrating γ/γ' interface show that, contrary to the prediction based on interface control dissolution of coherent particles, solute concentration at the γ/γ' interface can be expected to be at least commensurate with that expected on the basis of thermodynamic equilibrium. This implies that liquation can be expected once a γ' particle survives to a temperature where a γ-γ' eutectic-type reaction is possible as dictated by local thermodynamic equilibrium. Constitutional liquation of intergranular and intragranular γ' particles was observed in the present work in the weld HAZ of IN 738 alloy and in samples rapidly heated to 1165°C and held for 0.5s, and at all the other test temperatures above this temperature. Close examination of published micrographs of weld HAZ of Rene 80 superalloy [237] suggests that constitutional liquation of γ' particles is likely occurring during welding of this alloy as well, even though it was not so recognized.

4.4.5 Dissolution of γ' Phase Through Liquation and Its Effects on HAZ Liquation

The concentration of γ' forming elements in superalloys is usually below the limit of solid solubility of γ' in γ phase at the equilibrium solidus temperature. γ-γ'eutectic forms in these alloys as a non-equilibrium solidification product due to microsegregation during the solidification process. As such, the γ-γ'eutectic solid and the liquid produced

by this reaction could be essentially removed by appropriate heat treatment below the alloys equilibrium solidus temperature. At the onset of constitutional liquation of γ', the particles get surrounded by liquid film at the eutectic reaction temperature. On further heating or holding at this temperature, solute diffusion from the particles to the bulk γ matrix would occur through the surrounding liquid film as the particles continue to liquate. In addition, as discussed earlier, the liquid produced by constitutional liquation of γ' is expected to effectively wet the γ matrix and easily infiltrate the grain boundary regions. It is known that when solid solution grains are not in chemical equilibrium with the liquid in which they are embedded, equilibrium often occurs by dissolution and re-precipitation of saturated solution by liquid film migration process. The rate of re-solidification through LFM is very high since the process is controlled by a high diffusion rate in the liquid phase. Since diffusion through liquid is orders of magnitude faster than in solid state, dissolution of γ' particles through liquation can be expected to occur more rapidly than the rate predicted on the basis of solid state diffusion. This could probably be contributing to the observed deviation from the dissolution rate predicted by the solid-state diffusion based model, during continuous heating of Astroloy alloy [224]. It is possible that the γ' particles in their work did undergo some solid-state dissolution on reaching and exceeding the equilibrium solvus temperature during heating, but they did survive to a temperature where they could have liquated. This might be responsible for the faster rate of dissolution that they observed during the last stages of dissolution in their work. It should be mentioned that detecting liquation of γ' precipitates may require carefully designed experimental procedures. These procedures may involve exposure of limited time at the liquation temperature, use of good metallographic sample preparation,

and appropriate optimization of scanning electron microscope operating parameters to reveal the necessary microstructural details. Long holding time at the liquation temperature could cause complete isothermal re-solidification of the metastable liquid with some homogenization effect, which may remove all the features of liquation and thus limit or even prevent easy detection.

Nevertheless, due to the availability of limited integrated time during most fusion welding cycles, constitutional liquation of γ' may make a very significant contribution to intergranular liquation cracking and formation of microporosity in the HAZ. Apart from reducing the cohesive strength of grain boundaries through liquid film penetration, liquation of γ' at temperatures below the solidus temperature would also in effect increase the melting temperature range during heating and thus increase the width of crack susceptible region in the HAZ. Maximum crack length in a given alloy weldment has been found to correlate well with the size of crack susceptible region during heating. Besides, high volume fraction of liquating γ' phase would increase the thickness of intergranular liquid, which could cause solute segregation to occur during re-solidification with concomitant lowering of final re-solidification temperature. The benefit of LFM in improving resistance to liquation cracking could also be rendered ineffective by the high volume fraction of liquating γ' particles. This will be discussed in more detail in the next section. Re-solidification of completely liquated intragranular γ' particles can result in microporosity as was observed in weld HAZs and Gleeble simulated materials in the present work. This could be a concern in weldments of nickel base single crystal superalloys, which do not contain grain boundary.

Summary

The increase in propensity to HAZ cracking with increasing (Al + Ti) contents of nickel base superalloys has been mainly attributed to the effects of rapid re-precipitation of γ' particles during weld cooling. As a result, efforts toward minimizing HAZ cracking in these alloys have involved overaging the γ'precipitates (with coarse particle size) to induce better ductility during welding. It has, however, been discussed in this section, that occurrence of constitutional liquation of γ' particles is possible in these alloys during welding and is more likely to occur with coarse γ' particles for a given heating rate. Increase in (Al + Ti) contents of nickel base superalloys would not only increase the volume fraction of γ'particles capable of liquating but also reduce the minimum required heating rate for particles of a given size to liquate, and the maximum γ' particle size that can withstand a particular heating rate without liquating. Constitutional liquation of γ' particles could contribute to HAZ liquation cracking by reducing the grain boundary cohesive strength through liquid film penetration and also by increasing both the melting and re-solidification temperature ranges during welding.

4.5 Grain Boundary Liquid Film Migration

4.5.1 Introduction

It was reported in the previous sections that despite the large grain size of cast IN 738, occurrence of LFM was observed in Gleeble simulated materials and in actual TIG weld-HAZs of this alloy. The present first section briefly describes the phenomenon, followed by a discussion of the possible driving forces responsible for the process in the HAZ of IN 738 alloy and plausible reasons why the alloy is still susceptible to liquation cracking despite the occurrence of extensive LFM.

4.5.2 The Phenomenon of LFM

It has been recognised that when solid solution grains are not in chemical equilibrium with the liquid material in which they are embedded, equilibration frequently occurs by dissolution and re-solidification of saturated solid solution, rather than by solid-state diffusion [238]. At small volume fractions of liquid this mechanism has the appearance of liquid film migration and has been modeled by diffusion of components of the solid through the liquid film, driven by differences in solubility in the liquid between the dissolving grain and the growing grain. Considering the diffusion of a solute into two semi-infinite solids separated by a liquid film source, two mechanisms leading to equilibration can be contrasted: solid state diffusion and liquid film migration into one of the solids. The first is relatively easily formulated and solved. For isotropic diffusion, it yields the same diffusion profile in each grain and the mirror symmetry in the solution, which existed in the initial state, is maintained by the solid-state diffusion. This

symmetry is lost during LFM. The problem of predicting which mechanism should occur can be reduced to the question of what determines the symmetry breaking that leads to LFM, and to comparison of distances of LFM with those of diffusion. The same problem of symmetry breaking at interfaces occurs during equilibration of a polycrystalline solid without a liquid phase being present. When polycrystals are exposed to solute sources and solute diffuses along the grain boundaries, grain boundaries migrate against their radii of curvature and solid solutions form only in the regions swept by the moving grain boundaries. This phenomenon, known as diffusion-induced grain boundary migration (DIGM), is observed on alloying and dealloying, for symmetrical and asymmetrical grain boundaries, and in systems with positive and negative deviations from ideal solution thermodynamics [239, 240]. The phenomenon of LFM is analogous to DIGM. Therefore, several theories proposed for DIGM are applicable to LFM as well. One of these theories is the coherency strain mechanism.

According to the coherency strain theory [241], coherency strain arises because of solute flux along the grain boundary, which usually results in lattice diffusion adjacent to the grain boundary. Since the lattice parameter is a function of concentration of solutes in solid solution, most compositional inhomogeneities will lead to a stress field. Hence, lattice diffusion can cause such a composition dependent variation in lattice parameter within the diffusion layer. The temperatures at which DIGM process is observed are such that there is negligible lattice diffusion. However, the lattice diffusion is sufficient to enrich the surface layers of the boundary with the solute, causing the change in lattice parameter. The magnitude of the of the coherency strain energy is proportional to $(a_c - a_{co})^2$, where c is the solute composition in the surface layers of the boundary and c_o is the

nominal composition of the matrix. In the case of LFM the coherency strain is caused by a solute enrichment of the matrix due to re-solidification of a metastable grain boundary liquid by back diffusion as the system strives to equilibrate. Since coherency strains would be generated on both the solid-liquid interfaces, a driving force for migration would occur only when the coherency strain stresses are different at the two interfaces. This could result from anisotropy of elastic properties in the two adjacent grains, specifically elastic modulus.

The free energy-composition diagram for an unstressed solid would be different from that of a solid in the presence of coherent stresses, as shown schematically in figure 4.66. The corresponding curve for a liquid would remain unchanged since there is no stress in the liquid. However, the compositions of the solid and liquid in equilibrium, as determined by the common tangent on the two curves, would be different from the values predicted by the equilibrium diagram. Initial back-diffusion of solute from intergranular liquid into adjacent grains could cause the grains to be stressed differentially at the diffusion zone, if the difference in their orientation dependent elastic modulus is appreciable. In situations where the two solid-liquid interfaces are stressed differently, a concentration gradient will exist across the thickness of the liquid film as shown in figure 4.67. It is this concentration gradient in the liquid film that drives the solute flux and the attendant solidification through the interface migration. The coherency strain energy is given by,

$$\Gamma_{coherency} = Y(n)\,\varepsilon^2 \qquad (4.19)$$

where Y(n) is an orientation dependent elastic modulus and ε is the coherency strain,

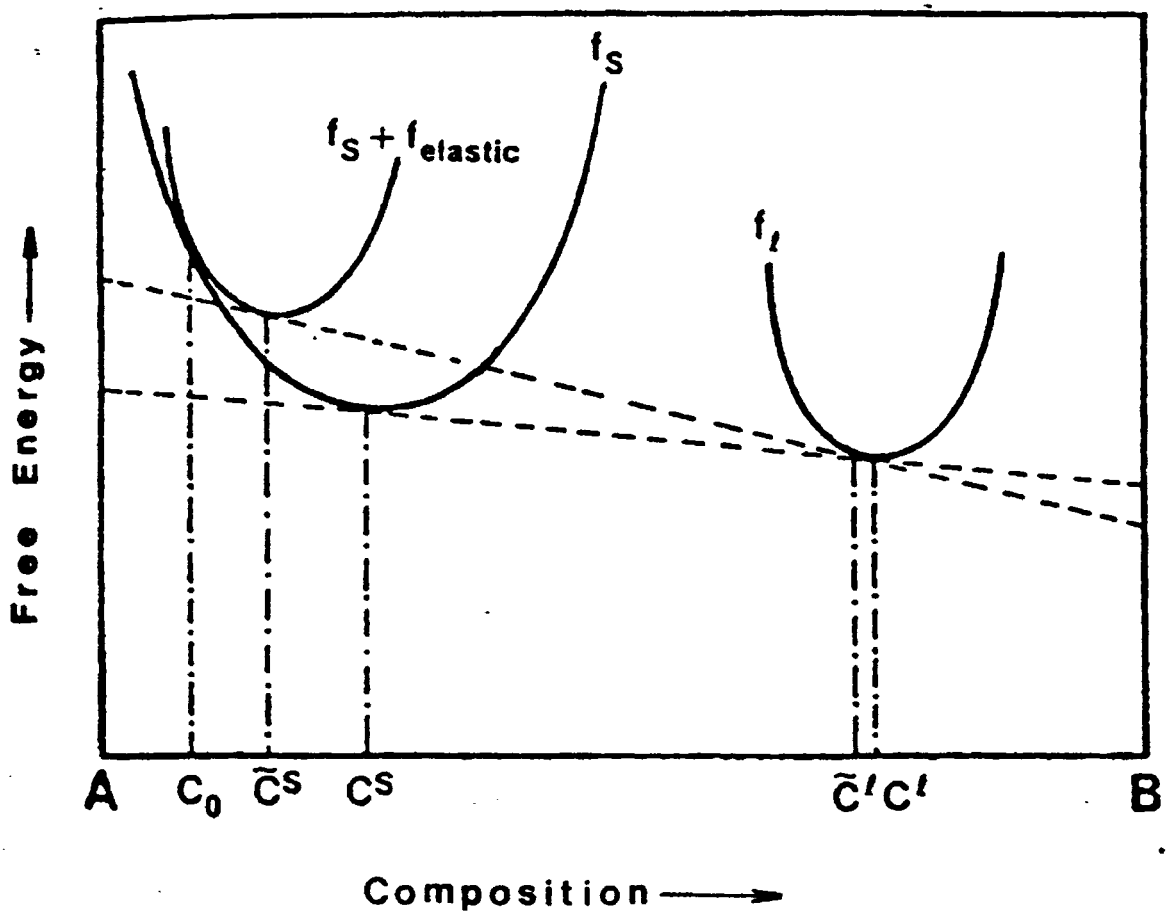

Figure 4.66: The effect of coherency stress in the matrix at the solid-liquid interface on the equilibrium compositions of solid and liquid [238].

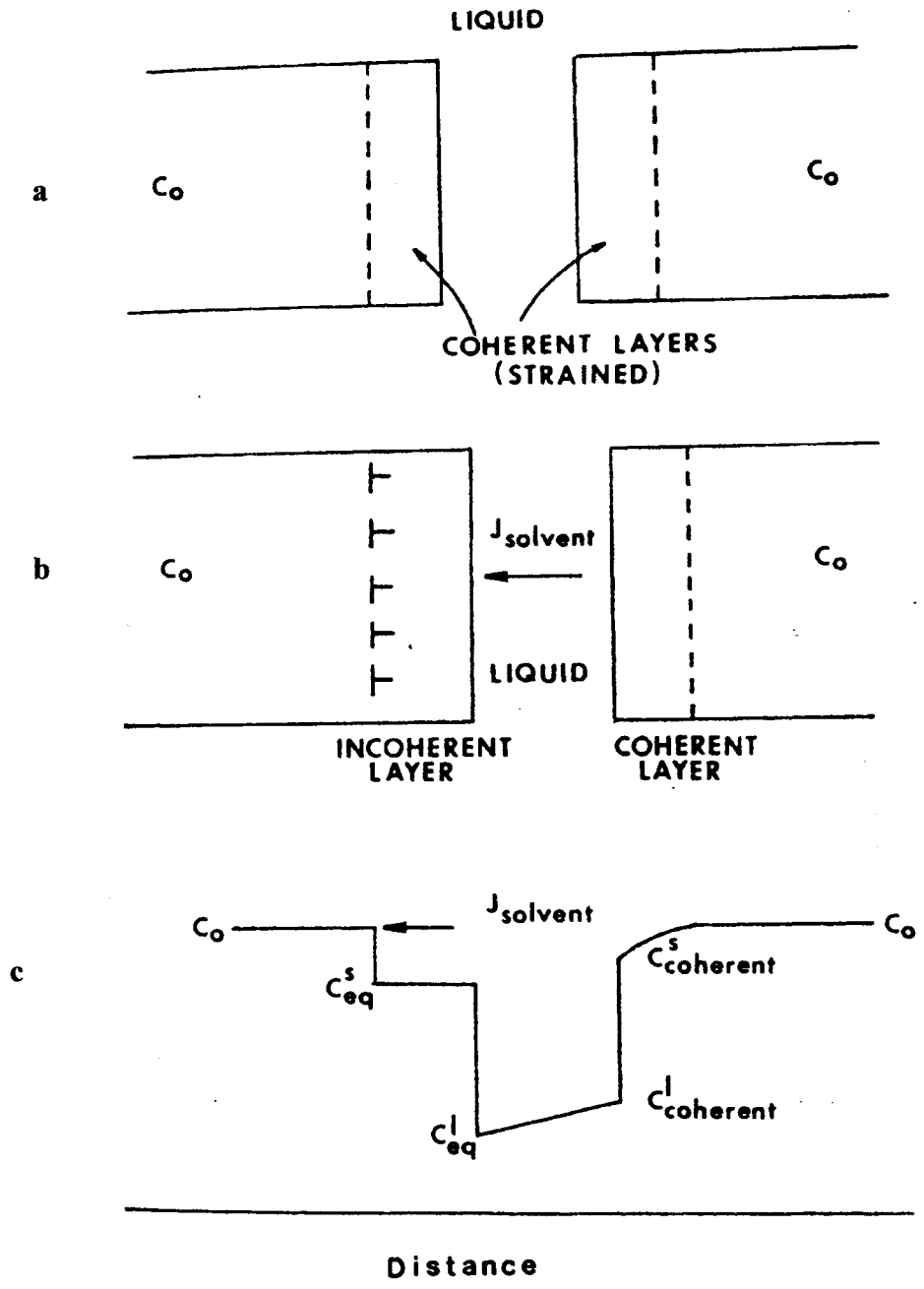

Figure 4.67: Schematic of LFM with coherency loss in one grain. (a) Diffusion in solid-liquid interface causes coherency strain in the matrix of the adjacent grains. (b) Stress relaxation occurs in one of the grains. (c) Concentration gradient set up in the liquid due to the unequal solubility of solute in the stressed and unstressed solids [238].

given by,

$$\varepsilon = (a_c - a_{co}) / a_{co} \qquad (4.20)$$

where a_c & a_{co} are the lattice parameters of the matrix in the solid-liquid interface and the grain interior respectively. As the boundary migrates, it leaves behind a solid solution, which is either alloyed or dealloyed, depending upon the sign of the concentration gradient in the liquid. The coherency strain energy is a function of the thickness of the migrated zone. At a critical thickness, the coherency strain energy becomes greater than the energy required to create dislocations in the matrix and relieve the stresses by plastic deformation in the matrix. Coherency loss can also occur nonuniformly across the grain boundary surface, because of the interaction between the coherency stress field and the local stress fields of dislocations existing in the matrix. This local stress relaxation could result in the often observed reversal in the direction of liquid film migration. The condition for equilibrium between a liquid and a stressed solid depends on the local orientation, the local curvature and the solute concentration of the interior solid. The velocity of LFM, which is a function of the differences in composition of the liquid between the two solid-liquid interfaces, can be derived from the basic laws of thermodynamics and kinetics [238].

In determining the concentration difference between the two solid-liquid interfaces and the velocity of migration, two cases are relevant. They are (i) initiation stage for the loss of coherency and (ii) steady state growth after the coherency loss. In considering the initiation of film motion, it is assumed that both grains are initially homogeneous and stress free. When solid-state diffusion begins, difference in stress forces the liquid film to migrate into the more highly stressed solid. After considerable

film migration has occurred, it is assumed that the growing grain is stress free while the dissolving grain remains coherently stressed. Before this loss of coherency in the growing grain, the concentration difference in the liquid between the two solid-liquid interfaces, ΔC, and the velocity of LFM, v, after the initial transient stage is determined by [238]

$$\Delta C = V_m/RT\ [[Y(\check{n}_A) - Y(\check{n}_B)]\eta^2(C_s - C_o)^2 + 2\sigma(K_A - K_B)]\ [C_L(1-C_L)/C_L-C_S)] \quad (4.21)$$

$$v = D_L\ V_m\ /\delta RT\ [[Y(\check{n}_A) - Y(\check{n}_B)]\eta^2(C_s - C_o)^2 + 2\sigma(K_A - K_B)]\ [C_L(1-C_L)/C_L-C_S)] \quad (4.22)$$

where D_L is the diffusivity of the solute in the liquid, δ is the width of the liquid film, $Y(\check{n}_A)$ and $Y(\check{n}_B)$ are the orientation dependent elastic modulus in grain A and B with local orientation $\check{n}_A$ and $\check{n}_B$ respectively. σ is the solid-liquid interfacial energy, C_L is the equilibrium composition of the liquid, V_m is the molar volume, η is a atomic misfit parameter and K_A and K_B are the mean radii of curvature of the solid-liquid interfaces of grains A and B, respectively.

Therefore, the velocity during initiation of migration prior to coherency loss is a function of the relative orientation difference and the difference in local curvature between the two grains. If the curvature difference is negligible, the initial direction of LFM is into the larger grain. After considerable migration has occurred, depending on the velocity, given by equation 4.22, coherency loss may occur in the growing grain or in the grain with higher Y. In the latter case, film migration, which would be initially in the direction of higher Y, would reverse directions. It can also be seen from equation 4.22 that in situations of closely matched values of Y and K, little liquid film migration occurs until stress relaxation and coherency loss occur locally. However, if the initial curvatures are so large that the $2\sigma(K_A - K_B)$ term is dominant in equation 4.22, the initial breakdown

of symmetry and direction of migration can be determined by the curvatures. The salient features of grain boundary migration by both LFM and DIGM can be summarized as:

(1) The migration results in the formation of alloyed or dealloyed zones on the concave side of the boundary, which is often revealed during metallographic observations as an etching contrast.

(2) The migration is sometimes characterized by the presence of reversal of curvature along the boundary.

(3) Both LFM and DIGM occur as a consequence of the system striving to attain equilibrium.

4.5.3 Possible Driving Forces Behind The LFM Process Observed in the Present Work.

While the phenomenon of DIGM is widely reported in the literature and occurs in several metallic and ceramic systems, the occurrence of LFM has been reported in fewer systems. Controlled studies of the migration process have been carried out by several novel techniques. One such technique involves the leaching out of the grain boundary liquid after a binary alloy is liquid-phase sintered. A ternary solute is then injected by liquid infiltration, which results in the formation of a metastable liquid. In the weld HAZ, a metastable grain boundary liquid film can form by infiltration of the grain boundary regions by liquid film produced by the constitutional liquation of second phase particles. This involves non-equilibrium melting of particle/matrix interface due to diffusion induced local concentration exceeding the liquidus composition at the peak temperature Alternatively, intergranular liquid film may also form when the local concentration

significantly lowers the melting point at the boundaries due to segregation of surface active solutes. Though microstructural evidence for LFM in the HAZ during welding existed in literature for a along time, it was not until about a decade ago that the phenomenon was recognised and attributed to LFM. Owczarski et al [4] have observed liquated grain boundary regions to migrate back and forth across a differentially etched band in simulated HAZ in Udimet 700. The occurrence of LFM in-situ in weld HAZ of superalloys has been so far reported only in wrought Inconel 718 [242] and Incoloy 903 [217] alloys, in which the liquid film is formed mainly by constitutional liquation of MC type carbides. Radhakrishnan et [242] observed LFM in the HAZ of arc spot welds in Inconel 718. Nakkalil et al [217] reported experimental evidence for the occurrence of LFM in the HAZ of electron beam welded Incoloy 903 with recrystallized grains decorated by MC carbides. As stated earlier, one of the most often reported mechanism that has been used to explain LFM is the diffusional coherency strain mechanism [241]. According to this, a rapid equilibration process is set up by lattice solute diffusion on introduction of a metastable liquid between two adjacent grains. If there is a sufficient size difference between the solute and matrix atoms, coherency strains could be developed as a result of lattice mismatch. This strain would cause a shift in the free-energy curve for the liquid-solid interface on the side of the film where coherency persists or is greatest [238]. A transverse compositional gradient in the liquid film is thus produced due to the effect of coherency strains on the free-energy curve. Solute flux down the concentration gradient in the liquid results in migration of the liquid film in order to maintain interface compositions as dictated by the free-energy curve.

In the present work, metastable grain boundary liquid was produced mainly by constitutional liquation of γ' precipitates. Constitutional liquation of γ' precipitates results in an intergranular liquid film enriched in γ' forming elements Al, Nb and Ta. The partitioning ratios of these elements (ratio of atomic concentration between γ' and γ phase) have been found to be always greater than unity in nickel base superalloys [243] including in IN 738 [136], indicating that they preferentially partition into γ' phase. In contrast however, Co and Cr exhibit a partitioning ratio less than unity [243] implying that they enrich the γ phase. The partitioning ratio of 1: < 0.5 was found consistently for Ta and Nb in all the nickel base alloys investigated by Kriege et al [243]. In the present work, EDS line scans across the migrated region and the adjacent matrix γ phase showed enrichment of the migrated regions by γ' forming elements. The substantial atomic size mismatch between γ' forming elements, especially Nb and Ta atoms, and γ matrix atoms could be a factor causing strained coherent layers which could be contributing to the forces driving the observed LFM. Even though coherency strain theory has been used to explain a number of LFM observations, some serious concerns have been raised about its role as being the major driving force behind the LFM phenomenon [244, 245].

Another principal driving force that has been recognized by several workers [217, 238, 245, 246] and integrated into LFM models as shown previously, is asymmetry of surface energy due to curvature at grain interfaces. It is known that even weak anisotropy of surface tension, as it exists at solid-liquid interface does have a strong relative effect on interface mobility. Differential surface energy at each of the solid-liquid interfaces due to grain boundary curvature can lead to variation in equilibrium solute concentrations at the interfaces. This could then set up a substantial concentration gradient within the

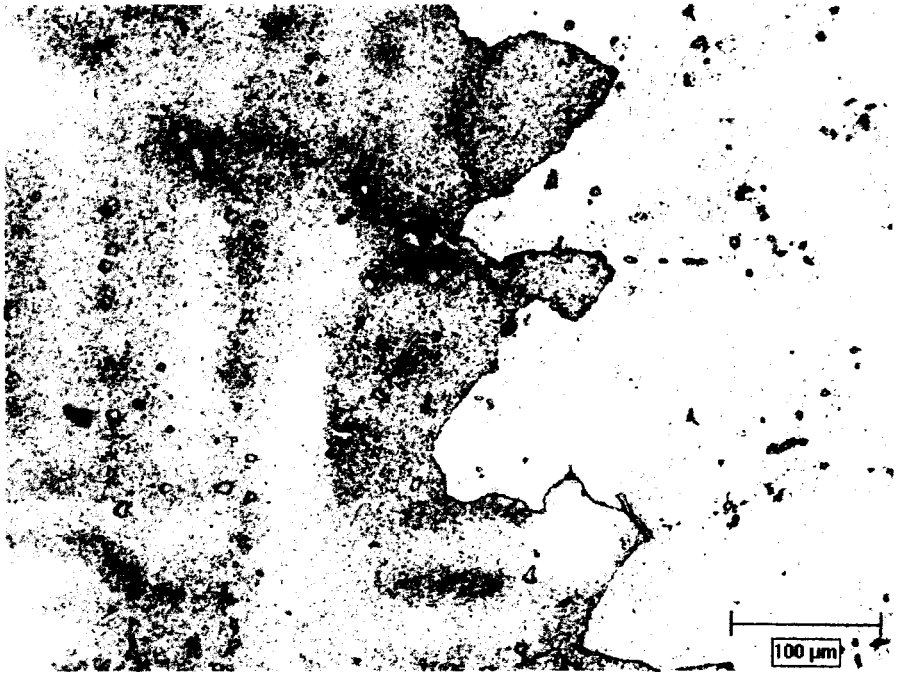

Figure 4.68: Serrated grain boundary in solution heat-treated alloy

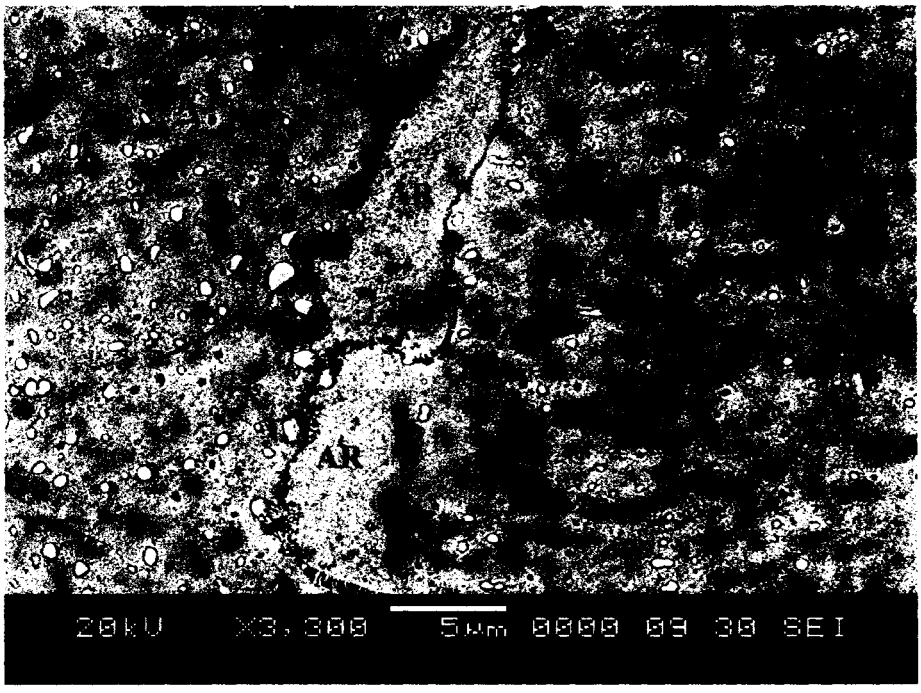

Figure 4.69: Actual Weld HAZ showing LFM features.

liquid needed for solute diffusive flux during LFM. Kirkaldy, [245] in an in-depth review and analysis of driving forces for LFM, has suggested that LFM is mainly a consequence of a broken symmetry due to unbalanced anisotropy of surface tension at the two solid-liquid interfaces. Nakkalil et al [217] have shown that grain boundary curvature is indeed a strong factor affecting migration of the grain boundary liquid film produced by constitutional liquation of Nb rich carbides in weld HAZ of Incoloy 903. In this context, straight grain boundaries or those with minimal curvature possess inherent low driving force for LFM as compared to boundaries with a considerable local curvature.

The cast IN 738 alloy used in this investigation is known to contain well rounded/ curved serrated grain boundaries even after the standard solution heat treatment [247], which was also observed in this work (figure 4.68). Consequently, asymmetry of surface energy at the solid-liquid interfaces due to significant local grain boundary curvature exhibited by this alloy could be a strong factor contributing to the occurrence of LFM in its HAZ. Furthermore, the inherent concentration gradient in liquid film produced by constitutional liquation of γ' particles [99] could also assist in driving the liquid film migration process.

4.5.4 Limitation of LFM in Precluding HAZ Liquation Cracking.

The occurrence of LFM in the HAZ of weldments has been reported by Nakkalil et al [217] to be beneficial in enhancing the resistance of an alloy to liquation cracking due to its effect in increasing the rate of elimination of grain boundary liquid film prior to the development of sufficient welding tensile stresses required to cause microcracking. In their work [217], a complete solidification of grain boundary liquid occurred via LFM

before enough thermal and mechanical restraints could be developed on weld cooling to induce cracking. However, the time required for complete migration of liquid film, which is required for total removal of the grain boundary liquid, can be expected to depend on the thickness of the film produced during welding operation. This suggestion is supported by the results of numerical modeling of the LFM process by Baker et al [248]. They showed that the time required for a liquid film of initial thickness $\delta(o)$ to completely solidify by LFM process is given by:

$$t = \delta_{(o)}/2kv_o, \tag{4.23}$$

where k is the partition coefficient of the solute and v_o is the initial migration velocity given by:

$$v_o = D_L(\Delta C)_o/(C_{L,T} - C_{S,T})\delta_{(o)}. \tag{4.24}$$

D_L is the solute diffusivity in the liquid phase, $(\Delta C)_o$ is the concentration difference across the liquid film at the start of the migration process, $C_{L,T}$ and $C_{S,T}$ are the equilibrium solute concentrations in the liquid and solid phases respectively, at the solidifying interface. It is apparent from these two expressions that an increase in film thickness will cause (1) reduction of the initial migration velocity and (2) increase in the time required for the total liquid film migration needed to remove all the liquid film. This time delay could be very significant during welding, where the time spent at welding temperatures is very limited. This model was based on the assumption that coherency is maintained in the shrinking grain while the growing grain is strain-free during migration. It was found that the coherency strain energy is a function of thickness of the migrated region [249]. At a critical thickness, the coherency strain energy becomes greater than the

energy required to create dislocations in the matrix. This could lead to loss of coherency in the shrinking grain and, of course, in the reduction of driving force for LFM. Such a reduction in driving force has been reported to result in immobility of liquid film [248]. Consequently, a thick liquid film will not only increase the time required for complete elimination of the liquid via LFM, it could also lead to a significant decrease in the driving force for the process. While a relatively thin liquid film could be effectively eliminated completely by LFM in the weld HAZ and thus preclude liquation cracking, LFM would not be as effective in this regard in systems containing thicker intergranular liquid. Therefore, the volume fraction of second phase particles, which are capable of liquating and contributing to intergranular liquid volume, would invariably affect the resistance to liquation cracking through their influence on the effectiveness of the LFM process in completely eliminating the liquid film before the onset of cracking under welding stresses.

Microstructural examination of actual weld HAZs in this work revealed the presence of LFM features, which were similar to those observed in the Gleeble simulated specimens, figure 4.68. Fine γ' precipitates, which were prevented from forming by water quenching the simulated samples, appeared to have formed during cooling within the alloyed migrated zones in weld HAZ (AR in figure 4.69). It was found that despite a considerable extent of LFM in the weld HAZ and in the Gleeble-simulated materials, grain boundary liquation cracking still occurred appreciably ahead of the migrated regions. This could be attributed to the formation of a relatively thick intergranular liquid film by constitutional liquation of intergranular and intragranular γ' precipitates, which could not be completely removed by LFM prior to the occurrence of sufficient tensile

stresses on cooling. In addition, Brechet et al [246] have made an important comment on LFM process which is applicable to discrete liquating precipitates, as were present in the present work. They stated that a complete elimination of the grain boundary liquid film would only occur under a non-steady state liquid film migration process in which no external source of solute is available. In a steady state condition where an appropriate solute source and solute transport path are provided to the grain boundary liquid film, a complete elimination of the liquid film by LFM might not be achievable. As can be seen in figure 4.47, the LFM process within sub-solidus HAZ region of IN 738 approaches a steady state migration process due to the presence of a steady source of atoms and solute transport path from liquated intragranular γ' particles into the grain boundary liquid layer. Consequently, continuous feeding of the grain boundary region with a liquid film from liquated intragranular γ' particles, which were present in significant volume (21%in ST and 30% in UMT) in pre-weld materials, coupled with a reduction in the driving force, as the migration distance increased, could be the reasons why LFM in this alloy could not prevent HAZ liquation cracking.

4.6 Mechanism of HAZ Microfissuring in IN 738

4.6.1 Introduction

In this section the results of Gleeble Hot ductility tests of IN 738 in ST and UMT heat treated conditions are first presented, follow by a discussion of the influence of grain boundary liquation on hot ductility behaviour of the alloy and occurrence of microfissuring in the HAZs.

4.6.2 Gleeble Hot Ductility Test Result

The result of Gleeble hot ductility tests of IN 738 alloy samples given the two pre-weld heat treatments (ST and UMT) are shown in Table 4.5. The alloy shows similar hot ductility behaviour in both the heat-treated conditions in terms of nil ductility temperature (NDT), nil strength temperature (NST) and low ductility recovery temperature (DRT). The alloy exhibits zero ductility at temperatures up to 1160°C and above in both ST and UMT conditions. The fracture strength decreased continuously with increase in peak temperature up to 1280°C, where the alloy exhibits practically zero strength. On cooling from 1245°C peak temperature, significant degree of ductility damage was observed in both ST and UMT samples. The alloy did not recover any noticeable ductility until the temperature was reduced to 1000°C for ST samples and 970°C for UMT samples. On-cooling strength was much less degraded compared to ductility, as substantial amount of load was required to fracture the samples during cooling to 1160°C and below in both the heat-treated conditions.

Table 4.5 Gleeble Hot Ductility Test Results

On-Heating Test				
Temperature (°C)	Ductility (Reduction in Area %)		Fracture Strength (MPa)	
	ST	UMT	ST	UMT
1050	4.5	7.5	547	475
1100	1.8	2.3	400	370
1160	nil	nil	192	162
1200	nil	nil	104	67
1245	nil	nil	81	53
1280	nil	nil	nil	nil

Table 4.5 (contd) Gleeble Hot Ductility Test Results

On-Cooling Test				
Temperature (°C)	Ductility (Reduction in Area %)		Fracture Strength (MPa)	
	ST	UMT	ST	UMT
970	1.8	0.8	660	330
1000	0.7	nil	354	302
1050	nil	nil	318	220
1100	nil	nil	134	120
1160	nil	nil	64	60
1200	nil	nil	53	49

Hot Ductility Parameter	ST Condition	UMT Condition
NDT (°C)	1160	1160
NST (°C)	1280	1280
DRT (°C)	1000	970

4.6.3 Grain Boundary Liquation, Hot Ductility and HAZ Microfissuring.

The metallurgical basis for HAZ microfissuring in fully austenitic iron and nickel base alloys has been recognised to involve the presence and persistence of low melting liquid phase on HAZ grain boundaries during welding cycle. Inability of the intergranular liquid to accommodate thermal and shrinkage stresses and mechanical constraint during cooling often lead to microfissuring. Several mechanisms have been proposed to explain HAZ grain boundary liquation. The most widely accepted being the grain boundary penetration mechanism, wherein liquid film from liquating particles like carbides, sulphide, boride etc, infiltrate and spread along the grain boundary regions. In the absence of liquating species on the grain boundaries, HAZ grain boundary liquid penetration requires the simultaneous occurrence of constitutional liquation of intragranular liquating species and grain boundary migration to the liquating particles. The penetration of the boundary by the liquid at the particle-matrix interface either pins the boundary or significantly slows its rate of migration and allows uniform wetting of the boundary by the liquid. Segregation of surface-active minor and tramp elements to grain boundaries could also cause local depression of melting temperature resulting in intergranular liquation. These liquid films serve to embrittle the HAZ grain boundaries and the presence of mechanical and/or thermally induced restraint imposed during welding and weld cooling lead to HAZ cracking.

The microstructural evidence presented in the previous sections indicates the presence of solute enriched low melting temperature liquid on the HAZ grain boundaries of IN 738 alloy. The grain boundaries in the base metal, IN 738, consist of γ-γ'eutectic constituent, M_2SC sulphocarbide particles, MC type carbides and γ' particles: The

constitutional liquation of pre-existing intergranular particles as well as some grain boundary penetration of the liquid formed by liquation of intragranular γ' and some MC carbides resulted in the formation of the low melting liquid phase on the HAZ grain boundaries. A portion of the liquid may also be associated with the grain boundary segregation induced precipitation of boron containing particles, especially in the UMT samples. The theories that have been generally adopted for explaining HAZ liquation cracking are primarily based on the concept that liquation of grain boundary locally reduces the alloys ductility and thus its capability of relaxing welding stresses. The ductility of a material during welding thermal cycle is often determined through hot ductility test. The test is based on the premise that the deformation behaviour of a material during welding thermal cycle would reflect its cracking tendency. Nippes and his associates [250] were the first to develop the technique using Gleeble system, but they have been followed by numerous other workers, who used a range of materials [251, 252].

According to this test, a material loses all ductility when the temperature reaches the nil ductility temperature on heating and exhibits practically no ductility at all the temperatures above the NDT. The nil ductility continues during cooling until the temperature is lowered to DRT where it starts to recover some ductility. It has been found that, provided the peak temperature exceeded the NDT, there is a loss of ductility and strength during cooling as compared to on-heating values, which tend to correlate with cracking behaviour. Several investigations [254-256] have shown that NDT coincides with the occurrence of grain boundary liquation in a number of different materials. It is

interesting to note that, the NDT observed in the present work coincides with the temperature at which liquation was observed in the alloy.

Lin et al [253] have developed a methodology, which characterizes a thermal crack susceptible region (CSR) in the HAZ. The CSR was theoretically derived based on the ductility of a material during welding, as obtained from Gleeble hot ductility tests and the criteria assumed in the development of liquation cracking theories. It can be described using the results of hot ductility test, by the temperature range between the liquidus T_L and NDT, which is hitherto represented by ZDRH (zero ductility range on heating). The ZDRH has been found to correlate with the width of HAZ regions in which grain boundary liquation may occur (crack susceptible region) during welding cycle. Though ZDRH represents the size of the HAZs over which liquation cracking may occur, actual occurrence of cracking will depend on some other equally important factors. These include, ductility recovery behaviour during cooling, liquid healing effect, local HAZ strain accommodation and degree of weld restraint. The ductility recovery behaviour of an alloy is normally represented by the temperature range between the peak temperature T_p and the corresponding ductility recovery temperature during cooling DRT, usually referred to as brittle temperature range BTR. This temperature range is equally important in describing susceptibility of an alloy to liquation cracking, since tensile strain (or stress) which causes cracking does not generally develop until the weld begins to cool [257]. BTR can be related to the period of time (for a given cooling rate) during which the ductility of the particular HAZ region (within the CSR) experiencing the peak temperature T_p remains negligible during cooling. The larger this zero ductility temperature range, the higher the possibility of weld cracking. The BTR, however, is a

function of the peak temperature T_p. A previous study [258] has shown that different peak temperatures resulted in a variation in the corresponding BTR. In general, an increase in the peak temperature produces a corresponding increase in the BTR. From a physical sense, different peak temperatures in an on-cooling test represent different locations in the HAZ. A peak temperature equal to the liquidus temperature T_L would represent a point at the weld fusion boundary. Farther away from the fusion line, the peak temperature decreases and the corresponding BTR decreases. There is a practical limitation on the peak temperature that can be used during a hot ductility test. This is due to the fact that the amount of melting which can be tolerated in conventional hot ductility test is limited by experimental difficulties to about 15-20% liquid. When this or smaller amounts of liquid are present, surface tension forces tend to keep a specimen intact for the brief period required to conduct the test. In practise, especially for cast materials, on-cooling hot ductility tests are usually conducted with T_p between NDT and NST. In contrast to BTR, ZDRH is constant and is material specific. This often allows the HAZ regions that are susceptible to liquation cracking to be quantified and facilitate comparison of cracking susceptibility of different alloy materials.

The DRT for a peak temperature of 1245°C in the present work was found to be about 1000°C for ST condition and 970°C for UMT condition, which are considerably below the on heating NDT (1160°C). This indicates that on-cooling ductility of IN 738 is significantly damaged by grain boundary liquation, which apparently is reflective with the alloys low resistance to HAZ microfissuring. The ZDRH of the present alloy can be estimated to be around 150°C (T_L – NDT). This relatively wide CSR compared to other austenitic alloy systems known to be resistant to HAZ cracking like Type 310 (61°C

[255]) and alloy IN 625 (102°C [255]) coupled with considerable loss of on-cooling ductility as reflected by high BTR could be an important factor contributing to the high susceptibility of IN 738 to HAZ. While the hot ductility data was useful in describing propensity of IN 738 to HAZ cracking, it does not appear to explain the alloy's differential microfissuring susceptibility as a function of the pre-weld heat treatment. As mentioned earlier, UMT condition was observed to produce a smaller degree of HAZ microfissuring as compared to ST material. The hot ductility data for the two materials, viz; ST and UMT treated is essentially the same, even slightly lower DRT in the UMT condition. This could not explain the relatively lower HAZ cracking susceptibility of the UMT treated samples.

Pre-weld heat treatment is expected to affect weldability behaviour of an alloy by influencing the following microstructural changes during heat treatment:

(i) Hardening of the material due to precipitate growth/dissolution.

(ii) Volume fraction of liquating particles.

(iii) Other phenomena like, grain growth, grain boundary segregation and atomic diffusion.

Intuitively, it could be expected that since UMT produces a softer alloy, this could be a major reason why the heat treatment is producing material with improved HAZ cracking susceptibility through its better ability to accommodate welding stresses. While this explanation might be appealing, it should also be considered that HAZ cracking is mainly taken to be caused by localized welding strain due to non-uniform contraction of the HAZs due to inhomogeneous thermal gradient as well as solidification shrinkage of the adjacent weld metal in conjunction with external mechanical restraint. Moreover base

metal hardness has not been consistent in describing HAZ cracking occurrence in superalloy weldments. In IN 718 weldment where heat treatment has also been found to influence HAZ microfissuring, it was recognised that change in hardness of the pre-weld alloy during age hardening heat treatment did not correlate with HAZ microfissuring [259]. It was rather mentioned that changes in extent of microfissuring due to pre-weld heat treatment, which was more pronounced in large grain size material, correlated with the movement of impurities to and from the grain boundaries. It is possible that the other two factors above could also be important contributing factors, considering that they determine the amount and distribution of intergranular liquid during welding cycle, which are known to significantly influence liquation cracking.

The UMT heat treatment produced higher volume fraction of γ' particles (30%) with possible grain boundary segregation of boron, both of which can result in higher volume (thicker) of intergranular liquid exhibiting excellent wetting properties during welding. This was observed in Gleeble simulated samples where thicker and continuous intergranular liquid was formed in UMT samples compared to ST samples at and above temperatures where liquation occurred. This was also apparent in welded UMT samples where higher portion of the HAZ showed evidence of liquation in the form of re-solidified constituents as compared to those in ST samples. There are several possible ways through which higher volume of intergranular liquid with good wetting properties could have promoted reduced susceptibility to microfissuring in UMT samples. It is known that for a given alloy and specific eutectic constituent, hot cracking susceptibility increases with the amount of eutectic present up to a point where the phenomenon of eutectic healing begins [87]. The amount of the constituent necessary to fully affect

eutectic/liquid healing is alloy dependent, but Clyne et al [92] suggest that at least 10 vol% is required. This value has been also supported by the work of Arata and co-worker [210]. Therefore, whether a crack will open up or not depends on the magnitude of thermal stresses/strains, amount of liquid and ease of liquid flow as controlled by wetting properties. If a large amount of liquid is present and has good wettability it can flow and heal a fissure. The observation of a number a highly liquated but seemingly uncracked grain boundaries in weld HAZ of UMT samples could be due to eutectic/liquid healing of incipient cracks caused by easy flow of large volume of intergranular liquid. To further comprehend the influence of the amount and distribution of intergranular liquid on formation of microfissuring in weld HAZs, it is in order to consider some theories that have been proposed and used to explain liquation cracking.

The cooling cycle of intergranular liquid in the HAZ is similar to the final stages of solidification of castings and welds, hence, to a first approximation, the criteria that govern weld solidification cracking can be adopted to explain liquation cracking in the HAZ of weldments. Several theories have been proposed to explain solidification cracking, these include, Shrinkage-Brittleness theory [85], the Strain theory [86] and the Generalized theory [87, 88]. The Shrinkage-Brittleness theory is of the view that at some point in the "mushy" stage between the liquidus and solidus temperatures, growing dendrites meet (coherency temperature) and interlock. During subsequent cooling, shrinkage strains develop and if a critical accommodation strain is exceeded, a tear would result in the solid-solid bridges. These newly formed fissures will then persist if there is insufficient liquid remaining to 'heal' the fissures. Pellini et al [86] in their Strain theory of hot cracking suggest that hot cracking is caused by the localized strains, set up by the

thermal gradients, tending to pull apart solid masses of material separated by essentially continuous films of liquid. In contrast to the Shrinkage-Brittleness theory, it is argued that hot tearing cannot occur during mushy stage of solidification, since the shrinkage strains are uniformly distributed. Cracking takes place only when the film stage is reached and the localized strains are exceedingly high. Borland [87, 88] in an attempt to combine the relevant ideas from the two previous theories developed the Generalized theory of hot cracking in welds and castings. According to this theory, cracking can occur in regions where high stresses can be built up between the grains such as:

(i) Separation (rupture) of highly stressed (strained) thin films separating the adjoining grains. Thick liquid films prevent cracking due to the ability of liquid volume to accommodate strains.

(ii) Breaking of solid-solid bonds in regions where the liquid coverage of grain surfaces is sufficiently extensive to allow 'breaking stresses' to be imposed on the solid-solid bridges. Extensive solid-sold bridging prevents cracking.

The observation of re-solidified constituents mostly on one side of microfissuring in the present work suggests that the microfissuring generally occurred by decohesion/separation across one of the solid-liquid interfaces rather than solid-solid fracture, thereby supporting the Strain theory and the Generalized theory, which is in agreement with most of the recent investigations on solidification cracking. According to these theories, cracking occurs during the film stage of solidification, which allows stresses to build up locally across the adjoining grains. It is considered that thick intergranular liquid would resist cracking by its capability of relaxing welding stresses by

the flow of liquid along the grain boundary regions. During solidification, as the temperature of the metal falls to a temperature which may be described, to be within the film stage, the films are relatively thick and completely continuous. At this time the extension required to develop fracture should be very high. As the metal approaches complete solidification the thickness and continuity of the films decreases in a regular fashion and accordingly the critical extension required to develop fracture should be greatly reduced. Subsequent investigations and modelling of solidification cracking in metals by other workers have suggested that when the fraction of solid, f_s, is significantly smaller than unity (typically $f_s < 0.7$ [260] or < 0.9 [92]) the flow of interdendritic / intergranular liquid relaxes the induced solidification stresses, thus reducing the stresses available for grain boundary separation to very small levels. However, when the fraction of solid approaches unity, the flow of the interfacial liquid can no longer act to reduce the strain and the remaining liquid film can act as crack initiators, since they offer little mechanical resistance.

In an alternate and/or complementary treatment, Borland [261] in his work on fundamentals of solidification cracking in welds, recognised that while continuous interfacial liquid phase provides easy extension path for an existing crack, the presence of the liquid does not necessarily account for an easy formation of the initial crack. He considered, the energies required for formation of a crack by decohesion/separation of solid-liquid components and that required to cause liquid penetration of grain boundary under the influence of stress. It was mentioned that when the liquid phase is constrained internally and is not exposed to the surface, the various possibilities are:

(i) Separation at the solid-liquid interface requiring $\gamma_{LV} + \gamma_{SV} + \gamma_{SL}$.

(ii) Separation within the liquid requiring $2\gamma_{LV}$

(iii) Penetration of liquid along the grain boundaries requiring $2\gamma_{SL} - \gamma_b$

where γ_{LV} is the liquid-vapour interfacial energy, γ_{SV} is the solid-vapour interfacial energy, γ_{SL} is the solid-liquid interfacial energy and γ_b is the solid-solid interfacial energy at the grain boundary. In order for the liquid to separate without first 'necking' down (since it is constrained by the solid walls) i.e. case (ii) above, the fracture stress would be exceedingly high and only a little less than the theoretical strength of solid. The remaining possibilities then are (i) and (iii) above i.e. that fracture initiates at the solid-liquid interface or that grain boundary penetration of the liquid occurs. He showed by assuming $\gamma_{SV} = 3\gamma_b$ and taking $\gamma_{LV} = 0$, that for systems exhibiting very low solid-liquid interfacial energy γ_{SL}, liquid penetration is the more likely event. This implies that in a good wetting system, stresses can be significantly relaxed by liquid penetration along the boundary regions. In a very recent work [262], experiments were performed to analyze the kinetics of grain boundary wetting in polycrystalline aggregates under the influence of an externally applied shear stress. It was found that in a wetting system the applied stress could be significantly relaxed by grain boundary liquid penetration.

In the above context, it is thus, possible that thicker intergranular liquid in HAZs of UMT samples with good wetting properties was more able to relax welding stresses than those present in the ST samples. It is also possible, as mentioned earlier, that such liquid flow was able to heal incipient cracks as they form in the UMT samples. A similar observation has also been reported in IN 718 superalloy where highly liquated grain boundaries caused by boron segregation appeared uncracked after welding [205]. Close examination of HAZ microfissuring in welded UMT and ST samples showed that in ST

samples, cracking occurred mostly on grain boundaries that showed smaller amount of liquation (figure 4.70). In contrast, however, several cases were observed in UMT samples, where cracking occurred mostly in front of a migration zone of highly liquated grain boundaries (figure 4.71). In addition, though some cracks were observed at the HAZ regions immediately adjacent to the fusion zone, a larger number of cracks occurred in regions quite removed from the fusion line. These cracks extended into the HAZ regions where a large portion of γ' precipitate particles had not completely liquated as can been seen in figures 4.70 and figure 4.71. Thermal simulation conducted on Gleeble system shows that these regions correspond to the sub-solidus portion of the HAZ where the peak temperature is below the bulk solidus temperature of the alloy. In lower sub-solidus HAZ regions of ST sample, intergranular liquid is more or less in the thin film stage, while thicker intergranular liquid is formed at corresponding region in UMT sample. Analysis of stresses during welding [263] has shown that the tensile stresses are generated in the HAZ after the passage of the arc i.e. during cooling, which could cause strain concentration to take place at the grain boundaries. The continuous thin intergranular liquid film in ST samples could enable such a strain concentration and thus become susceptible to cracking, which will preclude occurrence of LFM since LFM requires intimate contact between the liquid and the solid grain at both solid-liquid interfaces. In contrast, the thicker intergranular liquid in UMT samples may be able to relax the applied tensile stresses by intergranular liquid flow, which will in effect promote LFM process, until the liquid is reduced to thin film distribution ahead of the migration zone on further cooling and then become susceptible to cracking. Welding stresses may also increase with time during cooling.

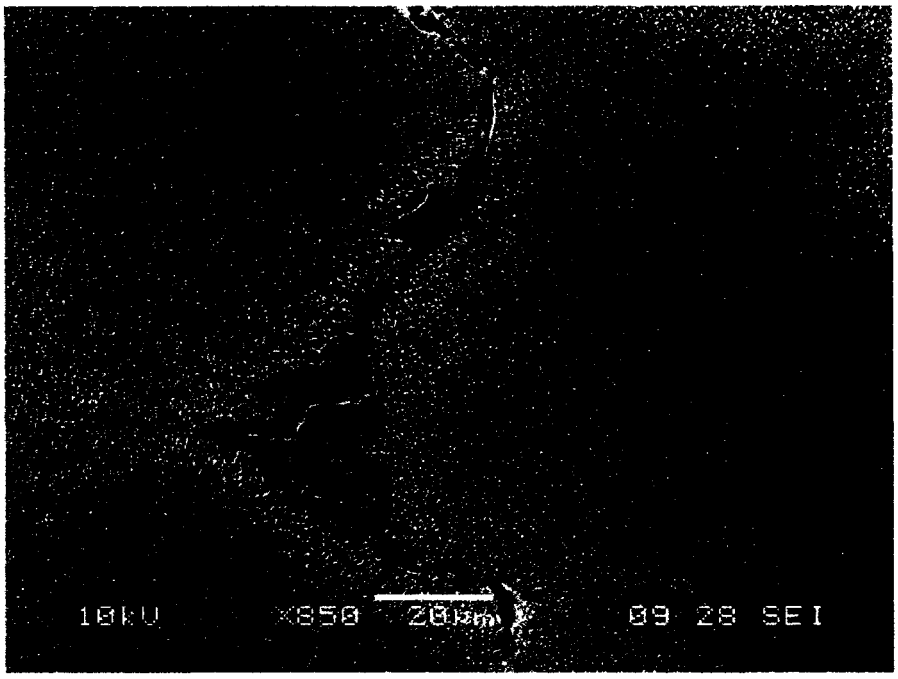

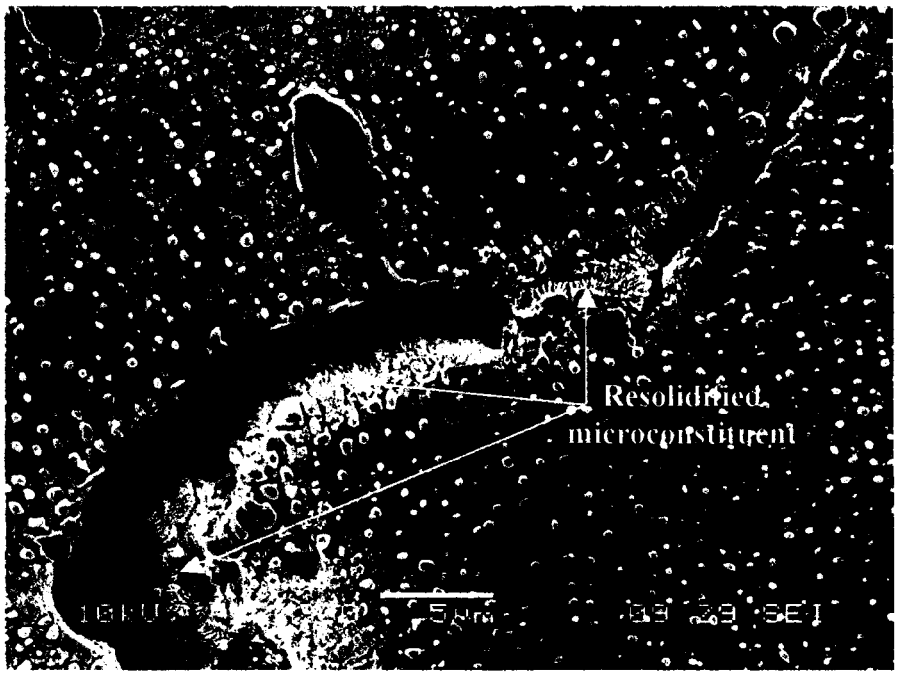

Figure 4.70: HAZ cracking in ST condition.

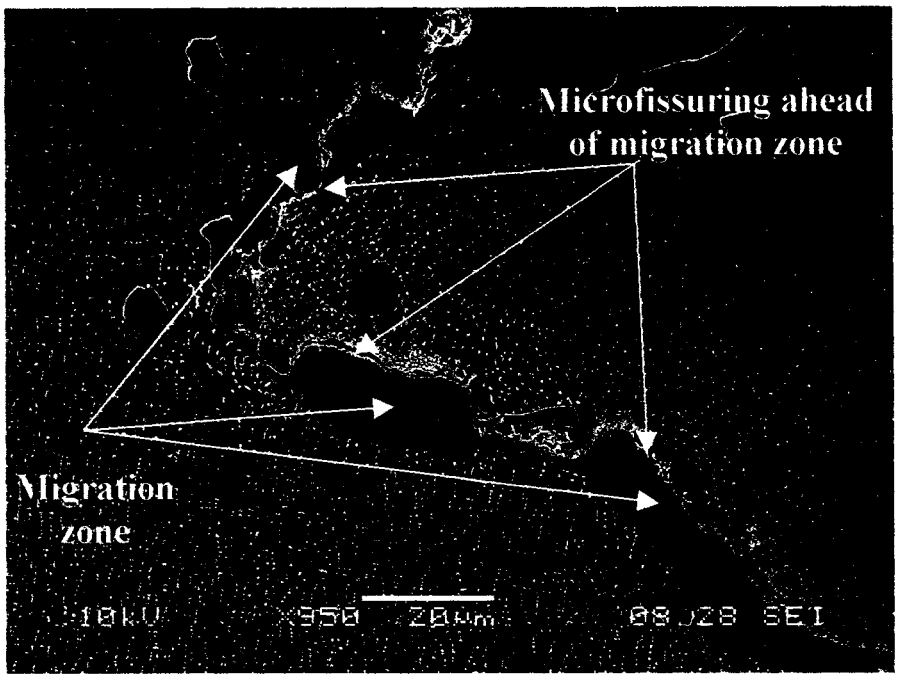

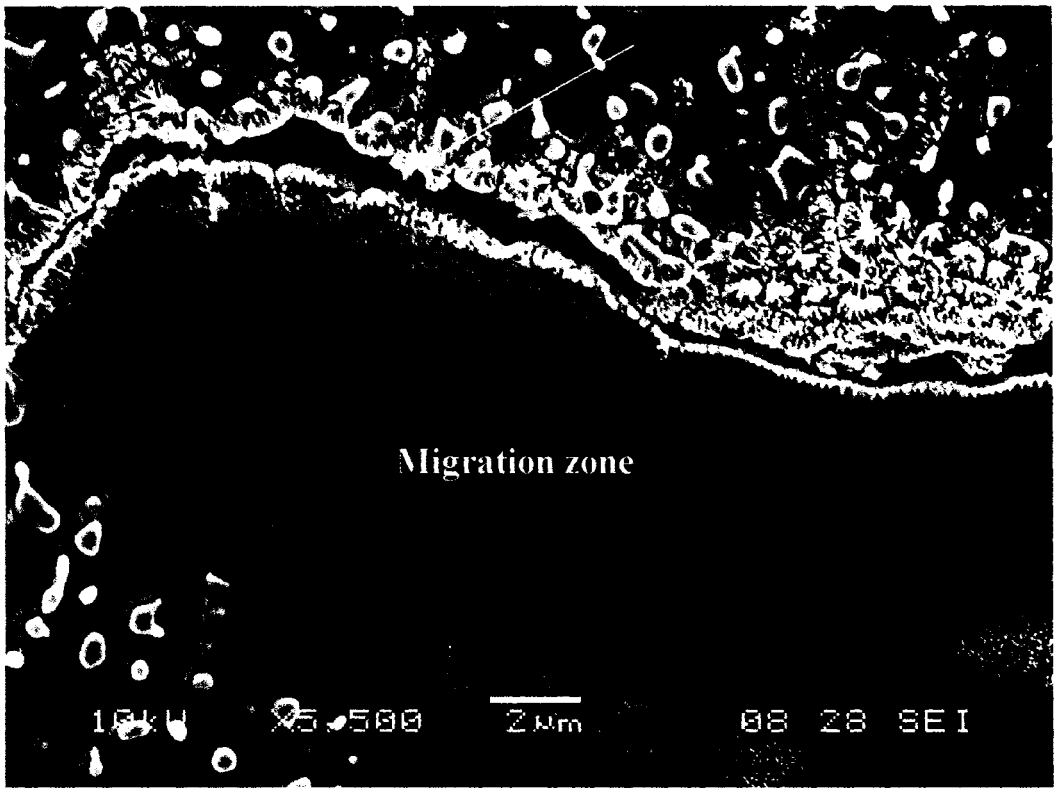

Figure 4.71: HAZ cracking in UMT condition.

This may account for the cracking observed in UMT samples ahead of the migration zones (figure 4.71). It should, however, be mentioned that even though a smaller degree of microfissuring occurred in the UMT samples after welding, the HAZ regions containing liquated but uncracked grain boundaries with re-solidified microconstituents could exhibit non-uniform deformation during stress relaxation of post weld heat treatment. This might result in crack initiation and/or propagation along such grain boundaries due to exhausting local strain concentration. It has been found that such liquated regions of welded Ni base superalloy components are most susceptible to post weld heat treatment cracking and also to rapid formation of deleterious sigma phase during service [5]. This aspect of UMT treated material needs to be studied.

Finally, it has been pointed out in many studies on fusion zone and HAZ microfissuring that the mere occurrence of a liquation reaction either by constitutional liquation or grain boundary segregation induced liquation is not sufficient to produce crack susceptible microstructure. It has been suggested that the liquid species penetrate and wet the grain boundaries in addition to causing an extended solidification temperature range. Cieslak [264] has shown that in alloy 625 even the existence of a large freezing range may not necessarily lead to microfissuring. He emphasized the need for continuous/semi-continuous distribution of intergranular liquid to incur cracking. Nakkalil et al [217] suggested that the existence of continuous/semi-continuous liquid films is not a sufficient condition to initiate microfissuring because there exists the possibility for the liquid to eliminate its supersaturation prior to crack initiation by LFM. It can be suggested from the present work that while LFM might be possible in a given system, it can be precluded by early crack formation and in cases where it happens to

occur, it can be limited in its effect by the presence of high volume fraction of liquating particles. Further, the mere presence of thick HAZ intergranular liquid with good wetting behavior does not appear to necessarily imply proportional high susceptibility to HAZ cracking. Stress relaxation by the flow of thick intergranular liquid aided by good wetting properties could promote resistance to HAZ microfissuring, coupled with the possibility of healing of incipient cracks that may form. HAZ is a complex phenomenon entwining more factors than the ones apparently known, therefore, further research on different microstructural conditions and different types of alloys is necessary to identify and confirm all the factors and their interdependence that are responsible for its occurrence.

Chapter 5

Summary and Conclusions

5.1 Base Metal Microscopic Examination

The microstructures of as-cast and those in samples given the standard solution heat treatment (ST) and the one developed at the University of Manitoba (UMT) were examined and analyzed by electron microprobe analyzer, optical, analytical scanning electron microscopy and analytical transmission electron microscopy.

1. The microstructure of as-cast IN 738 studied in this investigation consisted of γ-matrix, MC-type carbides, M_2SC sulphocarbides, γ-γ' eutectic, γ' precipitate particles and terminal solidification products.
2. The occurrence of a different eutectic-type microconstituent ahead of γ-γ' eutectic in the as-cast alloy, which is believed to be the product of terminal solidification reaction during the investment casting, was observed and discussed for the first time. The eutectic-type microconstituent consists of tetragonal M_3B_2 boride phase, Ni_5Zr and sometimes Ni_3Ti based intermetallic phases. The positive identification of M_3B_2 in the present work, which has been previously reported by x-ray diffraction analysis in heat-treated condition, shows that the boride particle is actually present in the alloy in as-solidified condition and is formed by a solidification reaction.
3. Incipient melting of the terminal solidification constituent was observed in sample heated to 1155°C at a rate of 38°C/min and held for 1 sec. This may be an important factor limiting higher solution treatment temperature (1170°C) that is

required to dissolve interdendritic γ' precipitates and eutectic γ' particles in cast IN 738 superalloy.

4. Contrary to the general believe that the MC-type carbides in this alloy are formed by crystallizing out of the liquid melt isothermally at a temperature above 1280°C, microstructural observations suggest that evolution of the carbides occurred by eutectic-type reactions over a range of temperatures which could be below 1200°C. Carbides that formed at lower temperatures were richer in severely segregating carbide forming elements Nb and Zr, as compared to those that formed at higher temperatures which were leaner in these elements but richer in Ta.
5. The standard solution heat treatment resulted in complete dissolution of γ'particles within the dendrite core with little dissolution of those within the interdendritic regions. The terminal solidification constituent consisted of M_3B_2 and Zr-rich carbides in ST condition with an apparent dissolution of the Ni-Zr intermetallic phase.
6. Microstructure of the UMT treated samples consisted of bimodal distribution of large cuboidal and smaller spheroids of γ'precipitates. A continuous network containing Cr-rich particles encased in γ' phase was observed along the interface of some γ-γ' eutectic and the adjoining grain boundaries in the UMT condition. It is suggested that these particles likely contain substantial amount of boron and/or surrounded layers of γ phase enriched with boron atoms by interfacial segregation of boron during the aging heat treatment.

5.2 Characterization of Fusion Zone Microstructure

1. The microsegregation pattern observed during solidification in the fusion zone indicated that while Co, Cr and W segregated to the γ dendrites, Nb, Ti, Ta, Mo, Al, and Zr were rejected into the interdendritic liquid.

2. The elemental partition coefficient at the beginning of solidification was determined for Cr, Co, Al, Ti, Nb, Ta, Mo, W and Ni. It is suggested that C and B also segregate into the interdendritic liquid.

3. The major secondary solidification constituent formed in the fusion zone from the interdendritic liquid consisted of cubic MC-type carbides and γ-γ' eutectic. The minor terminal solidification constituent was observed to be M_3B_2 boride and Ni_7Zr_2 intermetallic compound formed in front of some γ-γ' eutectic. The monoclinic Ni_7Zr_2 with lattice parameters a = 4.82 Å, b = 8.22 Å, c = 11.13Å and $\beta = 96.7^{o}$, was observed and reported for the first time in this investigation.

4. It is suggested that the formation of low melting terminal solidification constituent M_3B_2 and Ni_7Zr_2 in the fusion zone could pose a problem by incipiently melting during the initial stage of PWHT involving rapid heating to solution heat treatment temperature. In addition, in the case of multi-pass welding process, the terminal solidification product may reduce resistance to weld-metal liquation cracking in the underlying pass of the weldment by liquating at a relative low temperature.

5. A pseudo-ternary solidification diagram, based on Ni-Ti-C system, was developed to explain the solidification behavior of IN 738 alloy. A class II type reaction within the Ni-TiC-Ni_3Ti composition triangle adequately explained the

as-solidified microstructure of the alloy. The monovariant eutectic-type formation of MC carbides and γ-γ' eutectic as against isothermal transformation, which would be in violation of Gibbs's phase rule, was accounted for by the solidification diagram.

6. The pseudo-ternary model, in conjunction with available solidification theories were used to show that carbon addition to IN 738 contributes to the alloys relatively good resistance to solidification cracking. Carbon addition reduced the amount and influenced the distribution of interdendritic liquid towards the final stages of solidification, which promoted resistance to cracking.

5.3 HAZ Microstructure and Microfissuring

1. Even though limited information is available in the literature about weld HAZ liquation in IN 738 alloy which is known to be highly susceptible to HAZ cracking, nearly all the HAZ microfissuring observed in this work was associated with liquated grain boundaries.
2. The liquation process involved constitutional liquation of MC-type carbides, M_2SC sulphocarbide, terminal solidification constituent and γ' particles.
3. Constitutional liquation of γ' precipitate particles was observed and reported for the first time in the present investigation. Contrary to the generally accepted view that primary γ'precipitates undergo complete solid-state dissolution in the HAZ regions that experience peak temperatures above the γ' solvus temperature, it was reasoned that it is possible for these particles to survive during continuous heating, to a temperature where they can react with the γ matrix to produce liquid

phase by a eutectic-type reaction. It was shown that this occurrence would depended on the heating rate and initial particle size.

4. An alternate cause of high susceptibility of nickel-based superalloy with high content of γ'forming elements (Al + Ti >6wt%) has been proposed. Increase in (Al + Ti) contents of superalloys would not only increase the volume fraction of γ' particles capable of liquating but would also reduce the minimum heating rate required for the occurrence of constitutional liquation of γ' particle of a given size. Constitutional liquation of γ' particles can contribute to HAZ liquation cracking in the following ways: (i) by reducing the grain boundary cohesive strength through liquid film penetration (ii) by increasing the melting temperature range on heating (crack susceptible region) and re-solidification temperature range on cooling (brittle temperature range) and (iii) in cases of high volume fraction of liquating γ' particles, by limiting the benefit of liquid film migration process. In addition complete liquation of intragranular γ' particles can lead to formation of microporosity.
5. Samples given the ST pre-weld heat treatment were observed to exhibit higher degree of cracking compared to the UMT treated samples. However, more liquated but seemingly uncracked grain boundaries were observed in the UMT samples. Likewise more resolidified constituents were observed in the UMT HAZ regions than those in ST samples. Likewise, in Gleeble simulated samples, more grain boundary liquation was observed in the UMT condition as compared to ST at every temperature above 1150°C.

6. Extensive liquation of the grain boundary network containing Cr-rich $M_{23}X_6$ particles was observed in UMT sample which were simulated at 1150°C. This suggested that the network were probably surrounded by boron-enriched layers of γ and/or contained significant amount of boron, which would be aiding liquation at relatively low temperatures.
7. Grain boundary liquid film migration was observed in simulated HAZs and in actual weld HAZs of IN 738 alloy, and were reported for the first time. The suggested possible driving forces for its occurrence in the present alloy include (i) diffusional coherency strain caused by substantial atomic size mismatch between γ' forming elements, (ii) asymmetry of surface energy at the solid-liquid interfaces due to a significant local grain boundary curvature exhibited by the serrated grain boundaries of the alloy (iii) inherent concentration gradient in liquid phase produce by constitutional liquation phenomenon.
8. The benefit of LFM in preventing HAZ cracking was rendered ineffective in this alloy by the high volume fraction of liquating γ' particles. The continuous feeding of the grain boundary regions with a liquid film from liquated intragranular γ' particles couple with reduction in driving force as the migration distance increased for thick intergranular liquid, are suggested to be responsible for the inability of the LFM to preclude microfissuring.

5.4 Gleeble Hot Ductility Tests and Mechanism of HAZ Microfissuring in IN 738 alloy

1. The ST and UMT treated samples exhibited a similar hot ductility behavior, and the nil ductility temperature (NDT) and nil strength temperature (NST) for the alloy were estimated to be around 1160°C and 1280°C respectively.
2. The temperature at which grain boundary liquation was observed correlated with that at which the alloy exhibit zero ductility on heating. The on-cooling ductility was significantly damaged by liquation as evident in considerably low ductility recovery temperature (DRT) in samples heated to 1245°C peak temperature (T_p). The DRT for UMT and ST conditions is estimated to be around 970°C and 1000°C respectively.
3. The relatively wide crack susceptible region depicted by on heating zero ductility temperature range, estimated to be around 150°C (T_L – NDT) coupled with considerably lower on-cooling ductility recovery temperature as reflected by high brittle temperature range (T_p – DRT), are suggested to be plausible factors contributing to the high susceptibility of IN 738 to HAZ microfissuring.
4. The lower susceptibility of UMT treated samples to HAZ cracking cannot be explained by the hot ductility data in this investigation. Pertinent solidification theories were evoked to indicate that the higher intergranular liquid with good wetting properties could be a factor contributing to lower HAZ microfissuring in the UMT condition. It was reasoned that stress relaxation by the flow of thick intergranular liquid aided by good wetting properties promoted resistance to

HAZ microfissuring, in addition to the possibility of healing of incipient cracks in UMT samples.

5. The combination of a susceptible microstructure due to grain boundary liquation described in this work, thermal and shrinkage stresses generated and mechanical constraint imposed during weld cooling are salient factors contributing to HAZ microfissuring in cast IN 738 superalloy.
6. Adequate consideration of the different types of liquation phenomena elucidated by this study in conjunction with the effects of rapid precipitation of γ' is indispensable towards the development of appropriate and suitable pre-weld and post weld heat treatment to minimize HAZ microfissuring in IN 738 weldment.

Chapter 6

Suggestions for Future Work

1. The effect of heat treatment on solid state dissolution of the terminal solidification reaction product and, thus, on homogenization of the as-cast microstructure should be examined.
2. Several combinations of pre-weld heat treatments and different welding parameters with various welding techniques need to be studied to identify an optimum combination that produces minimal HAZ microfissuring. In order to reduce or prevent constitutional liquation of γ' precipitates, pre-weld heat treatment that would dissolve all the primary and eutectic γ' particles without causing incipient melting is recommended.
3. The use of pre-heating prior to welding of specimens given various pre-weld heat treatments should be studied to investigate the benefits of minimizing welding stresses on HAZ microfissuring through pre-heating technique.
4. The use of different filler alloys for welding the IN 738 in various pre-weld heat treated conditions, including sufficiently homogenized condition, should also be explored.
5. The effect of post weld heat treatment on liquation of terminal solidification microconstituents observed in the fusion zone in the present work, as well as on re-solidified product in the HAZ should be properly studied to improve the weldability of the alloy.

References

1. Bieber, G.C., and Mihalisin, R.J., 2nd International Conference on the Strength of Metals and Alloys, Asilomer, ASM Vol. IV, p. 1031.
2. Prager, M. & Shira, C. S., Welding Research Council Bulletin No 128, 1968.
3. Haafkens, M. H. and Matthey, G. H., Welding Journal, 61, 25 (1982).
4. Owczarski, W. A., Duvall, D. S. and Sullivan, C. P., Weld. Jour., 45, 145-s (1966).
5. Owczarski, W. A., Welding Research Council, New York, 6 (1969).
6. Ernst, S. C., Baeslack III, W. A. and Lippold, J. C., Weld. Jour., 68, 418-s (1989).
7. Alloy IN-738: Technical Data INCO, New York, p. 1- 11.
8. Kattus, J. R., Non Ferrous Alloys, March 1984, p. 7.
9. Koul, A.K. and Castillo, R., Metallurgical Trans., Vol. 19A, Aug. 1988, p. 2049.
10. Garosshen, T.J and McCarty, G.P., Metallurgical Trans., Vol. 16A, 1985, p. 1213.
11. Ardell, A. J., Metallurgical Trans., Vol. 16A, Dec. 1985, p. 2131.
12. Footner, P.K and Richards, B.P., Journal of Material Science, Vol. 17, 1982, p. 1007.
13. Larson, J. M., Metallurgical Trans., Vol. 7A, 1976, p. 1497.
14. Bradley, E. F., et al., "Superalloys: a Technical Guide" Metals Park, Ohio, ASM International, 1988, p. 58.
15. Rong, Y. H., et al., Electron Microscopy 1986, Vol. 1[Proc. Conf.], Kyoto Japan, 1986, p.879.
16. Hoffelner, W., Kny E. Stickler, R. and McCall, W. J., Z. Werktofftech, 10, 84 (1979).
17. McColvin G. M., Met. Sci., Vol. 11, 1977, p. 447.

18. Steven, R. A. and Flewitt, P. E. J., Journal of Mat. Sci., Vol. 13, 1978, p. 367.

19. Raynor D., and Silcock, J. M., Metal Sci., J., Vol. 4, 1970, p. 121.

20. Brown, L. M. and Ham, R. K., Strengthening Methods in Crystals, Elsevier, Amsterdam, 1971, p. 9 – 135.

21. Gerold, V., and Haberkorn, H., Phy. Stat. Sol., Vol. 16, 1966, p. 675.

22. Jackson, J. J., Donachie, M. J., Henricks, R. J., and Gell, M., Met. Trans., Vol. 8A, 1977, p. 1615.

23. Beardmore, P., Davies, R. G. and Johnston, T. L., Trans. of AIME, Vol. 245, 1969, p 1537.

24. Orowan, E., Symposium on Internal Stresses in Metals, Institute of Metals, London, 1948, p. 451.

25. Mitchell, W. I., Z. Metall., Vol. 57, 1966, p. 586.

26. Hazotte, A. and Simon, A., Proc. 1st ASM Europe Tech. Conf. On Advanced Materials and Processing, Techniques for Structural Applications Paris 7-9 Sept. 1987, (ed.) T. Khan, and A. Lasalmonie, p. 83.

27. Gentry, W. O. and Fine, M. E., Acta Met., Vol. 20, 1972, p. 181.

28. Grosdidier T., Hazotte, A. and Simon, A., Mat. Sci. and Eng., Vol. A256, 1998, p 183.

29. Ardell, A. J., Acta Met. Vol. 20, 1972, p 61.

30. Savage, W. F., Welding Design and Fabrication, Vol. 42, 1969, p. 56.

31. David, S. A. and Vitek, J. M., Inter. Mat. Rev., Vol. 34, 1989, p. 213.

32. David, S. A. and Liu, C. T., Weld. J., Vol. 61, 1982, p. 157s.

33. Savage, W. F., Weld. World, Vol. 18, 1980, p. 89.

34. Hellawell, A. and Herbert, P. M., Proc. Roy. Soc., Vol. A269, 1962, p 560.

35. Rohatgi, P. K. and Adams, Jr C. M., Trans. AIME Vol. 239, 1967, p. 1729.

36. Flemings, M. C., Poirier, D. R., Barone, R. V. and Brody, H. D., J. Iron Steel Inst., Vol. 208, 1970, p 371.

37. Hunt, J. D., 'Solidification and Casting of Metals', The Metals Society, London, 1979.

38. Flemings, M. C., Solidification Processing', McGraw-Hill, New York, 1974.

39. Bouchard, D. and Kirkaldy, J. S., Metall. Mater. Tran. Vol. 28B, p. 651, 1997.

40. Jordan, M. F. and Coleman, M. C., Br. Weld. J., Vol. 15, 1968, p. 552.

41. Brody, H. D., in 'Advances in Welding Science and Technology', (ed. David, S. A.) Vol. 83, 1987, ASM Inter. Metals Park, OH, USA.

42. Burden, M. H. and Hunt, J. D., J. Cryst. Growth, Vol. 22, 1974, p. 109.

43. Boettinger, W. J. and Coriell., S. R., Mater. Sci., Eng., Vol. 65, 1984, p. 27.

44. Easterling, K., in Introduction of the Physical Metallurgy of Welding, Butterworths, 1985.

45. Peacock, H. B., Weld. Res. Council Bull., No 177, 1972.

46. Schwenk, W. and Trabold, A. F., Weld. J., Vol. 42, 1963, p. 460s.

47. Owczarski, W. A. and Sullivan, C. P., Weld. J., 1965, p. 241s.

48. Adam P., in 'High Temperature Alloys for Gas Turbines', Applied Science Publishers, London, (ed. Coutsouradis et al), 1978, p. 737.

49. Wallace W., Proceedings of the Conference on Advanced Fabrication Techniques in Powder Metallurgy and their Economic Implications, AGARD-CP-200, SC. 7, 1976.

50. Owczarski, W. A., AGARD, NATO, No LS-91, 1977.

51. Owczarski, W. A., Duvall, D. S. and Sullivan, C. P., Weld. J., Vol. 46, 1967, p. 423s.

52. Radhakrishnan, B. and Thompson, R. G., Met. Trans. A, Vol. 23A, 1992, p. 1783.

53. Radhakrishnan, B. and Thompson, R. G., Met. Trans. A, Vol. 24A, 1993, p. 1409.

54. Baeslack, W. A. III, Lata, W. P. and West, S. L., Weld. J., Vol. 67, 1988, p. 77s.

55. Hughes W. P. and Berry, T. F., Weld. J., Vol. 46, 1967, p. 361s.

56. Carlton, J. B. and Prager, M., Weld. Res. Council Bull., No 150, 1970.

57. Thompson, E. G., Nunez, S. and Prager, M., Weld. J., Vol. 47, 1968, p. 299s.

58. D'Annessa A. T. and Owens, J. S., in 'Procedures for avoiding heat-treat cracking in nickel-base superalloy weldments', Technical Report AFML-TR-70-224, Air Force, Materials Laboratory, Wright-Patterson Air Force Base, Ohio, 1970.

59. Thamburaj, R., Goldak, J. A. and Wallace, W., SAMPE Q, Vol. 10, 1979, p. 6.

60. Jordan, D. E. and Richards, E. G., in 'Heat Treatment Aspects of Metal Joining Processes' The Iron and Steel Institute, London, 1972, 71

61. Burdekin, F. M., in 'Heat Treatment Aspects of Metal Joining Processes' The Iron and Steel Institute, London, 1972, 6.

62. Thamburaj, R., Wallace, W. and Goldak, J. A., in 'Powder metallurgy of superalloys. Aerospace materials for the 1980s', Metal Powder Report Conf., Zurich, Nov. 1980, Paper 25, Metal Powder Report Publishing Services.

63. Lucas, M. J. and Jackson, C. E., Weld. J., 1970, Vol. 49, p 46s.

64. Arata, Y., et al, Tran. JWRI, 1976, Vol. 5, p 119.

65. 1976 Welding Handbook, Vol. 1, 7th Edition, America Welding Society, Miami.

66. Boland, J. C., Br. Weld. J., Vol. 10, 1960, p.623.

67. Randall, M. D., Monroe, R. E. and Rieppel, P.J., DMIC Report 165, Columbus, OH, Battelle Memorial Institute, 1961.

68. Savage, W. F. and Lundin, C. D., Weld. J., Vol. 44, 1965, p. 433s.

69. Savage, W. F., Nippes, E. F. and Goodwin, G. M., Weld. J., Vol. 56, 1977, p. 245s.

70. Lundin, C. D., Lingenfelter, A. C., Grotke, G. E., Lessmann, G. G. and Matthews, S. J., Weld. Res. Council Bull., No 280, 1982.

71. Lessmann, G. G. and Gold, R. E., Weld. J., Vol. 50, 1971, p. 1s.

72. McKeown, D., Metal Construction, Vol. 8, 1970, p. 351.

73. Nippes, E. F., Savage, W. F., Bastian, B. J., Mason, H. F. and Curran R. M., Weld. J., Vol. 34, 1955, p.183s.

74. Lundin, C. D., Qiao, C. Y. P., Gill, T. P. S. and Goodwin, G. M., Weld. J., 1993, p 189s.

75. Muesch, H., Welding of Materials TP 347 mod., Mannesmann Research Institute, Duisburg, 1984.

76. Donati, J. R. and Zacharie, G., Review de Metallurgie, Vol. 71, 1974, p. 905.

77. Williams, C. S., Weld. J., Vol. 42, 1963, p. 1s.

78. Kriescher, C. H., Weld. J., Vol. 42, 1963, p. 49s.

79. Donati, J. R. and Zacharie, G., Revue de Metallurgie, Vol. 71, 1974, p. 905.

80. Owczarski, W. A., Weld. J., Vol. 46, 1967, pp. 63s,73s,93s.

81. Blum, B. S. and Witt, R. H., Weld. J., Vol. 42, 1963, p 365s.

82. Vagi, J. J. and Martin, D. C., Weld. J., Vol. 35, 1956, p 137s.

83. Yeniscavich, W., in Superalloy I, ed. Sims, C. T., Stoloff, N. S. and Hagel, W. C., 1987.

84. Lundin, C. D., Lee, C. H. and Qiao, C. Y. P., 'Weldability and Hot Ductility Behaviour of Nuclear Grade Austenitic Stainless Steels', Knoxville, TN, University of Tennessee.

85. Pumphrey, W. I. and Jennings, P. H., J. Inst. Metals, Vol. 75, 1948, p. 235.

86. Pellinni, W. S., Foundry, Vol. 125, 1952, pp. 124, 192, 194, 916, 199.

87. Borland, J. C., Br. Weld. J. Vol. 7, 1960, p. 508.

88. Borland, J. C., Welding and Metal Fabrication, Vol. 47, 1979, p. 19.

89. Vero, J., Metal Ind. (Lond.), Vol. 48, 1936, p 431,491.

90. Medovar, B. I., Automatic Welding, Vol. 7, 1954, p. 12.

91. Smith, C. S., Trans. AIME, Vol. 175, 1948, p. 15.

92. Clyne, T. W. and Davies, G. J., TMA Proc. Int. Conf. Solidification, Sheffield, p. 275.

93. Stoloff, N. S. and Kelly, M. J., Met. Trans. Vol. 6A, p. 159.

94. Nicholas, M. G. and Old, C. M., J. Mat. Sci., Vol. 14, 1979, p. 1.

95. Kamdar, M. H., in 'Embrittlement of Engineering Alloys', edited by Briant, C. L., and Banerji, Academic Press, New York, 1983, p. 361.

96. Roth, R. G., Weatherly G. C. and Miller, W. A., Acta Met., Vol. 26, p. 841.

97. Williams, J. A. and Singer, A. R. E., J. Inst. Metals, Vol. 96, 1968, p 5.

98. Robertson, W. M., Trans. AIME Vol. 236, 1966, p. 1478.

99. Pepe, J. J. and Savage, W. F., Weld. J., Vol. 46, 1967, p. 411s.

100. Aronson, A. N., M.S Thesis, Rensselaer Polytechnique Inst., Troy, New York, 1963.

101. Weiss, B., Grotke, G. E. and Stickler, R., Weld. J., Vol. 49, 1970, p. 471s.

102. Brooks, J. A., Weld. J., Vol. 53, 1974, p. 517s.

103. Nakkalil, R., Richards, N. L. and Chaturvedi, M.C., Metall. Trans. Vol. 24A, 1993, p. 1169.

104. McLean, D., Grain boundaries in Metals, Oxford University Press, Oxford, United Kingdom, 1957.

105. Hondros, E. D. and Seah, M. P., Int. Metall. Rev., 1977, p. 262.

106. Westbrook, J. H. and Aust, K. T., Acta Metall., Vol. 1, 1953, p. 1151.

107. Taylor, K. A., Metall. Trans., Vol. 23A, 1992, p. 107.

108. Guttmann, M., Surf. Sci., Vol. 53, 1975, p. 213.

109. Kujanpaa, V. P., David, S. A. and White, C. L., Weld. J., Vol. 66, 1987, p. 221s.

110. Thompson, R. G., Radhakrishnan, B. and Mayo, D. E., J. Phys., Vol. 49, 1988, p. 471.

111. Huang, X., Richards, N. L. and Chaturvedi, M.C., Metall. Mater. Trans. Vol. 27A, 1996, p. 785.

112. Chaturvedi, M.C., Chen, W., Saranchuk, A. and Richards, N. L., in Proc. of Superalloys 718, 625, 706 and Various Derivatives, (ed. Loria, E. A.), The Minerals, Metals and Materials Society, 1997, p. 743.

113. Kelly, T. J., in Advances in Welding Science and Technology, (ed. David, S. A.), ASM International, Metals park, OH, 1986, p. 623.

114. Guo, H., Chaturvedi, M. C., Richards, N. L., and McMahon, G. S., Scripta Mater. Vol. 40, 1999, p. 383.

115. Duvall, D. S. and Owczarski, W. A., Weld. J., Vol. 45, 1966, p 356s

116. Romig, A. D. Jr., Lippold, J. C. and Cieslack, M. J., Metall. Trans. 19A, 1988, p. 35.

117. Chou, Y. T., Li, Y. Z., and Liu, C. T., Metall. Mater. Trans. Vol. 27A, 1996, p 3473.

118. Gupta, S. P. and Nakkalil R., Acta Metall. Mater., Vol. 38, 1990, p. 1871.

119. Geise, J. and Herzig, C., Zeitschrift fur Metallkunde, Vol. 76, 1985, p 622.

120. Patil, R. V. and Sharma, B. D., Met. Sci., Vol. 16, 1982, p 389.

121. Savage, W. F. and Krantz, B. M., Weld. J., 1966, p. 13s.

122. Thompson, R. G. and Genculu, S., Weld. J., Vol. 62 1983 p. 337s.

123. Thakur, A., Richards, N. L. and Chaturvedi, M. C., Inter. Journal for Joining of Materials, 15, 21 (2003).

124. Goldstein, J. I., Newbury, D. E., Echlin, P., Joy, D. C., Fiori, C. E. and Lifshin, E., Scanning Electron Microscopy and X-ray Microanalysis, Plenum Press, New York, NY, 1981.

125. Lundin, C. D., Qiao, C. Y. P., Lee, C. H., Proc. of Weldability of Materials Conf. Detroit, Michigan; ASM International, Materials Park, OH. USA, 1990. p 1.

126. Tiller, W. A., Rutter, J. W., Johnson, K. A. and Chalmers, B., Acta Metall. Vol. 1, 1953, p. 428.

127. McLean, M and Schubert, F., in 'High Temperature Alloys for Gas Turbines', Applied Science Publishers, London, (ed. Coutsouradis et al), 1978, p. 423.

128. Quested, P. N. and McLean, M., Conf. On Solidification Technology in the Foundry and Cast House, Published by The Metals Society, England, pp. 586 (1980).

129. Taha, M. and Kurz, W., Z. Metallkd. 72 (1981) 546.

130. Bartholomew, D. M., Jezuit, M., Watts, B. and Hellawell, A., in Solidification of Metals and Alloys, The Metals Society, Sheffield, 1977, p. 29.

131. Doherty, R. D. and Feast, A., in The Solidification of Metals, Brighton, 1967, p. 102.

132. Nakao, Y. and Shinozaki, K., in Proceedings of International Conference on High Temperature Materials for Power Engineering II, Liege, Belgium, Sept. 1990, p 24.

133. Westbrook, J. H., Z. Kristallogr., Vol. 110, 1958, p. 21.

134. Ricks, A., Porter, A. J. and Ecob, R. C., Acta Metall., 1983, Vol. 31, p. 43.

135. Rosenthal R. and West D. R. F., Mat. Sci. and Tech., 15, 1387 (1999).

136. Zhang, J. S., Hu, Z. Q., Murata, Y., Morinaga, M. and Yukawa, N., Metall. Trans. Vol. 24A, 1993, p.2443.

137. Sallemark, R., Progress Report 2 Cost 50 Programme Sweden, 1975.

138. David, S. A., Vitek, J. M., Babu, S. S., Boatner, L. A. and Reed, R. W., Sci. and Tech. Weld. Joining, Vol. 2, 1997, p. 79.

139. Tewari, S. M., Vijayakumar, M., Lee, J. E., Curreri, P. A., Mater. Sci. Eng. A., Vol. A141, 1991, p. 97.

140. Zhu, Y., Zhang, S., Xu, L., Jing, B., Zhuangqi, H. and Shi, C., Superalloys 1988, The Metall. Society/AIME p. 703.

141. Whelan, E. P., J. Inst. Metals, Vol. 100, 1972, p. 333.

142. Scarlin, R. B., Scripta Metall., Vol. 10, 1976, p. 711.

143. Rosenthal R. and West D. R. F., Mat. Sci. and Tech., 2, 169 (1986).

144. Wallace, W. et al, J. Testing Evaluation, Vol. 3, 1975, p. 113.

145. Doherty, J. E. et al, Can. Met. Q., Vol. 13, 1974, p. 229.

146. Johnson, W. C. et al, Scripta Metall., Vol. 8, 1974, p. 971.

147. Whelan, E. P. and Grzedzielski, M. S., Metals Tech. Vol. 1, 1974, p. 186.

148. Nowotry, H. et al, Planseeber Vol. 12, 1964, p. 13.

149. Holt, R. T. and Wallace, W., Inter. Metals Rev. 1976, p. 1-21.

150. Collins, H. E., Trans. ASM, Vol. 62, 1969, p. 82.

151. Mihalisin, J. R., Biever, G. G. and Grant, R. T., Trans. TMS-AIME, Vol. 242, 1968, p. 2399.

152. Liu, L., Fu, H. Z. and Zhi, Z. X., Acta Metallurgica Sinica (English ed.) Vol. 3A, 1990, p. 46.

153. Liu, L., Sommer, F. and Fu, H. Z., Scripta Metall. Mater., Vol. 30, 1994, p. 587.

154. Bower, T. E., Brody, H. D. and Flemings, M. C., Trans. AIME, Vol. 236, 1966, p. 624.

155. Lecomte-Beckers, J., Metall. Trans., Vol. 19A, 1988, p. 2333.

156. Starink, M. J., Cama, H. and Thomson, R. C., Scripta Mater. Vol. 38, 1998, p. 73.

157. Vincent, R., Acta Metall., 33 (1985) 1205.

158. Ouichou, L., Lavaud, F. and Lesoult, G., Superalloys 1980, American Society for Metals, Metals Park, OH USA, 1980, p. 235.

159. Yunrong, Z., Yuping, W., Jizhou, X., Caron, P. and T. Khan, in Proceedings of Superalloys Conference 1988, edited by S. Reichman, D. N. Duhi, G. Maurer, S. Antolovich and C. Lund, (The Metall. Society/AIME, 1988) p. 335.

160. Zhu, Y., Zhang, S., Zhang, T., Zhang, J., Hu, Z., Xie, X. and Shi, C., Superalloys 1992, The Minerals, Metals and Materials Society, 1992, p. 145.

161. Zou, J., Wang, H. P., Doherty R. and Perry, E. M., in Proceedings of Superalloys Conference 1992, edited by S. D. Antolovich, R. W. Stusrud, R. A. Mackay, D. L. Anton, T. Khan, R. D. Kissinger and D. L. Klarstrom (The Minerals, Metals & Materials Society 1992) p. 165.

162. Zou, J., Wang, H. P., Doherty R. and Perry, E. M., in Proceedings of Modeling of Casting, Welding and Advanced Solidification Processes. VI, Florida, USA, 1993, published by The Minerals, Metals & Materials Society 1992, p. 95.

163. Willemin, P. and Durand-Charre, M., J. Mater. Sci. Vol. 25, 1990, p. 168.

164. Hu, Z. Q., Sun, W. R. and Guo, S. R., Acta Metall. Sinica, (English Ed.) Vol. 9, 1996, p. 443.

165. Sun, W. R., Lee, J. H., Seo, S. M., Choe, S. J. and Hu, Z. Q., Mater. Sci. Tech., Vol. 15, 1999, p. 1221.

166. Bouse, G. K., Proc. Conf. On 'Superalloys 96', Champion, PA, USA, 1996, paper 11.

167. Zhang, J. S., Hu, Z. Q., Murata, Y., Morinaga, M. and Yukawa, N., Metall. Trans. Vol. 24A, 1993, p.2451.

168. Cieslak, M. J., Knorovsky, G. A., Headley, T. J. and Romig, A. D. Jr., Metall. Trans. Vol. 17A, 1986, p. 2107.

169. Cieslak, M. J., Headley, T. J. and Romig, A. D. Jr., Metall. Trans. Vol. 17A, 1986, p. 2035.

170. Sahm, P. R. and Schubert, F., Proc. Conf. On Solidification and Casting of Metals, Sheffield, England, 1979, p. 389.

171. Scheil, E., Z. Metallk., Vol. 34, 1942, p. 70.

172. DuPONT, J. N., Robino, C. V., Marder, A. R. and Notis, M. R., Metall. Mater. Trans. Vol. 29A, 1998, p. 2797.

173. David, S. A., Vitek, J. M., Babu, S. S., Boatner, L. A. and Reed, R. W., Sci. & Tech. of Weld. & Join., 2, (2) 79 (1997).

174. Nakkalil, R., Richards, N. L. and Chaturvedi, M. C., Scripta Metall., 26, 545 (1992).

175. Cieslak, M. J., Stephens, J. J. and Carr, M. J., Metall. Trans., Vol. 19A, 1988, p 657.

176. Knornovsky, G. A., Cieslak, M. J., Headley, T. J., Romig, A. D. Jr. and Hammetter, W. F., Metall. Trans. Vol. 20A, 1989, p. 2149.

177. Thompson, R. G., Mayo, D. E. and Radhakrishann, B., Metall. Trans. Vol. 22A, 1991, p. 557.

178. Nash P. and Jayanth, C. S., Bull. Of Alloy Phase Diagrams, 5, 144 (1984).

179. Chen, G. H. and Chen, C., Scripta Metall. Mater. Vol. 27, 1992, p. 121.

180. Samuelsson, E., Keefe, P. W. and Furgason, R. W., in Proceedings of Superalloys Conference 1992, edited by S. D. Antolovich, R. W. Stusrud, R. A. Mackay, D. L. Anton, T. Khan, R. D. Kissinger and D. L. Klarstrom (The Minerals, Metals & Materials Society 1992) p. 361.

181. Murata, Y. and Yukawa, N., Scripta Metall., 20, 693 (1986).

182. Sellamuthu, R. and Giamei, A. F., Metall. Trans. Vol. 17A, 1986, p. 419.

183. Baldan, A., J. Mater. Sci., Vol. 25, 1990, p. 4341.

184. Liu, L., Zhen, B. L., Banerji, A., Reif, W. and Sommer, F., Scripta Metall. Mater. Vol. 30, 1994, p. 593.

185. Babu, S. S., David, S. A. and Vitek, J. M. and Miller, M. K., Journal De Physique IV 6 (C5) 253 (1996).

186. Yukawa, N., Murata, Y. and Noda, T., Superalloys Conf., USA, p. 83, (1984).

187. Sponseller, D. L., Superalloys Conf., USA, p. 259, (1996).

188. Backerud, L., Carlsson, B., Oskarsson, R. and Mikus, M., Scand. J. Metallurgy, Vol. 5, 1976, p. 49.

189. Rhines, F. N., Phase Diagrams in Metallurgy, McGraw-Hill Book Co., 1956.

190. Zupanic, F., Boncina, T. and Krizman, A. in Proceedings of Superalloys Conference 2000, edited by Pollock, T. M., Kissinger, R. D., et al, (The Minerals, Metals & Materials Society 2000) p. 239.

191. Campbell, J., Metallography, Vol. 4, 1971, p. 269.

192. Davies, V. L., A.F.S. Cast Met. Res. J., 1975, p. 33.

193. Bachelet, E. and Lesoult, G., 'High Temperature Alloys for Gas Turbines', Applied Science Publishers, London, (ed. Coutsouradis et al), 1978, p. 665.

194. Chen, Q, Z., Kong, Y. H., Jones, C. N. and Knowles, D. M., Scripta Mater. Vol.51, 2004, p. 155.

195. Li, H. and Chaki, T. K., Proc. High-Temperature Ordered Intermetallic Alloys VI. Part I; Boston, MA; USA, 1995. p. 375.

196. Superalloys II, ed. Sims, C. T., Stoloff, N. S. and Hagel, W. C., A Wiley-Interscience Publication John Wiley & Sons Inc. 1987.

197. Maxwell, D. H., Baldwin, J. F. and Radavich, J. F., Metallurgia and Metal Forming, 1975, p. 332.

198. Goldschmidt, H. J., J. Iron Steel Inst. Vol. 209, 1971, p. 910.

199. Kruger, R.M. and Was, G. S., Metall. Trans. Vol. 19A, 1988, p. 2555.

200. Karlsson, L. and Norden, H., Acta Metall. Vol. 36, 1988, p. 35.

201. Hu, B. and Li, H., Proc. Superalloys 1980 Conf., Champion; Pa, 1980. p. 423.

202. Carroll, K. G., Darken, L. S., Filer, E. W. and Zwell, L., Nature, Vol. 174, 1954, p. 978.

203. Delargy, K. M. and Smith, G. D. W., Metall. Trans. Vol. 14A, 1983, p. 1771.

204. Decker, R. F., in 'Source Book on Materials for Elevated Temperature Applications', ed. Bradley, E. F., ASM Metals Park, OH, 1979, p. 275-298.

205. Chen, W., Chaturvedi, M. C. and Richards, N. L., Metall. Mater. Trans. Vol. 32A, 2001, p. 931.

206. Radhakrishnan, B. and Thompson, R. G., Metall. Trans., 22A, 887 (1991).

207. Blavette, D., Duval, P., Letellier, L. and Guttmann, M., Acta Mater., 44, 4995 (1996).

208. Baeslack III, W. A., West, S. L. and Kelly, T. J., Scripta Meta., 22, 729 (1988).

209. Miller, W. A. and Chadwick, G. A., Acta Met., 15, 607, (1967).

210. Arata, Y., Matsuda, F. and Katayama, S., Trans. JWRI, 1977, p. 623.

211. Bailey, G. and Watkins, H., J. Inst. Metals, Vol. 80, 1951, p. 57.

212. Kny, E., Stolz, W. and Stickler, R., J. Vac. Sci. Tech. 17, 1208 (1980).

213. Aksay, I. A., Hoge, C. E. and Pask, J. A., J. Phys. Chem., 78, 1178 (1974).

214. Chatain, D., Rabkin, E., Derenne, J. and Bernardin, J., Acta Mater., 49, 1123 (2001).

215. Lehockey, E. M., Palumbo, G. and Lin, P., Metall. And Mat. Trans., 29A, 3069 (1998).

216. Kokawa, H., Lee, C. H. and North, T. H., Metall. Trans., 22A, 1627 (1991).

217. Nakkalil, R., Richards, N. L. and Chaturvedi, M. C., Acta Metall. Mater. 41, 3381 (1993).

218. Whelan, M. J., Metal Sci. J., Vol. 3, 1969, p. 95.

219. Aaron, H. B., Fainstein, D. and Kotler, G. R., J. Appl. Phy., Vol. 41, 1970, p. 4404.

220. Agren, J., Scan. J. Metall., Vol. 19, 1990, p. 2.

221. Grong, O., Metallurgical Modelling of Welding, 2nd edn. The Institute of Materials, London, 1997.

222. Christian, J. W., The Theory of Phase Transformations in Metals and Alloys, Pergamon Press, Oxford, 1975.

223. Bjorneklett, B. I., Grong, O., Myhr, O. R. and Kluken, A. O., Acta Mater., 46, 6257, (1998).

224. Soucail, M. and Bienvenu, Y., Mat. Sci. & Eng. A, 220, 215 (1996).

225. Madeleine Durand-Charre, The Microstructure of Superalloys, Gordon and Breach Science Pub. 1997.

226. Radhakrishnan, B., Interface Sci. Vol. 1, 1993, p. 175.

227. Aaronson, H. I., Decomposition of Austenite by Diffusional Processes (Wiley) 1962, p. 387.

228. Cahn, J. W., Hillig, W. B., and Sears, G. W., Acta Metall., Vol. 12, 1964, p. 1421.

229. Royer, A., Bastie, P. and Veron, M., Scripta Mater. Vol. 40, 1999, p. 955.

230. Stepanova, N. N., Sazonova, V. A. and Rodionov, D. P., Scripta Mater. Vol. 40, 1999, p. 581.

231. Nikolaev, B. and Tjaunov, G., J. Phy. Conden. Matter. Vol. 6, 1994, p. 9301.

232. Cahn, R. W., Siemers, P. A., Geiger, J. E. and Bardhan, P., Acta Metall. Vol. 35, 1987, p. 2737.

233. Watanabe, M., Horita, Z., Smith, David, J., McCartney, M. R., Sano, T. and Nemoto, M., Acta Metall. Mater. Vol. 42, 1994, p. 3381.

234. Janssen, M. M. P., Metall. Trans. Vol. 4, 1973, p. 1623.

235. Dupeux, M., Rouault-Rogez and Willemin, P., Mater. Res. Soc. Symp. Proc., Vol. 122, 1988, p. 169.

236. Karunaratne, M. S. A., Carter, P. and Reed, R. C., Acta Mater. Vol. 49, 2001, p. 861.

237. Lim, L. C., Yi, J. Z., Liu, N. and Ma, Q., Mater. Sci. Tech., Vol. 18, 2002, p. 407.

238. Handwerker, C. A., Cahn, J. W., Yoon, D. N. and Blendell, J. E., in Diffusion in Solids: Recent Developments (ed. Dayanada, M. D. and Murch, J. E.) T.M.S-AIME, Warrendale, Pa, 1986, p. 275.

239. Den Broeder, F. J. A., Acta Metall. Vol. 20, 1972, p. 319.

240. Tu, K. N., J. Appl. Phys., Vol. 48, 1977, p. 3400.

241. Hillert, M., Scripta Metall. 17, 237 (1983).

242. Radhakrishnan, B and Thompson, R. G., Scripta Metall. Mater. 24, 537 (1990).

243. Kriege, Owen H. and Baris, J. M., Trans. Of ASM, 62, 195 (1969).

244. Kuo, M. and Fournelle, R. A., Acta Metall. Mater. 39, 2835 (1991).

245. Kirkaldy, J. S., Acta Mater. 46, 5127 (1998).

246. Brechet, Y. and Purdy, G. R., Scripta Metall. 22, 1629 (1988).

247. Koul, A. K. and Thamburaj, R., Metall. Trans., 16A, 17 (1985).

248. Baker, S. W. and Purdy, G. R., Acta Mater. 46, 511 (1998).

249. Mattews, J. W., Misfit Dislocations: in Dislocations in Solids, Vol. 2 ed. F. R. N. Nabarro, North Holland, Amsterdam, 1979.

250. Nippes, E. F., et al, Weld. J., Vol. 34, 1955, p.183s

251. Qian, M. and Lippold, J. C., Acta Mater., Vol. 51, 2003, p 3351

252. Widgery, D. J., Metal Constr., Vol. 1, 1969, p. 328.

253. Lin, W., Lippold, J. C. and Baeslack, W. A. III., Weld. J., 1993, p. 135s.

254. Phillips, R. H. and Jordan, M. F., Metals Tech., Vol. 4, 1977, p. 396.

255. Lin, W., Nelson, T. W., Lippold, J. C. and Baeslack, W. A. III., International Trends in Welding Science and Technology; Gatlinburg, Tennessee; USA, 1993 p. 695.

256. Lundin, C. D., Qiao, C. Y. P. and Swindeman, R. W., International Trends in Welding Science and Technology; Gatlinburg, Tennessee; USA, 1993 p. 801.

257. Demyantsevich, V. P., Welding Production, Vol. 14, 1967, p. 1.

258. Lin, W., Baeslack, W. A. and Lippold, J. C., Recent Trends in Welding Science and Technology, ASM International, Materials Park, OH USA, 1989, p. 609.

259. Thompson, R. G., Dobbs, J. R. and Mayo, D. E., Weld. J., Vol. 65, 1986, p. 299s.

260. Dike, J. J., Brooks, J. A. and Li, M., in Mathematical Modelling of Weld Phenomena 4, ed. H. Cerjak, The Institute of Materials, London, 1988, p. 199.

261. Borland, J. C., Welding and Metal Fabrication, Vol. 47, 1979, p. 99.

262. Hier-Majumder, S, Leo, P. H. and Kohlstedt, D.L., Acta Mater. Vol. 52, 2004, p. 3425.

263. Masubuchi, K., J. Metals, Vol. 33, 1981, p. 19.

264. Cieslak, M. J., Weld. J., Vol. 70, 1991, p. 49s.

Refereed Journal Publications from the Present Thesis

1. Ojo, O.A., Richards, N.L and Chaturvedi, M.C., A Study of Fusion Zone and Heat Affected Zone Microstructures in TIG Welded IN 738LC Superalloy, Submitted to Metallurgical and Materials Transactions A, 2004.

2. Ojo, O.A., Richards, N.L and Chaturvedi, M.C., Microstructural study of weld fusion zone of TIG welded IN 738LC nickel-based superalloy. Scripta Materialia. Volume 51, 2004, pages 683-688.

3. Ojo, O.A., Richards, N.L and Chaturvedi, M.C., Liquid film migration of constitutionally liquated γ' in weld heat affected zone (HAZ) of Inconel 738LC superalloy. Scripta Materialia. Volume 51, 2004, pages 141-146.

4. Ojo, O.A., Richards, N.L and Chaturvedi, M.C., Contribution of constitutional liquation of gamma prime precipitate to weld HAZ cracking of cast Inconel 738. Scripta Materialia. Volume 50, 2004, pages 641-646.

5. Ojo, O.A., Richards, N.L and Chaturvedi, M.C., Liquation of various phases in the heat affected zone of IN 738 superalloy. Material Science and Technology, Volume 20, pages 206-213, 2004.

6. Ojo, O.A., Richards, N.L and Chaturvedi, M.C., On incipient melting during high temperature heat treatment of cast Inconel 738 superalloy. Journal of Material Science, Volume 39, pages 7401-7404, 2004.

Other Refereed Journal Publications

1. Ojo, O.A., Richards, N.L and Chaturvedi, M.C., Effect of gap size and process parameters on diffusion brazing of Inconel 738. Journal of Science and Technology of Welding and Joining, Volume 9, 2004, pages 209-220.

2. Chaturvedi, M.C., Ojo, O.A. and Richards, N.L, Diffusion brazing of cast Inconel 738 superalloy. Advances in Technology of Materials and Materials Processing Journal, Volume 6, 2004, pages 206-213.

3. Ojo, O.A., Richards, N.L and Chaturvedi, M.C., Isothermal solidification during liquid phase bonding of Inconel 738 superalloy. Journal of Science and Technology of Welding and Joining, 2004, (Accepted).

Conference Presentations

1. Ojo, O.A., Richards, N.L and Chaturvedi, M.C., On The Weld HAZ Liquation Cracking of Cast Inconel 738LC Superalloy. 15th Canadian Materials Science Conference, Halifax, Canada, June 2003.
2. Crouch, S. M., Ojo, O.A., Richards, N.L and Chaturvedi, M.C., Effect of Process Temperature on Formation of Non-Equilibrium Phases during Diffusion Brazing of IN 738 Superalloy. 15th Canadian Materials Science Conference, Halifax, Canada, June 2003.
3. Ojo, O.A., Richards, N.L and Chaturvedi, M.C., Transient Liquid Phase Brazing of Inconel 738 Superalloy. 14th Canadian Materials Science Conference, Winnipeg, Canada, June 8-11, 2002.

4. Ojo, O.A., Richards, N.L and Chaturvedi, M.C., Effects of Brazing Parameters on Diffusion Brazed Joint of Inconel 738 Superalloy. NSF Design, Service and Manufacturing Grantees and Research Conference, San Juan, Puerto Rico, January 7-10, 2002.
5. Ojo, O.A., Richards, N.L and Chaturvedi, M.C., Microstructural / Mechanical Property Correlation of Diffusion Brazed Inconel 738. 13th Canadian Materials Science Conference, Sudbury, Canada, June 5-8, 2001.